

# Jet-Reorientation in X-shaped Radio Galaxies

Dissertation  
zur  
Erlangung des Doktorgrades (Dr. rer. nat.)  
der  
Mathematisch–Naturwissenschaftlichen Fakultät  
der  
Rheinischen Friedrich–Wilhelms–Universität Bonn

vorgelegt von  
**Helge Rottmann**  
aus Aachen

Bonn, August 2001

Angefertigt mit Genehmigung  
der Mathematisch–Naturwissenschaftlichen Fakultät  
der Rheinischen Friedrich–Wilhelms–Universität Bonn.

1.Referent: Professor Dr. U. Klein  
2.Referent: Professor Dr. R. Wielebinski

Tag der Promotion: 4.9.2001

# Contents

<b>1</b>	<b>Introduction</b>	<b>5</b>	
1.1	Active Galactic Nuclei (AGN) . . . . .	5	
1.2	Unification Schemes for AGN . . . . .	6	
1.3	X-shaped Radio Galaxies . . . . .	7	
1.4	Outline of the Thesis . . . . .	8	
1.5	Conventions . . . . .	9	
<b>2</b>	<b>Introduction to X-shaped Radio Galaxies</b>	<b>11</b>	
2.1	Sample Selection . . . . .	11	
2.2	Notes on Individual Sources . . . . .	12	
2.3	First Conclusions . . . . .	17	
<b>3</b>	<b>Single-Dish Mapping of X-shaped Radio Galaxies</b>	<b>21</b>	
3.1	Observations and Data Reduction . . . . .	21	
3.1.1	The 32 GHz receiver . . . . .	22	
3.1.2	Data reduction at 32 GHz . . . . .	22	
3.2	The 32 GHz maps . . . . .	23	
3.3	The 10.45 GHz Maps . . . . .	29	
3.4	The 4.85 GHz Maps . . . . .	35	
3.5	The 2.7 GHz Maps . . . . .	41	
<b>4</b>	<b>Interferometric Images</b>	<b>43</b>	
4.1	WSRT Data . . . . .	43	
4.2	NVSS Data . . . . .	43	
4.3	WENSS Data . . . . .	44	
4.4	Miscellaneous Data . . . . .	44	
<b>5</b>	<b>Formation of X-shaped Radio Sources</b>	<b>Part I: Introduction</b>	<b>63</b>
5.1	Backflow . . . . .	63	
5.2	Buoyancy . . . . .	65	
5.3	Jet-reorientation & Beam Precession . . . . .	66	
5.3.1	Matter Accretion . . . . .	66	
5.3.2	Central Binary Black Holes . . . . .	67	
5.4	Steady Precession or Fast Realignment? . . . . .	69	
5.5	Summary and Conclusions . . . . .	71	

<b>6</b>	<b>Spectral Analysis</b>	<b>73</b>
6.1	Integrated Spectra . . . . .	73
6.2	Spectral Index . . . . .	73
6.3	Spectral Ageing . . . . .	74
6.4	Minimum Energy . . . . .	76
6.5	Results . . . . .	77
6.5.1	4C12.03 . . . . .	77
6.5.2	NGC 326 . . . . .	81
6.5.3	3C52 . . . . .	85
6.5.4	3C136.1 . . . . .	89
6.5.5	B2 0828+32 . . . . .	94
6.5.6	3C223.1 . . . . .	99
6.5.7	3C315 . . . . .	104
6.5.8	3C379.1 . . . . .	109
6.5.9	3C403 . . . . .	111
6.6	Summary . . . . .	117
<b>7</b>	<b>Formation of X-shaped Radio Sources      Part II: Revisited</b>	<b>119</b>
7.1	Reorientation and Flow Speeds . . . . .	119
7.2	Reorientation Angle . . . . .	121
7.3	Summary and Conclusions . . . . .	127
<b>8</b>	<b>Jet Reorientation: A Common Event?</b>	<b>131</b>
8.1	X-shaped Sources in Hiding . . . . .	131
8.2	Simulated Source Evolution . . . . .	132
8.3	Simulated Maps . . . . .	134
<b>9</b>	<b>Summary</b>	<b>141</b>
<b>A</b>	<b>Test Observations with the 100-m Telescope at 32 GHz</b>	<b>143</b>
<b>B</b>	<b>Projected Angle Distributions</b>	<b>147</b>
<b>C</b>	<b>Acronyms</b>	<b>169</b>
	<b>References</b>	<b>171</b>
	<b>Acknowledgments</b>	<b>177</b>

# 1

---

## Introduction

### 1.1 Active Galactic Nuclei (AGN)

The first discrete radio source was discovered by Hey et al. (1946). This source – Cygnus A – is known today to be the second brightest radio source in the northern hemisphere. With the help of better instrumentation soon more of such discrete radio sources were detected, e.g. 3C273, Cen A, and M87 to name a few. However, their nature remained mysterious until Bolton et al. (1949) succeeded in identifying two sources (M87 and Centaurus A) with two well-known and close-by elliptical galaxies. This, and further identifications of radio sources with known galaxies finally established the extragalactic origin of the discrete radio sources. The nature of the radio emission was found to be non-thermal and polarization studies indicated that the radiation process is synchrotron radiation from relativistic particles thus manifesting that the radio sources must possess magnetic fields. Being able to derive the distances of radio sources by measuring the redshifts of their host galaxies it became obvious that radio galaxies are reservoirs of enormous energy. Burbidge (1959) first pointed out that the *minimum* energy contained in a radio source like Cygnus A is of the order of  $10^{60}$  erg! This estimate was in fact so high that most classical processes that had been envisioned to be responsible for the observed radio activity (like the collision of two galaxies) had to be discarded. Furthermore,

the energy release occurs in an extremely compact region (comparable to the size of the solar system!) at the center of the host galaxy. The physical mechanism capable of releasing such amounts of energy in a tiny volume was not understood at the time and even though considerable progress has been made since then it is still not fully understood today. Lacking a clear understanding of the processes at work in the centers of these galaxies the “black-box” concept of a central engine, the so-called Active Galactic Nucleus (hereafter AGN) was introduced. Theoretical work done in the early 60’s revealed that the most efficient source of energy would be the release of gravitational potential energy. The possibility that supermassive black holes might exist finally led to the now widely accepted standard model of AGN. Today, it is believed that the main constituent of an AGN is indeed a supermassive black hole of mass  $10^7 - 10^9 M_{\odot}$ . Gas clouds in the vicinity are being accelerated by the potential of the black hole and will eventually form an accretion disk in its equatorial plane. Viscous drags lead to the outward transport of angular momentum and consequently to the infall of matter onto the black hole.

With the advent of modern high-resolution radio interferometry it was possible to resolve some of the nearby radio galaxies. It turned out that many objects (also Cygnus A) exhibit extended radio emission in the form of

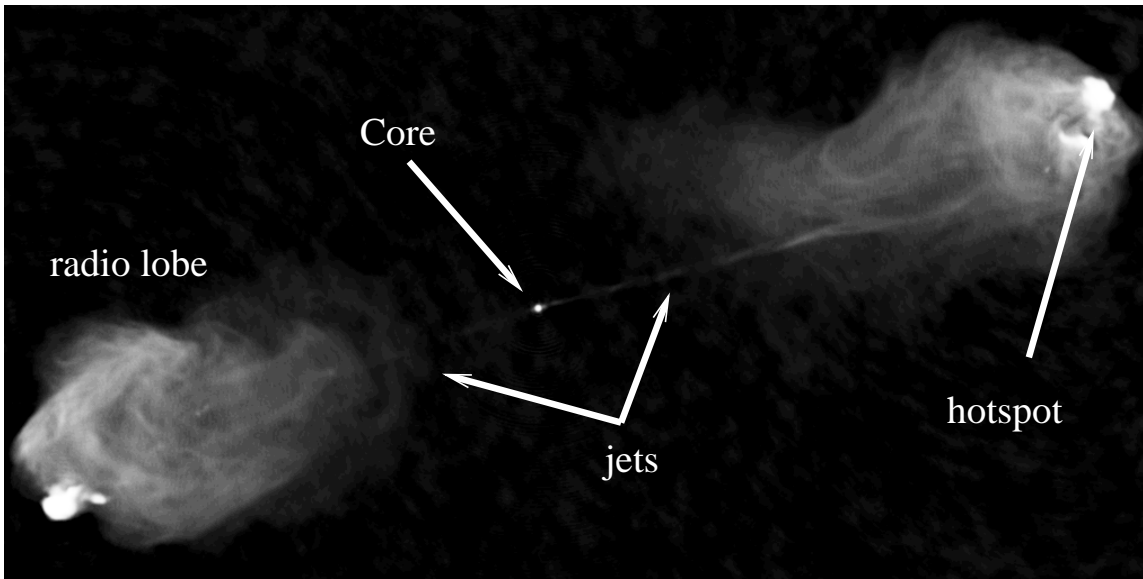


FIGURE 1.1— The prototypical radio galaxy Cygnus A. The original image has been published by Perley et al. (1984).

two so-called radio lobes (see Fig. 1.1). These radio lobes are usually located well outside of the host galaxy and can reach a length of several Mpc for the most extended Giant Radio Galaxies (GRGs). The radio lobes are connected to the core by two collimated beams, the jets. With modern VLBI methods the jets can indeed be traced to distances very close to the AGN. The jets consist of matter that is being accelerated to relativistic speeds and ejected by the central engine along the spin axis of the black hole. The exact mechanism by which jets form and stay collimated over large distances remains however unclear. The places at which the jet plasma finally interacts with the interstellar or intergalactic medium and loses its kinetic energy are marked by the bright hotspots.

Cygnus A is the prototypical high-luminosity so-called FR II radio galaxy. Fanaroff & Riley (1974) first noted a sharp dichotomy of radio galaxies into high and low luminosities sources. Radio galaxies with luminosities at 178 MHz of  $L_{178} > 6.3 \times 10^{25} \text{ W Hz}^{-1} h^{-2}$  ( $h = H_0/100$ ; where  $H_0$  denotes the Hubble Constant in  $\text{km s}^{-1} \text{Mpc}^{-1}$ ) are classified as

FR II type, whereas lower luminosity sources fall into the FRI category. Apart from the luminosities FRI and FR II radio galaxies also can be distinguished by their different morphologies. FRI objects do not have bright hotspots. Their brightest emission occurs in regions close to the core therefore they are often also referred to as being *edge-darkened*. As outlined above, FR II sources instead appear to be *edge-brightened*. The reason for this dichotomy is still under debate, but most likely reflects the transition from a transsonic, turbulent jet flow (FRI) to a supersonic, laminar flow (FR II).

## 1.2 Unification Schemes for AGN

Today, we know that radio galaxies, such as Cygnus A, represent only a subclass within the large “zoo” of various AGN types, such as quasars, Seyferts, BL Lac, LINERs etc.. The theory of relativistic aberration triggered attempts to unify all AGN by attributing their different properties to orientation-dependent effects. Relativistic beaming causes synchrotron radiation to be beamed into the direction of motion of the relativistic particles.

FIGURE 1.2— Sketch of the prevailing picture of the physical structure of AGN. At the center is a supermassive black hole surrounded by an accretion disk. Outside of the disk resides a torus (or a warped disk) of dust and gas. The broad line region (BLR) contains gas clouds that move with high velocities in the strong gravitational potential in the vicinity of the central black hole. Further out in the so-called narrow line region (NLR) one finds slower moving clouds. The radio jets transport particles outward perpendicular to the accretion disk. Radio-loud AGN can appear as narrow line radio galaxies (NLRG), broad line radio galaxies (BLRG), Quasars, or BL Lacs depending on their angle to the line of sight. Similarly, the distinction between radio-quiet Seyfert 1 and Seyfert 2 galaxies is a consequence of obscuration by the central dust torus on transverse line of sights.

Consequently the intensity of radiation is increased when we observe a relativistic plasma flow that is oriented towards us, and vice-versa is decreased when we observe a receding flow. Because we know that the jet particles move at relativistic speeds a strong dependence of the appearance of an AGN on the viewing angle is expected. Barthel (1989) has proposed a unification scheme that includes orientation effects due to beaming as well as by obscuration by a dust torus in the vicinity of the central black hole. Modern unification theories comprise – apart from orientation depend effects – also separate schemes for radio-loud and radio-quiet AGN. The prevailing view of the physical structure of AGN is illustrated in Fig. 1.2. At the center is a supermassive black hole that accretes matter through an accretion disk. Well outside the disk a torus of dust and gas obscures the radiation from the central source along some lines of sight. Gas clouds that move with high velocities in the potential of the central black hole form the so-called broad-line region. Beyond the torus slower moving clouds form the narrow line region. Ejection of jet material occurs along the spin-axis of the central black hole. The optical emission line properties of the various types of AGN then depend on (and determine) their orientation angle to the line of sight. If the central region is obscured by the dust torus we detect only narrow emission lines from the narrow line region. With decreasing viewing

angle we look deeper into the AGN and will observe broad emission lines from the broad line region. At yet smaller angles to the line of sight (near  $0^\circ$ ) AGN show very unusual spectra that lack strong absorption or emission features and probably reflect the relativistically beamed synchrotron continuum of the jet and central source. Even though many details of the unification model are under heavy debate there is considerable observational evidence in favor of the basic unification concept.

### 1.3 X-shaped Radio Galaxies

X-shaped radio sources form a peculiar and very small subclass of radio galaxies. They are distinguished from classical double-lobed radio sources like Cygnus A by their peculiar large-scale radio morphology (comp Fig.1.3). X-shaped radio galaxies exhibit large, symmetric, and low-luminosity extrusions of radio plasma that extend at some angle from the nucleus to (projected) distances comparable to or exceeding the length of the active radio lobes. These structures have also been referred to as ‘wings’. Due to their morphological similarity with radio lobes the term *secondary* lobes has been adapted throughout this thesis. At present only about a dozen of such sources have been found indicating that these objects either represent a very exotic type of AGN or that they are at the moment in an exceptional and/or short-lived phase of AGN evolution. The first X-shaped source, NGC326, was discovered and discussed by Ekers et al. (1978). The authors argued in favor of jet precession to explain the formation of their secondary lobes. However, as the quality of the radio images improved and new X-shaped source were discovered their morphology – most prominently of NGC 326 itself – could not be easily explained by a constant precession anymore. Other mechanisms were invoked to account for the formation of X-shaped radio sources which included buoyant bending of the radio lobes by the ambient medium, deflected backflows, gravitational interaction/merging by companion galaxies, relativistic Lense-Thirring precession

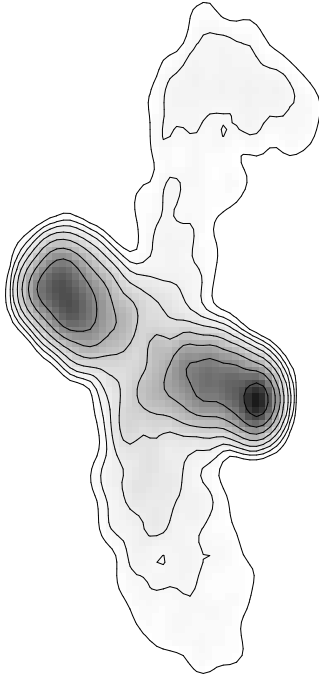


FIGURE 1.3— X-shaped radio galaxies are distinguished from their classical double lobe radio galaxies by their secondary radio lobes.

and precession due to binary black holes. Even though some mechanisms seem to be implausible nowadays the exact formation process of X-shaped radio galaxies remains puzzling. However, understanding these mechanisms can be highly beneficial in order to improve our knowledge of the physical structure of AGN. The large-scale radio emission of radio galaxies represents a snapshot of their activity history and yields valuable information of their evolution; information which cannot be inferred from high-resolution studies of the nuclear region. If the formation of X-shaped radio galaxies can be attributed to processes inherent to the AGN we can hope to answer questions of more general interest like which events trigger activity and on which timescales (if at all) does it seize. Is there a connection between merging and the (re)start of activity in AGN, and what feeds the central en-

gine? Finally: how does the phenomenon of X-shaped radio galaxies relate to other radio sources? Do all radio galaxies experience an X-shaped phase during their evolution and if yes how long does it last?

#### 1.4 Outline of the Thesis

Chapter 2 introduces the sample of X-shaped sources studied in this thesis. Selection effects that apply to X-shaped radio galaxies will be briefly discussed. For each source relevant properties and the most important findings from the literature are presented.

The observations and data reduction of the sample of X-shaped sources are presented in the Chapters 3 and 4.

This is followed by an introduction to the possible mechanisms proposed to be responsible for the formation of X-shaped sources in Chapter 5. The basic theory of these processes is outlined and the possibilities to test whether or not they are responsible for the genesis of X-shaped galaxies will be discussed.

Chapter 6 contains the multi-frequency spectral analysis of the sample of studies sources. A short review of the spectral ageing and minimum energy theories is given. For each source an integrated spectrum is constructed. In the following the multi-frequency data are used to produce images of the spectral index distribution, compute minimum magnetic fields, and derive break frequencies and spectral ages along the transition path connecting the primary to the secondary lobes. In the last section of Chapter 6 the results will be summarized and implications will be discussed.

Chapter 7 will apply the results of the spectral analysis to the formation models. In particular the speed and duration of the reorientation event and the most likely distribution of intrinsic angles between the secondary and primary lobes will be derived. These findings will be compared with the predictions made by the different proposed formation mechanisms. Chapter 8 examines the possibility that the phenomenon of jet reorientation is not restricted to the small class of X-shaped sources but instead does occur regularly also in other



“normal” double-lobed radio galaxies. Finally, in Chapter 9 a summary of the thesis is given and suggestions for future work are made.

## 1.5 Conventions

If not otherwise stated the following conventions were followed throughout the thesis.

- The spectral index is defined by the spectrum in the following way:  $S \propto \nu^\alpha$ .
- In the calculations a Hubble Constant of  $H_0 = 75 \text{ km s}^{-1} \text{ Mpc}^{-1}$  and  $q_0 = 0.5$  was used.

A list of acronyms can be found in Appendix C.



# 2

---

## Introduction to X-shaped Radio Galaxies

### 2.1 Sample Selection

In the framework of this thesis nine X-shaped radio galaxies have been studied in detail. A list of these sources together with their basic properties can be found in Tab. 2.1. The sources have been selected solely on the basis of their morphology. To this end published images have been inspected to identify sources which possess a pair of secondary lobes with a projected length similar to, or exceeding the length of the active radio lobes. It is important to note that the images on which the selection was based have been obtained with various instruments and with vast differences in sensitivity and resolution. Therefore, the sample of sources presented here is highly inhomogeneous and in no sense statistically complete. Apart from the biases introduced by selecting the sources from the literature there are other selection effects at work when studying X-shaped radio galaxies.

- **Orientation & projection.** The appearance of a particular X-shaped source can be heavily influenced by projection effects depending on the viewing angle of the observer with respect to the source. In extreme cases – when the inclination of the lobes (either primary or secondary) is close to the line-of-sight – the lobes will appear shortened to an extent that the object might not be classified as being X-shaped at all. Thus, this selection effect lets us preferentially pick out sources that have primary and secondary lobes close to

the plane of the sky.

- **Source structure.** The intrinsic source angle (the angle between the primary and the secondary lobes) has a large effect on whether or not a source would appear X-shaped to an observer. Objects with intrinsic angles close to  $0^\circ$  or  $180^\circ$  will very likely appear as normal radio galaxies because the secondary lobe emission will blend into the emission from the primary lobes. Consequently these sources would not be contained in the sample studied here.

In addition sources having longer secondary lobe lengths have a higher probability of being classified as being X-shaped.

- **Dynamic range & missing flux.** Large differences in the flux of the primary compared to the secondary lobes can effectively conceal the X-shaped nature of a source. This is mainly due to the imaging techniques employed when creating radio images. The sidelobe emission produced by bright primary radio lobes is often stronger than the underlying emission from the secondary radio lobes. Therefore, image cleaning has to be performed with great care and down to low residual flux levels in order to even notice the existence of any secondary lobes. In many cases the secondary lobe emission can be detected only after several iterations of self-calibration. In that

context it is noteworthy that in order to perform self-calibration one needs sufficiently good data with good uv-coverage and high signal-to-noise.

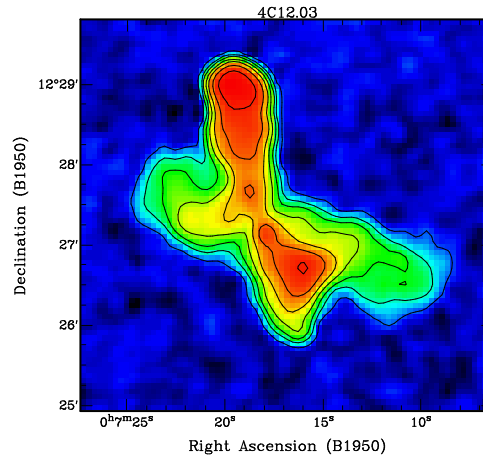
Interferometric imaging can introduce another effect that can conceal the presence of secondary lobes. Due to the incomplete coverage of the innermost regions of the uv-plane low spacial frequencies that represent the large-scale source structure might not be fully recovered (this is known as the missing-flux problem). The secondary lobes of radio galaxies usually exhibit little small-scale structure (probably because they are older and more relaxed) and thus they are more affected by missing-flux than the primary lobes. In adverse configurations of the interferometer with only few short baselines the secondary lobes can remain completely undetected. Therefore, we suspect that at least some known radio galaxies might possess up to now undetected secondary lobes.

## 2.2 Notes on Individual Sources

In the following the selected X-shaped sources will be presented and the most relevant findings from the literature will be briefly summarized.

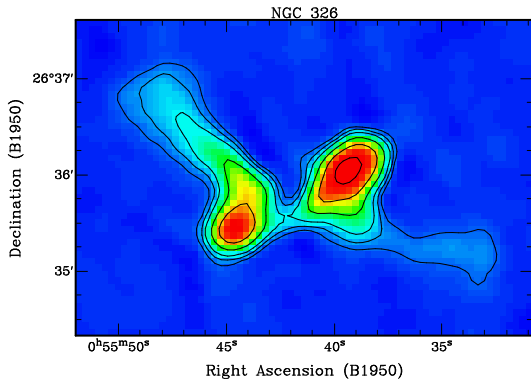
### 4C12.03

4C12.03 is associated with an E3 host galaxy at a redshift of  $z=0.11$  (Heckman et al. 1994). The source has been classified as a low-emission line radio galaxy (LERG) by Laing et al. (1983). With a luminosity at 178 MHz of  $1.36 \times 10^{26} \text{ W Hz}^{-1} h^{-2}$  4C12.03 barely lies above the FRI/FRII division (Fanaroff & Riley 1974). Also, morphologically 4C12.03 seems to be a transition case between FRI and FRII sources. Even though the radio source is clearly edge brightened it is missing bright and clearly defined hotspots. The high resolution maps presented by Leahy & Perley (1991) have revealed the X-shaped nature of 4C12.03.

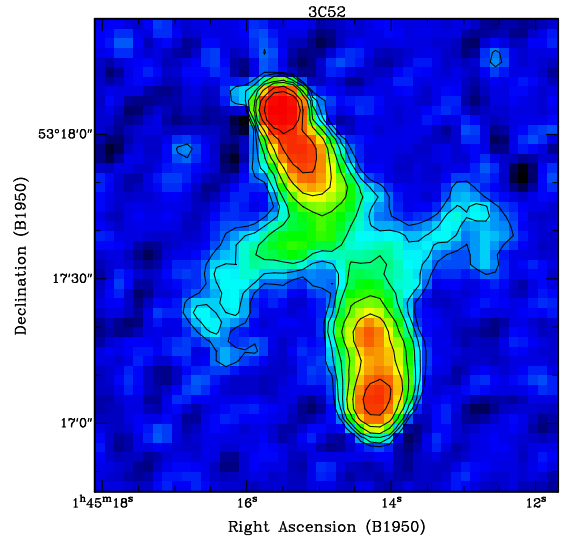


### NGC 326

This galaxy is the brightest member of the Zwicky cluster 0056.9+2636 (Zwicky & Kowal 1968). It is a dumbbell galaxy containing two equally bright nuclei with a projected separation of  $6''$  (Wirth et al. 1982). The host galaxy is accompanied by a smaller elliptical galaxy approximately  $2'$  to the northeast. Recently, Werner et al. (1999) have reexamined the cluster of galaxies around NGC 326. The authors have determined redshifts and velocity dispersions for 8 objects close to NGC 326 and could confirm their cluster membership. NGC 326 was the first X-shaped radio source discovered (Ekers et al. 1978). With a monochromatic luminosity at 178 MHz of  $L_{178}=1.25 \times 10^{25} \text{ W Hz}^{-1} h^{-2}$  it qualifies as a FRI object even though it lies very close to the FRI/FRII borderline. Our analysis suggests (see Sect. 6.5.2) that most probably the 178 MHz flux of NGC 326 has previously been underestimated. However, even with a reviewed luminosity of  $L_{178}=2.5 \times 10^{25} \text{ W Hz}^{-1} h^{-2}$  NGC 326 remains within the FRI class. Ekers et al. (1978) have proposed a precessing beam model to explain the unusual appearance of the source. However, deeper radio images presented by Formont (1981) and Ekers (1982) revealed the source to be much more extended than originally perceived. Furthermore, because the



secondary lobes do not show any curvature at larger distances from the core Wirth et al. (1982) concluded that steady jet precession must be ruled out as the formation mechanism. Instead the authors proposed a model in which the gravitational interaction of the two dumbbell cores effect the orientation of the radio jet. Golombek et al. (1988) have performed deep pointed IRAS observations of NGC 326 but have not detected any significant infrared emission. The X-ray properties of NGC 326 and the surrounding medium have been studied thoroughly by Worrall & Birkinshaw (1994) and Worrall et al. (1995). The authors detected bright asymmetrical X-ray emitting gas surrounding NGC 326. The X-ray emission is unusually extended ( $\approx 800$  kpc;  $H_0 = 50 \text{ km s}^{-1} \text{ Mpc}^{-1}$ ) and is rather of “cluster” than of “group” scale. The X-ray spectrum is best approximated by a single temperature Raymond-Smith model (Raymond & Smith 1977) with a temperature of  $kT \sim 2 \text{ keV}$ . The peak of the X-ray emission coincides with the position of the host galaxy. Worrall & Birkinshaw (1994) have demonstrated that the cluster gas is cooling too slowly for a cooling flow to have been initiated. Worrall et al. (1995) have proposed buoyancy to account for the formation of the secondary lobes.

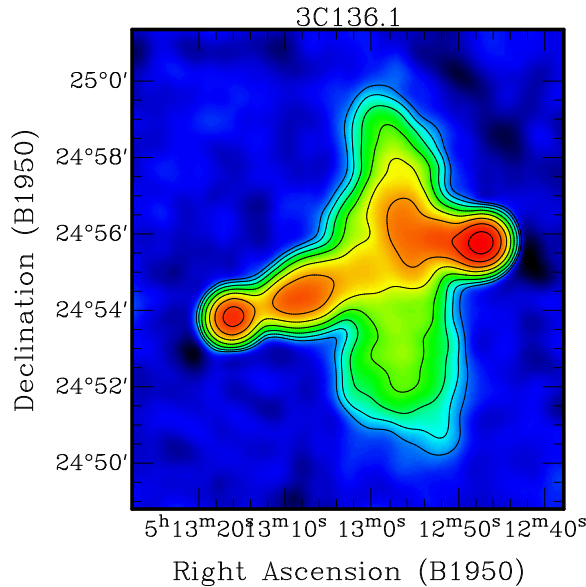


### 3C52

Located at a redshift of  $z=0.2845$  (Spinrad et al. 1985) 3C52 is the most distant X-shaped source presently known. 3C52 was reported to lie in a cluster by Wyndham (1966). HST imaging by de Koff et al. (1996) showed the galaxy to be elongated along the north-south axis and to exhibit a pronounced dust disk which might indicate a previous merger event. The emission line type of 3C52 is not yet determined due to the low galactic latitude of the object. In the radio regime 3C52 is the most luminous (at 178 MHz) of all known X-shaped sources. In fact, it is the only object which clearly qualifies as a FR II source. Radio maps of 3C52 were presented by Leahy & Williams (1984) and Pooley et al. (1987). A spectral analysis has been performed by Alexander & Leahy (1987).

### 3C136.1

Due to its low galactic latitude the host galaxy of 3C136.1 hasn't been studied in detail up to now. In particular, it is not known whether it is a broad- or narrow-line radio galaxy. However, strong  $[\text{OIII}]\lambda\lambda 4959, 5507$  emission lines have been reported by Smith et al. (1976). This suggests that 3C136.1 is a narrow-line radio galaxy, because these lines appear to be absent or at least very weak in broad-line spectra. Recently, HST images of the host



of 3C136.1 were presented by Martel et al. (1999). The galaxy appears flattened and warped and bears no resemblance to an elliptical galaxy. The authors report on two, possibly three nuclei and suggest that this galaxy is in the throes of a merger. With  $L_{178} = 6.9 \times 10^{25} \text{ W Hz}^{-1} \text{ h}^{-2}$  it barely qualifies as a FRII source. Radio images of 3C136.1 have been presented by Leahy & Williams (1984). High resolution maps of the hotspots can be found in Leahy et al. (1997). A spectral analysis of 3C136.1 has been performed by Alexander & Leahy (1987). The authors have derived spectral ages of 20 - 80 Myr across the lobes of 3C136.1.

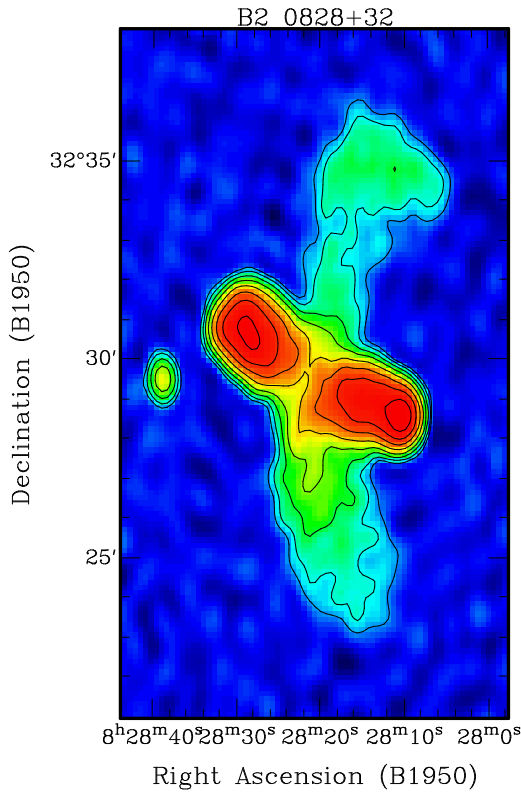
### B2 0828+32

B2 0828+32 is the most extended X-shaped source known at present. The secondary lobes have a projected linear size of  $612 \text{ kpc } h^{-1}$ .

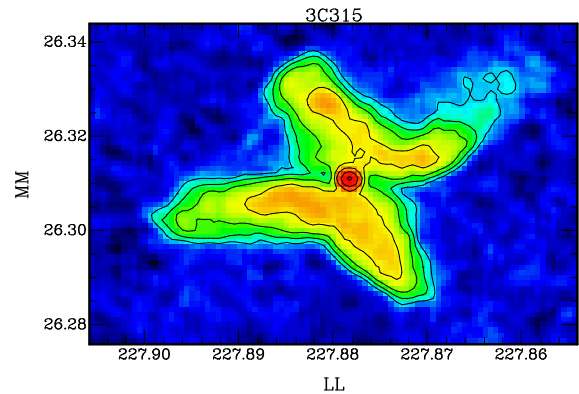
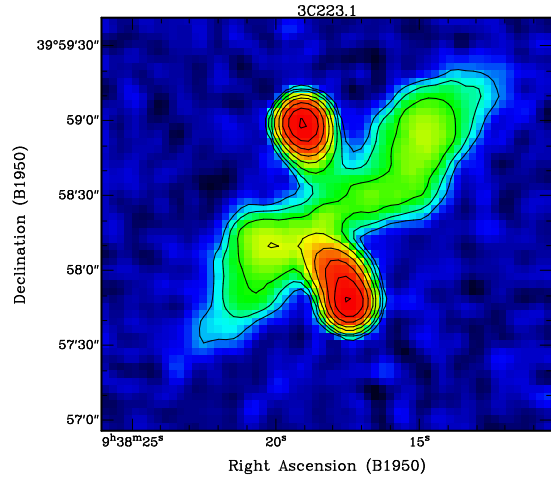
The host galaxy of B2 0828+32 has been studied by Ulrich & Rönnback (1996). The galaxy does neither have a double core nor a companion brighter than  $M_V = -16.7$ . The luminosity profile shows weak traces of a possible merger event  $\sim 10^8$  years ago. Furthermore, the host galaxy is not located in a cluster, even though it is surrounded by many faint galaxies. The radio luminosity is low. With  $L_{178} = 6.8 \times 10^{24} \text{ W Hz}^{-1} \text{ h}^{-2}$  it lies about one order of magnitude below the FRI/FRII division even though the morphology of the active lobes indicates FRII membership. Radio maps of B2 0828+32 in total, as well as in polarized intensity were presented by Parma et al. (1985). The authors report on high fractional polarization within the source with values up to 20-30%. The spectral index of the secondary lobes is quite steep but Parma et al. (1985) did not detect any significant spectral steepening within the lobes. Mack et al. (1994) confirmed the high degrees of polarization with values of up to 40% at 10.5 GHz in the secondary lobes. A thorough spectral analysis of the source was presented by Klein et al. (1995). The spectral index across the primary lobes is fairly constant ( $\alpha \sim 0.7$ ) but is steepening towards the secondary lobes ( $\alpha \sim 1.1$ ). A particle age for the secondary lobes of  $\sim 70$  Myr is derived. Klein et al. (1995) propose a modified precession model to account for the X-shaped morphology of B2 0828+32. Within this model the length of the precessing jet has decreased strongly over the last  $2 \times 10^8$  yr, resulting in a stretched elliptic path of the hotspots through the medium.

### 3C223.1

The host galaxy of 3C223.1 was classified as a DE4 with an asymmetrical envelope (Wyndham 1966) and was reported to be unusually red (Eisenhardt & Lebofsky 1987). 3C223.1 lies behind the Zwicky cluster Zw0938+399 but seems to be isolated or in a poor group itself (Sandage 1972). The Abell richness of this group was estimated to be  $\leq 1$  by Gregory & Burns (1982). Consistent with this finding is the non-detection of X-ray emis-



sion from 3C223.1 or its surroundings (Burns et al. 1981). The host galaxy was imaged as part of the HST Snapshot Survey (de Koff et al. 1996). The galaxy has a strong central bulge and a very pronounced dust disk. The secondary lobes are oriented perpendicular to the dust disk. 3C223.1 has been classified as a NLRG with strong [OIII] and [OII] emission lines (Cohen & Osterbrock 1981). An upper limit for the optical fractional polarization of 3.6% was given by Cimatti et al. (1993). The X-shaped morphology was first noticed by Strom & Conway (1985) who presented maps of the source at  $\lambda$  49 cm. The authors also note fractional polarization of  $\sim$  9% found in the northwestern secondary lobe. Maps at 1.4 GHz were presented by Gregorini et al. (1988), Vigotti et al. (1989), and Dennett-Thorpe et al. (1999). High resolution images at 8 GHz were shown by Black et al. (1992). Dennett-Thorpe et al. (1999) have studied the spectral index distribution of



3C223.1 and have found essentially no spectral gradients within the source. Also, the source shows little or no depolarization between 1.4 GHz and 8 GHz (Dennett-Thorpe 1996).

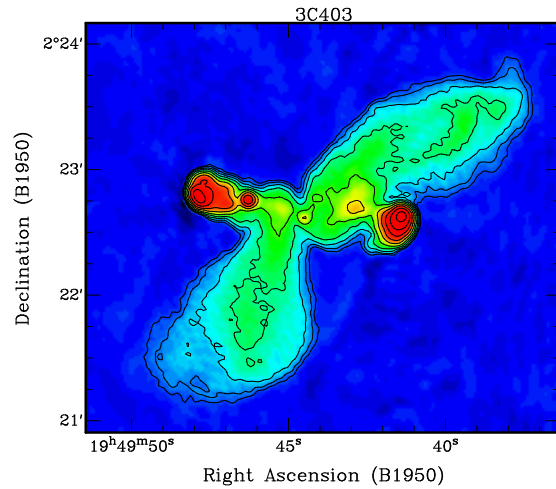
### 3C315

The host of this narrow-line radio galaxy is of dumbbell type with a DE2+DE2 double core in a common envelope (Matthews et al. 1964). The cores have a projected separation of  $8''$  (Goodson et al. 1979) and their op-

tical profiles show signs of interaction (Zirbel 1997). The northern core which also contains the radio source was imaged by the HST and was shown to be highly elliptical (de Koff et al. 1996). No optical polarization was detected towards 3C315 (Cimatti et al. 1993). Zirbel (1996) investigated the host galaxy environment of 3C315 and find it located in a poor cluster of richness 19.2 (number of galaxies brighter than  $19^m$  within a 0.5 Mpc radius of the galaxy). No X-ray emission was detected by the Einstein Observatory (Fabiano et al. 1984). Deep pointed IRAS observations were performed by Golombek et al. (1988) but did not detect any infrared emission towards 3C315. 3C315 is a FRII source but lies very close to the FRI/FRII borderline. Maps revealing the X-shaped morphology of 3C315 were displayed by Högbom & Carlsson (1974). Högbom (1979) presented new observations at 5 GHz and performed a spectral analysis. The author finds little spectral index variation across the source. New maps at 1.4 GHz were shown by Leahy & Williams (1984). A spectral analysis using images at 1.4 GHz and 5 GHz was presented by Alexander & Leahy (1987). The authors report age gradients across 3C315 with increasing spectral ages away from the nucleus.

### 3C379.1

3C379.1 was classified as a high-excitation narrow-line radio galaxy (HEG) by Spinrad et al. (1985). Optical imaging of the host galaxy using the HST revealed the nucleus to be elongated along the radio axis (de Koff et al. 1996). The host galaxy exhibits extended [OIII] emission with a total extent of  $9''$ . The line emitting region is elongated and within  $20^\circ$  coincident with the radio axis (McCarthy et al. 1995). Radio maps of 3C379.1 at 1.4 GHz and 4.9 GHz including polarization were presented by Spangler & Sakurai (1985). The authors find no significant depolarization across the source. The Faraday rotation is constant and is attributed to foreground rotation by our Galaxy. Tadhunter et al. (1992) did not find significant optical polarization



above the detection limit of 1.4% fractional polarization. The secondary lobes of 3C379.1 are short in projected length. Strictly, this object does not meet the criterion of being an X-shaped source as the length of the secondary lobes is smaller than that of the active lobes. The morphology as well as the 178 MHz luminosity clearly classifies 3C379.1 as an FRII radio galaxy.

### 3C403

The host of 3C403 is a DE3-4 galaxy (Wynham 1966). Tadhunter et al. (1993) have reported a high-ionization emission-line spectrum with unusually narrow emission lines. The continuum colors are typical of an early-type galaxy. The host galaxy of 3C403 was mapped by the HST as part of the snapshot survey of 3CR radio sources (Martel et al. 1999). The galaxy appears to be a smooth elliptical. However, the authors note an apparent separation of the source into a central elliptical region and a low surface-brightness halo which is probably due to intervening dust. The host galaxy does not have any bright companion and is located in a very low-density local galaxy environment (Heckman et al. 1986). The source was not



detected in the ROSAT all-sky survey and an upper limit to the X-ray luminosity (0.5-2.4 keV) of  $L < 42.51$  was given by Siebert et al. (1996). 3C403 is the only X-shaped radio galaxy with high infrared luminosity. The source has been detected in the three shortest wavelength channels of the IRAS all-sky survey (Golombek et al. 1988). The association of the IRAS source F19497+0222 with 3C403 has been confirmed by Condon et al. (1995). Imaging of the extended emission line gas of 3C403 was presented by Baum et al. (1988). The continuum image reveals a disturbed morphology with a possible broad extension or fan. The  $H\alpha$  image shows an elliptical line emitting region 14 kpc in extent. The major axis is misaligned with the radio axis by  $54^\circ$ . Long-slit spectroscopy along the major and minor axes of this region showed a rotation curve characteristic of symmetric rotation (Baum et al. 1990a, Baum et al. 1992). The rotation axis is within  $20^\circ$  aligned with the radio axis. The (projected) rotational velocities lie in the range of  $100\text{-}220 \text{ km s}^{-1}$  which likely indicates that the gas was acquired in a tidal interaction rather than by cooling flow accretion. Radio maps of 3C403 were presented by Black et al. (1992), Condon et al. (1995), and Dennett-Thorpe et al. (1999). The radio core power is unusually low for a narrow-line radio galaxy with strong emission lines (Morganti et al. 1997). A spectral analysis was presented by Dennett-Thorpe et al. (1999), revealing that even the secondary lobes of 3c403 show essentially no spectral break or curvature.

### 2.3 First Conclusions

At this early point it is worthwhile to summarize some of the properties for the sample of X-shaped sources studied here.

- **Host galaxy type.** X-shaped radio sources seem to reside in different types of host galaxies. A total of six X-shaped sources have fairly regular elliptical hosts (4C12.03, 3C52, B2 0828+32, 3C223.1, 3C379.1, 3C403). Some of these were reported to be slightly elongated and in

several pronounced dust disks have been found. Two sources from the sample are dumbbell galaxies with clearly separated double nuclei (NGC 326, 3C315). Only one X-shaped source (3C136.1) shows clear signs of an ongoing merger. The host of 3C136.1 is irregular and appears to be disrupted by tidal forces.

- **Environment.** The environments of X-shaped sources seem to be rather poor. None of the source studied here are part of rich galaxy clusters or groups. Four sources have been reported to be located in galaxy groups or clusters (NGC 326, 3C223.1, 3C315, 3C403). However, the density of these groups is low in all cases. All four sources have been studied in the X-ray regime, but only one of them (NGC 326) was found to be embedded in hot cluster gas. NGC 326 is also the only X-shaped source having a close companion galaxy. In none of the other sources companions have been found.
- **Emission line types.** Most X-shaped sources of the studied sample (3C223.1, 3C315, 3C379.1, 3C403) have been classified as narrow line radio galaxies (NLRG). For two sources (4C12.03, 3C136.1) the spectra are somewhat unusual but also seem to indicate membership to the NLRG class. The spectra of NGC 326, 3C52, and B2 0828+32 have not been classified so far. The tendency of the studied sources to belong to the NLRG class does not necessarily have to be intrinsic to the class of X-shaped sources. As was outlined above orientation effects are responsible for a strong selection bias. In the frame of the unified scheme broad-line radio galaxies (BLRG) would indicate smaller inclination towards the line-of-sight in which case relativistic beaming would increase the dynamic range between primary and secondary lobes which would make detection of the secondary lobes in these objects increasingly difficult.

- **FRI-FRII division.** Interestingly nearly all studied sources seem to occupy the luminosity range close to the FRI-FRII borderline. The 178 MHz luminosity indicates that seven X-shaped radio galaxies are of FRII type, whereas two objects are of FRI type. However, of all nine X-shaped sources seven sources have  $L_{178}$  luminosities within 1 order of magnitude of the FRI/FRII dividing luminosity of  $6.3 \times 10^{25} \text{ W Hz}^{-1} h^{-2}$ . Only two sources (3C52, 3C379.1) have luminosities that exceed the critical value by more than 1 order of magnitude. Whether or not this apparent property is intrinsic to all X-shaped sources or whether it is due to selection effects is unclear. Especially at the high luminosity end X-shaped sources can easily remain undetected due to the adverse dynamic range between the primary and secondary lobes.

Source	IAU name	position (J2000)	$z$	distance (Mpc $h^{-1}$ )	$S_{178}$ (Jy)	$L_{178}$ W Hz $^{-1}$ $h^{-2}$	scale (kpc $h^{-1}$ / $''$ )	LAS ( $''$ )	D (kpc $h^{-1}$ )
4C12.03	0007+124	00 09 52.2 +12 44 08.0	0.1100	338.4	10.0 <sup>(4)</sup>	$1.36 \times 10^{26}$	1.33	215	286
NGC 326	0055+265	00 58 22.2 +26 52 02.0	0.0474	143.7	5.1 <sup>(3)</sup>	$1.26 \times 10^{25}$	0.64	270	170
3C52	0145+532	01 48 29.0 +53 32 35.0	0.2854	909.2	14.7 <sup>(1)</sup>	$1.45 \times 10^{27}$	2.67	83	222
3C136.1	0512+248	05 16 03.1 +24 58 25.0	0.0640	194.8	15.3 <sup>(1)</sup>	$6.92 \times 10^{25}$	0.83	480	398
B2 0828+32	0828+324	08 31 27.5 +32 19 26	0.0507	153.9	2.4 <sup>(3)</sup>	$6.8 \times 10^{24}$	0.68	900	612
3C223.1	0938+399	09 41 23.9 +39 44 41.7	0.1075	330.5	8.1 <sup>(2)</sup>	$1.05 \times 10^{26}$	1.31	140	183
3C315	1511+263	15 13 40.1 +26 07 31.0	0.1083	333.0	20.6 <sup>(1)</sup>	$2.72 \times 10^{26}$	1.31	180	236
3C379.1	1852+743	18 24 32.9 +74 21 00.0	0.2560	811.1	8.06 <sup>(1)</sup>	$6.32 \times 10^{26}$	2.49	80	199
3C403	1949+023	19 52 15.8 +02 30 24.0	0.0590	179.4	28.3 <sup>(2)</sup>	$1.09 \times 10^{26}$	0.78	230	179

TABLE 2.1— Positions and redshifts from NED except for NGC326 which was taken from Werner et al. (1999) and for B2 0828+32 (taken from Meier et al. (1979)). (1)  $S_{178}$  from Kellermann et al. (1969) and adjusted to the scale of Roger et al. (1973), (2)  $S_{178}$  from Leahy et al. (1997), (3)  $S_{178}$  from Pilkington & Scott (1965), (4) from Williams et al. (1968)



# 3

---

## Single-Dish Mapping of X-shaped Radio Galaxies

This chapter presents radio continuum observations of several X-shaped radio galaxies performed with the Effelsberg 100-m telescope. Maps including full polarization have been obtained at 4 frequencies (32 GHz, 10.45 GHz, 4.85 GHz, 2.7 GHz) in the period from 1996 to 1999. The data reduction process will be described only briefly except when deviations from the standard procedure were necessary (mostly at 32 GHz). The maps will be shortly discussed.

**S**INGLE-DISH observations of extended radio sources are – at the cost of resolution – in some respects superior to interferometric data for quantitative analyzes. The most severe drawback of interferometers is their inability to cover the innermost region of the uv-plane and thus to recover the total-flux of the source. The amount of missing-flux cannot be estimated a-priori as it depends on the spatial frequency distribution of the source. Whereas the high spatial frequencies of a mapped object might be fully recovered the low spatial frequencies (representing the extended emission) might not be. This will result in an incorrect flux distribution in the source image. Such effects can be fatal for a spectral analysis because artificial steep (or flat) spectral slopes can be easily created in this way.

Single-dish data on the other hand cover the whole uv-plane up to the diffraction limit and therefore are not affected by missing flux. For a spectral analysis single-dish maps are thus crucial to trace the spectral shape and to disclose possible missing flux problems of interferometric datasets also included in the analysis. This is especially true for the

high-frequency domain where artificial spectral slopes can lead to severe misinterpretations of spectral ages.

In the following the obtained Effelsberg maps at the various frequencies will be displayed and shortly discussed. Note that due to their small angular sizes some of the X-shaped sources are only slightly resolved or remain unresolved at some of the frequencies. These data have been used only to derive the total flux and construct the integrated source spectrum. The discussion of these unresolved sources will therefore be very brief.

### 3.1 Observations and Data Reduction

The standard procedure for the reduction of radio continuum multi-feed data acquired with the 100-m telescope has been described in great detail elsewhere (e.g. Gregorini et al. 1992, Mack 1996). The data obtained at 10.45 GHz, 4.85 GHz and 2.7 GHz were reduced following this standard procedure. Due to the generally higher demands and difficulties when dealing with high-frequency data

and due to technical problems of the 32 GHz system at the time of observation, the reduction of the 32 GHz data required some deviations of the standard data reduction procedure. These will be described in the following.

### 3.1.1 The 32 GHz receiver

The new 32 GHz receiver system was installed in the secondary focus of the 100-m telescope in 1996. It is a 3-feed system with feed separations of  $4'3''$  and  $2'$ . The HPBW of the 32 GHz system is  $27''$ . The receiver bandwidth is 2 GHz.

First tests performed in 1997 revealed that the system does not reach the anticipated performance. Further investigations have shown that the cooled HEMTs are not sufficiently stable, thus considerably raising the noise level in the uncorrelated total intensity channels. The correlated Stokes U and Q channels are free of instabilities and reach the expected noise levels. Due to the instability problems a second 3-feed module has been recently added to the 32 GHz system. The second module has been designed as a beamswitch correlation system. The output channels yield correlated total intensity signals but no polarization information. The upgraded 32 GHz receiver has however not been used for the observations used in this thesis.

In the period from end of 1998 until beginning of 1999 the dish surface of the 100-m telescope has undergone a major upgrade. The outer 25 meters of wire-mesh panels were replaced by semi-solid aluminum panels to increase the effective collecting area at short wavelengths. The panels were replaced but only coarsely adjusted over a 12 month period leading to a gradual decline of the quality of the reflecting surface. In summer 1999 tests of the main beam characteristics were performed (see Appendix A). The main beam was found to be strongly distorted depending on the elevation of the telescope. Consequently observations at 32 GHz had to be stopped until the readjustment of the panels towards the end of 1999. The consequences of the distorted beam for data obtained within the upgrade period will

be discussed in the next section.

### 3.1.2 Data reduction at 32 GHz

The treatment of 32 GHz data deserves – even though standard methods can be used – special attention at several points during the data reduction process.

- **Elevation selection.** As mentioned above the quality of the reflecting surface of the 100-m telescope has degraded due to the replacement of surface panels in 1998. Unfortunately there has been no inspection of the beam and gain properties of the telescope accompanying the refurbishment process. Tests made in summer 1999 reflect the beam status of the telescope *after* the replacement of the panels had been completed. These tests have shown that observations made at elevations exceeding  $35^\circ$  should be discarded from the analysis entirely. The impact of the beam deformation and gain loss on the data obtained in the course of 1998 (even though certainly less than in summer 1999) cannot be assessed anymore. Individual coverages of the X-shaped sources are too noisy to perform Gaussian fitting to estimate possible beam deformations. In order to avoid calibration and beam problems in the combined final images we have therefore discarded all 1998/1999 datasets obtained at elevations higher than  $35^\circ$ .
- **Pointing.** Accurate pointing generally becomes more difficult at higher frequencies. On the one hand the HPBW becomes smaller, so that the pointing errors become larger with respect to the beam size. On the other hand, due to the power-law synchrotron spectra of the pointing sources it becomes more and more difficult to find sufficiently strong sources close to the target of observation. As a result at 32 GHz pointing errors can accumulate to  $10''$  even when pointing checks are performed on an hourly basis. In 1999 pointing errors exceeding

25'' were encountered, which was probably due to a defect in the focusing system of the telescope. As a result the pointing of individual maps obtained at 32 GHz has to be checked before they are combined to yield the final map. The standard method to check for pointing errors is to perform a Gaussian fit to a bright source component to determine its position. However, this method is not applicable for any of the X-shaped sources mapped here. The snr of an individual coverage is generally too low to perform Gaussian fitting. Therefore, we have carried out a 2D cross-correlation analysis of the individual coverages. To this end we have first combined all individual maps to construct a preliminary final map with high snr. The individual maps have then been cross-correlated with this reference map. For some of the very weak X-shaped objects it was necessary to average several consecutive coverages to increase the snr before cross-correlating them with the reference map. The pointing shift for a particular coverage can then be obtained by a Gaussian fit to the 2D cross-correlation function. An example for such an cross-correlation function is shown in Fig. 3.1.

### 3.2 The 32 GHz maps

#### 4C12.03

The final map of 4C12.03 (Fig. 3.2) has been constructed using 21 total intensity coverages and 26 polarized intensity maps. The RMS noise is 6 mJy/beam in total intensity and 0.65 mJy/beam in polarized intensity. At 32 GHz only the brightest source feature – the northern hot spot – is visible above the noise. The projected magnetic field in this region is aligned parallel to the jet. The maximum fractional polarization with values up to 20% is observed coincident with the northern hotspot.

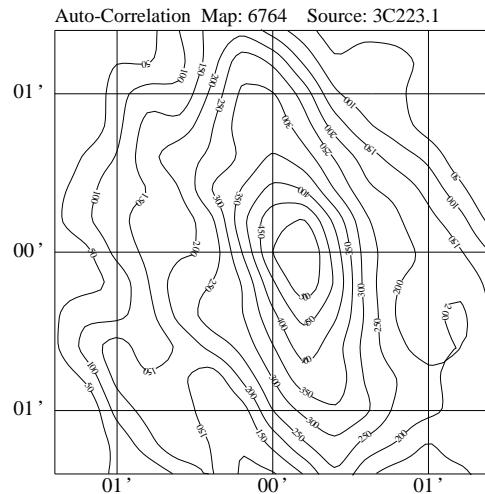


FIGURE 3.1— Auto-correlation of one individual coverage of 3C223.1 with the combined reference map. The maximum of the cross-correlation is off-centered, thus indicating a pointing shift that has to be corrected before constructing the final map. The size of the required shift is estimated from a Gaussian fit to the cross-correlation function.

#### NGC326

NGC 326 is weak at 32 GHz. Significant emission is seen only from the brightest parts of the north-western lobe and in some areas of the connected tail. The total intensity map shown in Fig. 3.3 has been obtained from 10 coverages. The RMS noise obtained is 6.5 mJy/beam. The polarized intensity image exhibits no significant signal above the noise (1 mJy/beam) and is not shown.

#### 3C52

The final map of 3C52 is shown in Fig. 3.4. Seven individual coverages have contributed to the final total intensity and polarized intensity images. The noise levels reached are 8 mJy/beam and 1 mJy/beam correspondingly. Both primary lobes are clearly visible at 32 GHz. The southern lobe also exhibits signs of the secondary lobe extending to the west. The corresponding secondary eastern lobe remains undetected. In both radio lobes the projected magnetic field is oriented in a

Source	Fig.	Contour Levels [mJy/beam]
4C12.03	3.2a	18,25
	3.2b	2,3,4
NGC326	3.3a	20,28
3C52	3.4a	24,34,48,68,96,136
	3.4b	3,4,5,6,7
3C223.1	3.5a	12,17,24,34,48
	3.5b	1.2,2,3,4,5
3C315	??a	12,17,24,34
	??b	1.6,2.2,2.8,3.6
3C379.1	??a	15,21,30,42,60
3C403	3.8a	15,21,30,45,60,84,120,170
	3.8b	3,4,5,6,8,10

TABLE 3.1— Contour levels of the 32 GHz maps.

direction perpendicular to the jet. The polarized intensity image shows polarized emission originating in both radio lobes, but no emission from the secondary lobes can be traced. The fractional polarization is low, with maximum values of 7.5% in the northern lobe.

### 3c223.1

A total of 41 total intensity and 99 polarization coverages have been combined to yield the final maps of 3C223.1 shown in Fig. 3.5. The noise level reached is 3.5 mJy/beam in total and 0.4 mJy/beam in polarized intensity. The secondary lobes are clearly visible – most prominently the western one. Polarized emission is detected from both primary lobes as well as from the western secondary radio lobe. Maximum values of  $\sim 10\%$  fractional polarization are detected coincident with the northern hotspot.

### 3C315

The final maps of 3C315 are displayed in Fig. ???. The RMS noise achieved in total and polarized intensity is 4.3 mJy/beam and 0.5 mJy/beam respectively. The total intensity image is a combination of 25 coverages, the polarized intensity image consists of 35 coverages. The core of 3C315 is the brightest source feature at 32 GHz. Only the brightest knots of the lobes are visible above the noise. The

core as well as most parts of the lobes do not exhibit significant polarization. However polarized emission is detected from the tips of the radio lobes located north and south of the core. In these areas the fractional polarization partly exceeds 20%.

### 3C379.1

No significant polarized emission was detected from 3C379.1 above a noise level of 0.7 mJy/beam. Figure ?? displays the total intensity map which has been constructed from 20 individual coverages. The RMS noise level reached is 5.5 mJy/beam. In total intensity the primary lobes are visible but no emission from the secondary lobes can be traced.

### 3C403

The final maps of 3C403 are displayed in Fig. 3.8. The total intensity image is a combination of 39 single coverages and has an RMS noise of 3.5 mJy/beam. The polarized intensity map has been combined out of 45 coverages and has a noise level of 0.6 mJy/beam. The secondary lobes can be clearly traced in total as well as in polarized intensity. The fractional polarization is high (up to 20%). The highest degrees of polarization are seen towards the far ends of the secondary lobes. The projected magnetic field traces the jet within the primary lobes. In the secondary



lobes the field tends to follow the direction of transition from the primary to the secondary lobes.

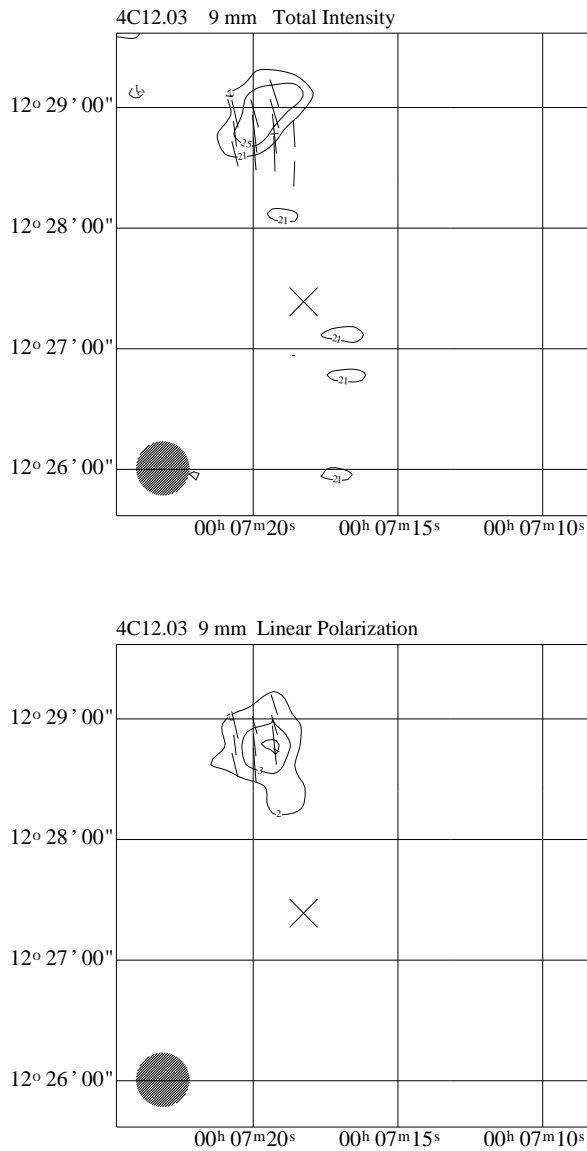


FIGURE 3.2— Maps of 4C12.03 at 32 GHz. The contour levels are given in Tab. 3.1. The map layout is identical to Fig. 3.12

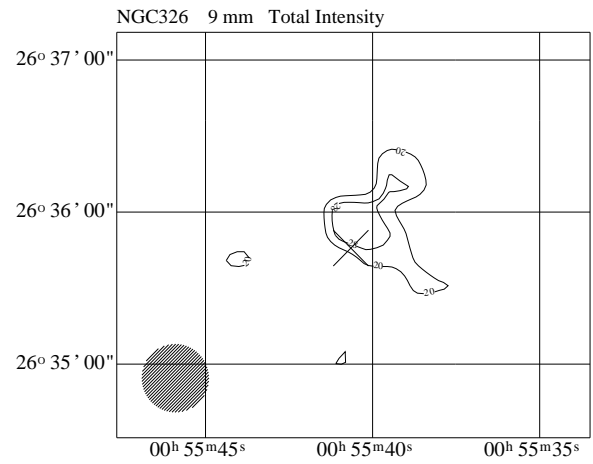


FIGURE 3.3— Map of NGC326 at 32 GHz. The contour levels are given in Tab. 3.1. The map layout is identical to Fig. 3.12

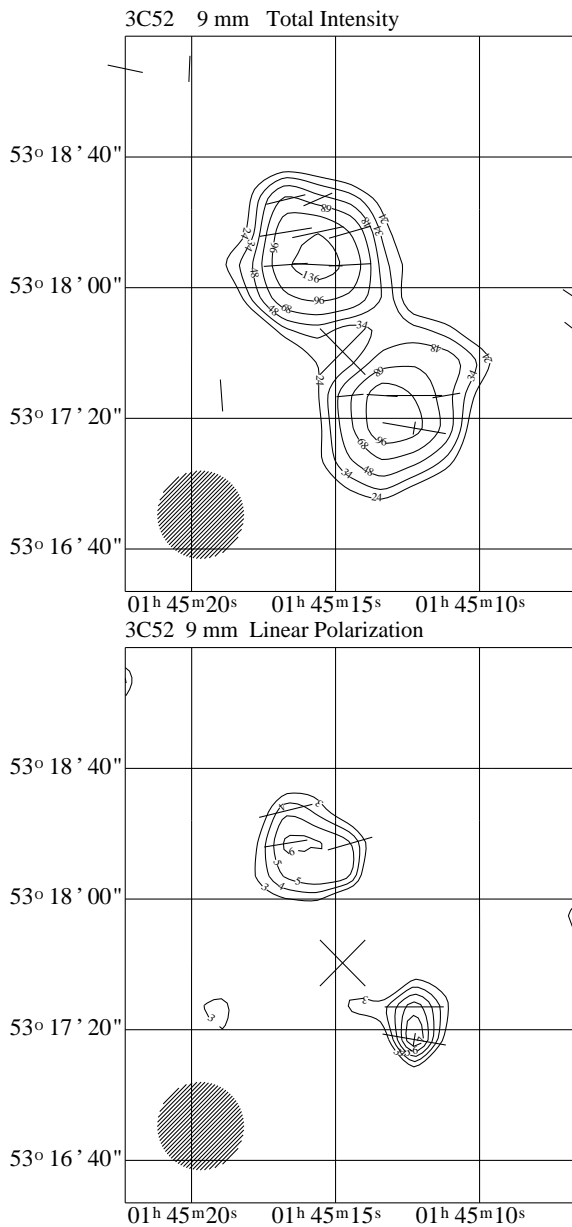


FIGURE 3.4— Maps of 3C52 at 32 GHz. The contour levels are given in Tab. 3.1. The map layout is identical to Fig. 3.12

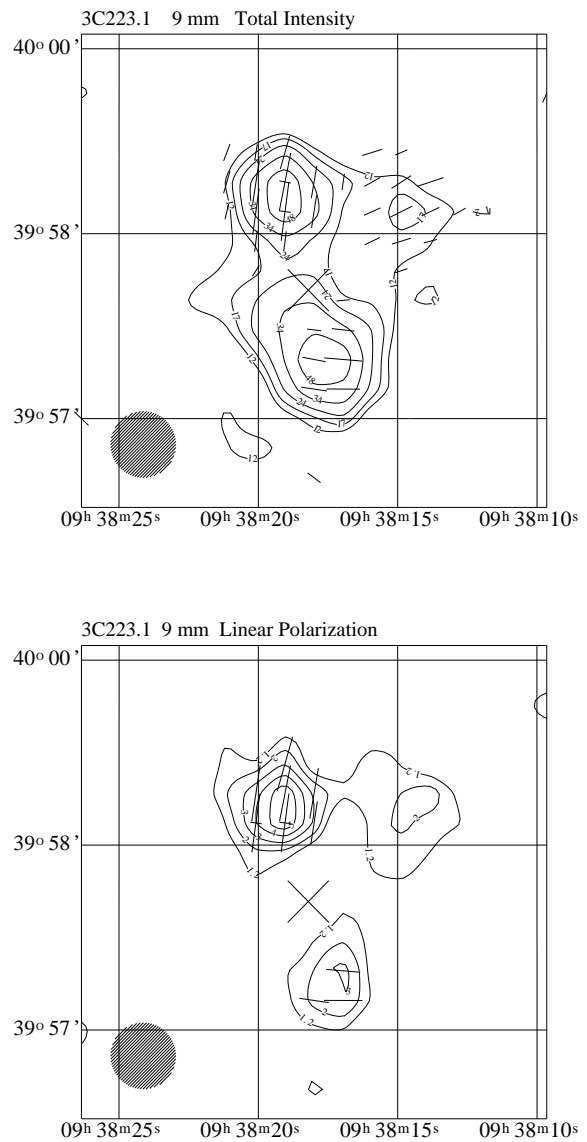


FIGURE 3.5— Maps of 3C223.1 at 32 GHz. The contour levels are given in Tab. 3.1. The map layout is identical to Fig. 3.12

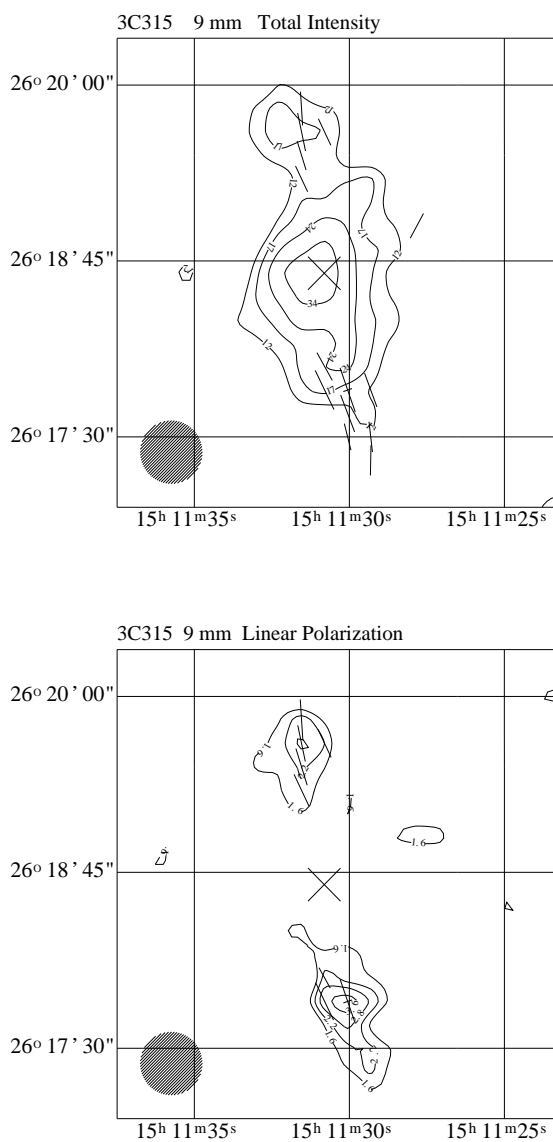


FIGURE 3.6— Maps of 3C315 at 32 GHz. The contour levels are given in Tab. 3.1. The map layout is identical to Fig. 3.12

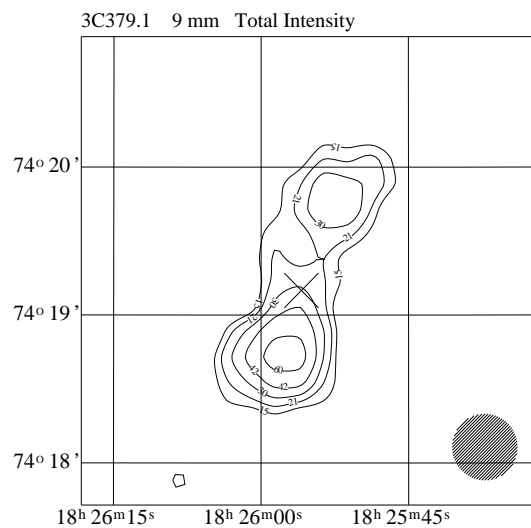


FIGURE 3.7— Maps of 3C379.1 at 32 GHz. The contour levels are given in Tab. 3.1. The map layout is identical to Fig. 3.12

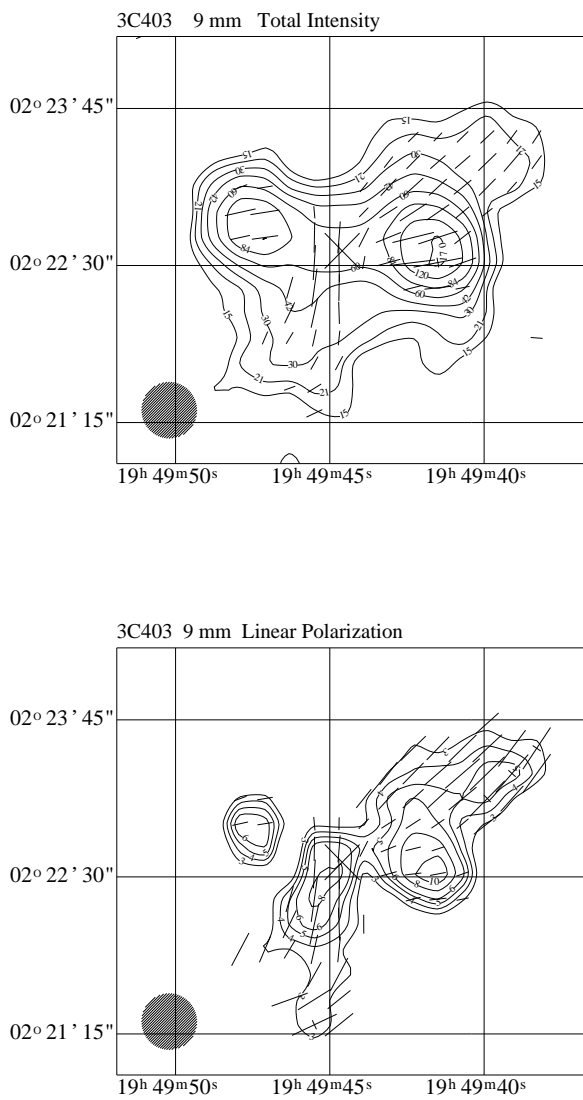


FIGURE 3.8— Maps of 3C403 at 32 GHz. The contour levels are given in Tab. 3.1. The map layout is identical to Fig. 3.12

### 3.3 The 10.45 GHz Maps

#### 4C12.03

The final maps of 4C12.03 at 10.45 GHz are displayed in Fig. 3.9. The noise levels reached in total and polarized intensity are 0.9 mJy/beam and 0.4 mJy/beam respectively. The total intensity image is a combination of 7 coverages. The polarized intensity image has been constructed using 10 individual maps. The secondary lobes are only slightly resolved. The source is strongly polarized with values of the fractional polarization exceeding 20%. The polarization is highly asymmetric, with the northern lobe being more pronounced in polarized emission. The primary and secondary southern lobes can be distinguished in the polarized intensity image. The projected magnetic field is aligned with the current jet direction in the active radio lobes. In the secondary southern lobe the field is aligned along the major axis of the radio lobe.

#### NGC326

A total of 6 coverages have contributed to the total and polarized intensity images shown in Fig. 3.10. The RMS noise levels are 3 mJy/beam and 1 mJy/beam respectively. The secondary lobes are resolved and can be traced out to distances of more than  $2'$  from the core. The source is strongly polarized but the polarized intensity distribution is asymmetric. The polarized emission from the eastern active and northern secondary lobes is considerable stronger than from the south-western lobe system. The fractional polarization is highest in the northern secondary lobe where it exceeds 20%. The projected magnetic field traces the transition path from the secondary to the primary lobes.

#### 3C52

3C52 is only slightly resolved at 10.45 GHz. The image shown in Fig. 3.11 is elongated along the major axis of the source but the secondary lobes cannot be distinguished. Three coverages were used to yield the final images in

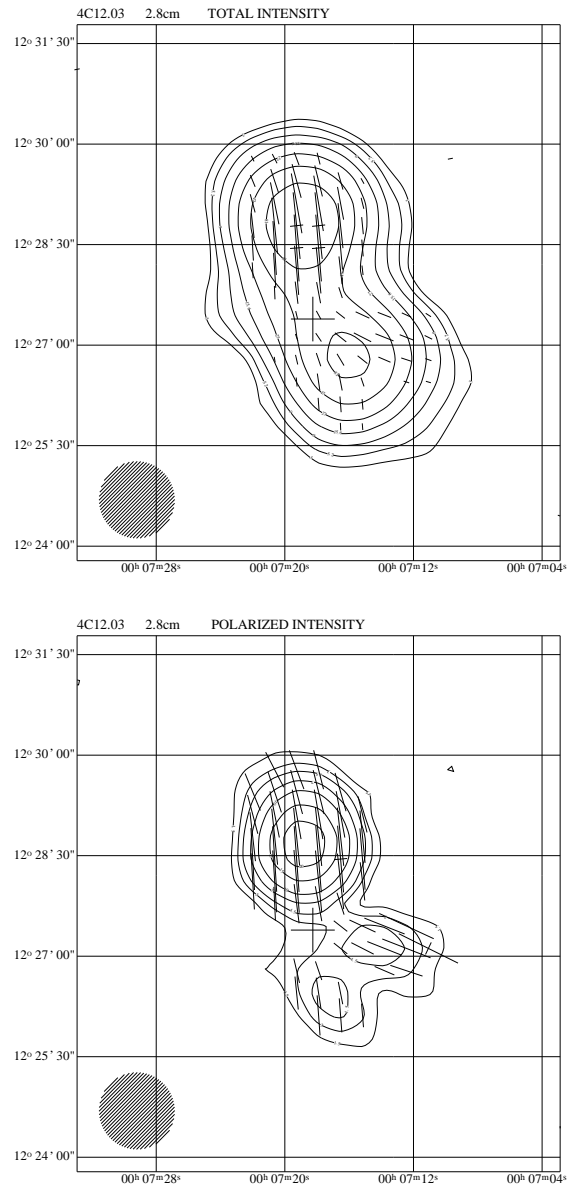


FIGURE 3.9— Maps of 4C12.03 at 10.45 GHz. The contour levels are given in Tab. 3.2. The map layout is identical to Fig. 3.12

total and polarized intensity. The RMS noise is 5.5 mJy/beam and 1.3 mJy/beam respectively. The source is asymmetrically polarized with no significant polarized emission from the southern lobe and hotspot. The maximum fractional polarization of 10% is located coincident with the northern hotspot. The orientation of the projected magnetic field in the northern lobe is perpendicular to the jet direction.

Source	Fig.	Contour Levels [mJy/beam]
4C12.03	3.9a	3,5,2,9,15,6,27,47,81
	3.9b	1.5,3,4.5,7,10,15,20
NGC326	3.10a	7.5,11,15,21,30,42,60,85,120
	3.10b	2,4,6,9,12,16
3C52	3.11a	20,40,60,100,150,200,280,360,450,550
	3.11b	5,11,18,25,35
3C136.1	3.12a	4,6,8,10,15,20,30,40,50,60,80,100,120,140
	3.12b	1.2,2.4,3.6,5,7,9,11,13
B2 0828+32	3.13a	1.5,2.4,3.8,5.9,9.3,15,23,37,58,92,145
	3.13b	0.9,2,3.5,5.5,8,12,16
3C223.1	3.14a	10,20,40,60,80,100,140,180,220
	3.14b	3,5,7,9,11,14,17
3C315	3.15a	4,8,15,30,50,70,90,120,160,200,250
	3.15b	2,4,6,9,12,15,18,22,26
3C379.1	3.16a	30,45,60,80,110,140,170,200
	3.16b	4,5,5,7,9,11
3C403	3.17a	4.5,7.8,13.5,23.4,40.5,70.1,122,210,365
	3.17b	1.4,2.4,4.2,7.3,10.8,21.8,32.4

TABLE 3.2— Contour levels of the 10.45 GHz maps.

*3C136.1*

3C136.1 is well resolved by the 69'' beam. The final map at 10.45 GHz is displayed in Fig. 3.12. A total of 19 maps have been added to yield the total intensity image; 20 coverages have been used for constructing the polarized intensity map. Whereas strong polarized emission is detected from the whole source the highest values of the fractional polarization ( $\sim 50\%$ ) can be found in the secondary lobes. In the primary lobes the projected magnetic field is aligned parallel to the jet direction. Subsequently the field orientation is turning towards the secondary lobes, where the fields run parallel to the major lobe axis.

*B2 0828+32*

Due to the steep synchrotron spectrum of B2 0828+32 only part of the secondary lobes can be detected at 10.45 GHz. The maps presented in Fig. 3.13 consist of data already presented by Mack et al. (1994). A few more coverages obtained at excellent weather conditions have been added. Also the data have been cleaned to remove heavy sidelobe re-

sponses still visible in the original maps. The obtained RMS noise is 0.53 mJy/beam in total intensity (39 coverages) and 0.3 mJy/beam in polarized intensity (44 coverages). Whereas only the brightest knot of the northern secondary lobe is visible the southern lobe can be traced out to some distance. Polarized emission is detected from the primary lobes and from the source area connecting the primary and the southern secondary lobe.

*3C223.1*

The secondary lobes of 3C223.1 are unresolved in the total intensity image (Fig. 3.14). However, both primary lobes as well as the western secondary lobe can be distinguished in the polarized intensity image. The RMS noise is 3 mJy/beam in total and 1 mJy/beam in polarized intensity. The fractional polarization reaches maximum values of 20% towards the tips of the western secondary lobe. The projected magnetic field is oriented perpendicular to the jet within the primary radio lobes and hotspots. In the secondary lobes the field is aligned along the major lobe axis.

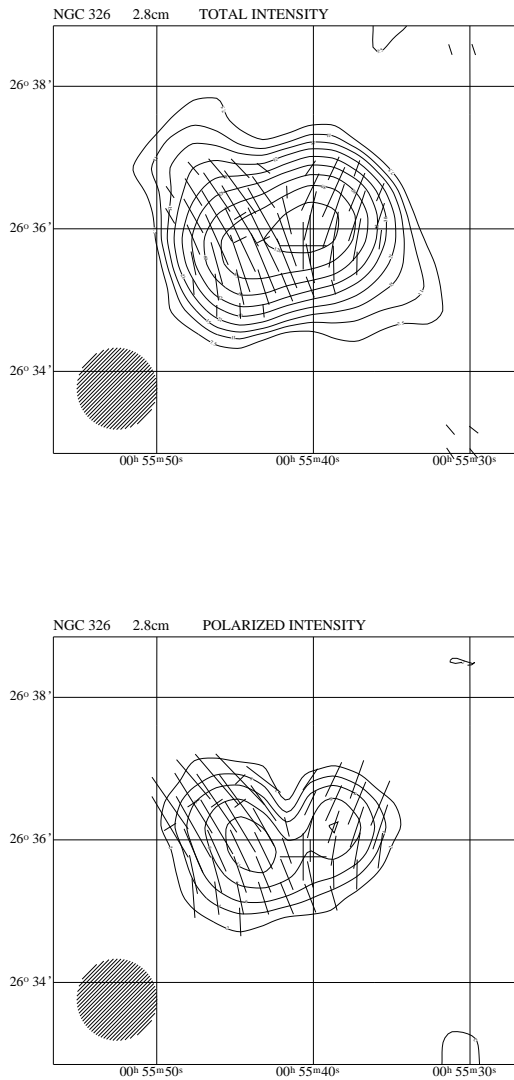


FIGURE 3.10— Maps of NGC326 at 10.45 GHz. The contour levels are given in Tab. 3.2. The map layout is identical to Fig. 3.12

### 3C315

The final map displayed in Fig. 3.15 is a combination of 13 individual coverages. The RMS noise achieved is 1.2 mJy/beam in the total intensity and 0.4 mJy/beam in the polarized intensity image. In total intensity the source structure is not well resolved. However the secondary lobe extending toward the east can be seen as a deformation of the contours. Due

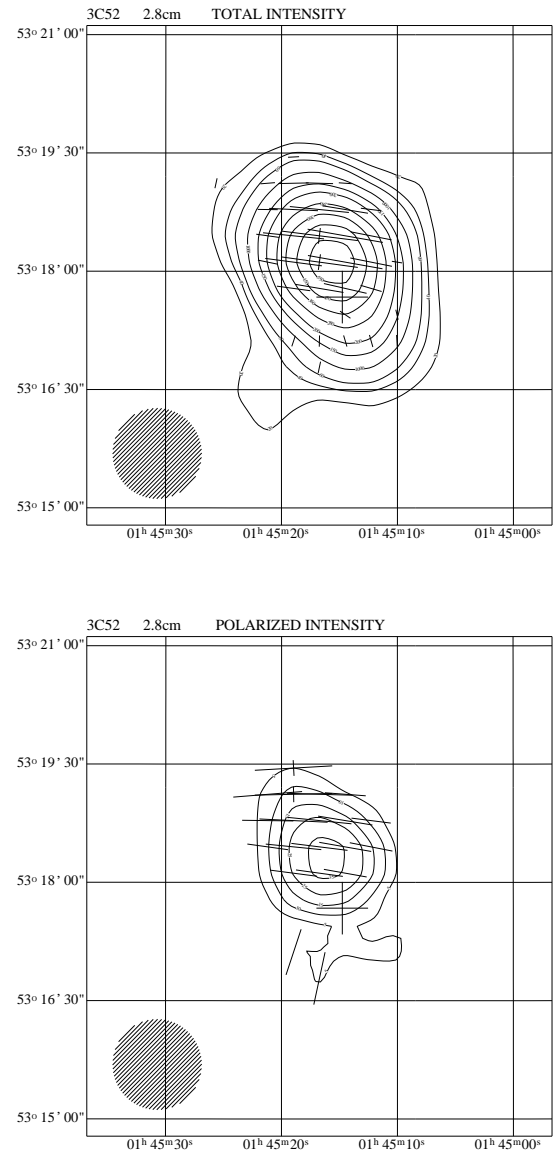


FIGURE 3.11— Maps of 3C52 at 10.45 GHz. The contour levels are given in Tab. 3.2. The map layout is identical to Fig. 3.12

to the slightly better resolution the X-shaped morphology of 3C315 can be more clearly seen in the polarized intensity image. The fractional polarization is again reaching maximum values (exceeding 40%) towards the outer ends of the secondary lobes. The projected field is aligned along the transition path between primary and secondary lobes.

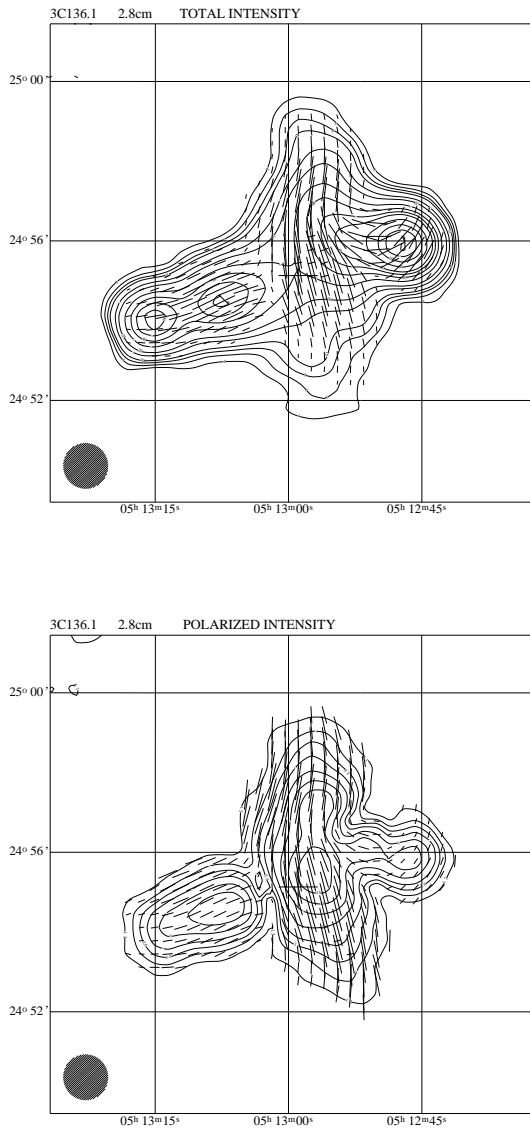


FIGURE 3.12— Maps of 3C136.1 at 10.45 GHz. The contour levels are given in Tab. 3.2. The cross marks the position of the nucleus. The hatched circle in the lower left corner of the plot indicates the 3 dB beam size. (**upper panel**) Contours of the total intensity superimposed by polarization vectors. These have been rotated by  $90^\circ$  in order to depict the projected magnetic field. Their lengths are proportional to the polarized intensity. (**lower panel**) Contours of the polarized intensity, superimposed by polarization vectors. Again the vectors have been rotated by  $90^\circ$ . Their lengths are proportional to the fractional polarization.

### 3C379.1

3C379.1 is not resolved by the  $69''$  beam. The final maps are displayed in Fig. 3.16. The

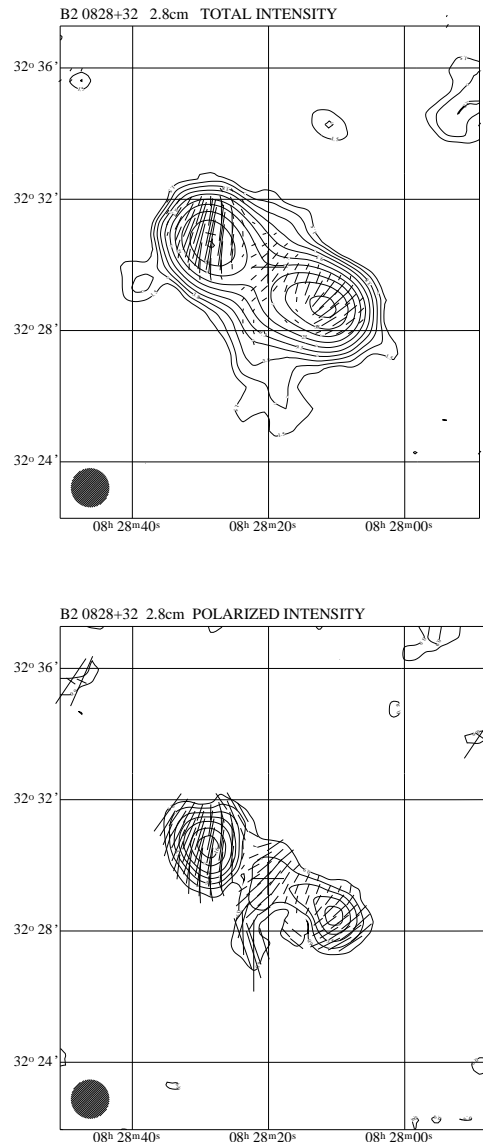


FIGURE 3.13— Maps of B2 0828+32 at 10.45 GHz. The contour levels are given in Tab. 3.2. The map layout is identical to Fig. 3.12

source is elongated along the major source axis but the secondary lobes remain unresolved. The polarized intensity image discloses polarized emission close to the core but no significant contribution from the secondary lobes has been detected. The fractional polarization has maximum values of 15%. The projected magnetic field is aligned along the major lobe axis.



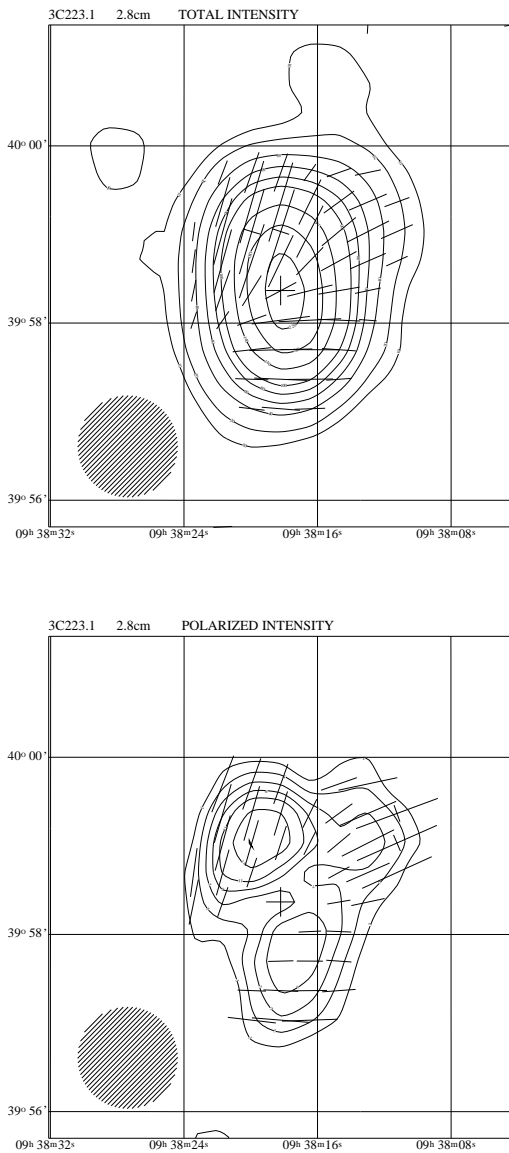


FIGURE 3.14— Maps of 3C223.1 at 10.45 GHz. The contour levels are given in Tab. 3.2. The map layout is identical to Fig. 3.12

### 3C403

The secondary lobes of 3C403 are slightly resolved by the 10.45 GHz beam. The final maps (Fig. 3.17) have been constructed out of 9 individual coverages. The rms is 1.5 mJy/beam in total intensity and 0.35 mJy/beam in polarized intensity. The fractional polarization is reaching maximum values of 30% at the tips of the secondary lobes.

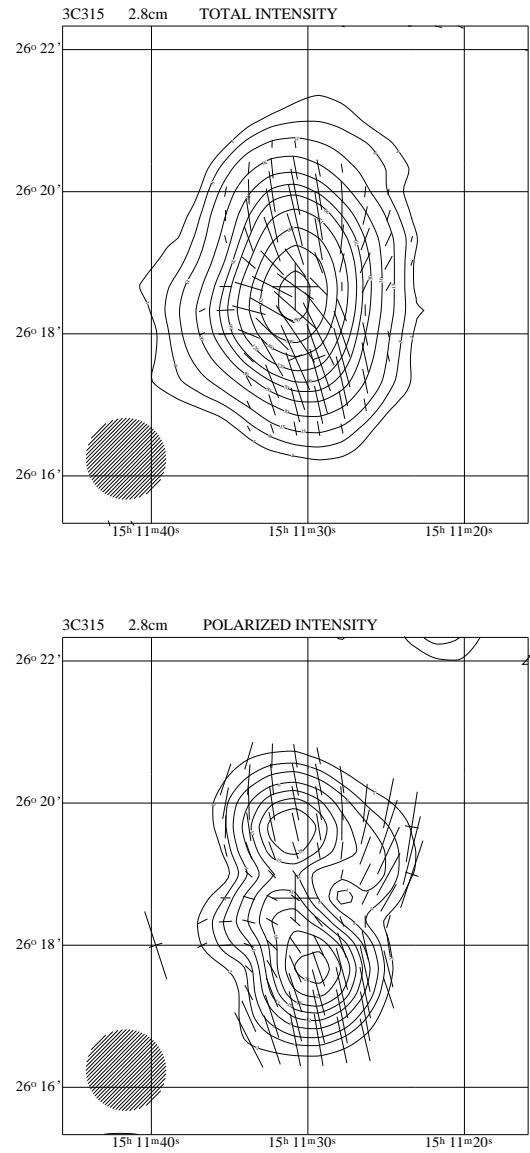


FIGURE 3.15— Maps of 3C315 at 10.45 GHz. The contour levels are given in Tab. 3.2. The map layout is identical to Fig. 3.12

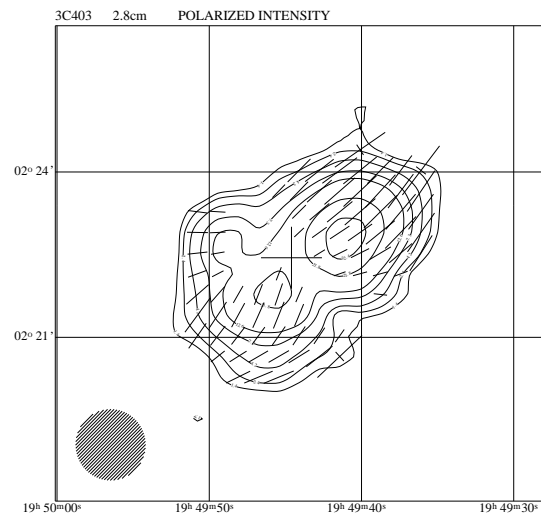
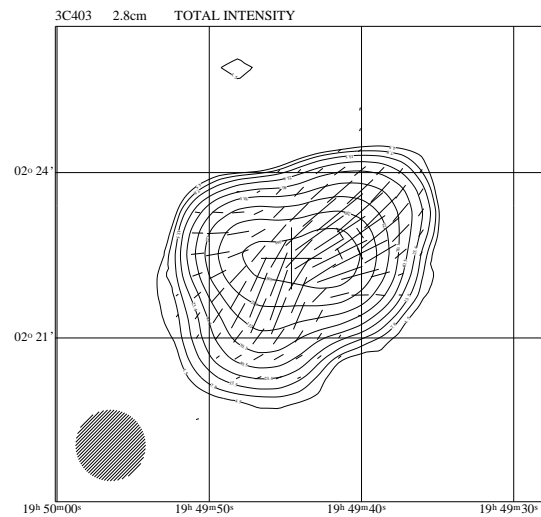
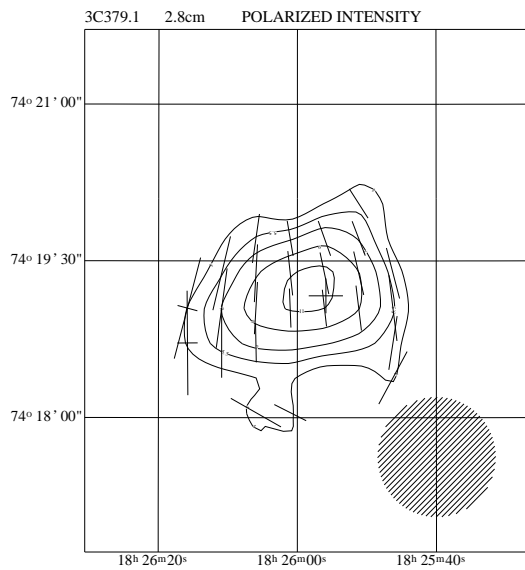
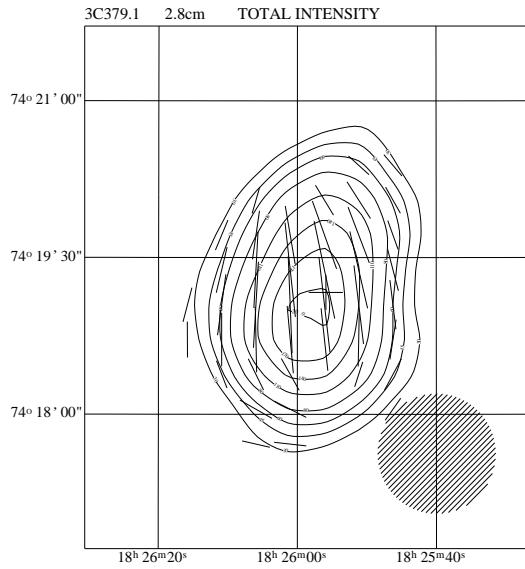


FIGURE 3.16— Maps of 3C379.1 at 10.45 GHz. The contour levels are given in Tab. 3.2. The map layout is identical to Fig. 3.12

FIGURE 3.17— Maps of 3C403 at 10.45 GHz. The contour levels are given in Tab. 3.2. The map layout is identical to Fig. 3.12

### 3.4 The 4.85 GHz Maps

#### 4C12.03

4C12.03 is marginally resolved at this frequency. The maps shown in Fig. 3.18 have been combined from 5 coverages in total power (RMS: 2 mJy/beam) and 4 coverages in polarized intensity (RMS 0.3 mJy/beam). Similar to what was already seen at 32 GHz and 10.45 GHz the bulk of the polarized emission originates in the northern radio lobe. The projected magnetic field is aligned with the major source axis.

#### NGC 326

Six coverages in total intensity (RMS: 3 mJy/beam) and 5 coverages in polarized intensity (RMS: 0.8 mJy/beam) have contributed to the maps of NGC 326 shown in Fig. 3.19. The source is unresolved in total intensity and slightly resolved in polarized intensity. The fractional polarization is smaller than 15%. The magnetic field structure is similar to what is seen in the 10.45 GHz image.

#### 3C52

The combined maps of 3C52 (Fig. 3.20) consist of 2 coverages in total intensity (RMS: 3.5 mJy/beam) and 3 coverages in polarized intensity (RMS: 1 mJy/beam). The source is unresolved. The polarized intensity image shows the asymmetric distribution of the polarized emission. The fractional polarization reaches maximum values of 15%.

#### 3C136.1

Due to its large angular size 3C136.1 is sufficiently resolved at 4.85 GHz. Figure 3.21 shows the final maps. The total intensity image is a combination of 16 coverages and has an RMS noise level of 0.8 mJy/beam. The polarized intensity image consists of 19 coverages and has an RMS of 0.25 mJy/beam. Similar to what is seen at 10.45 GHz the source is strongly polarized. The fractional polarization reaches maximum values of more than 40% within the secondary radio lobes.

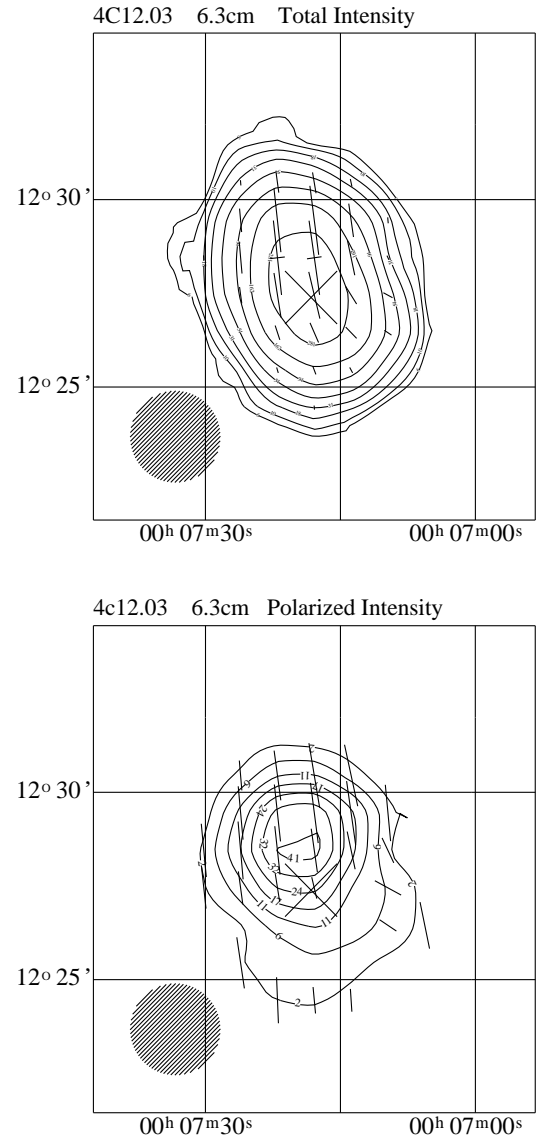


FIGURE 3.18— Maps of 4C12.03 at 4.85 GHz. The contour levels are given in Tab. 3.3. The map layout is identical to Fig. 3.12

#### B20828+32

The final images of B20828+32 displayed in Fig. 3.22 have been constructed by combination of 14 maps in total and 12 maps in polarized intensity. The RMS noise levels are 0.7 mJy/beam and 0.15 mJy/beam respectively. In total intensity only part of the secondary lobes were detected. In polarized emission however they can be seen clearly. The

Source	Fig.	Contour Levels [mJy/beam]
4C12.03	3.18a	6,10,18,31,54,94,162,281
	3.18b	2,6,11,17,24,32,41
NGC326	3.19a	9,16,27,47,81,140,243,420
	3.19b	3,7,12,18,25,33
3C52	3.20a	15,26,45,78,135,234,405,701,1200
	3.20b	10,17,28,39
3C136.1	3.21a	3,5,2,9,16,27,47,81,140,240,410
	3.21b	2.5,4,6,9,12,18,25,32,42,53,65
B2 0828+32	3.22a	2.5,4,3,7.5,13,22.5,39,67.5,117,203,290
	3.22b	1,2,3,4.5,6.5,9,13,18,24,31
3C223.1	3.23a	15,26,45,78,123,235,405
	3.23b	7.5,11,14.5,18
3C315	3.24a	15,26,45,78,135,233,405,700
	3.24b	5,9,13,18,25,32,42,53,65
3C379.1	3.25a	15,26,45,78,135,233,405
	3.25b	3,5,7.5,10,15,20
3C403	3.26a	25,43,75,130,225,390,675,1200
	3.26b	6,10,15,21,28,36,45,54,64,75,87

TABLE 3.3— Contour levels of the 4.85 GHz maps.

bright emission in the north-western corner of the map originates from background sources unrelated to B2 0828+32. The fractional polarization is high with values exceeding 50% in the secondary lobes.

### 3C223.1

Figure 3.23 shows the final maps of 3C223.1 at 3.85 GHz constructed from 3 coverages. The source is unresolved. No significant fractional polarization was detected.

### 3C315

A total of 5 coverages have been combined to yield the final images of 3C315 displayed in Fig. 3.24. The RMS noise levels are 2.5 mJy/beam in total and 0.6 mJy/beam in polarized intensity. The source is slightly resolved in polarized intensity only. The polarized emission region is elongated along the major axis of the north-south radio lobes. Similar to the other frequencies the fractional polarization is high with values of 30% towards the tips of the northern and southern lobes.

### 3C379.1

3C379.1 is unresolved at 4.85 GHz. The final maps displayed in Fig. 3.25 is a combination of 9 individual coverages. The RMS noise is 3 mJy/beam and 0.5 mJy/beam for total and polarized intensity respectively.

### 3C403

The images of 3C403 in total and polarized intensity can be seen in Fig. 3.26. The RMS noise is 7 mJy/beam (6 coverages) and 1 mJy/beam (4 coverages) respectively. The source is unresolved in total intensity. It is slightly elongated along the major source axis in polarized intensity.

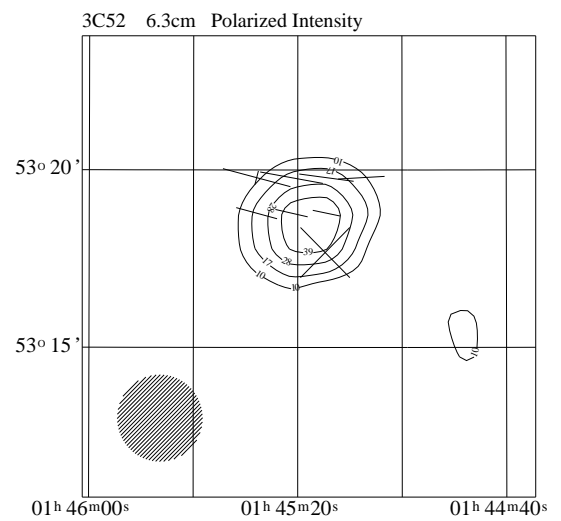
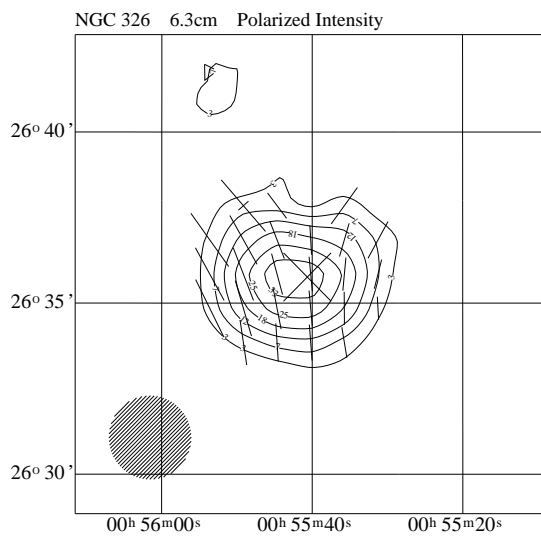
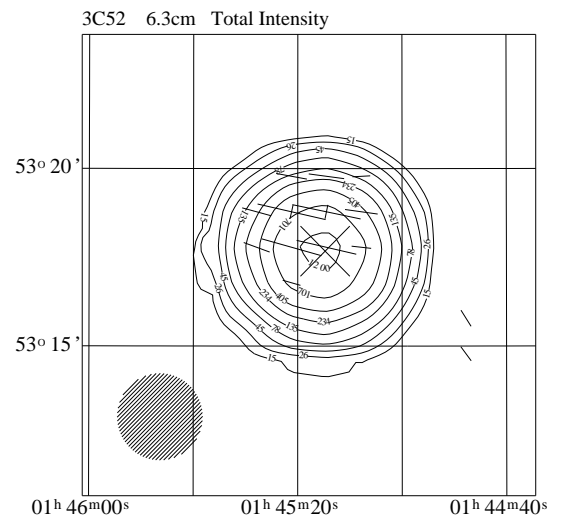
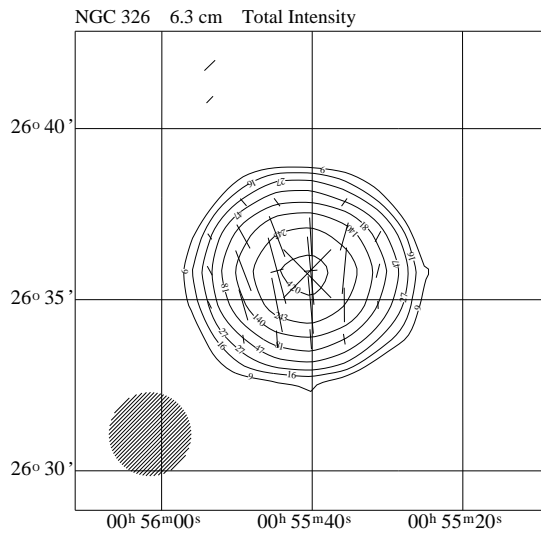


FIGURE 3.19— Maps of NGC326 at 4.85 GHz. The contour levels are given in Tab. 3.3. The map layout is identical to Fig. 3.12

FIGURE 3.20— Maps of 3C52 at 4.85 GHz. The contour levels are given in Tab. 3.3. The map layout is identical to Fig. 3.12

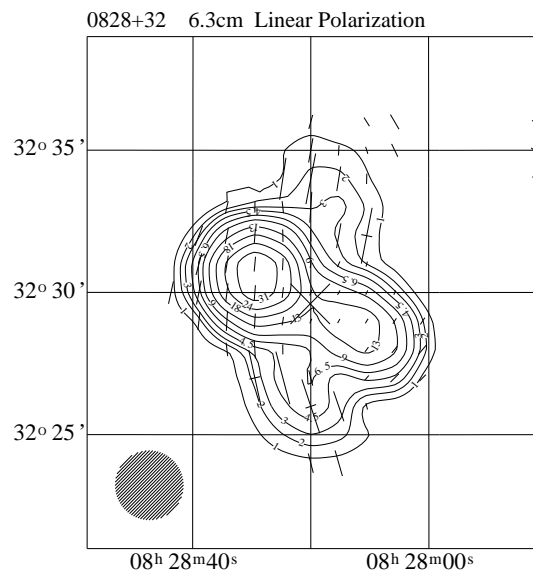
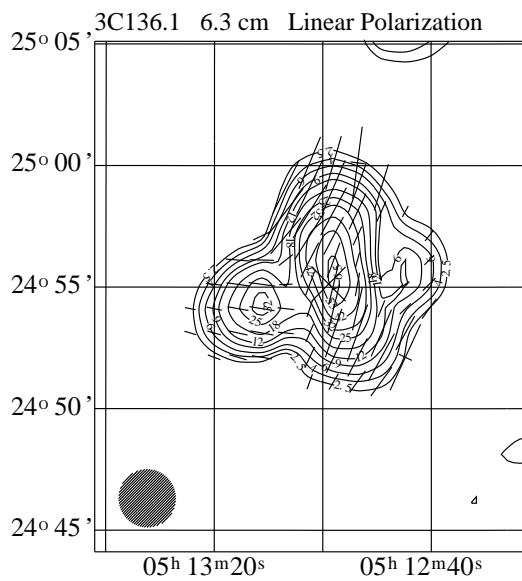
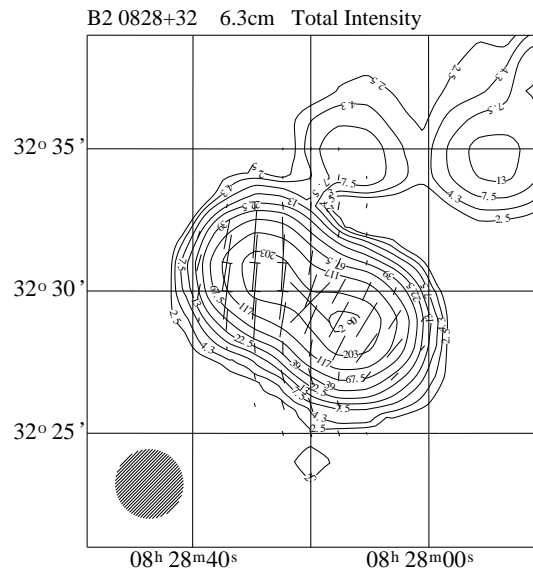
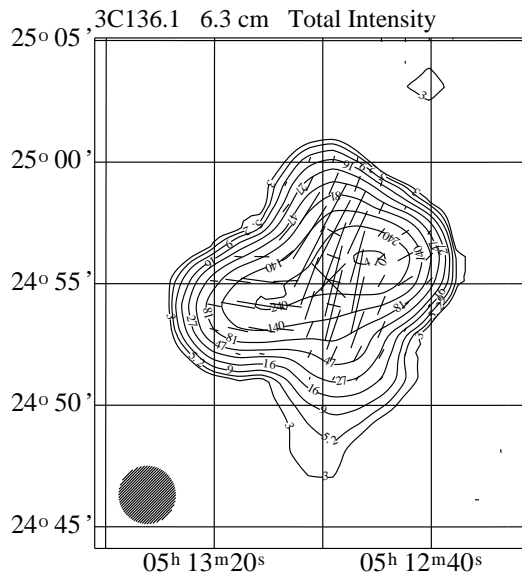


FIGURE 3.21— Maps of 3C136.1 at 4.85 GHz. The contour levels are given in Tab. 3.3. The map layout is identical to Fig. 3.12

FIGURE 3.22— Maps of B2 0828+32 at 4.85 GHz. The contour levels are given in Tab. 3.3. The map layout is identical to Fig. 3.12

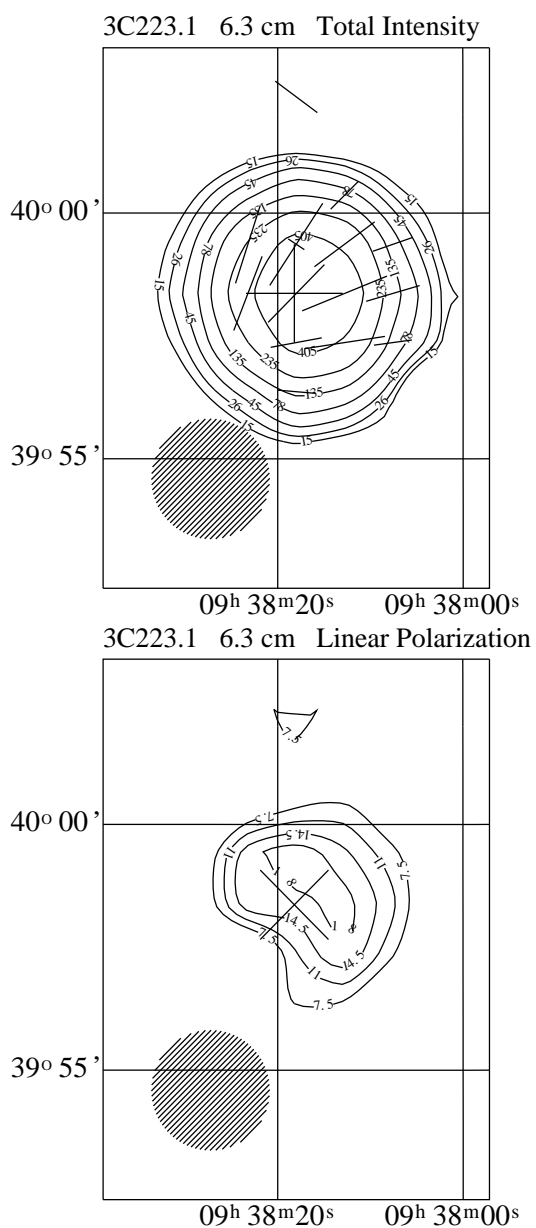


FIGURE 3.23— Maps of 3C223.1 at 4.85 GHz. The contour levels are given in Tab. 3.3. The map layout is identical to Fig. 3.12

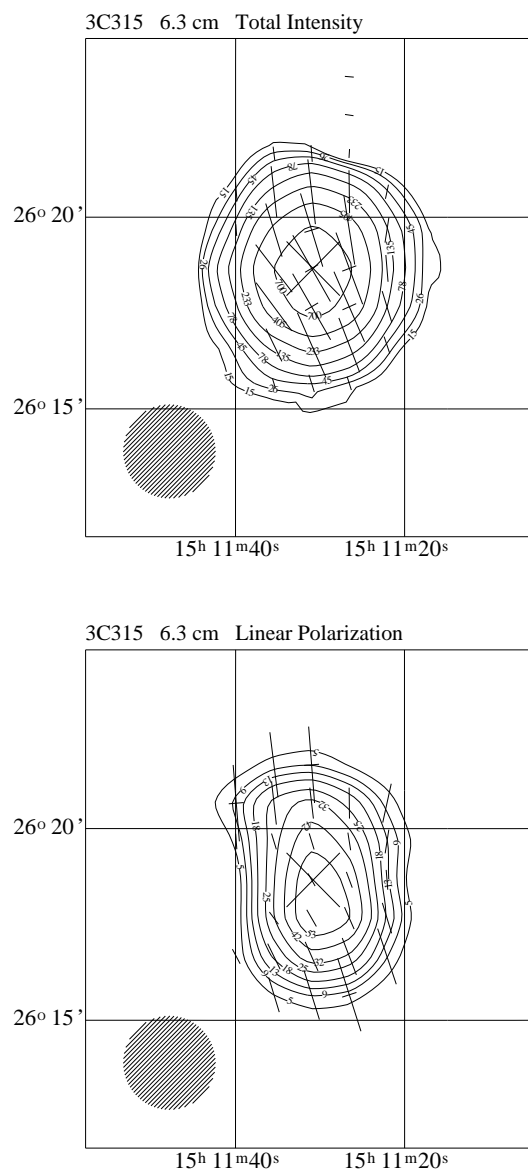


FIGURE 3.24— Maps of 3C315 at 4.85 GHz. The contour levels are given in Tab. 3.3. The map layout is identical to Fig. 3.12

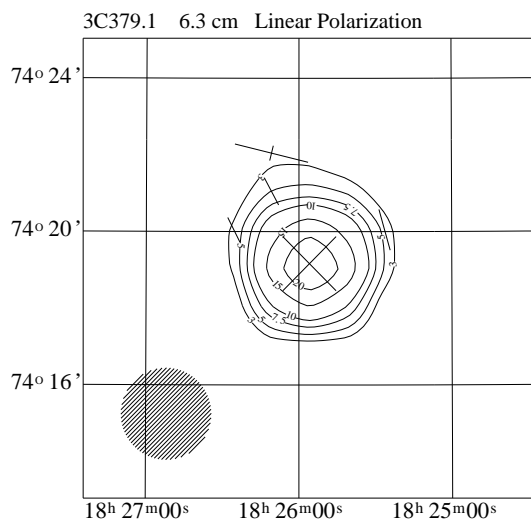
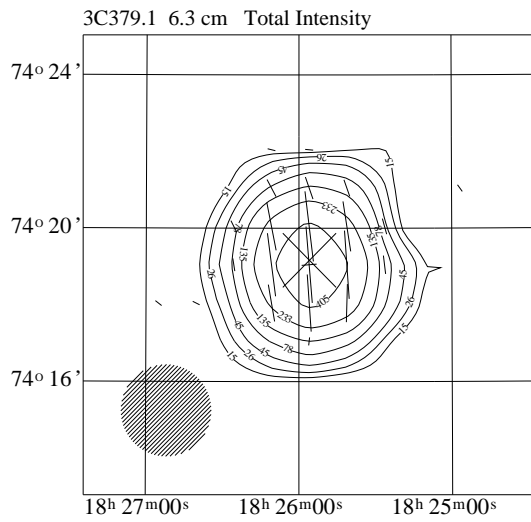


FIGURE 3.25— Maps of 3C379.1 at 4.85 GHz. The contour levels are given in Tab. 3.3. The map layout is identical to Fig. 3.12

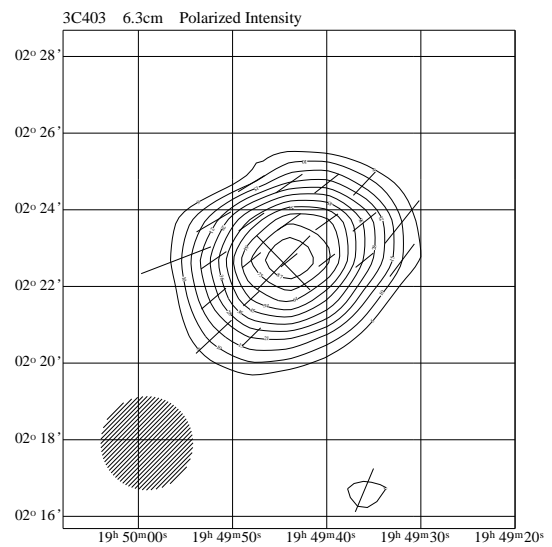
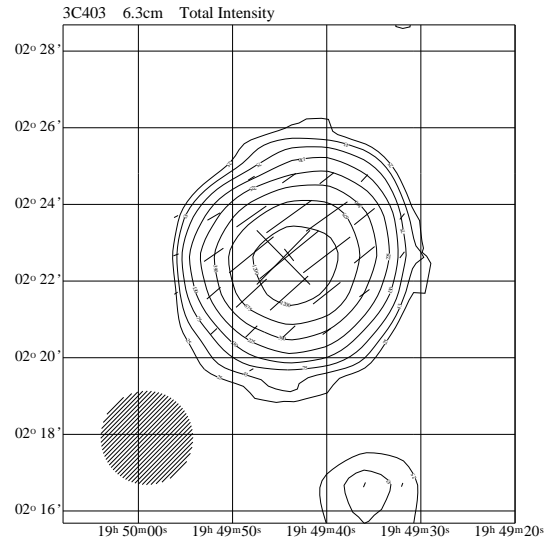


FIGURE 3.26— Maps of 3C403 at 4.85 GHz. The contour levels are given in Tab. 3.3. The map layout is identical to Fig. 3.12



### 3.5 The 2.7 GHz Maps

#### 3C136.1

3C136.1 is marginally resolved at this frequency (Fig. 3.27). The southern secondary lobe is clearly visible, whereas the northern counterpart is not resolved. The central part of the source is polarized. The polarized emission is elongated along the axis defined by the secondary lobes. No polarized emission is detected from the primary lobes and hotspots. The fractional polarization is less than 10%. A total of 10 coverages have been added. The RMS noise is 4 mJy/beam in total and 2.5 mJy/beam in polarized intensity.

#### B20828+32

The final maps of B20828+32 are displayed in Fig. 3.28. The RMS noise is 4 mJy/beam in total and 2.5 mJy/beam in polarized intensity. The source is partly resolved. The emission of the secondary lobes is visible as a slight deformation of the contours. The extended feature located to the north-west are unresolved background objects blending into the source and are completely unrelated with B20828+32. Some polarized emission is detected from a region close to the core of B20828+32. The fractional polarization is below 20%.

#### 3C223.1

3C223.1 is not resolved at 2.75 GHz. Eight coverages have been combined to yield the final maps displayed in Fig. 3.29. The RMS noise levels are 5 mJy/beam (total intensity) and 2.5 mJy/beam (polarized intensity). 3C223.1 is weakly polarized at this frequency. The fractional polarization is below 10%.

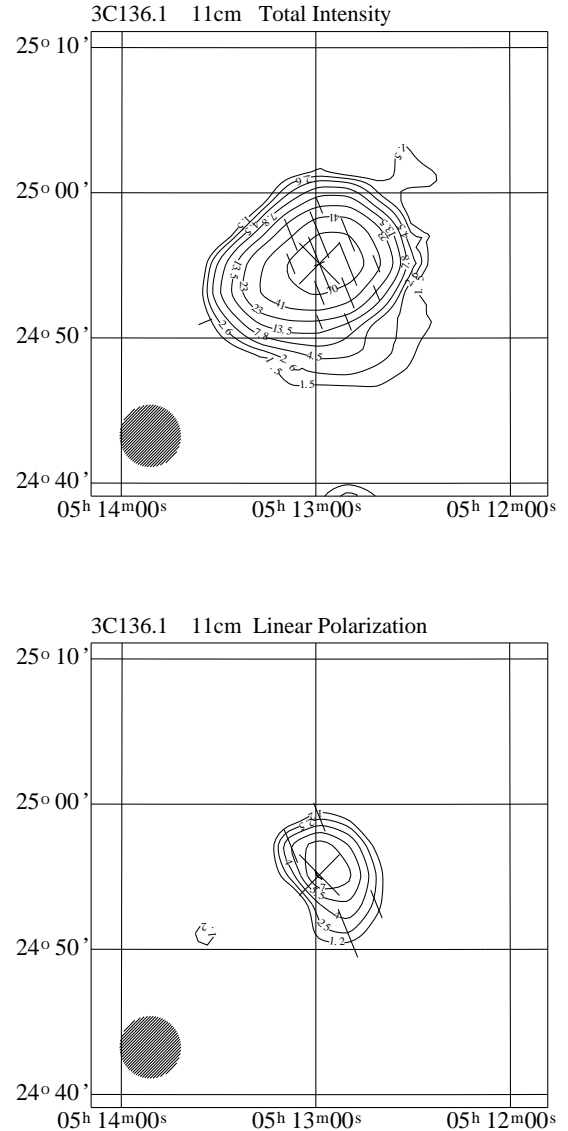


FIGURE 3.27— Maps of 3C136.1 at 2.7 GHz. The contour levels are given in Tab. 3.4. The map layout is identical to Fig. 3.12

Source	Fig.	Contour Levels [mJy/beam]
3C136.1	3.27a	15,26,45,78,135,230,410,700
	3.27b	9,13,18,24,31,39
B2 0828+32	3.28a	12,21,36,62,108,187,324,560
	3.28b	9,13,18,24,31,39,48
3C223.1	3.29a	18,31,54,94,162,280,486,840
	3.29b	6,9,13,18,24

TABLE 3.4— Contour levels of the 2.7 GHz maps.

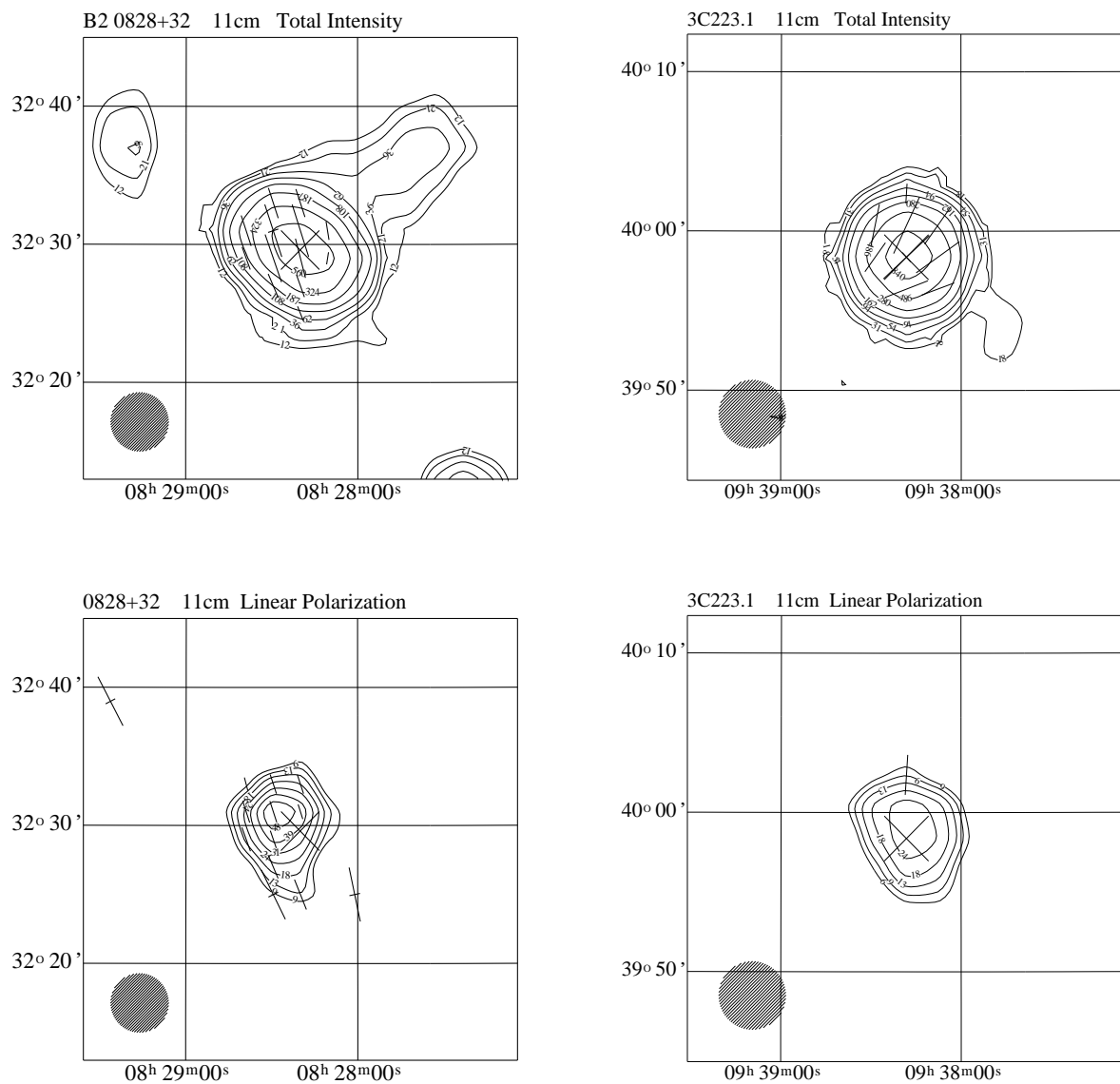


FIGURE 3.28— Maps of B2 0828+32 at 2.7 GHz. The contour levels are given in Tab. 3.4. The map layout is identical to Fig. 3.12

FIGURE 3.29— Maps of 3C223.1 at 2.7 GHz. The contour levels are given in Tab. 3.4. The map layout is identical to Fig. 3.12

# 4

## Interferometric Images

This chapter presents interferometric radio data that has been used as part of the spectral analysis of X-shaped radio galaxies complementary to the single-dish images discussed in the previous chapter. The data were obtained either from own observations with the Westerbork Synthesis Radio Telescope (WSRT) or were extracted and re-reduced from the WSRT archive. In addition use was made of radio data contained in the Westerbork Northern Sky Survey (WENSS) and the NRAO VLA Sky Survey (NVSS). The data reduction will be discussed only briefly. The final images will be presented and discussed shortly.

### 4.1 WSRT Data

Observations of five X-shaped sources were carried out with the WSRT at 1.369 GHz. The time on source was 12 hours for each proposed object and setup. All sources were observed with the shortest baseline (9A) of 36 m, except 3C136.1 for which two setups with 9A=36 m and, 72 m were chosen in order to eliminate the impact of 1st order grating rings across the source. The linear dipoles (X,Y) of the WSRT were set to parallel at  $0^\circ$ . The backend produces all possible 4 combinations (XX, YY, XY, YX) thus allowing to recover the full polarization information. The data were obtained in full-redundancy mode yielding a total of 88 (40 unique, 48 redundant) baselines. The initial data calibration was performed using the NEWSTAR package. Thanks to the excellent gain and phase stability of the WSRT one calibrator measurement prior and after the observation is sufficient to calibrate a full 12-hr continuous run. The obtained gain and phase correction are then interpolated between these measurements and applied to the data using the NCALIB task. The polarization calibration requires correction of geometric dipole offsets from their

ideal position. The TASK NCALIB (option POLAR) determines necessary corrections by evaluating the X and Y signals obtained from an unpolarized or weakly polarized source (usually 3C147). As a second step possible non-zero phase differences between the X and Y signals of all feeds have to be eliminated. This is done with the option VZERO with the help of a strongly polarized source (typically 3C48). After completion of the calibration the data were exported to the FITS format using NSCAN. Further imaging (cleaning and self-calibration) were performed in AIPS and DIFMAP (Shepherd et al. 1995).

The data of B2 0828+32 and 3C52 were heavily affected by interference. The impact on the data turned out to be so severe that even major data flagging and selfcalibration did not lead to images of sufficient quality. Consequently the data for the affected sources were discarded from the analysis entirely. Table 4.1 lists the rms noise of the final images.

### 4.2 NVSS Data

The NRAO VLA Sky Survey (NVSS) is a radio continuum survey covering the sky north of  $-40^\circ$  declination at a frequency of 1.4 GHz

Source	Fig.	rms I [mJy/beam]	rms Q [mJy/beam]	rms U [mJy/beam]	rms PI [mJy/beam]
3C136.1	4.9	0.73	0.25	0.21	0.25
3C223.1	4.19	0.12	0.08	0.07	0.08
3C379.1	4.26	0.28	0.23	0.11	0.20

TABLE 4.1— Properties of the WSRT images. The rms noise is listed for Stokes parameters I,Q,U as well as for the polarized intensity (PI) maps.

(Condon et al. 1998). The NVSS is flux complete down to a level of 2.5 mJy. All fields have been observed in Stokes parameters I,Q and U. The images have been restored with a clean beam of  $45'' \times 45''$  in order to yield high signal to noise. The rms noise is  $\approx 0.45$  mJy/beam (Stokes I) and  $\approx 0.29$  mJy/beam (Stokes U and Q). The data is available to the public either in the form of processed  $(u, v)$  datasets or as fully reduced image cubes. For the multi-frequency analysis performed within the framework of this thesis the available images proved to be of sufficient quality and they have been used without re-reducing the  $(u, v)$  datasets. The  $4^\circ \times 4^\circ$  image cubes have been loaded from the NRAO ftp server. The cubes were imported to AIPS and the relevant sub-fields were extracted using SUBIM. The epoch was switched from J2000.0 to B1950.0 using REGRD in order to match the other datasets used for the multi-frequency data analysis. Also a frequency axis and the clean beam size had to be added to the FITS-header manually. The source list and the actual noise levels of the images can be found in Tab. 4.2.

### 4.3 WENSS Data

The Westerbork Northern Sky Survey (WENSS) is a low-frequency (325 MHz) radio survey that covers the whole sky north of  $\delta=30^\circ$  (Rengelink et al. 1997). The limiting flux density is approximately 18 mJy at the  $5\text{-}\sigma$  level. The resolution of the survey is  $54'' \times 54'' \cdot \text{cosec}(\delta)$ . Due to the declination limit only 4 X-shaped sources were part of the WENSS (3C52, B2 0828+32, 3C223.1, 3C379.1) and only B2 0828+32 is sufficiently resolved to be used for spectral

index mapping. The total intensity image of B2 0828+32 is displayed in Fig. 4.14. The data of the other 3 unresolved sources have been used to determine the total flux for the integrated spectra and the images will be not shown here.

### 4.4 Miscellaneous Data

Additional data at different frequencies have been extracted mainly from the WSRT archive. These data have been re-reduced including calibration. Other datasets have been kindly provided by various persons.

#### 4C12.03

Figure 4.1 presents a VLA map of 4C12.03 at 1.5 GHz. The image was kindly made available by Leahy & Perley (1991). The image reveals the peculiar morphology of 4C12.03. The two bright knots on either side of the core suggest a two sided jet. There is no indication of a hotspot in the southern lobe. The brightest feature of the south→west lobe can be found between the primary and the secondary lobe.

The NVSS maps (Fig. 4.2) reveal the high fractional polarization of the northern (13%) and the western (15%) radio lobes. The southern and eastern lobes exhibit a mean fractional polarization of 9%.

#### NGC 326

The total intensity image of NGC 326 displayed in Fig. 4.4 was originally published by Condon et al. (1991). The authors have kindly made this image available to the public through NED. The rms noise is 4.5 mJy/beam. The HPBW is  $15'' \times 15''$ . As

Source	Fig.	rms I [mJy/beam]	rms Q [mJy/beam]	rms U [mJy/beam]	rms PI [mJy/beam]
4C12.03	4.2	0.64	0.28	0.31	0.32
NGC 326	4.3	0.66	0.3	0.28	0.3
3C52	4.5	0.67	0.35	0.33	0.38
3C136.1	4.10	0.6	0.43	0.41	0.47
0828+32	4.16	0.45	0.3	0.3	0.32
3C223.1	4.20	0.57	0.3	0.3	0.31
3C315	4.25	0.73	0.37	0.34	0.35
3C379.1	4.27	0.54	0.29	0.31	0.31
3C403	4.28	0.83	0.38	0.41	0.42

TABLE 4.2— X-shaped sources included in the NVSS. The rms-noise is given in mJy/beam for Stokes parameters I,U,Q and the polarized intensity (PI).

Source	Beam	rms [mJy/beam]
3C52	67.4'' $\times$ 54''	3.7
B2 0828+32	100.5'' $\times$ 54''	6.2
3C223.1	84.1'' $\times$ 54''	3.8
3C379.1	56.1'' $\times$ 54''	5.2

TABLE 4.3— Source list of X-shaped radio galaxies contained in the WENSS. Listed are the beam size and the rms-noise level

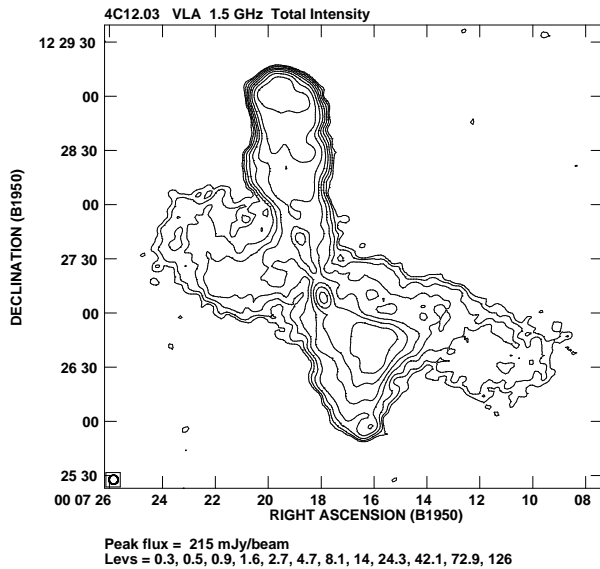


FIGURE 4.1— Total intensity image of 4C12.03 at 1.5 GHz. The map has been originally published by Leahy & Perley (1991) and has been kindly made available by the authors.

can be seen the secondary lobes appear to be straight. The northern lobe in particular does not show any significant curvature. Deep radio images like this have made the original proposition of steady jet precession (Ekers et al. 1978) quite unlikely.

The NVSS image (Fig. 4.3) confirms the tail of radio emission extending westward from the tip of the northern secondary lobe visible in the 1.4 GHz map presented by Worrall et al. (1995). Polarized emission is detected only from the active lobes with the average fractional polarization being low ( $\approx 1.5\%$ ). The secondary lobes appear to be unpolarized.

### 3C52

Total intensity maps of 3C52 at 1.4 GHz, 1.6 GHz and 2.7 GHz are available from NED. The original data has been published by Alexander & Leahy (1987). These images have a common resolution of  $5'' \times 4''8$ . The rms noise is 1.13 mJy/beam, 0.75 mJy/beam,

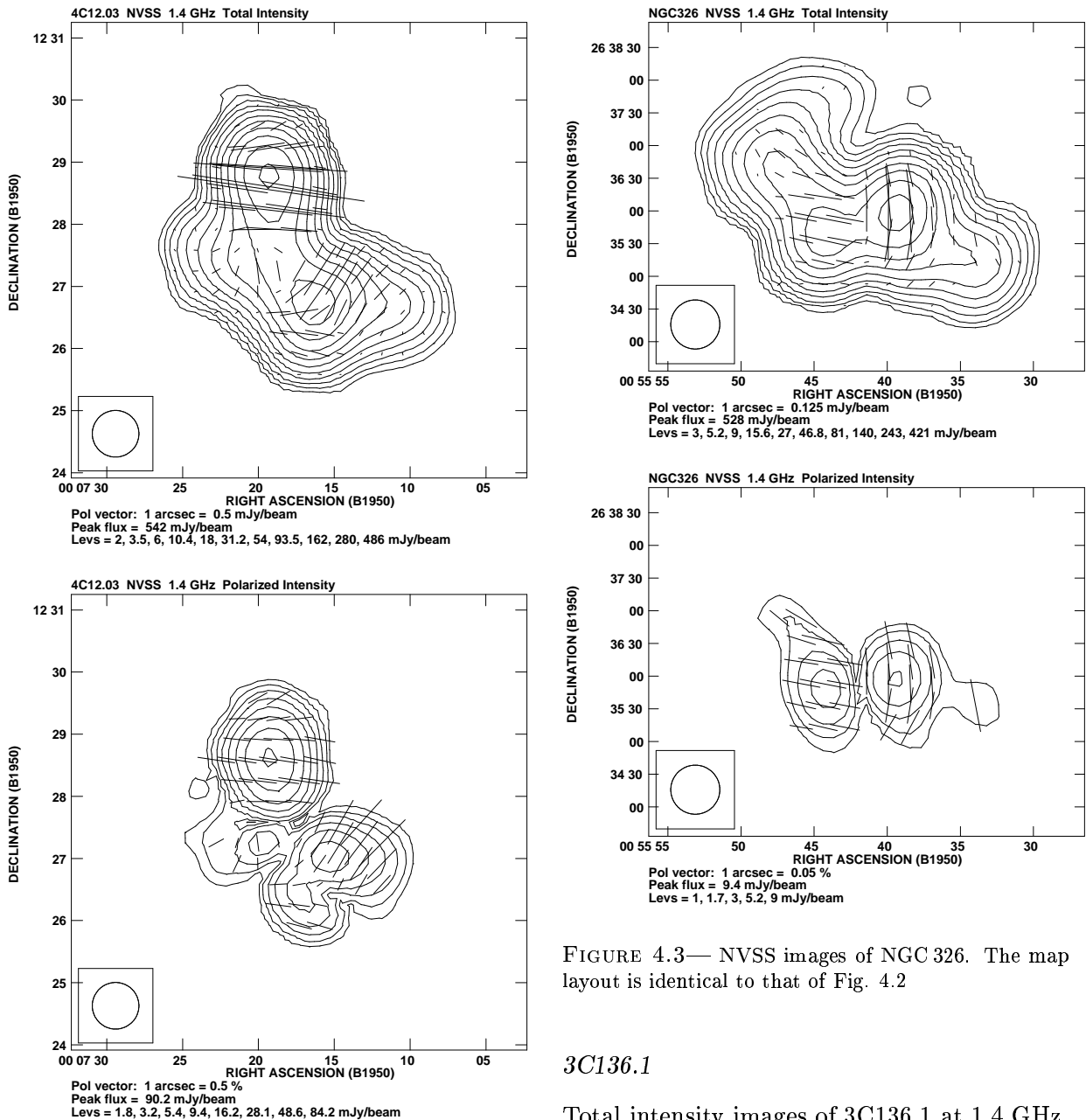


FIGURE 4.2— NVSS image of 4C12.03. The upper panel shows the total intensity image with superimposed E-vectors. The length of the vectors is proportional to the polarized intensity. The image of the polarized intensity is displayed in the lower panel. The length of the superimposed E-vectors is now proportional to the fractional polarization. The contour levels and the scale of the polarization vectors can be found below the images.

and 3.8 mJy/beam for the 3 frequencies respectively. Plots of the images can be found in Figs. 4.6-4.8.

FIGURE 4.3— NVSS images of NGC 326. The map layout is identical to that of Fig. 4.2

### 3C136.1

Total intensity images of 3C136.1 at 1.4 GHz, 1.6 GHz and 2.7 GHz originally published by Alexander & Leahy (1987) were kindly made available by the authors. The map noise is 0.42, 0.45 and 1.1 mJy/beam for the three frequencies respectively. The images are displayed in Figs. 4.11-4.13. The 1.4 GHz and 1.6 GHz data has been observed with the VLA in C configuration, the 2.7 GHz image has been obtained with the 5-km telescope. Considering the large extent of 3C136.1 and inspecting the images we suspect that all images suffer from missing flux (comp. Sect. 6.5.4).

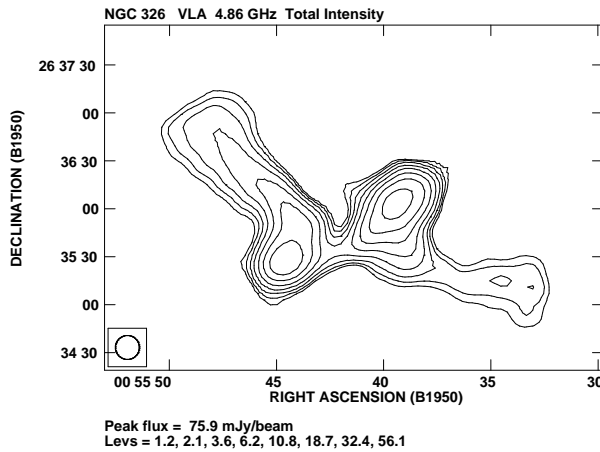


FIGURE 4.4— Total intensity image of NGC 326 at 4.86 GHz. The data were originally published by Condon et al. (1991) and have been kindly made available by the authors.

### B20828+32

WSRT archive data of B2 0828+32 at a frequency of 608.5 MHz were extracted and re-reduced including calibration. Careful flagging and multiple phase-selfcalibration resulted in an rms-noise in the final map of  $\sim 0.45$  mJy/beam, which is better by a factor of two compared to what was achieved in the original publication (Parma et al. 1985). The total intensity and polarized intensity images can be seen in Fig. 4.15. The source is highly polarized. The primary lobes exhibit fractional polarization of 10-15% whereas the secondary lobes show considerably higher mean polarization ( $\sim 40\%$  in the north and  $\sim 25\%$  in the south). The highest fractional polarization ( $\sim 70\%$ ) one finds on the ridge of emission that extends from the core into the northern secondary lobe.

At 1.4 GHz two 8-hr full synthesis datasets were extracted from the WSRT archive. No polarization information was available. The uv-data were edited and calibrated separately and were then merged into a combined uv-dataset using DBCON. Further imaging and phase-selfcalibration was performed in DIFMAP. The final total intensity image is displayed in Fig. 4.17. The rms noise is 0.4 mJy/beam and the clean beam size is

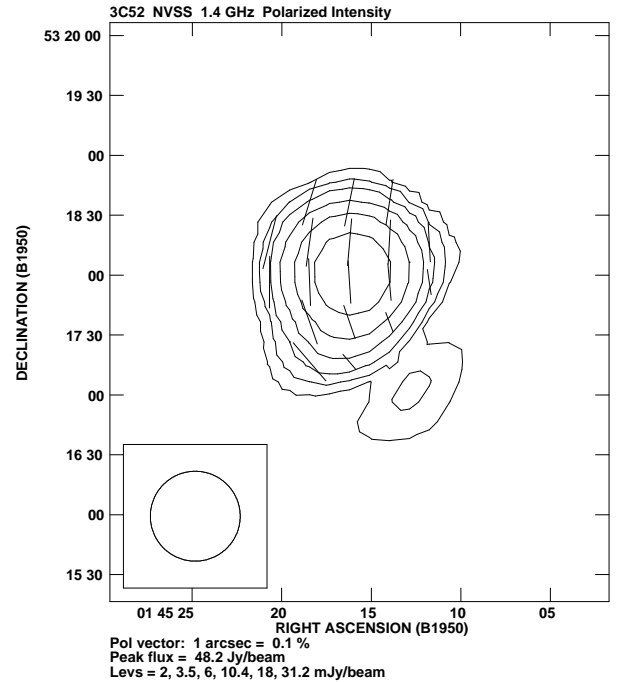
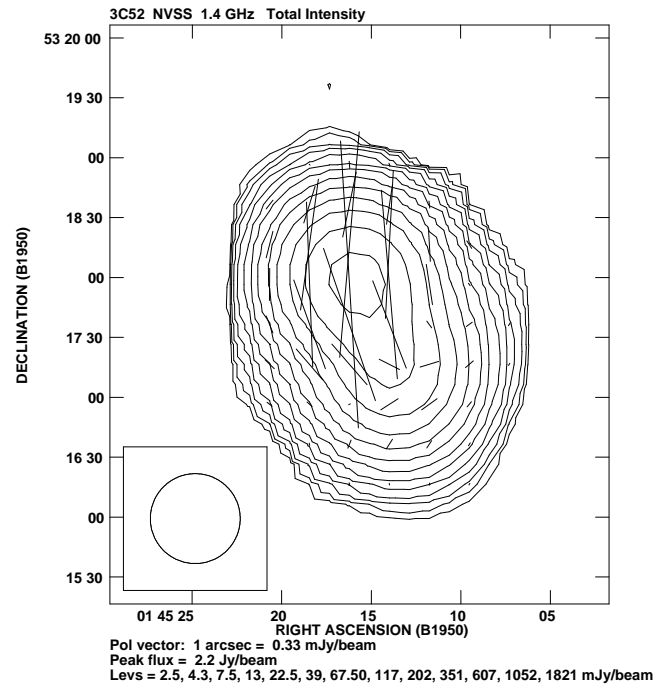


FIGURE 4.5— NVSS images of 3C52. The map layout is identical to that of Fig. 4.2

$46''1 \times 27''5$ .

### 3C223.1

VLA images of 3C223.1 at 1.5 GHz (L-band), 4.9 GHz (C-band) and 8.4 GHz (X-band) were

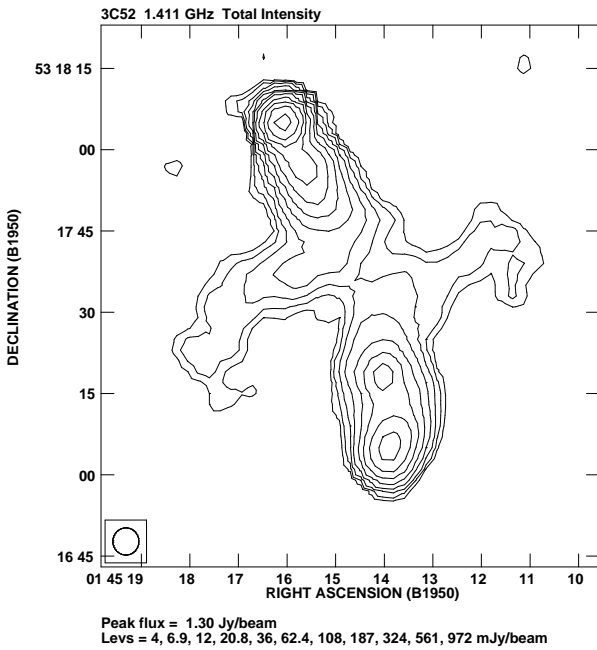


FIGURE 4.6— Total intensity image of 3C52 at 1.411 GHz. The data has been previously published by Alexander & Leahy (1987). The map layout is identical to that of Fig. 4.2

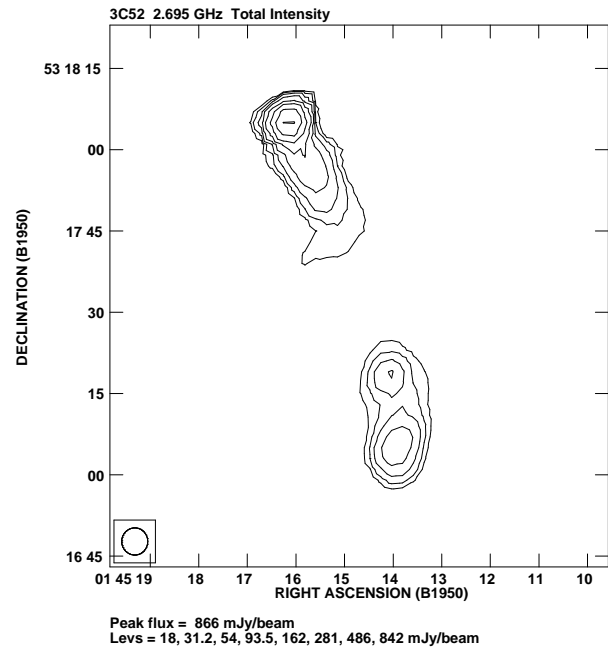


FIGURE 4.8— Total intensity image of 3C52 at 2.695 GHz. The data has been previously published by Alexander & Leahy (1987). The map layout is identical to that of Fig. 4.2

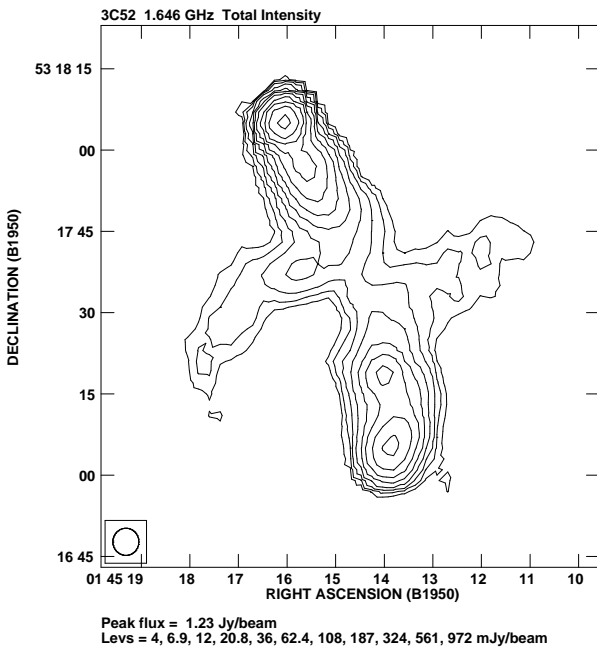


FIGURE 4.7— Total intensity image of 3C52 at 1.646 GHz. The data has been previously published by Alexander & Leahy (1987). The map layout is identical to that of Fig. 4.2

kindly provided by J. Dennett-Thorpe and are displayed in Figs. 4.21-4.23. The resolution of the images is  $10'' \times 10''$ . A detailed discussion of the employed imaging and data reduction procedure can be found in Dennett-Thorpe (1996) and Dennett-Thorpe et al. (1999). The 8.4 GHz data have been previously published by Black et al. (1992) at a resolution of  $2''.5 \times 2''.5$ . The magnetic field vectors swing smoothly from the active to the secondary lobes and are aligned parallel to the source edges. At the tips of the secondary lobes the field orientation is parallel to the lobe axis. Much of the source is highly polarized (15-30%). The peak of fractional polarization ( $\sim 40\%$ ) is found coincident with the brightness maximum of the north-western secondary lobe.

Snapshot observations of 3C223.1 at a frequency of 609 MHz have been extracted from the WSRT archive. The original observation took place in 1983. The time on source is split into 4 intervals of 14 minutes each. These intervals are evenly spread in hour an-



gle in order to give a well defined  $uv$  coverage. The  $uv$  dataset have been calibrated and re-reduced. However the information about the ionospheric conditions at the time of observation could not be retrieved anymore. Therefore the polarization data was not used in the following. The total intensity map is shown in Fig. 4.18. The rms-noise is 25 mJy/beam.

### 3C315

Total intensity images of 3C315 at three frequencies (1.4 GHz, 1.6 GHz and 2.7 GHz) are provided to the public by Alexander & Leahy (1987) via NED (Fig. 4.24). The morphology of 3C315 is quite peculiar. Due to the absence of hotspots it is unclear which part of the source represents the active and which part the secondary lobes. Within this thesis we will refer to the northern and southern lobes as the active ones. This is motivated by the fact that the northern lobe is considerably brighter than its western counterpart. The south→east lobe does not show any similar brightness asymmetry. If at all, the brightest feature there is located in the eastern lobe close to the core. In contrast to the other X-shaped sources studied here, 3C315 exhibits a bright and pronounced radio core. The NVSS image (Fig. 4.25) reveals 3C315 to be highly polarized. The highest fractional polarization is found at the tip of the southern lobe (&40%) and the tip of the western lobe (&35%) whereas the northern and eastern lobes are considerably less polarized ( $\sim 20\%$  and  $\sim 10\%$  respectively).

### 3C379.1

Figure 4.26 presents the total and polarized intensity images of 3C379.1 obtained with the WSRT. The source has only short secondary lobes at 1.4 GHz which do not exhibit any significant polarized emission. The primary lobes are polarized between 20% and 30% except in the hotspot areas where the fractional polarization is somewhat lower (5% – 8%).

### 3C403

Images of 3C403 at 1.4 GHz (Fig. 4.29) and 8.35 GHz (Fig. 4.30) were kindly made avail-

able by J. Dennett-Thorpe. The 8.35 GHz data have been previously published and discussed by Black et al. (1992). The imaging procedure and data reduction techniques for the 1.4 GHz image were discussed in detail in Dennett-Thorpe (1996) and Dennett-Thorpe et al. (1999). The rms-noise is 0.14 mJy/beam and 1.5 mJy/beam for the two frequencies respectively. The beam size is  $4''5 \times 4''5$ . The images reveal the complex structure of 3C403. A weak radio jet connects the core and the eastern primary lobe. The jet and lobe show strong signs of twisting and bending. The western primary lobe has a strikingly similar appearance. The core is clearly visible in total intensity. A peculiar, compact and bright knot can be seen in the eastern radio lobe along the path of the jet. 3C403 is strongly polarized with the mean fractional polarization exceeding 15% in all parts of the source. The secondary lobes exhibit somewhat higher fractional polarization with mean values of 25%. The highest fractional polarization ( $\sim 50\%$ ) can be found in the low luminosity regions at the western rim of the southern lobe and the eastern rim of the northern lobe. Other places of strong polarization are the tips of the secondary lobes with values of  $\sim 40\%$ . These extremely polarized areas most probably mark shock regions where the lobe material interacts with the ISM/IGM and the magnetic fields are being compressed. The magnetic field (comp. Black et al. 1992) is oriented parallel to the jet within the primary lobes. In the secondary lobes the field lines run in loops tangential to the source edges.

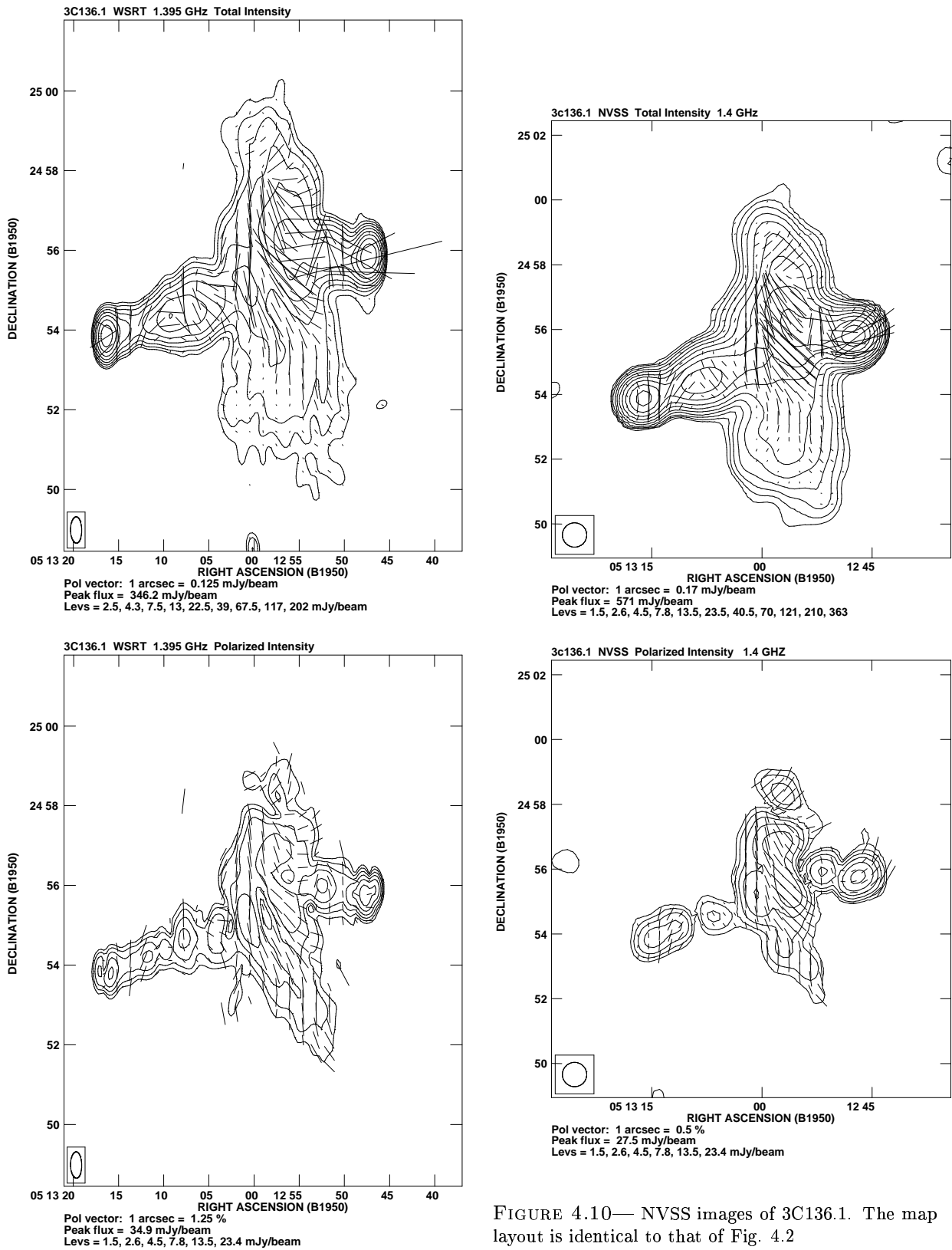


FIGURE 4.10— NVSS images of 3C136.1. The map layout is identical to that of Fig. 4.2

FIGURE 4.9— Total intensity (top) and polarized intensity (bottom) images of 3C136.1 obtained with the WSRT at 1.395 GHz. The beam size is  $39''.7 \times 16''.8$ . The layout of the maps is identical to Fig. 4.2

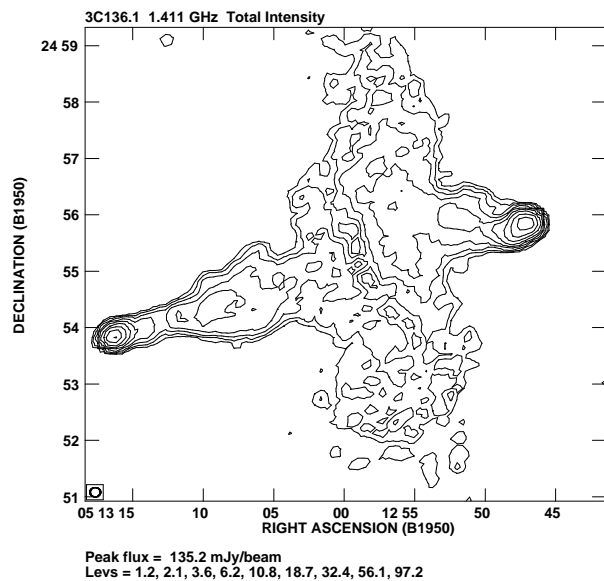


FIGURE 4.11— Total intensity image of 3C136.1 at 1.411 GHz. The data has been previously published by Alexander & Leahy (1987). The map layout is identical to that of Fig. 4.2

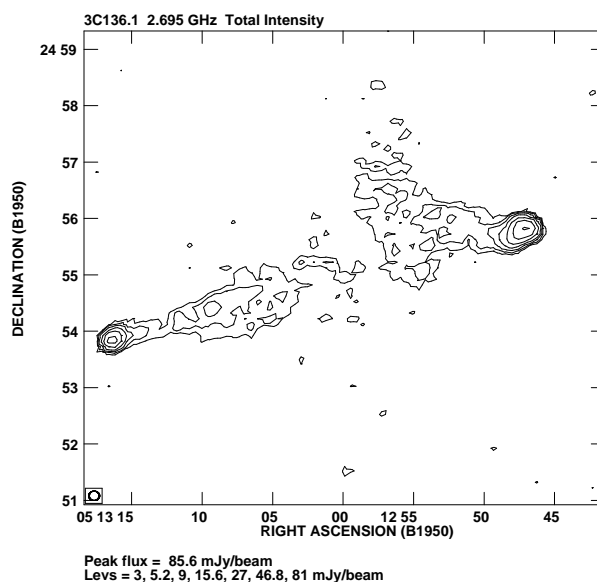


FIGURE 4.13— Total intensity image of 3C136.1 at 2.695 GHz. The data has been previously published by Alexander & Leahy (1987). The map layout is identical to that of Fig. 4.2

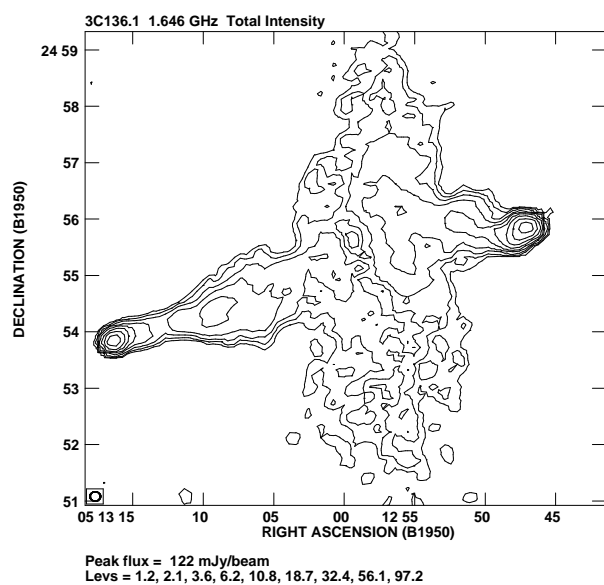


FIGURE 4.12— Total intensity image of 3C136.1 at 1.646 GHz. The data has been previously published by Alexander & Leahy (1987). The map layout is identical to that of Fig. 4.2

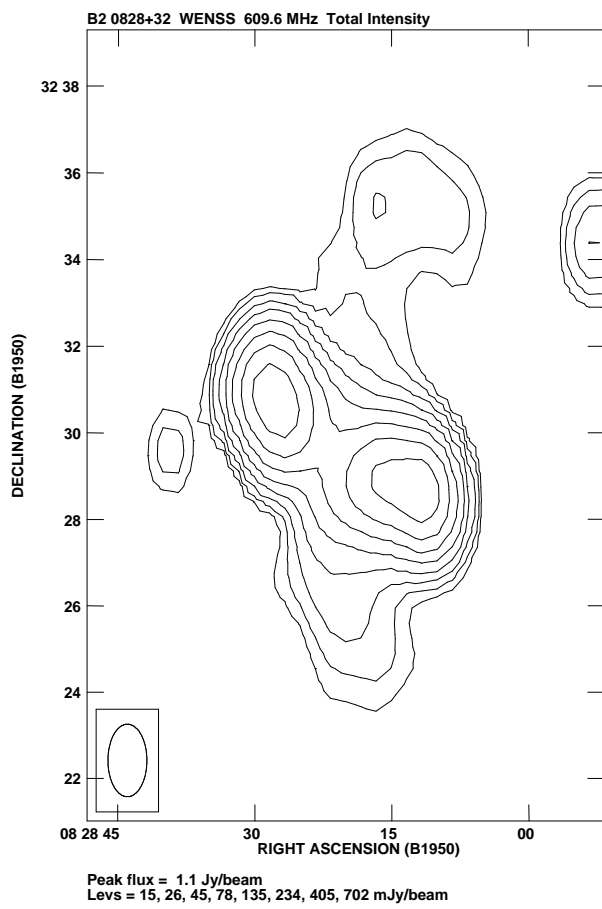


FIGURE 4.14— WENSS total intensity images of B2 0828+32.

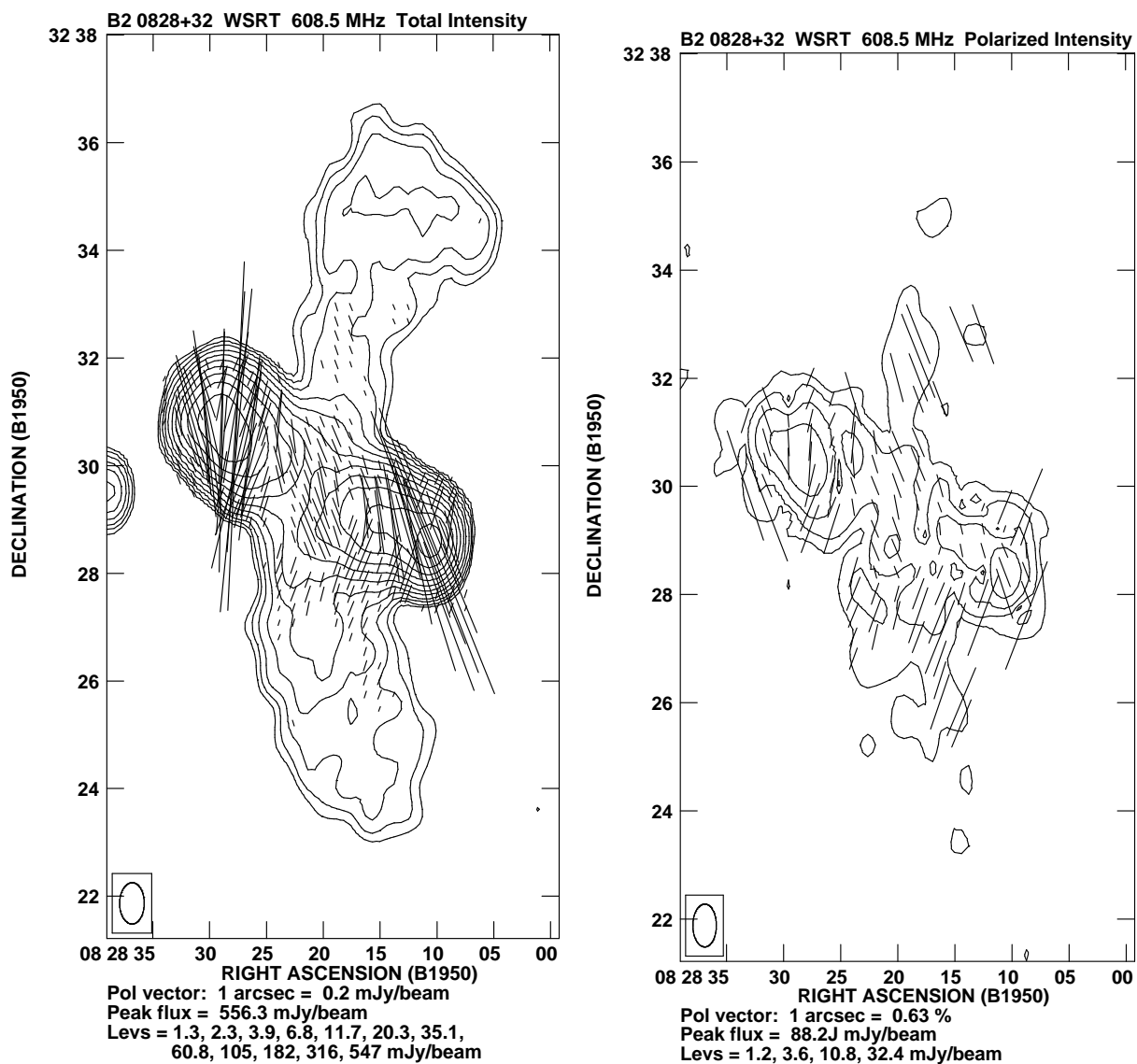


FIGURE 4.15— Total intensity (left) and polarized intensity (right) images of B2 0828+32 at 608.5 MHz.

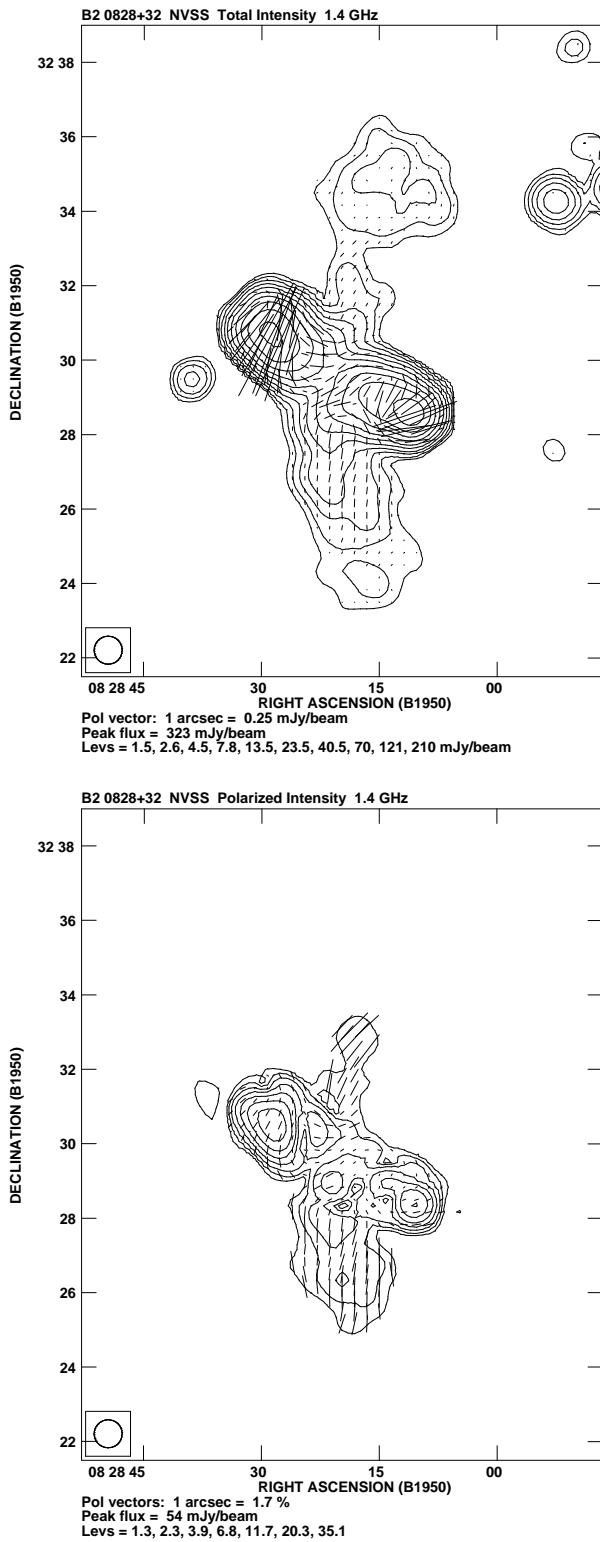


FIGURE 4.16— NVSS images of B2 0828+32. The map layout is identical to that of Fig. 4.2

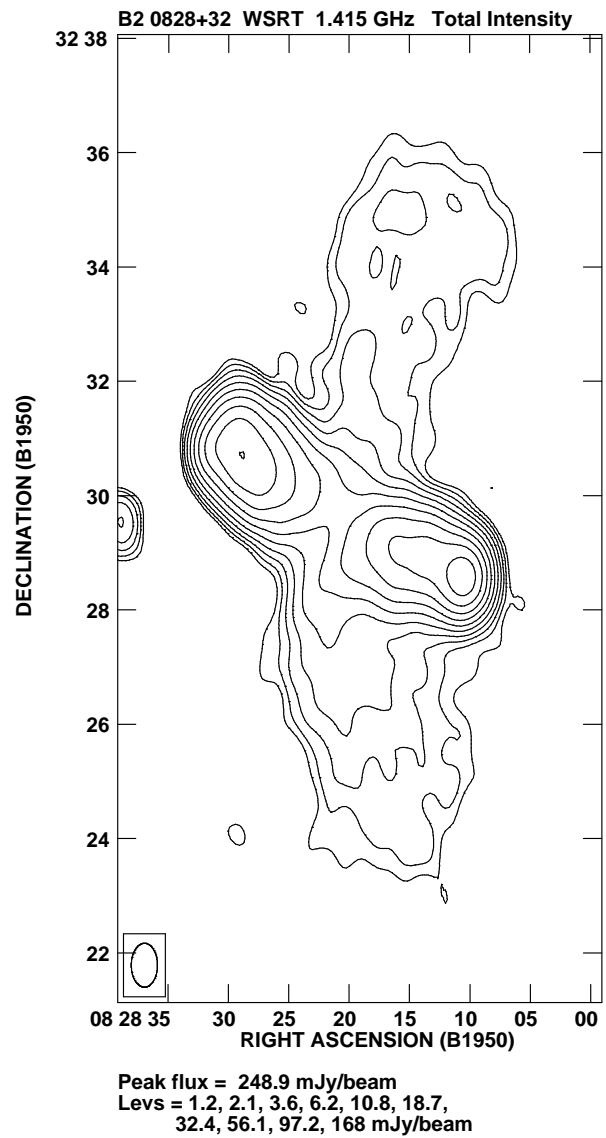


FIGURE 4.17— Image of B2 0828+32 at 1.415 GHz. The map layout is identical to that of Fig. 4.2

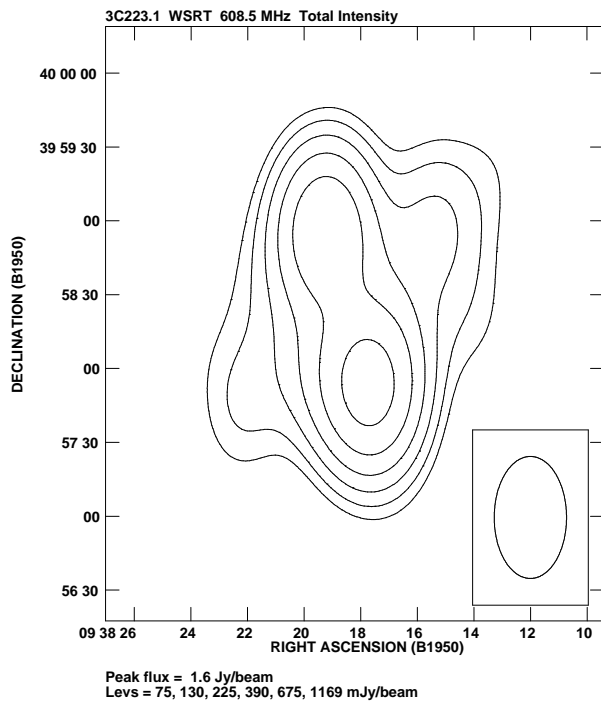


FIGURE 4.18— Total intensity image of 3C223.1 at 609 MHz. The beam size is  $49''.6 \times 29''.4$ . The map layout is identical to Fig. 4.2

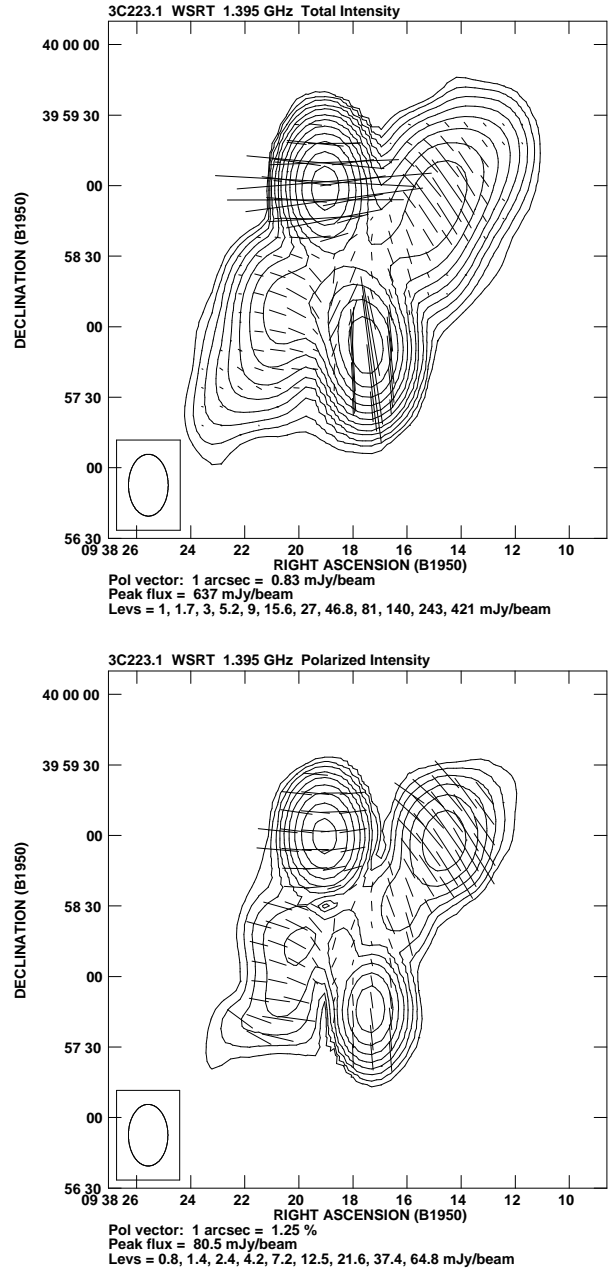


FIGURE 4.19— Total intensity (top) and polarized intensity (bottom) images of 3C223.1 obtained with the WSRT at 1.395 GHz. The beam size is  $26''.3 \times 16''.9$ . The layout of the maps is identical to Fig. 4.2

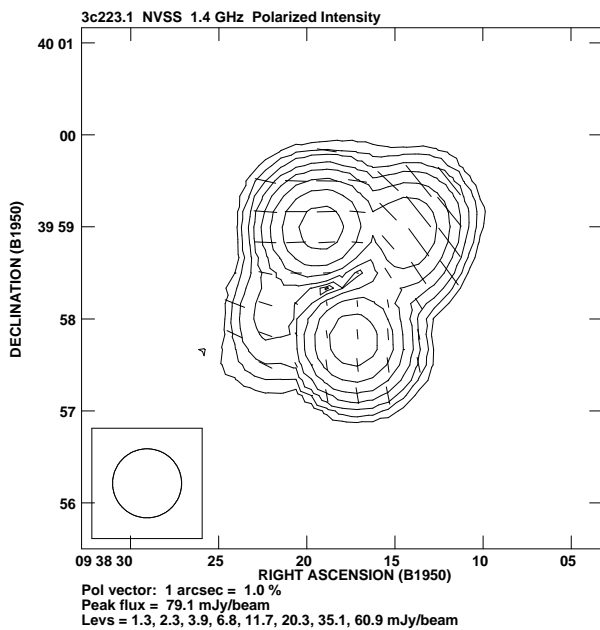
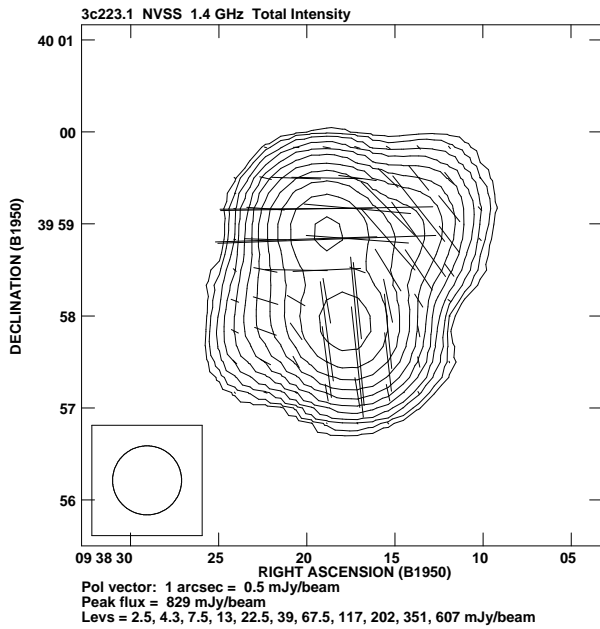


FIGURE 4.20— NVSS images of 3C223.1. The map layout is identical to that of Fig. 4.2

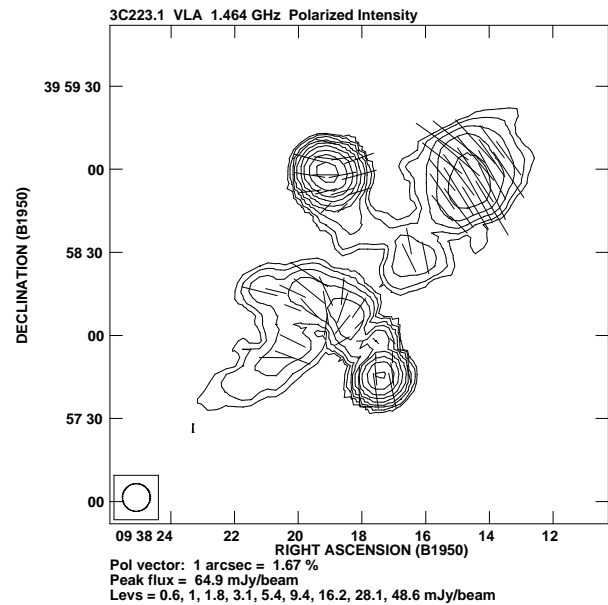
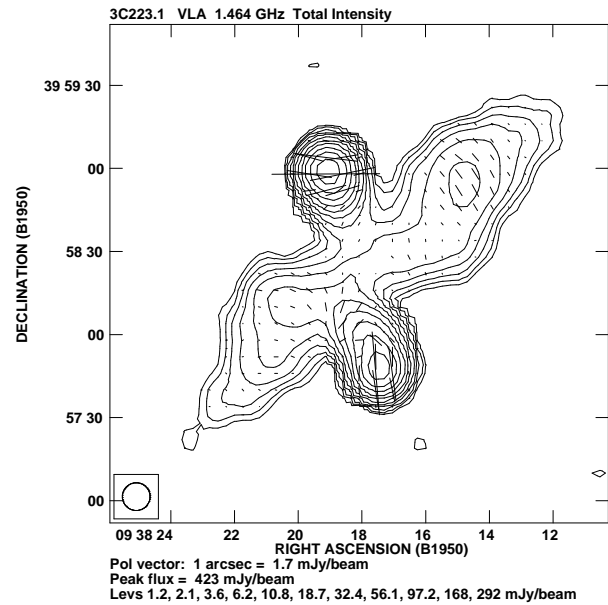


FIGURE 4.21— VLA images of 3C223.1 at 1.5 GHz. The data were kindly provided by J. Dennett-Thorpe. The beam size is  $10'' \times 10''$ . The map layout is identical to that of Fig. 4.2



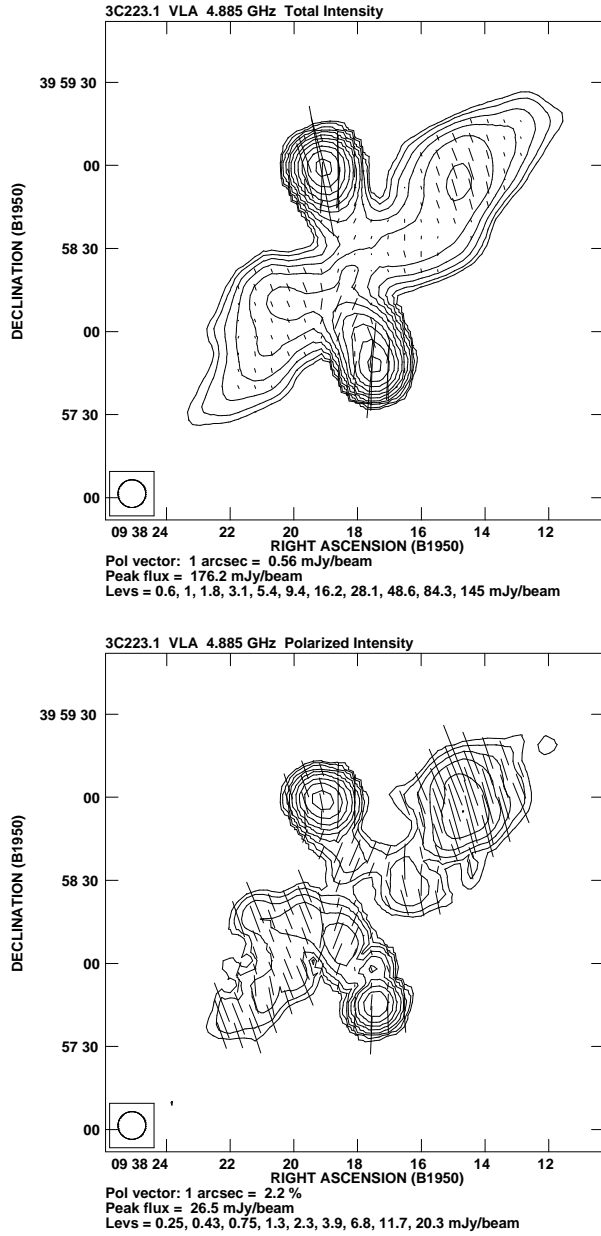


FIGURE 4.22— VLA images of 3C223.1 at 4.9 GHz. The data were kindly provided by J. Dennett-Thorpe. The beam size is  $10'' \times 10''$ . The map layout is identical to that of Fig. 4.2

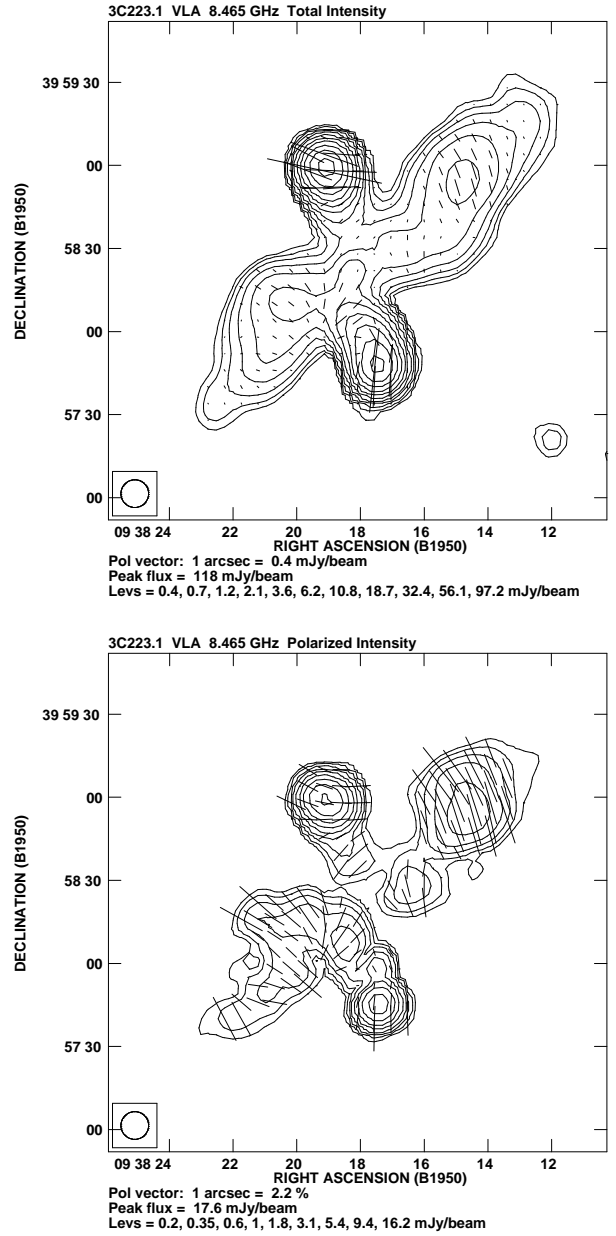


FIGURE 4.23— VLA images of 3C223.1 at 8.5 GHz. The data were kindly provided by J. Dennett-Thorpe. The beam size is  $10'' \times 10''$ . The map layout is identical to that of Fig. 4.2

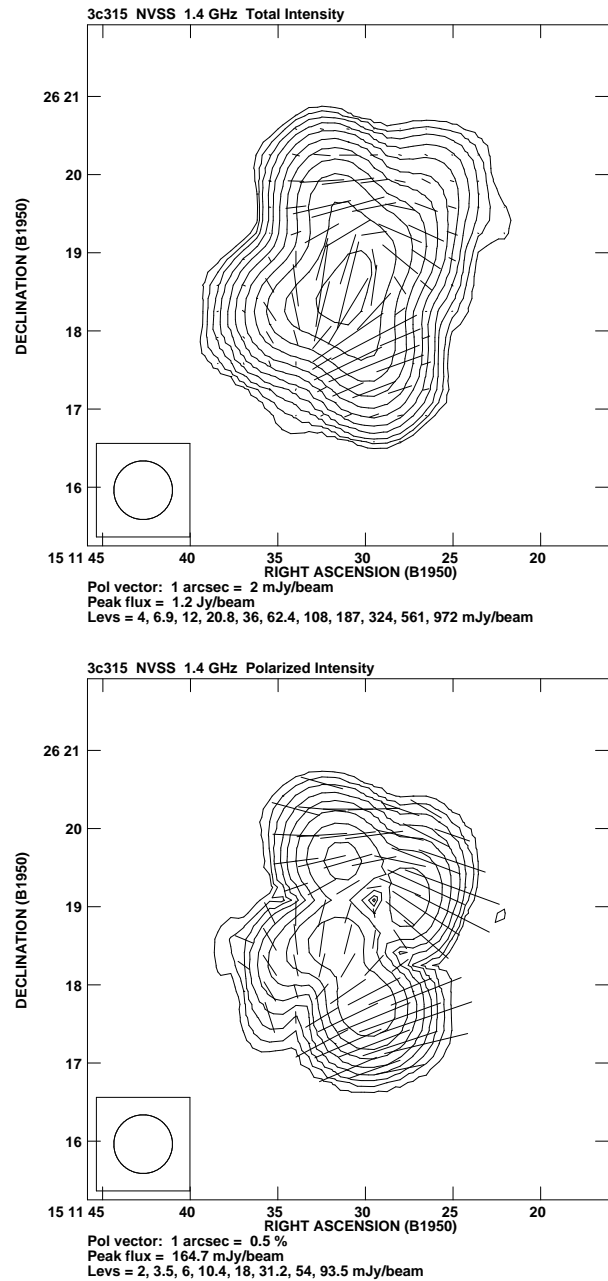
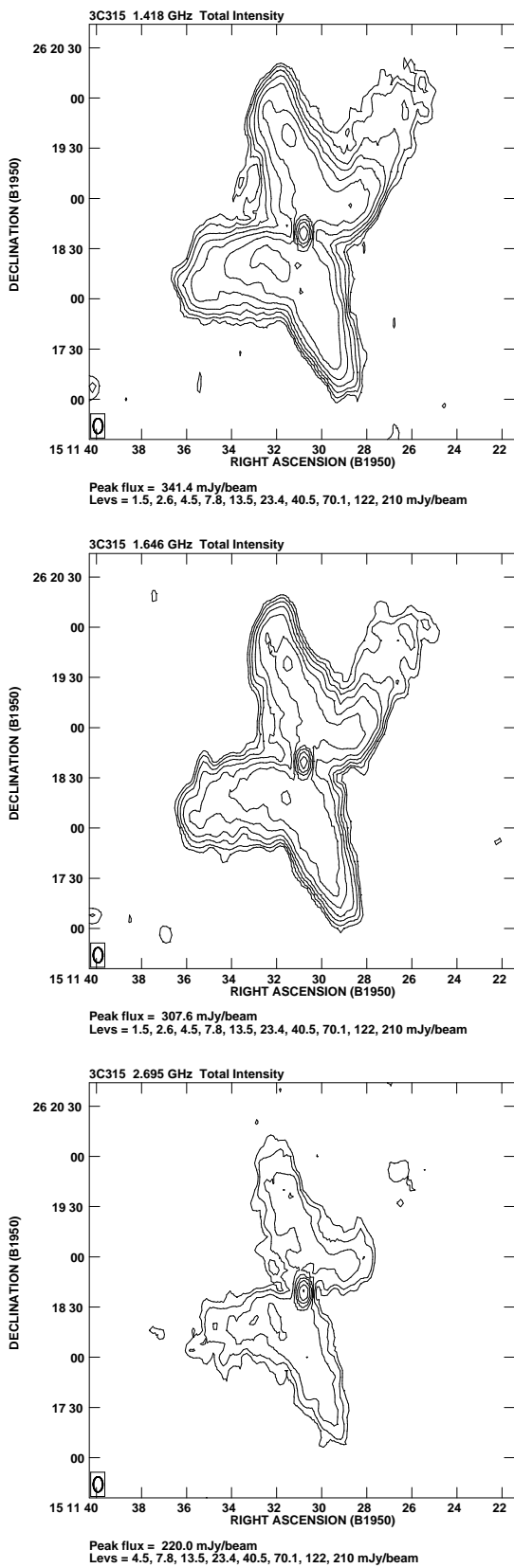


FIGURE 4.25— NVSS images of 3C315. The map layout is identical to that of Fig. 4.2

FIGURE 4.24— Total intensity images of 3C315 at 1.4 GHz (top), 1.6 GHz (middle) and 2.7 GHz (bottom). The data has been published by Alexander & Leahy (1987) and has been kindly provided by the authors. The beam size is  $5''.5 \times 9''.1$

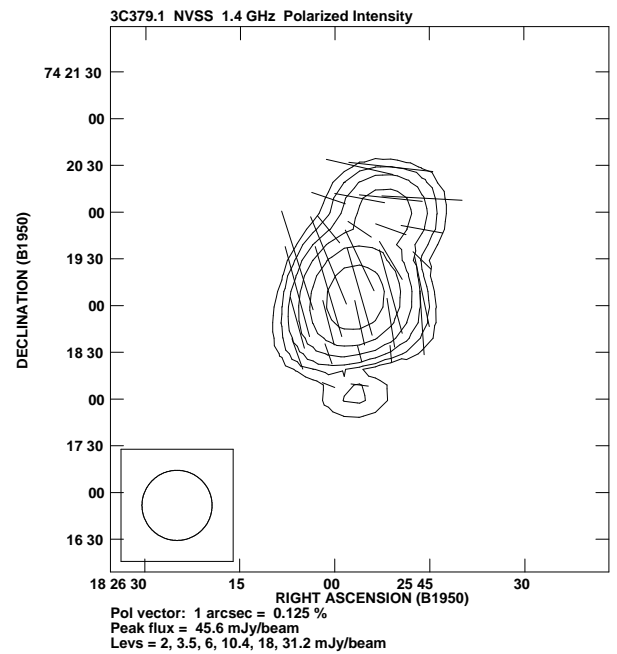
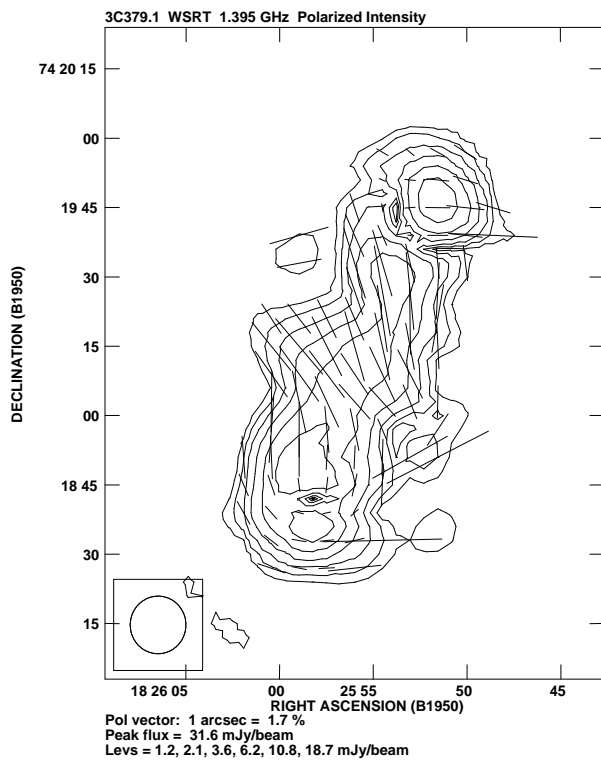
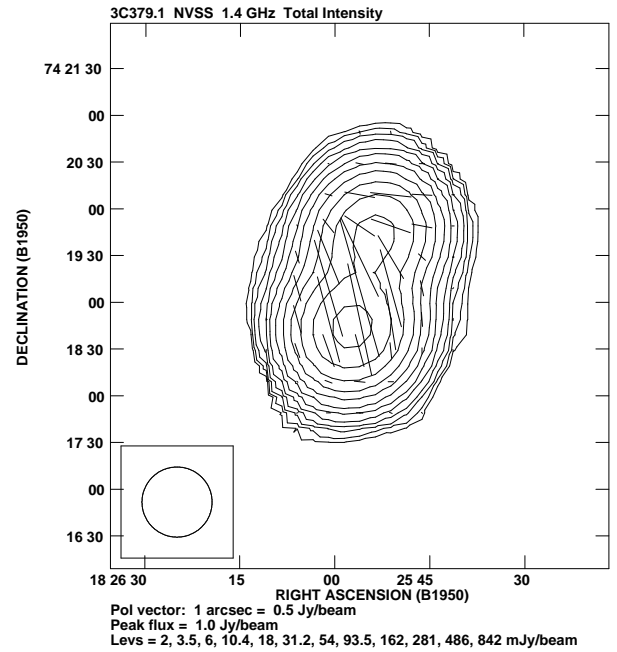
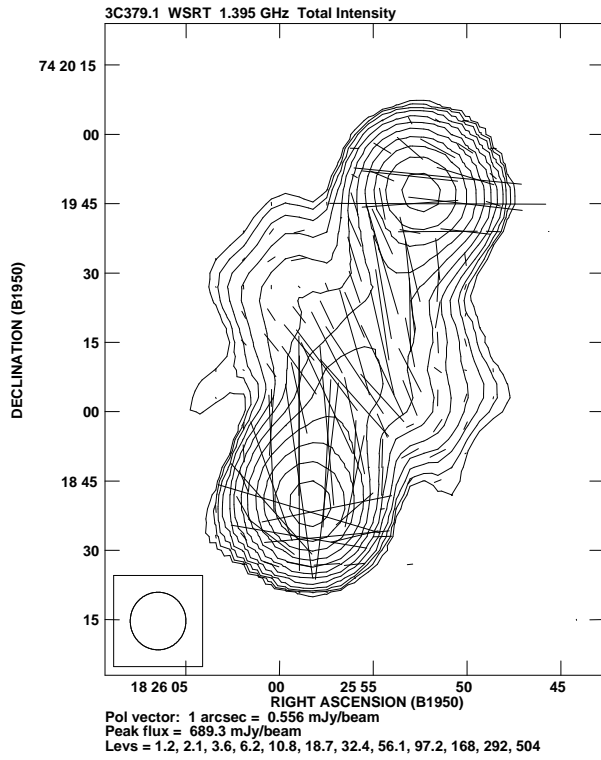


FIGURE 4.27— NVSS images of 3C379.1. The map layout is identical to that of Fig. 4.2

FIGURE 4.26— WSRT images of 3C379.1 at 1.395 GHz. The beam size is  $12''.45 \times 12''.05$ . The map layout is identical to that of Fig. 4.2

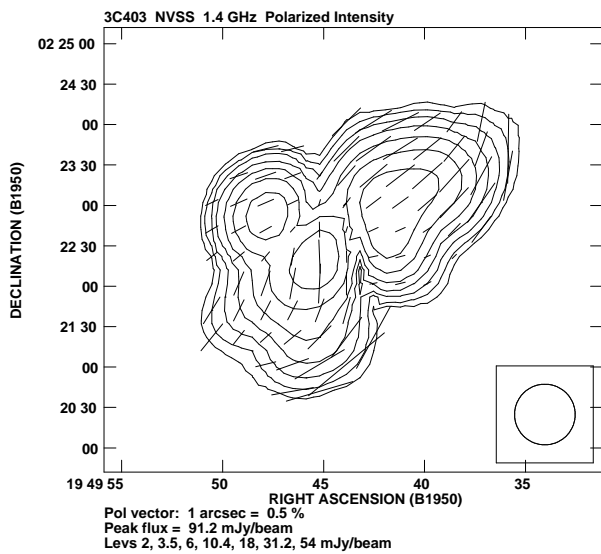
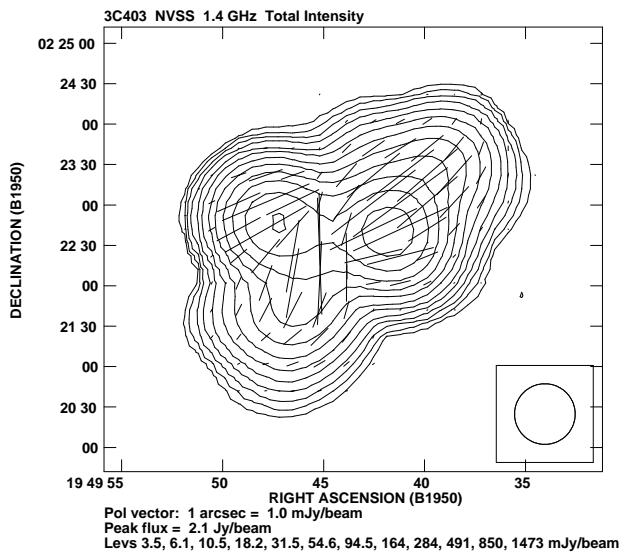


FIGURE 4.28— NVSS images of 3C403. The map layout is identical to that of Fig. 4.2

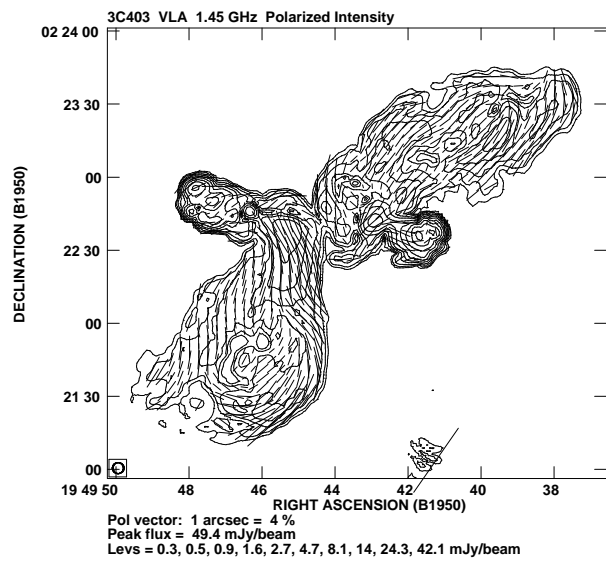
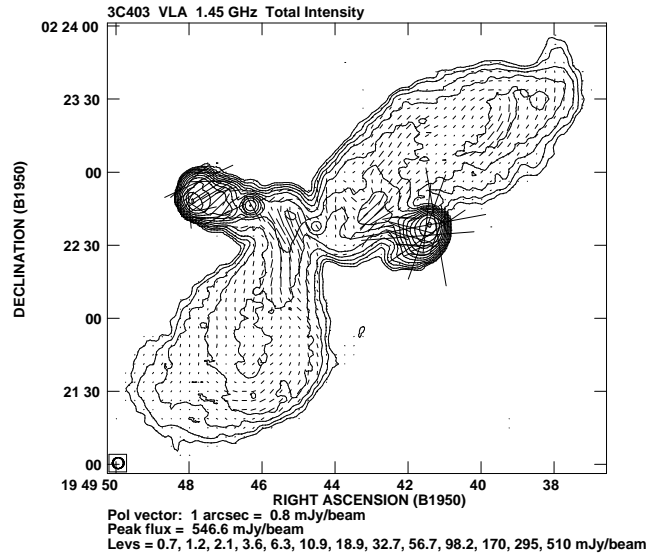


FIGURE 4.29— VLA images of 3C403 at 1.45 GHz. The data were kindly provided by J. Dennett-Thorpe. The beam size is  $4'' \times 4'' \cdot 5$ . The map layout is identical to that of Fig. 4.2

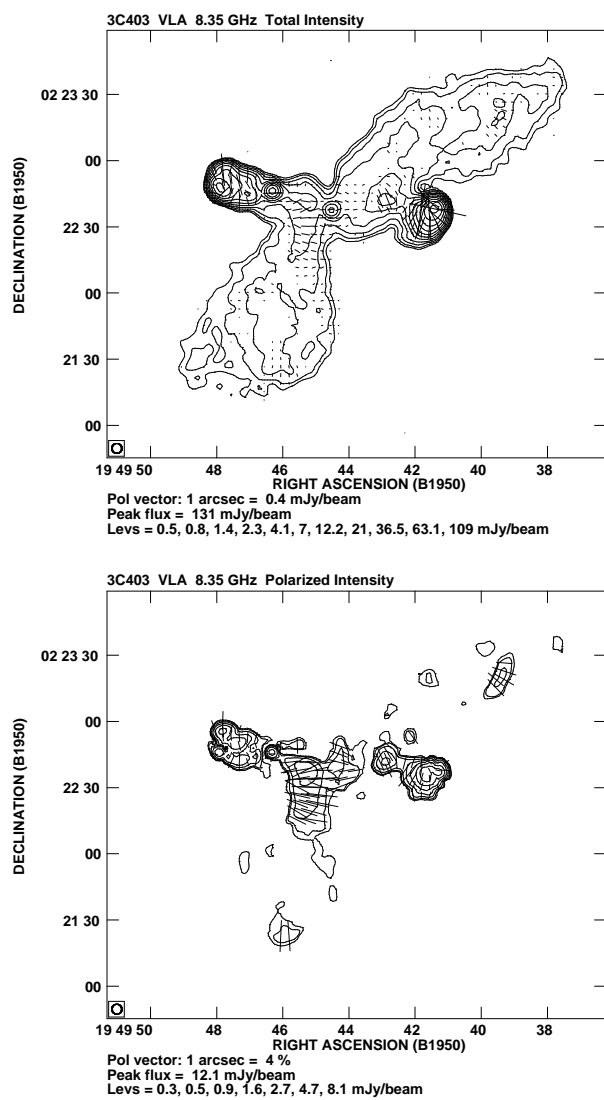


FIGURE 4.30— VLA images of 3C403 at 8.35 GHz. The data were kindly provided by J. Dennett-Thorpe. The beam size is  $4''.5 \times 4''.5$ . The map layout is identical to that of Fig. 4.2



# 5

---

## Formation of X-shaped Radio Sources Part I: Introduction

The most intriguing fact about X-shaped radio galaxies is the apparently low number of sources of that type. Even though some X-shaped objects might remain in hiding due to projection and other selection biases the total number of sources is certainly not *dramatically* lowered by these effects. Possible explanations for the small number of X-shaped sources are:

- they are very exotic objects that form only rarely and under extraordinary circumstances.
- they are normal radio galaxies that are currently in an short-lived and/or rare phase of their evolution.

In order to distinguish between these scenarios it is necessary to understand which formation process can be responsible for the X-shaped phenomenon.

This chapter will briefly introduce the most important formation mechanisms that have been proposed in the literature. In Chapter 7 these models will be reviewed again and discussed in greater detail in the light of the result of the spectral analysis presented in Chapter 6.

### 5.1 Backflow

Leahy & Williams (1984) have argued in favor of backflow being responsible for the forma-

tion of the secondary lobes of X-shaped radio galaxies. Backflow is formed by jet material that is released by the hotspots and is then streaming back towards the host galaxy. In the model proposed by Leahy & Williams (1984) the backflowing material remains collimated until it meets the backflow from the opposite hotspot and expands laterally into a fat disk oriented perpendicular to the radio lobe axis. The authors point out several difficulties this model has in reproducing the X-shaped morphology. The formation of the disk would be axisymmetric with respect to the radio lobe axis, whereas X-shaped sources exhibit *rotational* symmetry. Leahy & Williams (1984) have proposed two symmetry-breaking mechanisms that would lead to bending of the backflow into opposite directions (see Fig. 5.1): (1) A spheroidal gas distribution that is misaligned with the radio axis would deflect any backflowing material, preferentially in the direction parallel to the major axis of the gas distribution. (2) An old cavity in the ISM/IGM would provide a channel into which the backflow would preferentially stream. However, in order to create such a cavity in the past the radio jet must have been oriented in that direction. In that sense this scenario is not a pure backflow model but would require a mechanism that has realigned the radio jet. Considering the large linear sizes

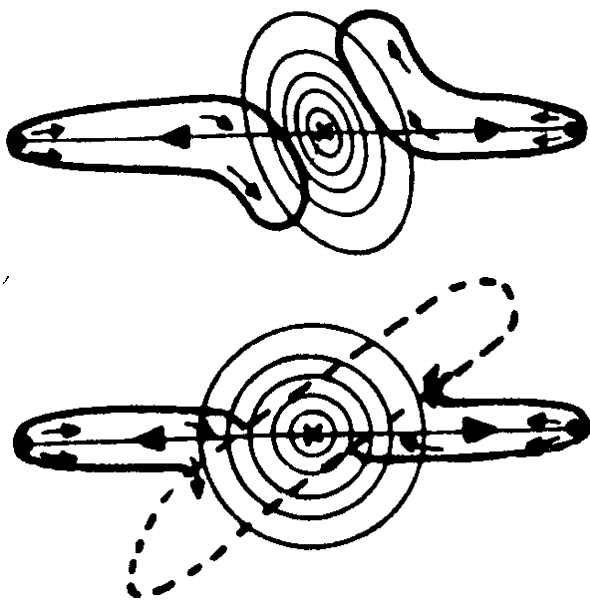


FIGURE 5.1— Sketch of two symmetry-breaking mechanisms proposed by Leahy & Williams (1984) to model directed backflows. In the upper graph a non-aligned spheroidal gas distribution within the host galaxy is deflects the backflowing material into opposite directions. The lower graph sketches the situation in case of a prior reorientation of the jet axis. The former radio lobes provide a low-density cavity into which the backflowing material will preferentially stream.

of some of the secondary lobes a crucial question is whether the speed of the backflow is sufficient to form them within the lifetime of the source. The speed of the backflow cannot be directly observed. However the sound speed provides a firm upper limit to the velocity of the backflow. This picture is supported by numerical simulations (e.g. Norman 1996, Aloy et al. 1999) that predict subsonic backflows. Also, observations of the lobes of radio galaxies have not revealed any evidence for strong shock that would be produced by supersonic flows.

In magnetized plasmas matter moves subsonically below the magnetosonic sound speed given as:

$$v_g = \sqrt{c_s^2 + v_a^2} \quad (5.1)$$

Here  $c_s$  is the thermal sound speed and  $v_a$  denotes the Alfvén velocity

$$c_s = \sqrt{\frac{kT}{m_p}} \quad v_a = \frac{B}{\sqrt{\mu_0 \rho}} \quad (5.2)$$

where  $k$  is Boltzmann's constant,  $T$  is the temperature,  $m_p$  denotes the proton mass,  $B$  is the magnetic field strength,  $\mu_0$  is the magnetic field constant and  $\rho$  is the mass density of the medium. For physical conditions prevailing in the lobes of radio galaxies the dominant term is the Alfvén velocity. Assuming typical values of  $B = 5 \times 10^{-10}$  T and  $\rho = 5 \times 10^{-27}$  kg m<sup>-3</sup> we obtain an Alfvén velocity of  $v_a \sim 6 \times 10^6$  m s<sup>-1</sup>. The thermal sound speed corresponding to  $kT = 2$  keV (for NGC 326, see Worrall et al. 1995) is  $c_s = 1.4 \times 10^4$  m s<sup>-1</sup> and can be neglected. We conclude that subsonic flows can occur at velocities of a few percent of the speed of light within typical radio lobe environments. Similarly high backflow speeds have been inferred from a statistical analysis of the jet/counterjet arm-length ratio in a sample of radio galaxies by Scheuer (1995).

Assuming backflow velocities close to the magnetosonic sound speed and typical secondary lobe lengths of a few hundred kiloparsec one requires flow times in the order of a few  $10^7$  yr for matter to flow from the core to the tips of the secondary lobes. This is somewhat less than the typical maximum radio source lifetime of  $\sim 10^8$  yr. One should note however, that this is an optimistic estimate. The true lobe lengths are larger if projection effects are taken into account which would increase the required flow speeds. Also, real flows will occur at speeds somewhat lower than  $v_g$  if no low-density cavity exists in the IGM/ISM. Once the backflowing matter leaves the primary lobes and has to penetrate into the ambient medium we expect the flow to be decelerated by ram-pressure. Realistically the required flow times will thus be closer to a few  $10^8$  yr which would make backflow unlikely as the dominant formation mechanism unless X-shaped sources prove to be unusually old. A more detailed analysis of the required flow times will be presented in Chapter 7 after spectral ages have been determined for all the sources.



## 5.2 Buoyancy

The prevailing picture of radio galaxies suggests that the radio lobes have a lower density than the surrounding medium. In the case of Cygnus A numerical simulations have shown that the density ratio between the lobe and the ambient medium is of the order of  $10^{-4}$  (Williams 1991). Therefore we expect buoyancy to have impact on the large scale morphology of the radio lobes. Buoyant forces can cause bending of the lobes towards regions in the ISM/IGM that provide density equilibrium between the lobe and the surrounding medium. The buoyancy model has been first introduced by Gull & Northover (1973) in connection with luminous radio sources like Cyg A. Later the concept was recalled by Cowie & McKee (1975) to explain the strong bending of tailed radio sources and was successfully applied to several WAT radio sources located in clusters (e.g. Burns & Balonek 1982, Sakelliou et al. 1996). In the buoyancy model the radio lobes are being described as a non-relativistic, hydrodynamical flow which follows Euler's equation:

$$\frac{\partial v}{\partial t} + (v \cdot \nabla)v = -\frac{\nabla P}{\rho_l} + g, \quad (5.3)$$

where  $v$  is the flow velocity and  $\rho_l$  is the density of the plasma in the radio lobes. The radio lobe material is subject to a pressure gradient  $\nabla P$  and gravity  $g$ . If the lobe backflow is steady ( $\frac{\partial v}{\partial t} = 0$ ) and the X-ray gas with density  $\rho_x$  is in hydrostatic equilibrium, so that:

$$g = \frac{\nabla P}{\rho_x} \quad (5.4)$$

equation 5.3 can be simplified to:

$$\frac{v^2}{2R} \approx \left( \frac{1}{\rho_x} - \frac{1}{\rho_l} \right) \frac{dP}{dr} \quad (5.5)$$

which relates the radial pressure gradient  $\frac{dP}{dr}$  to the curvature radius  $R$  of the lobes. Worral et al. (1995) have applied this model to NGC 326. The source is embedded in an asymmetrical X-ray emitting gas of temperature  $kT \sim 2$  keV. The authors determined the

pressure gradient as well as  $\rho_x$  by fitting models to the X-ray observations. The curvature radius was extracted from the radio maps and the flow speed was assumed to be  $3000 \text{ km s}^{-1}$ . The resulting density ratio  $\rho_x/\rho_l$  is positive for both radio lobes up to distances of  $300''$  (east) and  $100''$  (west) thus indicating a buoyant flow. It is important to note that the density ratio depends strongly on the adopted parameters in particular on the unknown backflow velocity. A somewhat lower velocity of  $v = 600 \text{ km s}^{-1}$  would bring the density ratio to unity and therefore would diminish the effect of buoyancy. As was pointed out in the last section backflow velocities of a few percent of the speed of light might actually occur in the radio lobes but one can expect considerable deceleration once the deflected flow has to penetrate into the ISM/IGM to form the secondary lobes. The buoyancy model – while possibly important for NGC 326 – is most probably unable to generally account for the formation of X-shaped radio galaxies. Studies of the gaseous environments of several X-shaped sources were not able to detect significant cluster gas emission with the exception of NGC 326. Whereas this might be due to a lack of sensitivity for the more distant sources the close-by objects should have been detected if they had X-ray luminosities comparable to NGC 326.

Even in the presence of so far undetected cluster environments the buoyancy model is also faced with the problem of reproducing the striking rotational symmetry of X-shaped radio galaxies. Buoyant bending will occur along the path of maximum pressure gradients within the cluster gas. There is no obvious reason why these gradients should be symmetric with respect to the radio source. The two angles between the primary and secondary lobes of an X-shaped source are typically equal to within  $\pm 10^\circ$ . If buoyancy would be the dominant formation process one would expect to find a more random distribution of these angles.

Interestingly in some sources (e.g. 3C403) the secondary lobes are considerably wider at

their tips than close to the core which is what would be expected for an buoyant expanding bubble. Adiabatic expansion would also lead to a shift of the synchrotron spectrum towards lower frequencies (Carilli et al. 1991) and its fingerprint should be visible during a spectral analysis.

We conclude that buoyancy will influence the large scale structure of radio galaxies *only* in dense cluster environments (like in the case of cluster WAT sources). In order to reproduce X-shaped morphologies by buoyancy forces alone would also require an unlikely configuration of the ISM/IGM.

### 5.3 Jet-reorientation & Beam Precession

A natural way to explain the presence of a pair of secondary radio lobes is a change of the jet-axis at some point in the history of the source. The secondary lobes would then simply be the relic emission of the previously active radio lobes. Because radio jets are believed to emerge along the spin axis of the massive central black hole, a mechanisms for jet realignment must ultimately explain a change of the spin angular momentum of the central massive object. Furthermore, the jet reorientation must occur in a timescale less than the lifetime of the source. Two such mechanisms have been proposed and will be discussed in the following two sections: accretion of matter with orbital angular momentum misaligned with the spin of the BH or alternatively a binary black hole (BBH) in the center of the host galaxy.

#### 5.3.1 Matter Accretion

The continuous disposition of matter carrying angular momentum that is misaligned with the spin angular momentum of the central black hole will ultimately realign the spin axis of the BH. Such a misalignment of angular momentum can occur if the host galaxy has recently undergone merging with a companion galaxy. Tidal forces will severely disturb the initial ISM distribution of the host which can change the angular momentum of matter

falling onto the accretion disk surrounding the central BH. On the other hand the freshly deposited matter of the merged companion will almost certainly have different angular momentum than the ISM in the host galaxy prior to the merger. Eventually this gas will sink into the gravitational center and will realign the spin of the central BH via accretion. The timescale on which the spin axis becomes realigned with the angular momentum vector of the disturbed accretion flow is however not immediately obvious. Apart from viscosity, that will lead to a outward transport of angular momentum of the accreted matter one also has to take into account the general relativistic Lense-Thirring effect. Lense & Thirring (1918) have pointed out that a rotating mass (e.g. a Kerr black hole) produces a gravitational field that is not spherically symmetric and that leads to a coupling between the spin of the BH and the angular momentum of an orbiting mass. For orbits not in the equatorial plane, the central BH will exert a torque on – and will experience an equal absolute torque by – the test particle. Consequently, the orbit of the particle and the rotation axis of the mass will undergo precession. The Lense-Thirring effect provides a mechanism that can realign the spin axis of the central BH more rapidly than viscosity alone. Bardeen & Petterson (1975) have applied this concept to accretion disks around rotating black holes (see also: Rees 1978, Rees 1984, Scheuer & Feiler 1996, Armitage & Natarajan 1999, Natarajan & Armitage 1999). A segment of the accretion disk that has angular momentum misaligned with the BH spin axis will experience Lense-Thirring precession with angular velocity of:

$$\omega \approx 2Jr^{-3} \quad (5.6)$$

where  $J$  denotes the angular momentum of the BH. The differential precession will introduce a warp in the accretion disk. As was pointed out by Bardeen & Petterson (1975) there exists a critical radius  $r_b$  at which the infall time  $t_{in}(r)$  of matter onto the black hole is equal to the orbital time  $t_{orb}(r)$ . For orbits with  $r < r_b$  the combined influence of differential

precession and viscosity leads to a decay of the warp and ensures the alignment of the inner disk with the equatorial plane of the BH, irrespective of the in-falling material's original angular momentum. For  $r \gg r_b$  the precession can build up over several orbits and the disk will develop a stable large-scale warp. The warped disk exerts a torque on the black hole and causes it to precess. The disk material at large radii provides a large angular momentum reservoir which eventually causes a change of the spin axis of the BH towards the direction of the angular momentum vector of misaligned outer disk. An analytical calculation of the timescale on which the spin of the BH will be realigned has been presented by Scheuer & Feiler (1996) in the approximation of small angles between the two involved angular momentum vectors. The timescale is given (for a maximally rotating BH) as:

$$t_{re} = 3 \frac{M}{\dot{M}} \left( \frac{R_S}{R_{warp}} \right)^{1/2} \quad (5.7)$$

where  $M$  denotes the mass of the BH,  $\dot{M}$  is the mass accretion rate,  $R_S = 2GM/c^2$  is the Schwarzschild radius, and  $R_{warp}$  denotes the radius of the warp. For typical parameters ( $M = 10^8 M_\odot$ ,  $\dot{M} = \dot{M}_E = 3M_\odot \text{yr}^{-1}$ ,  $R_{warp} = 1000R_S$ ) the realignment timescale is of the order of  $10^6$  yr. For accretion rates below the Eddington limit  $\dot{M}_E$  the timescales become somewhat longer ( $t_{re} = 3 \times 10^7$  yr for  $\dot{M} = 0.1\dot{M}_E$ ). Natarajan & Armitage (1999) have obtained essentially identical results by numerically solving a generalized version of the Scheuer & Feiler equations.

In summary the chronology of this process is as follows:

- **Precession.** Once the in-falling matter reaches radii comparable to the radius of the outer accretion disk the Lense-Thirring effect will induce a precessional motion of the central BH and consequently of the jet axis.
- **Realignment.** Depending on the configuration (mass and accretion rate) of

the central engine the BH will become realigned within  $10^6$  to  $10^7$  years.

### 5.3.2 Central Binary Black Holes

The possibility that AGN might contain massive binary black holes (BBH) was first proposed by Begelman et al. (1980) and is justified by two widely accepted assumptions: that most galaxies contain massive central black holes and that galaxies frequently merge. The spin axis of each BH will then undergo geodesic precession about the total angular momentum of the binary system with the precessional period of the more massive BH given as (Roos 1988):

$$t_{prec} = 9.3 \times 10^8 r^{5/2} q^{-1} M_8^{-3/2} \quad [\text{yr}] \quad (5.8)$$

where  $q$  is the mass ratio  $m_8/M_8$  of the two black holes ( $M_8$  being the bigger mass expressed in units of  $10^8 M_\odot$ ) and  $r$  denotes the orbital radius in parsec. Assuming that the radio jets emerge along the spin axis of the more massive BH the precessional motion should manifest itself in a large-scale beam reorientation. Whether or not this effect can account for the formation of the X-shaped radio galaxies depends critically on the evolution and stability of the binary system.

The formation and evolution of a binary black hole system has been described extensively by Begelman et al. (1980) (see also Roos 1981). A binary black hole will form in a merger of two galaxies which both contain a central black hole. The shrinking of orbits (that is the loss of orbital angular momentum) is governed by three processes: dynamical friction, star ejection and gravitational radiation.

At large separation radii dynamical friction of the dense stellar clusters surrounding the two black holes leads to merging of the cores within a timescale of  $10^8$  yr. The less massive BH continues to sink towards the center of the newly formed core under the influence of dynamical friction until the two black holes become bound at the radius  $r_b$ . As the binary system becomes harder and the orbital period becomes shorter the loss of angular momentum due to dynamical friction eventually

ceases. This is because the transfer of energy from the binary system to a field star becomes inefficient if the encounter lasts longer than one orbit (Heggie 1975). When the binary separation is approaching the cusp radius<sup>1</sup>:

$$r_h = 10.7 \frac{M_8}{\sigma_{200}^2} \quad [\text{pc}] \quad (5.9)$$

the dominant process to extract orbital angular momentum is star ejection. Stars passing the binary on certain, so called loss cone orbits, will be ejected and will carry off binding energy that will lead to further shrinking of the binary orbit. The final and rapid phase of the binary evolution begins when the orbit shrinks to a radius where gravitational radiation becomes dominant and the black holes finally coalesce. We can suspect that the final merging of the black holes will cause a rapid realignment of the spin axis of the merged black hole.

Whether or not the central BBH can account for the formation of X-shaped radio galaxies depends on which timescales the shrinking and final merging of the binary system occurs.

Inspecting Eq. (5.8) it is obvious that for large portions of the merging event (that is, for large separation radii of the two black holes) the precession period is much too long (compared to typical source lifetimes) to cause any observable curvature of the large-scale radio jets. Feasible precession periods that will have impact on the large-scale radio morphology have to be comparable or less than the source lifetime and thus will range from  $10^6$  to  $10^8$  years. The radius  $r_8$  at which the precession period becomes less than  $10^8$  yr is given (in units of the cusp radius  $r_h$ ) by:

$$\frac{r_8}{r_h} = 3.8 \times 10^{-2} \left( \frac{q}{M_8} \right)^{2/5} \sigma_{200}^2 \quad (5.10)$$

Figure 5.2 plots  $r_8/r_h$  against  $M_8$  for different values of  $q$ . One can see that for all feasible binary configurations the critical radius

<sup>1</sup> $M_8$  denoted the mass of the more massive BH in units of  $10^8 M_\odot$  and  $\sigma_{200}$  is the one-dimensional velocity dispersion of the stars in the central core expressed in units of 200 km/s

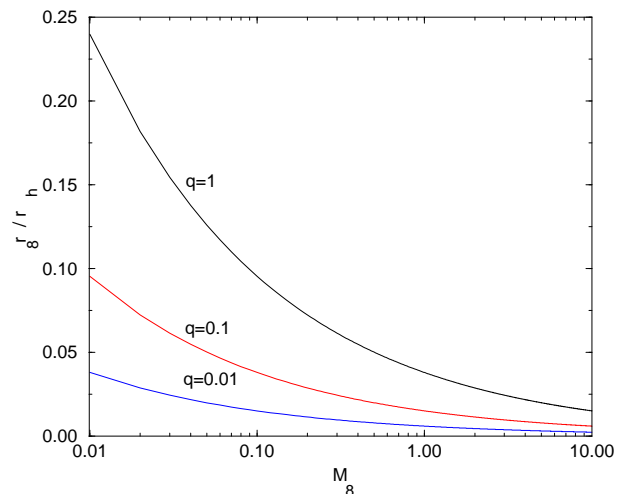


FIGURE 5.2— Plot of the critical radius  $r_8$  expressed in units of the cusp radius  $r_h$  as a function of the BH mass  $M_8$  for  $q=1, 0.1,$  and  $0.01$ .  $r_8$  denotes the separation radius at which the precessional period of the central BH becomes less than  $10^8$  yr.  $\sigma_{200}$  was taken to be unity.

lies well below the cusp radius. At radii below  $r_h$  the loss of angular momentum is dominated by star ejection. Begelman et al. (1980) have pointed out that the time spent by the source in this stage depends critically upon the efficiency of repopulating stellar loss cone orbits. Stars that were originally orbiting the binary system on loss cone trajectories will eventually all become ejected and further shrinking of the binary orbit stops. For all feasible mass configurations of the BBH system this occurs much before gravitational radiation becomes important. Consequently the binary would become stable at a radius with a corresponding precessional period that is too large to cause any observable curvature of the secondary lobe within a source's lifetime.

In order to allow further shrinking and the eventual merging of the binary the loss cone orbits need to be refilled. Loss cone filling can occur e.g. by star-star scattering. However, Quinlan (1996) have inferred from numerical simulations that this process probably is too slow to ensure BH merging within the lifetime of most sources. Quinlan & Hernquist (1997) have investigated the effect of wandering of the binary within the stellar core due to the change of gravitational potential imposed by

the continuous ejection of stars. The authors conclude that the motion of the binary enhances the interaction cross section and can further shrink the binary orbit. If however it is enough to ensure merging of the two black holes remains unclear.

Recently Zier (2000) presented new results concerning BBH merging. Assuming realistic, non-uniform stellar core distributions and solving for the restricted 3-body equations the numerical simulations suggest that star ejection is sufficient to shrink the orbits in order to allow fast merging of the binary by gravitational radiation if the mass of the central stellar core and the binary are comparable. The derived timescales of merging are of the order of  $10^6$  to  $10^7$  yr depending on the assumed masses of the stellar core and the two black holes.

The chronology of BBH merging is as follows:

- **Long period precession.** The host galaxies merge and the two black holes form a bound binary system. The timescale of this phase is of the order of  $10^8$  years. The precessional period within this phase is large compared to the typical source lifetime therefore no observable curvature of the secondary lobes is caused.
- **Short period precession.** Once the binary separation reaches the critical radius  $r_8$  the precessional period becomes comparable to the source lifetime and the precession will cause observable curvature of the radio lobes. The time the binary spends in this phase is short ( $10^6$  to  $10^7$  years) if the loss cone orbits will be refilled as shown by Zier (2000) or infinitely long if no loss-cone feeding takes place.
- **BH merging.** During the final BH merging the precession will cease and the spin of the merged central BH will be rapidly realigned.

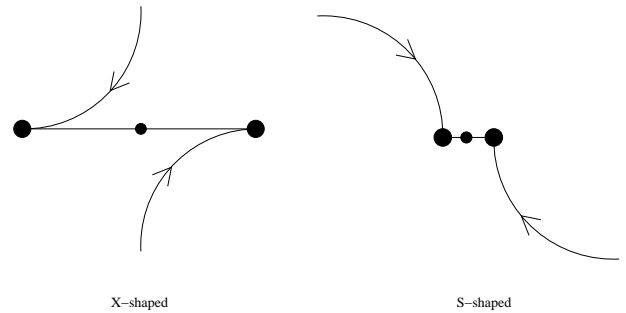


FIGURE 5.3— This sketch illustrates the idea of steady beam precession as the formation mechanism of X-shaped radio sources. The motion of the hotspots at the end of a pair of precessing beams will 'draw' elliptical tracks into the plane of the sky. Leahy & Williams (1984) have pointed out that randomly oriented precessing sources should appear as X-shaped (left) and S-shaped sources (right) with equal probabilities.

#### 5.4 Steady Precession or Fast Realignment?

The original interpretation of X-shaped morphologies given for NGC 326 was steady jet precession Ekers et al. (1978). However, present day deep radio images of NGC 326 (comp. Fig. 4.3) and other X-shaped sources make this interpretation highly unlikely. Precession over timescales comparable to the source lifetime with constant opening angle should 'draw' elliptical tracks in the plane of the sky. Instead the observed morphology is better described by straight active and secondary lobes and strong curvature of the lobes on a relatively short distance close to the radio core. Leahy & Williams (1984) have argued against steady jet precession on statistical grounds: randomly oriented precessing sources should appear as X-shaped and S-shaped sources with equal probability (see Fig. 5.3) which is not the case. Apparently the radio jets have been stable for a considerable time span, then have undergone a short period of reorientation and presently are in a stable state again. Both processes outlined above predict such a fast reorientation of the radio jets. A potential problem is posed by the fact that both mechanisms also require beam precession to occur prior to the realignment. However, in some circumstances precession can occur without leaving a visible im-

print on the large-scale radio morphology of a source if

- the precession period is long compared to the timescale of jet realignment. In such a case only a small fraction of a total precession period would be completed before the precession would cease. The introduced lobe bending is then too small to be visible on large scales.
- the precession amplitude (the opening angle of the precession cone) is small. Small amplitude precession would be visible on small scales only as a wiggling motion of the jet. The large scale morphology of these sources would not be significantly influenced.

In case of Lense-Thirring precession due to matter accretion onto the BH the precession period depends on the radius  $R$  of the accretion disk warp. For a maximally rotating BH it is given as (Armitage & Natarajan 1999):

$$t_{prec} = \frac{\pi R^3}{2c} \left( \frac{c^2}{GM} \right)^2 \quad (5.11)$$

The precession period is plotted as a function of the warp radius in Fig. 5.4 together with the realignment timescale given by Eq. (5.7). Because of the strong dependence of  $t_{prec}$  on the warp radius a proper treatment of the problem would require a detailed understanding of fueling of the accretion disk at small radii. However, it is generally assumed that a disk warp would form at a few thousand Schwarzschild radii (Bardeen & Petterson 1975). As can be seen in Fig. 5.4 at these radii the precession period is considerably longer than the reorientation timescale and thus precession would leave no visible imprint on the large-scale morphology of the source. There exists a critical radius however, at which  $t_{prec}$  becomes smaller than  $t_{re}$ . Whether or not this fast precession in the final stage prior to jet realignment does have impact on the source morphology then depends only on the precession amplitude. Viscous forces will certainly lead to a decay of the warp and a relaxation

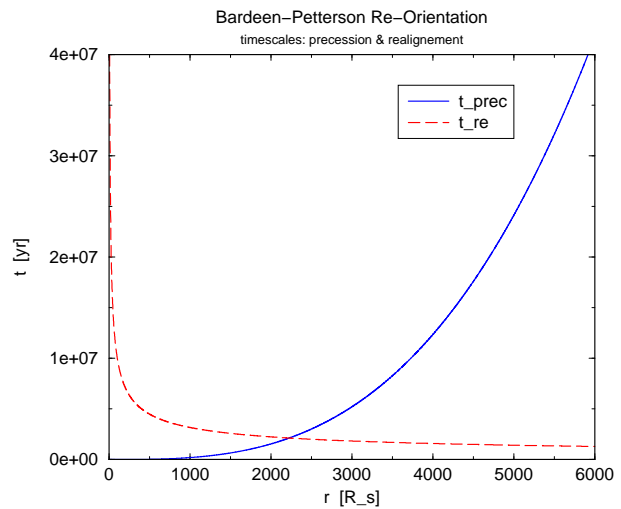


FIGURE 5.4— Plot of the realignment timescale  $t_{re}$  compared to the precession period  $t_{prec}$  in case of jet reorientation due to matter accretion. The warp radius  $r$  is plotted in units of the Schwarzschild radius  $R_S$ . A mass of  $M = 1 \times 10^8 M_\odot$  and an accretion rate of  $\dot{M} = \dot{M}_E = 3M_\odot/\text{yr}$  has been assumed.

of its inclination into the equatorial plane of the accretion disk as it is moving inward. The exact course of events of the warp decay depends however on many largely unknown parameters (mainly the viscosity) and cannot be estimated with accuracy. It is therefore possible that Lense-Thirring precession of the accretion disk would lead to visible, fast precession for a short time span just prior before the precession will stop and the jet will become realigned.

In the case of central binary black holes the situation is somewhat more simple. The precession period depends on the binary separation as given by Eq. (5.8). This relation is plotted in Fig. 5.5 for different binary configurations. Precession periods should be less than about  $1 \times 10^8$  years in order to leave a visible imprint on the large-scale morphology. For all feasible BBH setups this is the case at radii considerably smaller than the cusp radius. As was pointed out by (Zier 2000) in this stage the merging of the binary proceeds within some  $10^6$  years. Furthermore, the merging timescale once gravitational radiation becomes important is  $\propto r^4$  (Begelman et al. 1980). This ensures that the precession

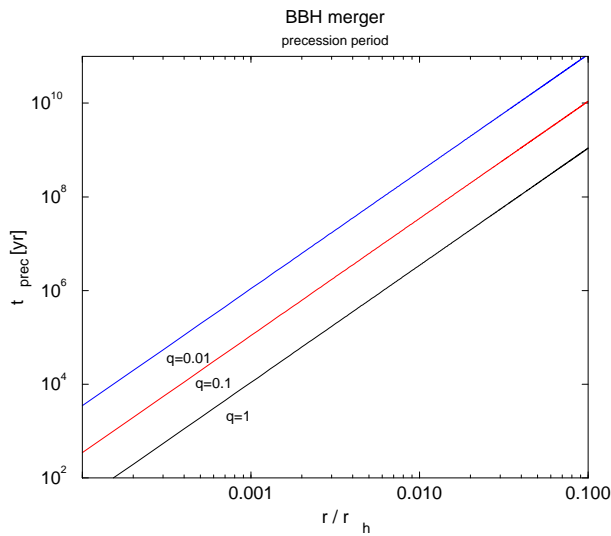


FIGURE 5.5— Plot of  $t_{prec}$  of a central binary black hole as a function of the separation radius expressed in units of the cusp radius  $r_h$ . The precession period is displayed for the case of  $q=1$ ,  $q=0.1$ ,  $q=0.01$  and a BH mass of  $M=1 \times 10^8 M_\odot$ .

period ( $\propto r^{5/2}$ ) is always long with respect to the reorientation timescale. Thus, beam precession will never have impact on the large-scale radio morphology.

## 5.5 Summary and Conclusions

On morphological grounds the favored explanation for the genesis of X-shaped radio galaxies is a fast realignment of the radio jets. The two fast reorientation mechanisms outlined in this chapter – BBH merging and misaligned matter accretion – both seem feasible of reproducing X-shaped sources. However, much depends on the involved timescales and how they fit to the actual source lifetimes that will be derived in the next chapter. Critical in the context of the BBH merging is the question whether or not the binary will always merge and if so on which timescales. Even though Zier (2000) has shown that stellar loss cone feeding does result in fast binary merging the numerical simulations make rigid assumptions about the structure of the central stellar core of which little is known. If fast merging does always occur then BBH merging is the most likely formation process of X-shaped ra-

dio sources.

Misaligned accretion onto the black hole can quickly realign the spin of the central BH and the orientation of the large-scale jets. Problematic can be that the jets might undergo rapid precession in the final stage of the realignment which should leave its imprint on the radio morphology. Much depends on the details of gas funneling onto the accretion disk. At present numerical simulations lack the resolution to determine the fate of the gas down to scales of the accretion disk. Therefore, it might turn out that matter accretion is not feasible to form X-shaped sources.

The ‘environmental’ formation processes – buoyancy and backflow – are most probably not the dominant formation mechanism of X-shaped radio sources. Backflow likely is too slow to be able to form the secondary radio lobes within a source lifetime unless backflows are supersonic (for which there is no indication) or the backflow would stream into an old cavity (which would require beam reorientation). Buoyancy on the other hand might have impact on the large scale morphology of some of the X-shaped sources located in denser environments (e.g. NGC 326). However, almost all X-shaped sources live in poor environments which disqualifies buoyancy to be the main formation process of these objects. In order to reproduce the rotational symmetry of X-shaped sources buoyancy would also require an unlikely configuration of the ambient medium.





# 6

## Spectral Analysis

### 6.1 Integrated Spectra

The total fluxes of all available observations were determined and combined with source fluxes compiled from the literature to construct integrated synchrotron spectra. These spectra have been determined for the whole source and also – when the resolution was sufficient – for individual source components. The geometry of the images at the various frequencies was adjusted in order to match in size and sampling using the AIPS task HGEOM. All maps were then smoothed to a common beam and their pointing was aligned. The required positional shifts to further align the images were applied using LGEOM. Finally all maps were combined in an image cube using MCUBE. The fluxes were then extracted with BLSUM from the image cube. Literature fluxes were extracted from NED and complemented with fluxes from Kellermann et al. (1969) (re-calibrated to the Baars-scale with conversion factors given by Laing & Peacock 1980). The flux errors were computed including noise and systematic contributions:

$$\Delta S_{tot} = \sqrt{\Delta S_{rms}^2 + \Delta S_{sys}^2} \quad (6.1)$$

The systematic term includes calibration errors and errors introduced by the imaging procedure (mainly cleaning and self-calibration). The systematic contributions cannot easily be quantified because of the complex and sometimes subjective nature of the imaging pro-

cess employed to produce radio images. Consequently the values of the systematic errors have been chosen somewhat subjectively depending on the quality of the datasets. Typically we have assumed systematic errors of 5-10%. In the case of the 9 mm single dish data we have adopted higher values of 15% due to the problems encountered during the data reduction (comp. Sect 3.1).

The error introduced by map noise  $\sigma$  depends on the integration area  $A$  (in beam areas) over which the flux has been determined:

$$\Delta S_{rms} = \sigma\sqrt{A} \quad (6.2)$$

Typically this term is rather small and the total error is dominated by the systematic contributions.

### 6.2 Spectral Index

The spectral index between two frequencies  $\nu_1$  and  $\nu_2$  is defined as:

$$\alpha = \frac{\log(S_1) - \log(S_2)}{\log(\nu_1) - \log(\nu_2)} \quad (6.3)$$

where  $S_1$  and  $S_2$  are the fluxes obtained at these frequencies. The error of the spectral index is calculated as:

$$\Delta\alpha = \frac{1}{\log(\frac{\nu_1}{\nu_2}) \ln(10)} \sqrt{\left(\frac{\Delta S_1}{S_1}\right)^2 + \left(\frac{\Delta S_2}{S_2}\right)^2} \quad (6.4)$$

Spectral index maps are created by calculating the spectral index for every map pixel. This

calculation has been performed with the AIPS task COMB. As preparatory work it is necessary to smooth all images to a common beam size. Furthermore, HGEOM has to be run in order to ensure matching pixel sampling, coordinates and reference pixels. Crucial in the calculation of spectral index maps is the accurate alignment of the images. When both maps contain a strong point source the alignment can be checked by fitting a Gaussian to this component in order to derive necessary shift parameters. However, a more reliable method is to perform a cross-correlation of the images similar to what has been described in Chapter 3 for the single-dish data. Such cross-correlation has been done with the IMDIFF task contained in the MIRIAD package.

### 6.3 Spectral Ageing

Relativistic electrons lose energy through various loss processes. For the conditions prevailing in radio lobes the most relevant loss mechanisms are synchrotron losses ( $\propto E^2$ ), inverse-Compton losses ( $\propto E^2$ ) and losses due to adiabatic expansion of the emitting plasma ( $\propto E$ ). Due to the energy dependence of these processes high-energy electrons become depleted faster than their low-energy counterparts. This leads to a break in the initial power law distribution of electron energies. Consequently the radiation spectrum with an initial slope of  $\alpha_{inj}$  will become steeper for frequencies higher than a characteristic so-called break frequency  $\nu_b$ . Such theoretical radiation spectra have been computed making different assumptions (for a summary see Myers & Spangler 1985). These models are:

- The KP model (Kardashev 1962, Pacholczyk 1970) assumes a one-time injection of particles. The pitch-angle scattering is assumed to take place on timescales much larger than the radiation lifetime. The high-frequency spectral slope is then  $\frac{4}{3}\alpha_{inj} - 1$ .
- The JP model (Jaffe & Perola 1973) is identical to KP, except that it allows for

fast pitch-angle isotropization. For frequencies exceeding  $\nu_b$  this leads to an exponential steepening of the spectrum.

- The continuous injection or CI model describes the radiation spectrum in the case where a powerlaw distribution of fresh particles is continuously re-injected into the radio lobes. The superposition of electron populations of various ages results in a high-frequency spectral slope of  $\alpha_{inj} - 0.5$ . The CI model is also used to represent spectra of compact, non-resolved sources.

The spectral break moves to lower frequencies with time and thus the current location of  $\nu_b$  provides a tool to estimate the age of the radiating plasma. The break frequency  $\nu_b$  is related to the spectral age as given by Alexander & Leahy (1987):

$$t = 1.59 \times 10^3 \frac{\sqrt{B}}{B^2 + B_{IC}^2} \frac{1}{\sqrt{\nu_b(1+z)}} \text{ [Myr]} \quad (6.5)$$

where  $B$  is the source magnetic field strength,  $B_{IC} = 3.25(1+z)^2$  denotes the equivalent field strength of inverse-Compton scattering with the cosmic microwave background (both in  $\mu\text{G}$ ) and  $\nu_b$  is the break frequency in GHz. The spectral age is defined as the time since the electrons have been accelerated for the last time. In the case of radio galaxies this is thought to happen in the hotspots. The break frequency can be determined by fitting spectral models to the synchrotron spectra as it has been done by e.g. Carilli et al. (1991). Throughout this thesis the SYNAGE software (Murgia 1996) has been used to derive the break frequencies. As an improvement to older fitting algorithms SYNAGE is able to independently fit the break frequency and the injection index  $\alpha_{inj}$  (the spectral index of the unaged initial radiation spectrum). Also the program properly treats losses due to adiabatic expansion as well as the impact of synchrotron-self absorption on the low-frequency shape of the spectrum (Murgia et al. 1999). The minimum number of frequencies that have to be available to perform

a fit to the synchrotron spectrum is three. When flux measurements at only two frequencies exist, Myers & Spangler (1985) have discussed a method to calculate spectral ages from the two-point spectral index if a value for  $\alpha_{inj}$  is assumed a priori. One should keep in mind however that the ages are extremely sensitive to the assumed  $\alpha_{inj}$ . The actual errors of course depend on the redshift and the source magnetic field, but as a rule of thumb a variation of  $\pm 10\%$  in  $\alpha_{inj}$  typically results in age differences of  $\sim 40\text{-}50\%$ ! Consequently ages derived from two point spectral indices have to be interpreted with caution. Whereas the  $\nu_b$  can be determined quite accurately if the frequency range covered by observations is sufficiently large and well sampled, the inability to directly measure the source magnetic field strength introduces a major uncertainty in the calculation of spectral ages. In order to estimate  $B$  one usually has to rely on minimum energy or equipartition arguments (these will be discussed in greater detail in the next section). Figure 6.1 displays the spectral age as a function of  $B$  for different values of  $\nu_b$  and  $z$ . As can be seen rather small errors in the derived  $B$  values can introduce large errors in  $t$ . This is especially true at low redshifts and for small break frequencies. To avoid the problems of poorly determined values of  $B$  one can instead calculate the maximum age (which occurs for  $B_{IC} = \sqrt{3}B$ ) for a given  $\nu_b$  and  $z$ :

$$t_{max} = 1.55 \times 10^2 \frac{1}{\sqrt{\nu_b(1+z)^3}} \text{ [Myr]} \quad (6.6)$$

Apart from the uncertainties introduced by calculating  $B$  some general caveats concerning the interpretation of spectral ages exist (see Eilek 1996a, Eilek 1996b). First of all the spectral ageing theory assumes uniform magnetic fields which is almost certainly far from the true physical conditions in radio sources. In many radio galaxies that have been studied with sufficient resolution we find the emission to be highly filamentary (e.g. in M87 see Owen et al. 1998), which is very likely, at least in part, due to fluctuations of the magnetic field strength. In such a situation electrons in the low field regions of the source

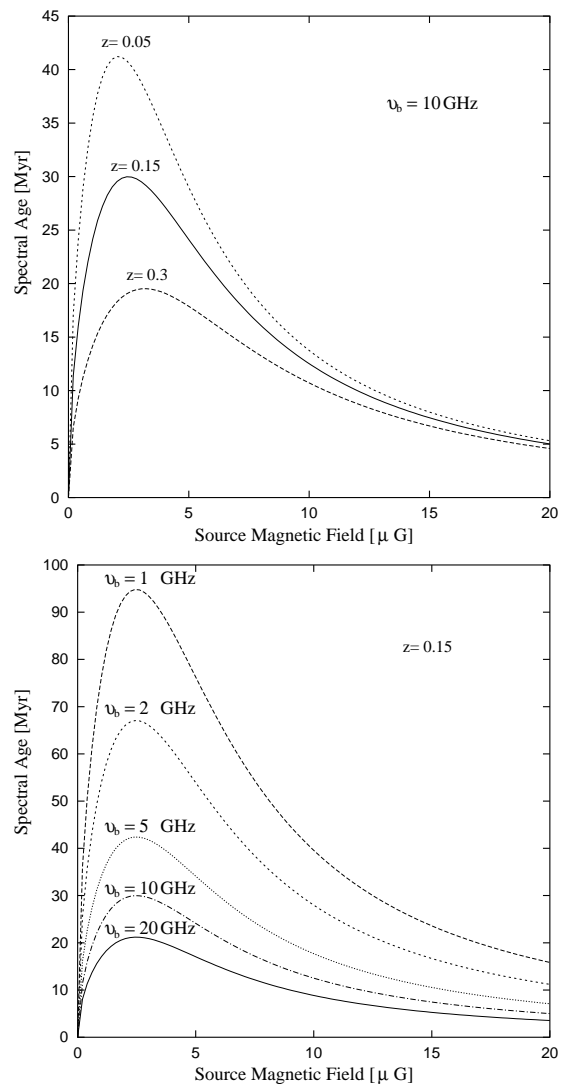


FIGURE 6.1— Spectral age as a function of source magnetic field strength. **(top)** The upper panel shows the age for different redshifts and a fixed break frequency of 10 GHz. Due to the redshift dependence of the inverse-Compton losses the derived spectral ages are higher for small  $z$  for a given break frequency. **(bottom)** The lower plot displays the dependence of the age on the source magnetic field for different values of  $\nu_b$  and a fixed redshift of  $z = 0.15$ . As can be seen rather small uncertainties in the assumed value of  $B$  can introduce large errors in the derived ages. This is especially true for low break frequencies and redshifts.

lose energy only very slowly until they diffuse into the high field regions where they start losing energy according to the standard synchrotron ageing theory. Thus, the derived spectral ages would be highly underestimated. Furthermore, stochastic, turbulent reaccelera-

tion of the particles can lead to a synchrotron spectrum resembling that of a usual ageing-only model (Borovsky & Eilek 1986). The decay of the break frequency is however taking place much slower than predicted by the standard model. Finally, the ad-hoc assumption of a powerlaw distribution of electron energies does not need to be true (Eilek & Arendt 1996). In summary it is important to note that spectral ages calculated using minimum fields are not necessarily equal to, but rather provide a firm lower limit to the true source ages.

#### 6.4 Minimum Energy

As was outlined above the determination of spectral ages relies quite heavily on the estimation of the source magnetic field  $B$ . We cannot, however, determine the value of  $B$  directly from the observations. The radio luminosity  $L_\nu$  determines only the product  $V\kappa B^{1+\alpha}$ , where  $V$  is the volume of the source,  $\kappa$  is defined by the electron energy spectrum ( $N(E)dE = \kappa E^{-p}$ ). Consequently it is impossible to decide whether a high luminosity is produced by either a low electron flux in a high field, or vice versa. There is, however, a way to estimate a *minimum* value for  $B$  for a given luminosity and volume. The general concepts of calculating  $B_{min}$  will be outlined briefly in the following. For a more detailed discussion see Longair (1997).

The total energy of a radio source is the sum of the particle and the magnetic energy:

$$W_{total} = V\epsilon_e + V\frac{B^2}{2\mu_0},$$

where  $\epsilon_e$  denotes the energy density of the relativistic electrons. To take into account the particle energy present in the form of relativistic protons  $\epsilon_p$  one assumes that the protons have  $\beta$  times the energy of the electrons:

$$\begin{aligned}\epsilon_p &= \beta\epsilon_e \\ \epsilon_{total} &= (1 + \beta)\epsilon_e \\ &= \eta\epsilon_e\end{aligned}$$

To calculate the particle energy a powerlaw electron energy spectrum with a minimum and

maximum energy cutoff ( $E_{min}$  and  $E_{max}$ ) is assumed. Furthermore, electrons of a particular energy are taken to radiate monochromatically at their critical frequency so that:

$$E_{max} \propto \nu_{max}^{1/2} \quad E_{min} \propto \nu_{min}^{1/2}$$

Finally we receive for the total energy:

$$W_{total} = G\eta L_\nu B^{-3/2} + V\frac{B^2}{2\mu_0}, \quad (6.7)$$

where  $G$  is a function of  $\alpha$ ,  $\nu_{min}$ , and  $\nu_{max}$  (see Longair 1997). Minimizing this term we receive for the minimum energy:

$$W_{min} = \frac{7}{6\mu_0} V^{3/7} \left[ \frac{3\mu_0}{2} G\eta L_\nu \right]^{4/7} \quad (6.8)$$

and for the minimum magnetic field:

$$B_{min} = \left[ \frac{3\mu_0}{2} \frac{G\eta L_\nu}{V} \right]^{2/7} \quad (6.9)$$

At this point it is worth to review again the caveats of the minimum energy theory:

- The total energy of the source is sensitive to the value of  $\eta$ . We know little about its actual value but it is commonly assumed to be unity. However, Eilek & Hughes (1991) have demonstrated that some particle acceleration mechanisms can produce 400 times more energy in protons than in electrons.
- The cutoff frequencies are commonly assumed – somewhat arbitrarily – to be  $\nu_{min} = 10$  MHz and  $\nu_{max} = 100$  GHz. The energy estimate depends however only weakly on these parameters.
- The total energy calculation depends on the volume  $V$  of the source and assumes that the particles and magnetic fields fill the emitting volume uniformly. However high-resolution maps indicate that the emission from radio sources is to some extent filamentary. Therefore a filling factor  $\phi$  is used to describe the fraction of the volume contributing to the emission. The value of  $\phi$  and whether it is constant for all radio sources is unknown. Usually  $\phi$  is assumed to be unity.

Throughout the thesis  $B_{min}$  and  $W_{min}$  have been calculated following Longair (1997). The parameters entering the calculation have been taken as:  $\nu_{min} = 10$  MHz,  $\nu_{max} = 100$  GHz,  $\eta = 1$  and  $\phi = 1$ . The cosmological parameters have been chosen as  $h = 0.75$  and  $q_0 = 0.5$ . The source volumes have been calculated assuming a cylindrical shape for the radio lobes and following the method described by Burns et al. (1979).

## 6.5 Results

### 6.5.1 4C12.03

Figure 6.2 displays the integrated spectrum of 4C12.03 in the frequency range from 80 MHz to 10.45 GHz. The 80 MHz datapoint (extracted from the Parkes Catalogue) is inconsistent with the flux measurements at 178 MHz and 408 MHz. At 178 MHz two independent measurements have yielded identical fluxes. We thus believe the 80 MHz datapoint to be erroneous and have flagged it during the fitting procedure. The solid line represents the best fitting CI model with  $\alpha_{inj} = -0.43$ . The spectral fit indicates a low frequency break at  $\nu_b = 931$  MHz. Tests of the stability of the fit solution have been performed by consecutively flagging all low frequency datapoints and repeating the fit. It has turned out that the low frequency break persists even when all frequencies below 1.4 GHz have been flagged. The impact on  $\nu_b$  and  $\alpha_{inj}$  was marginal. Consequently we consider the low-frequency spectral break to be real.

Spectral index maps at a resolution of  $69'' \times 69''$  have been obtained between 1.4 GHz and 10.45 GHz, and between 1.5 GHz and 10.45 GHz (Fig. 6.3). The trend of the spectral index along equidistant points connecting the primary to the secondary lobes are displayed in Fig. 6.4. The spectral index is marginally steepening from the primary ( $\alpha \approx -0.8$ ) towards the secondary lobes ( $\alpha \approx -1$ ). Break frequencies have been derived from spectra including 3 frequencies (1.4 GHz, 1.5 GHz and 10.45 GHz). Due to the poor frequency coverage the injection index had to be fixed to  $\alpha_{inj} = -0.434$  as in-

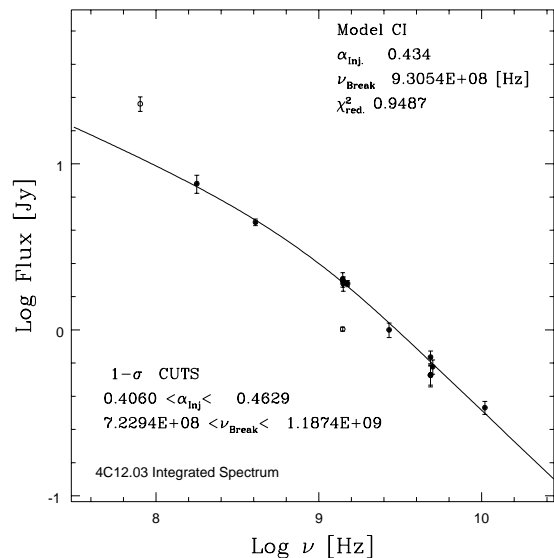


FIGURE 6.2— Integrated Spectrum of 4C12.03. The datapoints have been compiled from the literature and were complemented with fluxes obtained from the multi-frequency radio images. The solid line represents the best fitting CI model. datapoints marked by open circles have been flagged for the fitting procedure. The fit parameters and errors can be found in the figure legend.

indicated by the fit to the integrated spectrum. The trend of  $\nu_b$  is displayed in Fig. 6.5. There is a gradual decrease of break frequency from  $\nu_b \approx 16$  GHz (primary lobes) to  $\nu_b \approx 10$  GHz (secondary lobes). The trend of break frequencies is very similar for the north→east and the south→west lobes. One should keep in mind that the break frequencies might have been underestimated due to the fairly bad coverage in frequencies. As mentioned above the integrated spectrum seems to indicate a spectral break below 1 GHz. In such a case our frequency coverage – with the lowest frequency being 1.4 GHz – might be ill-suited to obtain reliable values of  $\nu_b$ . In case of 4C12.03, radio observations at 608 MHz would be necessary to properly confine the low-frequency spectral break.

Minimum energy and fields have been calculated at various points in the primary and secondary lobes (see Fig. 6.4). In order to decrease the errors fluxes have been integrated in  $41 \times 41$  pixel boxes centered on

the marked locations. The values of  $B_{min}$  and other calculated properties are listed in Tab. 6.1. The minimum magnetic field of the north→east lobe progressively declines from  $B_{min} = 4.2\mu\text{G}$  to  $B_{min} = 2.1\mu\text{G}$ . In the south→west lobe the highest magnetic fields ( $B_{min} = 4.3\mu\text{G}$ ) are not coincident with the tip of the active southern lobe, but instead can be found in the high brightness region connecting the active to the secondary lobes (between regions 2 and 3).

Synchrotron ages have been calculated using the derived magnetic fields (see Tab. 6.1). The trend of  $t_{syn}$  is displayed in Fig. 6.6. There is indication for an age gradient from the active to the secondary lobes. Typical ages of  $\approx 25$  Myr one finds at the tips of the primary lobes whereas the secondary lobes exhibit higher ages of  $\approx 33$  Myr. It is worth to mention again that due to the uncertainties of the derived break frequencies the true spectral ages might also be somewhat higher than the derived values.

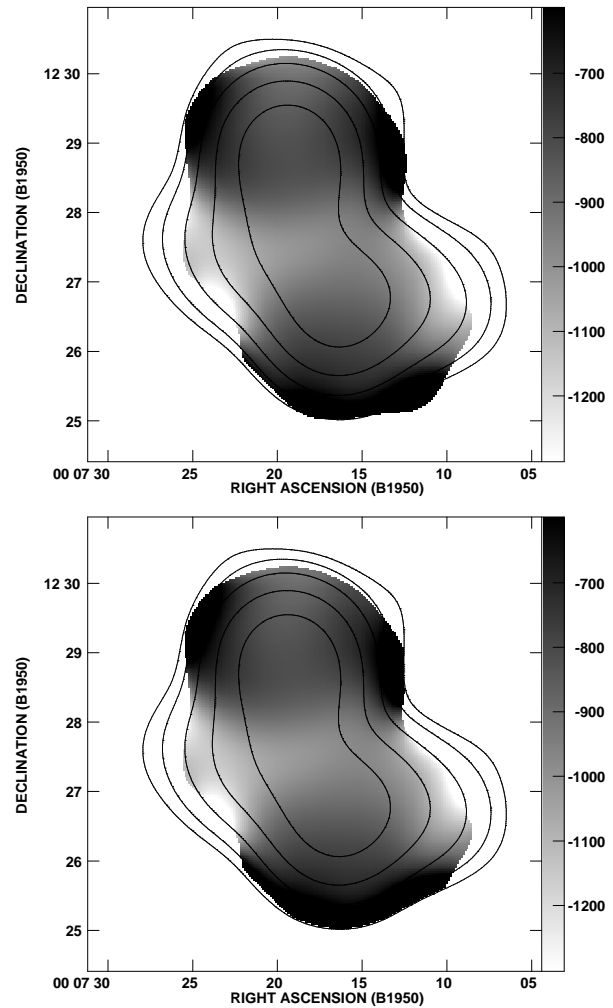


FIGURE 6.3—  $3\sigma$  spectral index maps of 4c12.03 between 1.4 GHz and 10.45 GHz (upper panel), and between 1.5 GHz and 10.45 GHz (lower panel). The superimposed contours represent the total intensity at 1.5 GHz.

Lobe	Region	Luminosity [erg/s]	$U_{min}$ [erg]	$u_{min}$ [erg/cm <sup>3</sup> ]	$B_{min}$ [ $\mu$ G]	$t_{syn}$ [Myr]	$t_{max}$ [Myr]
north → east	1	$2.1 \times 10^{42}$	$1.5 \times 10^{58}$	$1.6 \times 10^{-12}$	4.2	23.2	33.3
	2	$1.4 \times 10^{42}$	$1.2 \times 10^{58}$	$1.3 \times 10^{-12}$	3.7	24.8	33.8
	3	$9.3 \times 10^{41}$	$9.3 \times 10^{57}$	$1.0 \times 10^{-12}$	3.3	27.8	36.2
	4	$6.3 \times 10^{41}$	$5.9 \times 10^{57}$	$1.1 \times 10^{-12}$	3.4	29.6	39.1
	5	$4.3 \times 10^{41}$	$5.6 \times 10^{57}$	$7.0 \times 10^{-13}$	2.7	33.0	41.3
	6	$3.3 \times 10^{41}$	$5.3 \times 10^{57}$	$5.3 \times 10^{-13}$	2.4	34.8	43.0
	7	$2.6 \times 10^{41}$	$5.1 \times 10^{57}$	$4.1 \times 10^{-13}$	2.1	33.5	41.5
south → west	1	$1.5 \times 10^{41}$	$2.1 \times 10^{57}$	$6.4 \times 10^{-13}$	2.6	26.5	32.9
	2	$5.8 \times 10^{41}$	$4.5 \times 10^{57}$	$1.4 \times 10^{-12}$	3.9	25.5	35.3
	3	$8.6 \times 10^{41}$	$5.7 \times 10^{57}$	$1.8 \times 10^{-12}$	4.3	25.3	37.2
	4	$3.1 \times 10^{41}$	$5.0 \times 10^{57}$	$5.4 \times 10^{-13}$	2.4	31.0	38.3
	5	$1.7 \times 10^{41}$	$3.5 \times 10^{57}$	$3.7 \times 10^{-13}$	2.0	32.0	39.8
	6	$1.1 \times 10^{41}$	$2.7 \times 10^{57}$	$2.9 \times 10^{-13}$	1.8	33.3	42.1

TABLE 6.1— Physical properties and spectral ages of 4C12.03. For the positions of the various regions see Fig. 6.4.

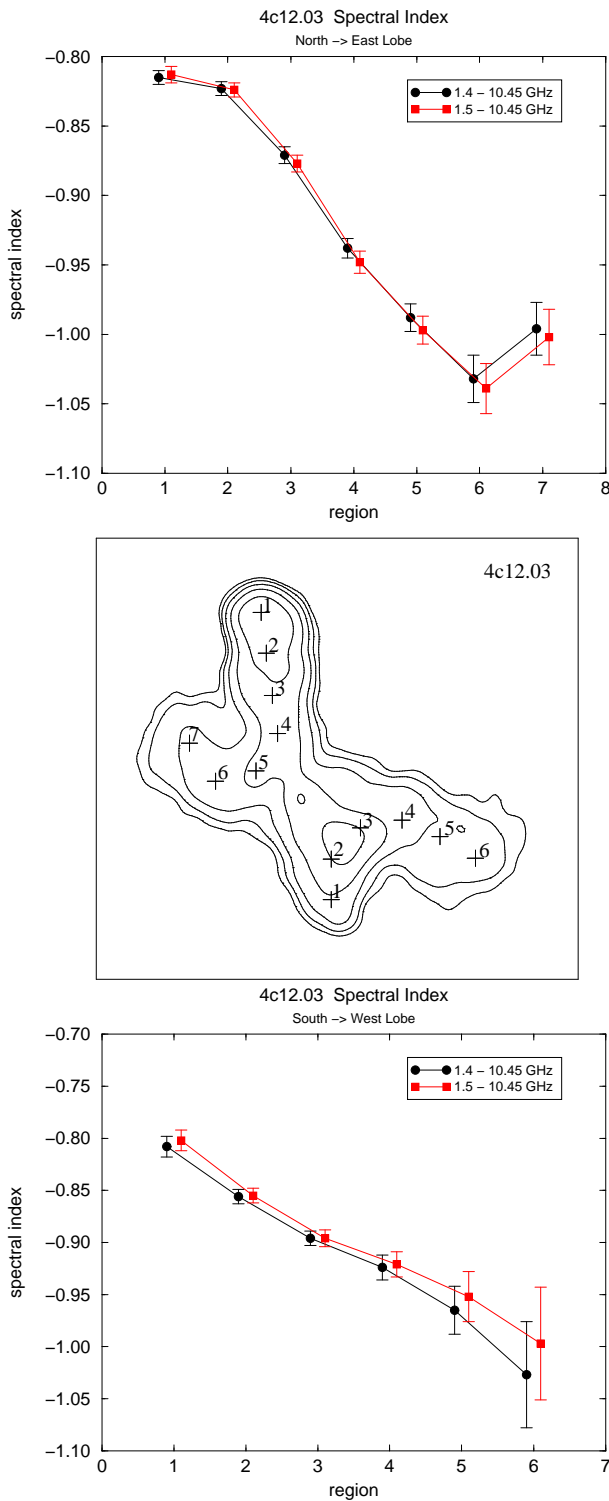


FIGURE 6.4— Trend of the spectral index between 1.4 GHz and 10.45 GHz, and between 1.5 GHz and 10.45 GHz along the line connecting the active to the secondary lobes. The *top panel* represents the north→east the *bottom panel* the south→west transition. Spectral indices have been calculated in  $41 \times 41$  pixel boxes centered on the positions marked by crosses in the *middle panel*.

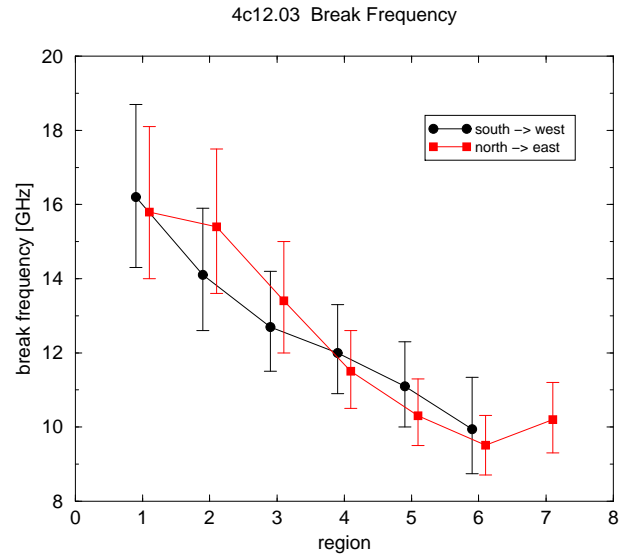


FIGURE 6.5— Trend of the break frequency across the north→east, and south→west lobes. The regions are marked by crosses in the finding chart of Fig.6.4.

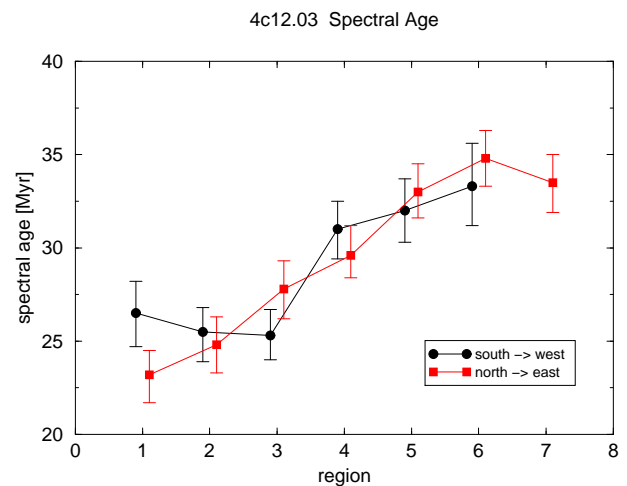


FIGURE 6.6— Trend of the spectral age in 4C12.03 along the north→east and south→west lobes.



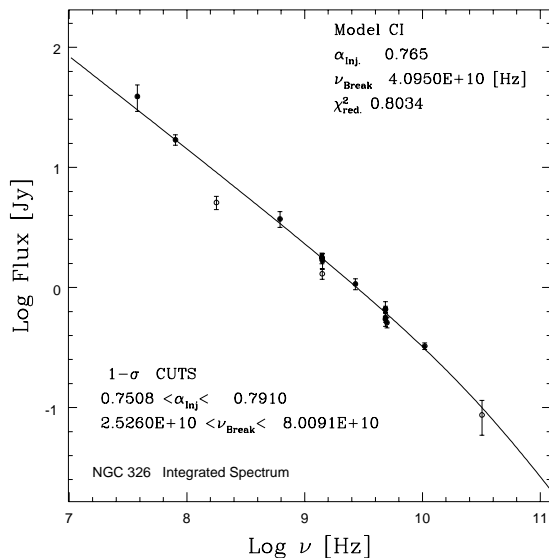


FIGURE 6.7— Integrated spectrum of NGC 326. The datapoints have been compiled from the literature and have been supplemented by fluxes obtained from available datasets. The solid line represents the best fitting CI-model. The fit parameters and errors can be found in the plot legend. Datapoints marked by open circles have been flagged for the fitting procedure.

### 6.5.2 NGC 326

The integrated spectrum of NGC 326 is displayed in Fig. 6.7. Fluxes have been compiled from the literature and have been supplemented with values obtained from the available observations. Obviously there is an inconsistency of fluxes at low frequencies. In particular the 178 MHz datapoint (from Pilkington & Scott 1965) lies significantly lower than the 38 MHz and 80 MHz fluxes. Due to the influence of confusing background sources, low frequency fluxes are known to be overestimates in many cases. To clarify the spectral shape at low frequencies we have investigated different scenarios by fitting spectral models with different datapoints below 1.4 GHz flagged. The lowest  $\chi^2$  values were obtained when the 178 MHz flux has been flagged and the 38 MHz and 80 MHz datapoints were included. In the opposite case (with the 38 MHz and 80 MHz datapoint being flagged) the best  $\chi^2$  was a factor of 2 higher. Also, when including the 178 MHz datapoint we obtain an

injection index of  $\alpha_{inj} = -0.375$  which is considerably lower than the canonical minimum of  $\alpha_{inj} = -0.5$  predicted by shock acceleration theory. We therefore conclude that most likely the 178 MHz flux value reported by Pilkington & Scott (1965) is erroneous. Extrapolating the 178 MHz flux to what is suggested by the best fitting spectral model we obtain a luminosity  $L_{178} = 2.5 \times 10^{25} \text{ W Hz}^{-1} \text{ h}^{-2}$ . The corrected luminosity moves NGC 326 closer to the FR/FR II boundary even though the source is still of FR I type. The best fitting spectral model (see Fig. 6.7) suggests an injection index of  $\alpha_{inj} = -0.765$  and a break frequency of  $\nu_b = 41 \text{ GHz}$ .

A resolved spectral analysis has been carried out using maps at 3 frequencies (1.4, 4.86 and 10.45 GHz). The images were convolved to a common resolution of  $69'' \times 69''$ . The spectral index maps are displayed in Fig. 6.8. The analysis revealed that the 4.85 GHz data severely suffers from missing flux in the region of the secondary lobes. This is demonstrated in Fig. 6.9 which exhibits a spectrum extracted at the tip of the southern secondary lobe. Consequently, the data at this frequency were discarded from the spectral ageing study of NGC 326. Figure 6.11 exhibits the trend of spectral index between 1.4 GHz and 10.45 GHz calculated at equidistant points along the east→north and west→south radio lobe (see Fig. 6.10). The spectral index of the primary lobes is quite steep with  $\alpha \approx -0.8$ . One finds a gradual steepening from the primary towards the secondary lobes. The tip of the southern lobe exhibits a relatively flatter spectrum ( $\alpha \approx -1.0$ ) than the tip of the northern counterpart ( $\alpha \approx -1.2$ ). Break frequencies have been determined from the two-point spectral index between 1.4 GHz and 10.45 GHz. We have fixed the injection index to  $\alpha_{inj} = -0.765 \pm_{0.014}^{0.026}$  as indicated by the integrated spectrum. A plot of  $\nu_b$  across NGC 326 can be found in Fig. 6.12. There is a decrease in break frequency from the active to the secondary lobes. The active lobes exhibit extremely high values of  $\nu_b$ . Considering the uncertainties of the two-point spectral in-

dex the spectral shape is also consistent with a straight power law. The secondary lobes show break frequencies below 100 GHz. The northern secondary lobe has relatively lower values of  $\nu_b$  than its northern counterpart.

Minimum energies and magnetic fields have been calculated for the east→north and west→south lobes of NGC 326. The relevant physical properties together with the obtained particles ages are listed in Tab. 6.2. The minimum magnetic fields are high for the primary lobes (5.7 and 6.5  $\mu\text{G}$ ) and are somewhat lower within the secondary lobes (4.5 and 3  $\mu\text{G}$ ). Figure 6.13 represents the trend of  $t_{syn}$  along equidistant points connecting the active to the secondary lobes. As can be seen there is a gradual increase in age towards the tips of the secondary lobes. The east→north lobe has an overall higher age than the south→west counterpart. The inferred ages of the primary lobes are around 1 Myr. These are the lowest values of  $t_{syn}$  derived for any of the sources in the studied sample. Even though the age calculations are based on the two-point spectral index and therefore are subject to fairly large uncertainties the morphology of NGC 326 supports the picture of very young primary lobes. Of all known X-shaped sources NGC 326 exhibits the shortest primary lobes. If this was due mainly to projection then we would expect to find a large asymmetry in luminosity between the two lobes because of relativistic beaming which is not the case. Most probably the short length of the primary lobes is therefore intrinsic. In case of jet reorientation this would indicate that the formation event has happened fairly recently which is consistent with the findings presented in this section.

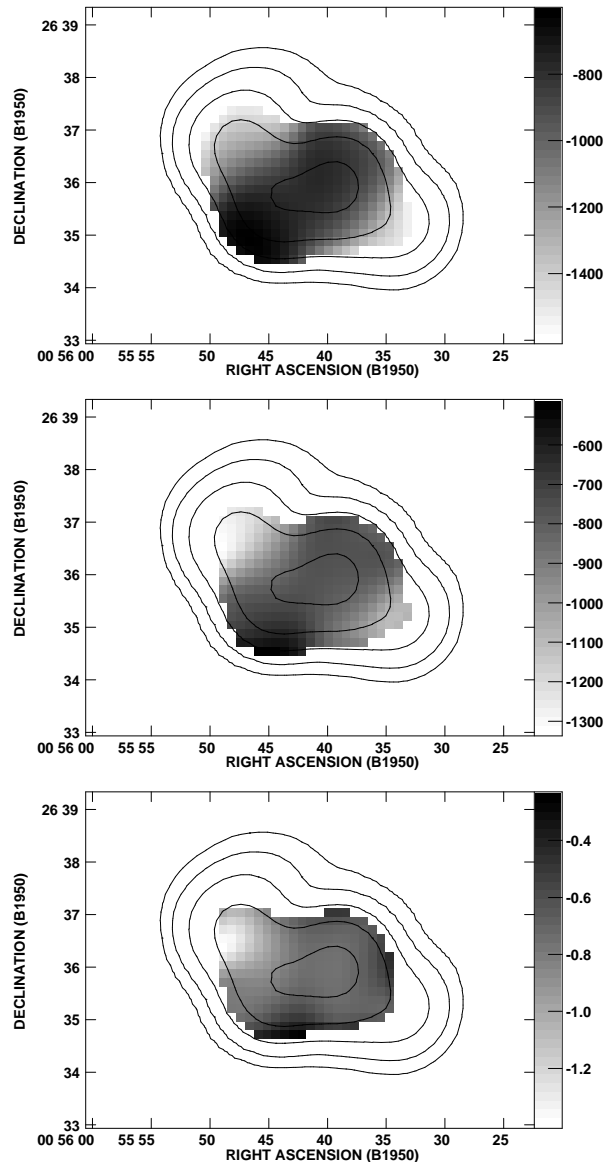


FIGURE 6.8— Spectral index maps of NGC 326 (greyscale) superimposed by contours of the 4.86 GHz total intensity. The *upper panel* represents the spectral index between 1.4 GHz and 4.86 GHz, the *middle panel* between 1.4 GHz and 10.45 GHz, and the *lower panel* between 4.86 GHz and 10.45 GHz. The calculation of spectral indices has been clipped for fluxes below  $3\sigma$ .

Lobe	Region	Luminosity [erg/s]	$U_{min}$ [erg]	$u_{min}$ [erg/cm <sup>3</sup> ]	$B_{min}$ [ $\mu$ G]	$t_{syn}$ [Myr]	$t_{max}$ [Myr]
East → North	1	$3.0 \times 10^{41}$	$2.6 \times 10^{57}$	$3.0 \times 10^{-12}$	5.7	0.5	0.8
	2					3.5	6.2
	3	$2.2 \times 10^{41}$	$2.7 \times 10^{57}$	$1.8 \times 10^{-12}$	4.5	11.7	16.7
	4					19.7	28.3
	5					23.5	33.8
West → South	1	$4.5 \times 10^{41}$	$3.2 \times 10^{57}$	$3.9 \times 10^{-12}$	6.5	0.6	1.2
	2					0.9	1.8
	3	$1.4 \times 10^{41}$	$3.1 \times 10^{57}$	$8.3 \times 10^{-13}$	3.0	3.8	4.5
	4					9.4	11.0
	5					16.6	19.3
	6					19.2	22.4

TABLE 6.2— Physical properties of NGC 326 for the source regions marked in Fig. 6.10. The minimum energy/field calculations have been done for larger areas, that combined several regions as indicated in the table.

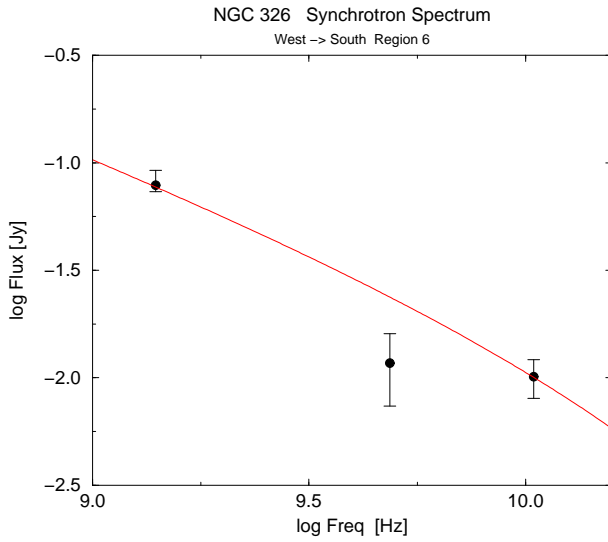


FIGURE 6.9— Spectrum of NGC 326 extracted at the tip of the southern secondary lobe. Clearly the 4.86 GHz datapoint is severely affected by missing flux.

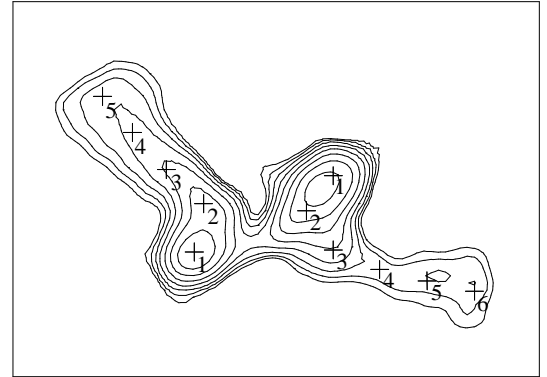


FIGURE 6.10— Finding chart of NGC 326. Fluxes have been integrated in  $7 \times 7$  pixel boxes centered on the position marked by crosses.

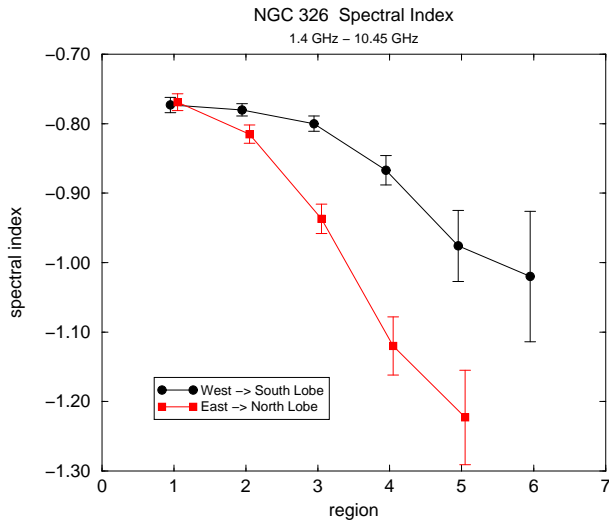


FIGURE 6.11— Trend of the spectral index between 1.4 GHz and 10.45 GHz along the east→north and the west→south transition line. The regions are marked by crosses in Fig. 6.10.

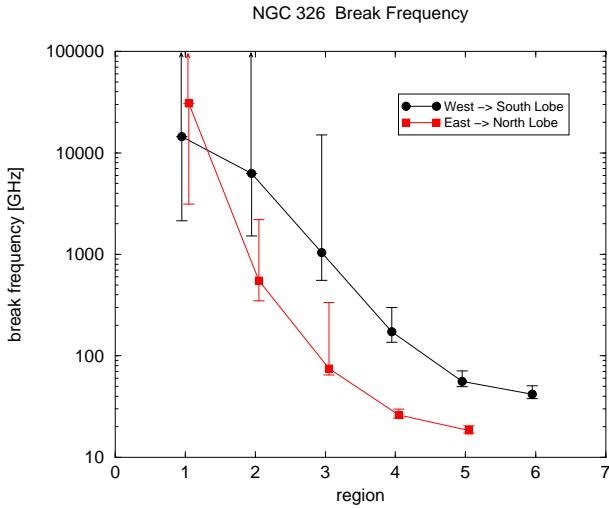


FIGURE 6.12— Trend of the break frequency along the east→north , and the west→south transition line calculated from the two-point spectral index between 1.4 GHz and 10.45 GHz. An injection index of  $\alpha_{inj} = -0.765$  has been assumed. The errorbars reflect the break-frequencies obtained for  $\alpha_{inj} = -0.751$ , and  $\alpha_{inj} = -0.791$  as determined by the fit to the integrated spectrum. Note that the y-axis has been plotted on logarithmic scale. The regions on the x-axis are marked by crosses in Fig. 6.10.

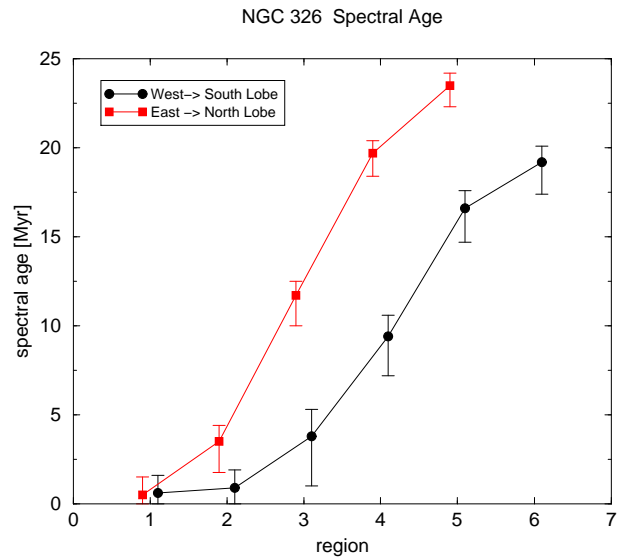


FIGURE 6.13— Trend of the spectral age along the east→north , and the west→south transition line connecting the active to the secondary lobes. For the location of the source regions see Fig. 6.10.

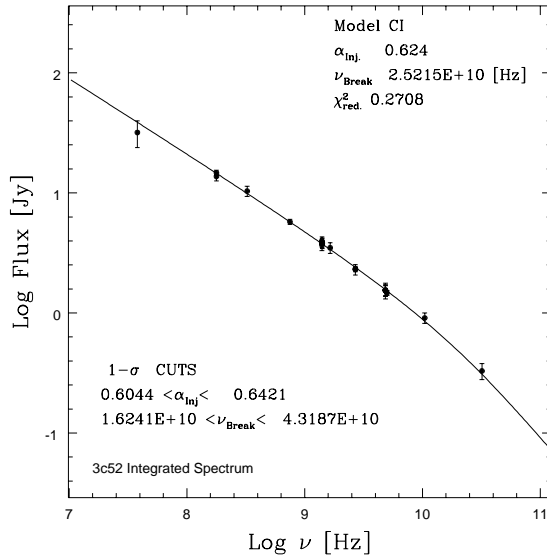


FIGURE 6.14— Integrated spectrum of 3C52. The datapoints were compiled from the literature and were complemented with fluxes obtained from the multi-frequency radio images. The solid line represents the best fitting spectral model. The fit parameters and errors can be found in the plot legend.

### 6.5.3 3C52

The integrated spectrum of 3C52 displayed in Fig. 6.14 is composed of 19 datapoints of which 11 were extracted from the literature. The covered frequency range extends from 38 MHz to 32 GHz and the spectrum shows curvature over essentially the full range. The solid line represents the best fitting spectral model, which was obtained for a CI model with  $\alpha_{inj} = -0.624$  and  $\nu_b = 25.2$  GHz. The fit result does not crucially depend on the high and low frequency datapoints. Stability test with the 38 MHz and 32 GHz datapoints being flagged yielded identical results within the errorbars. Spectral index maps have been constructed at a resolution of  $5'' \times 4''.8$  using images at 1.4 GHz, 1.7 GHz and 2.7 GHz (see Figs. 4.6-4.8). Due to the rather small angular size of 3C52 neither the low frequency WENSS nor the high-frequency single-dish data (except at 32 GHz where the secondary lobes were not detected) provides sufficient resolution to include them in this analysis. As a result the frequency range for which a resolved

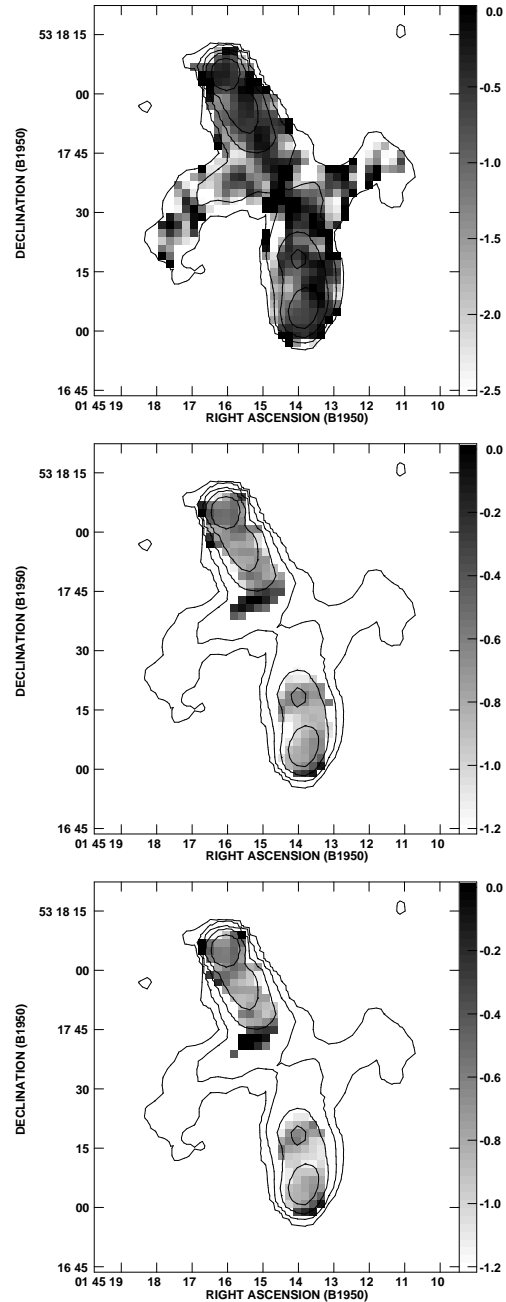


FIGURE 6.15— Spectral index greyscale maps of 3C52 between 1.4 GHz and 1.7 GHz (top), between 1.4 GHz and 2.7 GHz (middle), and 1.7 GHz and 2.7 GHz (bottom). Superimposed are contours showing the total intensity at 1.4 GHz. The spectral index cutlevels are  $4\sigma$  for the top, and  $6\sigma$  for the middle and bottom map.

spectral analysis can be performed is rather small (1.4, 1.7 and 2.7 GHz). The spectral index maps are presented in Fig. 6.16. Even though the spectral index maps are rather

noisy (due mainly to the presence of artificial sidelobe-structure in the 2.7 GHz image) there is indication for a spectral steepening towards the secondary lobes. To increase the snr, spectral indices have been determined by integrating fluxes over  $7 \times 7$  pixel areas at equidistant points along the north→east and south→west lobes. The relevant positions of these points are marked by crosses in the middle panel of Fig. 6.16. The trend of the spectral index between 1.4 GHz and 2.7 GHz, and between 1.7 GHz and 2.7 GHz is displayed in Fig. 6.16. Even when integrating fluxes in larger areas the error of the spectral index remains large in the secondary lobes. However, in the south→west lobe one can see a spectral steepening to occur from region one up to region 4. In the north→east lobe the situation is less clear. The calculated spectral indices seem to indicate a steeper spectrum at the tips of the secondary lobe. However, the errors are also consistent with an almost constant spectral index across the whole lobe. To further constrain the spectral shape higher-frequency maps with sufficient resolution would be needed. Alexander & Leahy (1987) have performed a spectral analysis of 3C52 between 1.4 GHz and 5 GHz. The spectral index distribution presented by the authors shows more clearly than our result a gradual spectral steepening towards the secondary lobes. In order to derive spectral ages, break frequencies have been obtained by fitting model spectra. Due to the poor quality of the available data and the fairly limited frequency range, the injection index had to be fixed a priori to a value of  $\alpha_{inj} = -0.624$  as indicated by the integrated spectrum. The trend of  $\nu_b$  is displayed in Fig. 6.17. As expected the uncertainties of  $\nu_b$  are quite large. For most regions of the north→east lobe no upper limits of  $\nu_b$  could be obtained because the datapoints were – within the errorbars – consistent with a pure powerlaw shape of the spectrum. In case of the south→west lobe there is however indication for a gradual decrease in break frequency from the primary towards the secondary lobe.

Table 6.3 lists the physical properties and spectral ages calculated in the various source regions of 3C52. The minimum magnetic field gradually decreases from the primary towards the secondary lobes. The highest field strength ( $B_{min} = 17.7 \mu\text{G}$ ) is coincident with the location of the northern hotspot. The magnetic field of the southern hotspot is somewhat lower ( $B_{min} = 11.9 \mu\text{G}$ ). At the tips of the secondary lobes we find typical fields strengths of  $B_{min} \approx 7.5 \mu\text{G}$ . Of all X-shaped radio galaxies studied, 3C52 exhibits the highest minimum magnetic fields and is also the most luminous source. Likely, this is due to 3C52 being located in a cluster. The interaction of the radio emitting plasma with the ambient (presumably dense) cluster medium effectively alligns the magnetic fields. The confinement of the ambient medium prevents expansion and thereby enhanced radiation losses as has been discussed in the case of Cyg A by Barthel & Arnaud (1996).

Figure 6.18 presents the trend of the spectral age along the north→east and south→west lobes. Despite the large errors the observed age gradient from the primary towards the secondary lobes is significant. The southern primary lobe has a spectral age of  $t_{syn} = 5 \pm 3.2$  Myr and then progressively ages to  $t_{syn} = 21.2 \pm 8.1$  Myr in region 4. The north→east lobe shows a similar behaviour but seems to be younger by a few Myr.

Lobe	Region	Luminosity [erg/s]	$U_{min}$ [erg]	$u_{min}$ [erg/cm <sup>3</sup> ]	$B_{min}$ [ $\mu$ G]	$t_{syn}$ [Myr]	$t_{max}$ [Myr]
north → east	1	$4.4 \times 10^{43}$	$4.8 \times 10^{58}$	$2.9 \times 10^{-11}$	17.7	< 2.9	< 17.8
	2	$2.3 \times 10^{43}$	$4.5 \times 10^{58}$	$1.4 \times 10^{-11}$	12.1	4.6	17.7
	3	$8.9 \times 10^{42}$	$2.6 \times 10^{58}$	$7.8 \times 10^{-12}$	9.2	3.0	8.5
	4	$2.8 \times 10^{42}$	$1.0 \times 10^{58}$	$5.9 \times 10^{-12}$	8.0	13.2	32.8
	5	$1.5 \times 10^{42}$	$5.6 \times 10^{57}$	$5.5 \times 10^{-12}$	7.7	27.4	66.0
south → west	1	$1.4 \times 10^{43}$	$2.8 \times 10^{58}$	$1.3 \times 10^{-11}$	11.9	5.0	18.8
	2	$1.2 \times 10^{43}$	$3.3 \times 10^{58}$	$8.9 \times 10^{-12}$	9.8	7.9	23.9
	3	$1.0 \times 10^{43}$	$2.9 \times 10^{58}$	$8.4 \times 10^{-12}$	9.5	9.5	27.9
	4	$1.7 \times 10^{42}$	$5.8 \times 10^{57}$	$6.4 \times 10^{-12}$	8.3	21.2	54.6
	5	$1.1 \times 10^{42}$	$4.4 \times 10^{57}$	$5.2 \times 10^{-12}$	7.5	15.7	36.9

TABLE 6.3— Physical properties and spectral ages of 3C52. The locations of the relevant regions can be found in Fig. 6.16. The spectrum for region 1 in the northern lobe is best approximated by a pure power law. The given upper limit of the spectral age refers to the lower limit of  $\nu_b$  as obtained from the spectral fit.

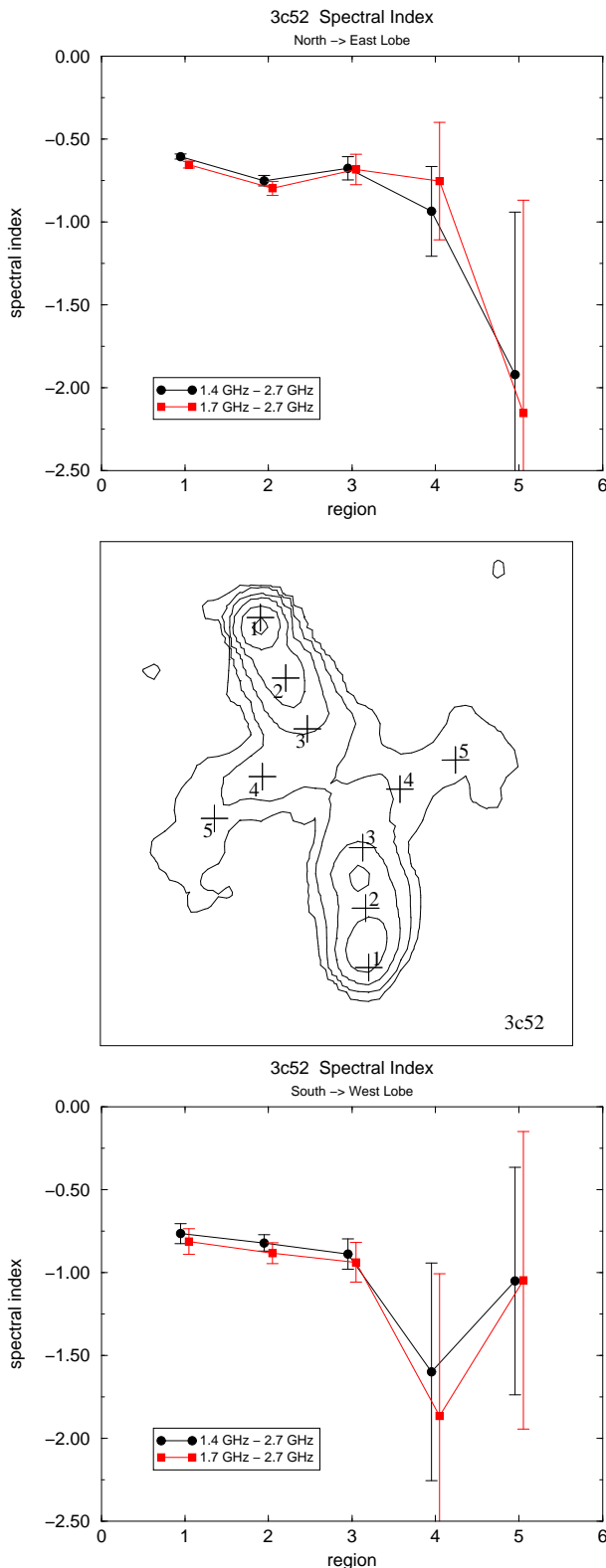


FIGURE 6.16— Trend of the spectral index between 1.4 GHz and 2.7 GHz, and between 1.7 GHz and 2.7 GHz. The upper plot represents the spectral index distribution for the north→east lobe, the lower one for the south→west lobe. The spectral indices have been computed from fluxes obtained in  $7 \times 7$  pixel boxes centered on the position marked by crosses in the middle panel.

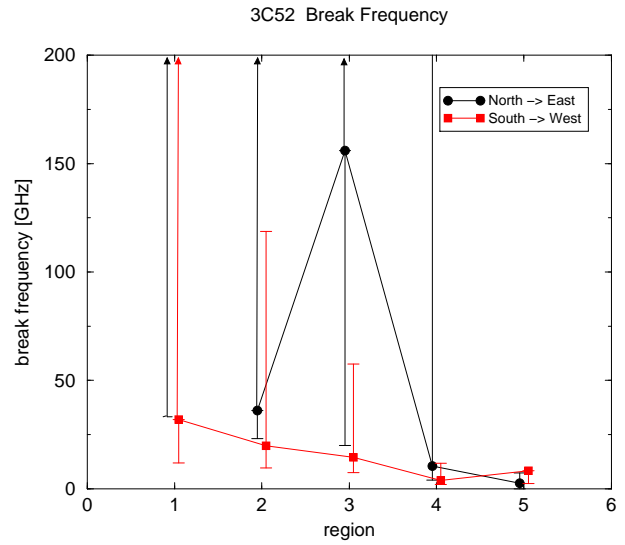


FIGURE 6.17— Trend of the break frequency across the north→east and south→west lobes of 3C52. Errorbars marked by arrows indicate that no upper limit of  $\nu_b$  could be obtained from the spectral fits. The spectra of these datapoints were consistent within the errorbars with a pure powerlaw shape.

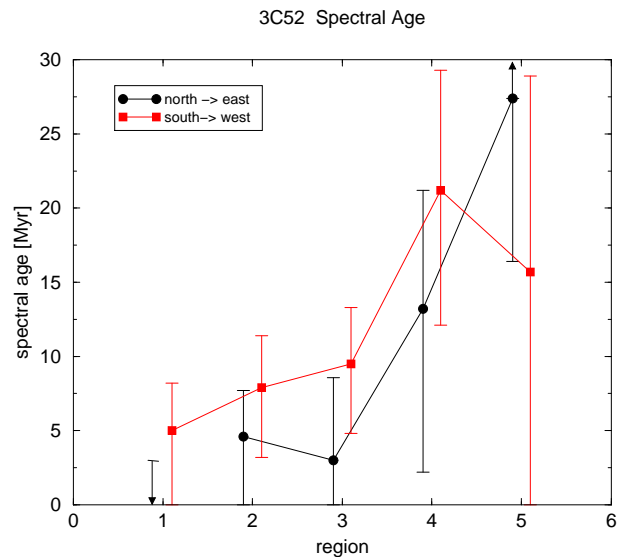


FIGURE 6.18— Spectral ages of 3C52 along the north→east and south→west transition connecting the active to the secondary lobes. The positions corresponding to the regions are marked by crosses in Fig. 6.16. For region 1 of the northern lobe only an upper limit of the spectral age could be obtained.



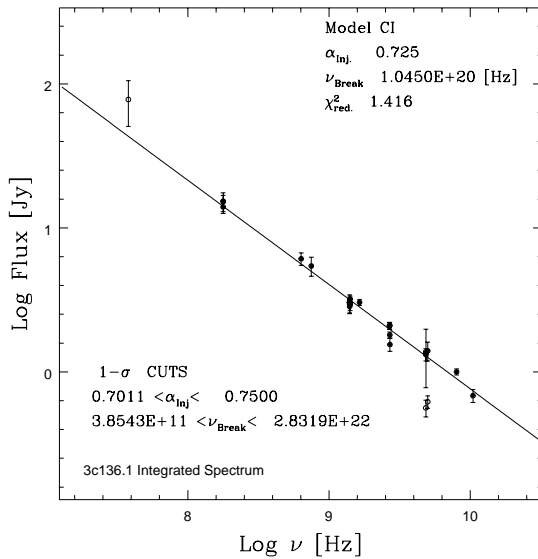


FIGURE 6.19— Integrated spectrum of 3C136.1 ranging from 38 MHz to 10.45 GHz. The solid line represents the best fitting spectral model. The datapoints marked by open circles have been flagged during the fitting procedure. The best fitting model for 3C136.1 is a pure powerlaw spectrum with a slope of  $\alpha = -0.725$ . The fit results and errors can be found in the plot legend.

#### 6.5.4 3C136.1

The integrated source spectrum of 3C136.1 is displayed in Fig. 6.19. The spectrum exhibits no curvature and is best fitted by a pure powerlaw with a slope of  $\alpha_{inj} = -0.725$ . Multi frequency image cubes for further spectral analysis have been constructed at a resolution of  $69'' \times 69''$  (including data at 1.37, 1.4, 1.41, 1.65, 2.7 and 10.45 GHz), as well as at a resolution of  $147'' \times 147''$  (additionally including 4.85 GHz data). The spectral analysis has revealed that the data at 1.41, 1.65 and 2.7 GHz had to be discarded entirely due to their small image sizes. Convolution to larger beams has introduced severe flux errors towards the map edges. Unfortunately nothing could be done about the map sizes because these images were provided by Alexander & Leahy (1987) “as-is”. Furthermore, the 2.7 GHz image suffers heavily from missing flux. This can be clearly seen in the component spectra of 3C136.1 (see Fig. 6.22). The 2.7 GHz datapoint system-

atically lies below the solid line marking the best fitting spectral model. The effect is more severe in the secondary than in the primary lobes.

Spectral index maps of 3C136.1 including data at 1.37 GHz, 4.85 GHz and 10.45 GHz are displayed in Fig. 6.20. The source exhibits a spectral gradient from the primary towards the secondary lobes. The spectral indices of the active lobes range about  $-0.5$  to  $-0.65$  which are rather typical values for hotspots in extended radio sources. Towards the northern and southern secondary lobes the spectrum is progressively steepening. This can be more clearly seen in Fig. 6.21. Spectral indices have been calculated along the ridge of maximum brightness for 6 source regions in the west→north and east→south lobes. Fluxes were integrated in  $10 \times 10$  pixel areas centered on the positions marked in Fig. 6.21. Fluxes of the 1.37 GHz and 1.4 GHz images were averaged. The progressive steepening from the active towards the secondary lobes can be seen clearly. The spectral gradient is more pronounced in the east→south lobe where the spectral index (between 1.4 GHz and 10.45 GHz) is varying from  $\alpha = -0.6$  at the hotspot to  $\alpha = -1.0$  at the tip of the secondary lobe. In the west→north lobe we find only moderate steepening ranging from  $\alpha = -0.7$  at the hotspot to  $\alpha = -0.85$  towards the tip of the northern lobe. The overall steeper spectrum between 4.85 GHz and 10.45 GHz indicates that the synchrotron spectrum of 3C136.1 exhibits some curvature at frequencies above 5 GHz. Figure 6.22 shows spectra of the various source regions (see Fig. 6.21) with superimposed best fitting spectral models. For all regions the lowest  $\chi^2$  values were obtained using JP models.

Figure 6.23 displays  $\nu_b$  along the ridge of maximum brightness connecting the active to the secondary lobes. There is a trend of decreasing break frequency from the active towards the secondary lobes. The west→north lobe shows overall higher break frequencies than the east→south lobe.

The physical properties and spectral ages of

the various source regions of 3C136.1 are listed in Tab. 6.4. The calculated minimum magnetic fields are relatively weak. The field strength is below  $3\mu\text{G}$  everywhere in the source. Also, we find a decrease in  $B_{min}$  from the active towards the secondary lobes.

The trend of spectral ages along the east→south and west→north lobes is presented in Fig. 6.24. There is indication for a moderate age gradient from the active to the secondary lobes up to region 5. The situation at the very tip of the secondary lobes is less clear. While in the southern lobe  $t_{syn}$  is increasing to  $33.9\pm_{4}^{3.7}$  Myr the northern lobe indicates lower ages of merely  $18.5\pm_{3.2}^{3.6}$  Myr in region 6. The spectral indices and ages derived in regions coincident with the active lobes are in good agreement with the results presented by Alexander & Leahy (1987). The authors have made use of the maps at 1.41, 1.65 and 2.7 GHz which were discussed in this section. The somewhat steeper age gradient in the eastern lobe which was claimed by the authors is therefore very likely a consequence of the influence of missing flux.

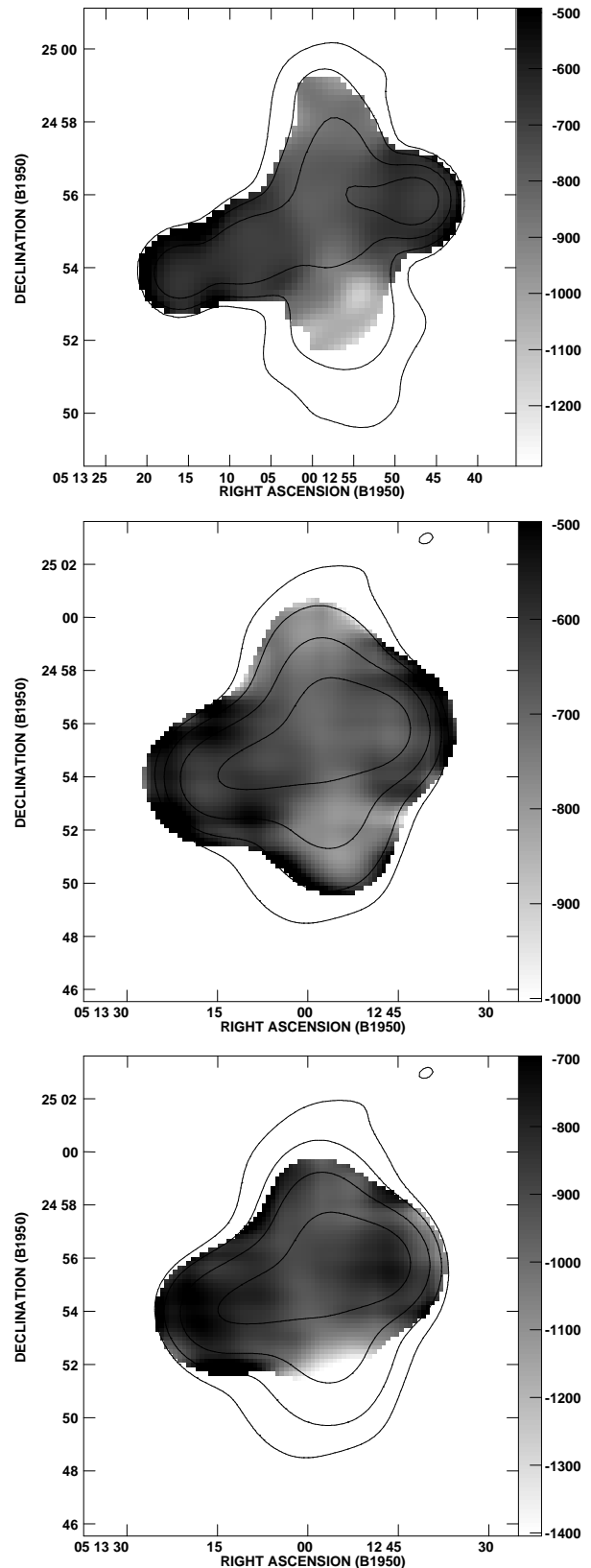


FIGURE 6.20— Spectral index maps of 3C136.1. The top panel shows the spectral index distribution between 1.37 GHz and 10.45 GHz at a resolution of  $69''\times 69''$ . Spectral index maps at a resolution of  $147''\times 147''$  can be found in the middle (1.37-4.85 GHz) and lower (4.85-10.45 GHz) panels.

Lobe	Region	Luminosity [erg/s]	$U_{min}$ [erg]	$u_{min}$ [erg/cm <sup>3</sup> ]	$B_{min}$ [ $\mu$ G]	$t_{syn}$ [Myr]	$t_{max}$ [Myr]
East → South	1	$4.2 \times 10^{41}$	$8.0 \times 10^{57}$	$5.9 \times 10^{-13}$	2.5	21.9	25.1
	2	$7.7 \times 10^{41}$	$1.8 \times 10^{58}$	$4.6 \times 10^{-13}$	2.2	24.3	27.6
	3					26.2	29.7
	4	$1.5 \times 10^{41}$	$6.0 \times 10^{57}$	$3.2 \times 10^{-13}$	1.9	26.9	30.7
	5	$8.9 \times 10^{40}$	$4.5 \times 10^{57}$	$3.4 \times 10^{-13}$	1.9	24.7	28.2
	6	$4.7 \times 10^{40}$	$2.7 \times 10^{57}$	$2.7 \times 10^{-13}$	1.7	33.9	39.1
West → North	1	$7.7 \times 10^{41}$	$1.5 \times 10^{58}$	$8.5 \times 10^{-13}$	3.0	18.2	21.7
	2	$3.7 \times 10^{41}$	$7.9 \times 10^{57}$	$7.3 \times 10^{-13}$	2.8	20.3	23.8
	3	$3.9 \times 10^{41}$	$8.2 \times 10^{57}$	$8.9 \times 10^{-13}$	3.0	21.9	26.3
	4	$1.8 \times 10^{41}$	$5.7 \times 10^{57}$	$5.1 \times 10^{-13}$	2.3	25.0	28.5
	5	$1.2 \times 10^{41}$	$4.3 \times 10^{57}$	$4.3 \times 10^{-13}$	2.2	23.6	26.8
	6	$6.0 \times 10^{40}$	$3.2 \times 10^{57}$	$3.1 \times 10^{-13}$	1.8	18.5	21.2

TABLE 6.4— Physical properties and spectral ages of various regions of 3C136.1. In regions 2 and 3 of the eastern lobe the calculation of the minimum energy/field has been done in the combined region.

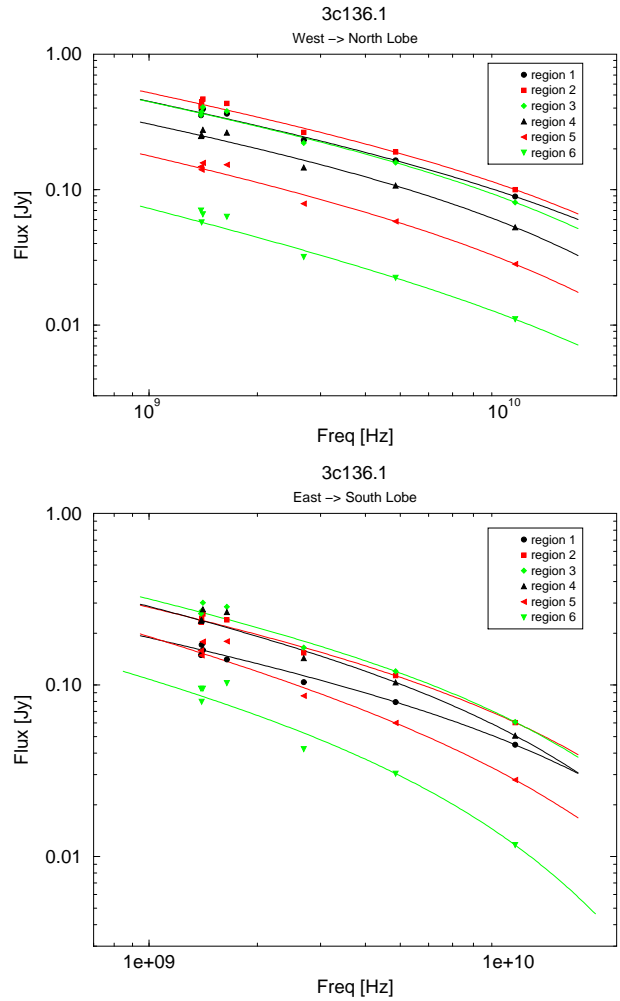
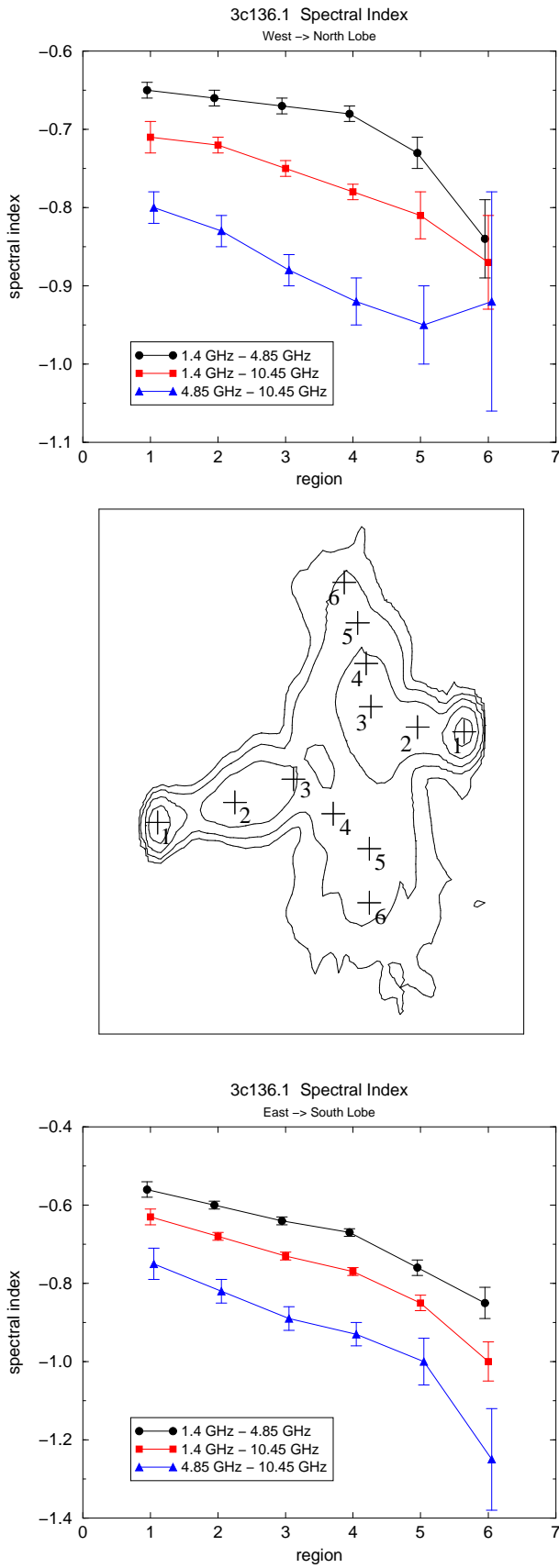


FIGURE 6.21— Trend of the spectral index along the west→north (upper panel) and east→south lobes (lower panel). Fluxes have been integrated in  $10 \times 10$  pixel areas centered on the positions marked by crosses in the middle panel.

FIGURE 6.22— Spectra extracted at source regions across the ridge of maximum brightness for the west→north lobe (top panel), and the east→south lobe (lower panel). The solid line indicates the best fitting spectral model. The datapoints at 1.41, 1.65 and 2.7 GHz suffer from missing flux and convolution errors due to the small image sizes. These images have not been used in the spectral analysis.

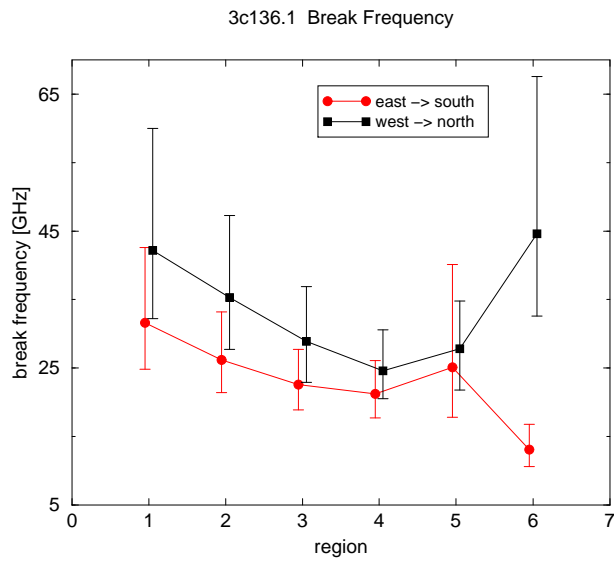


FIGURE 6.23— Break frequency distribution along the east→south and west→north transition from the active to the secondary lobes (see Fig. 6.21).

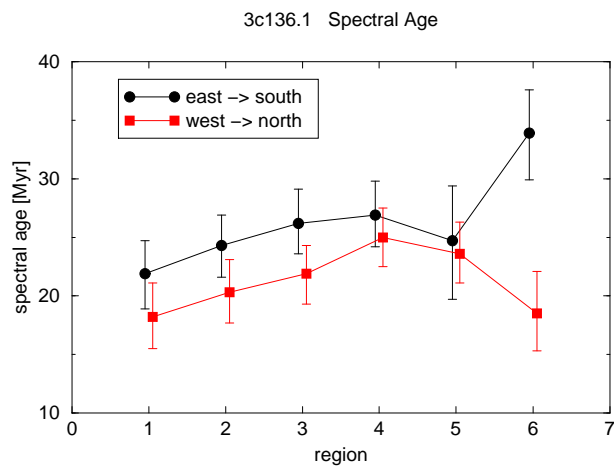


FIGURE 6.24— Trend of the spectral age along the east→south and west→north lobe. The location of the regions can be found in Fig. 6.21.

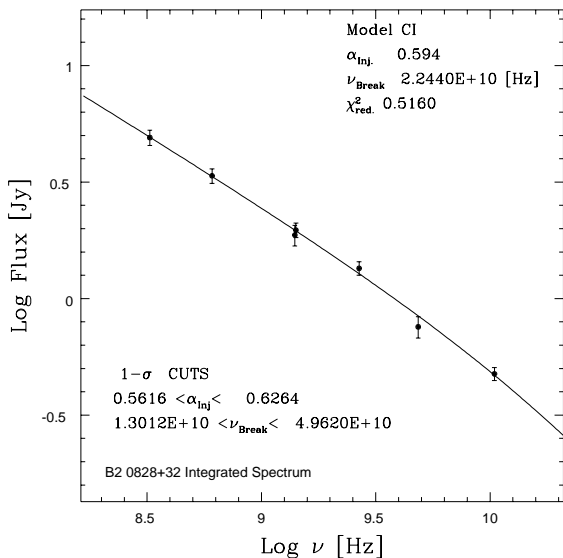


FIGURE 6.25— Integrated spectrum of B2 0828+32. The datapoints were compiled from the literature and were complemented with fluxes obtained from the multifrequency radio images. The solid line represents the best fitting CI spectral model. The fit parameters can be found in the plot caption.

### 6.5.5 B2 0828+32

The integrated spectrum of B2 0828+32 (Fig. 6.25) is best approximated by a CI model with  $\alpha_{inj} = -0.59$  and  $\nu_b = 22.4$  GHz. The spectrum has been constructed out of 7 frequencies ranging from 325 MHz to 10.55 GHz. The resolved spectral analysis has been performed using 6 frequencies (325 MHz, 609 MHz, 1.4 GHz, 1.42 GHz, 10.55 GHz) smoothed to a common resolution of  $101'' \times 75''$ . Figure 6.26 presents spectral index maps between 325 MHz and 609 MHz, and between 1.4 GHz and 10.55 GHz. In addition, spectral indices have been calculated by integrating fluxes in  $9 \times 9$  pixel boxes centered on equidistant points along the east→north and west→south lobes (see Fig. 6.27). The trend of the spectral index is displayed in Fig. 6.28. The high-frequency spectral index (1.4 GHz - 10.55 GHz) exhibits a gradual steepening from the primary towards the secondary lobes. This can be more clearly seen for the west→south lobe due to the higher signal-to-noise as compared to the east→north lobe. The spectral

index of the active lobes is  $\alpha \approx -0.7$  and then progressively steepens to values of  $\alpha \approx -1.1$  in the southern, and  $\alpha \approx -1.3$  in the northern secondary lobe. Whereas the spectral index of the west→south lobe gradually steepens, one can see a rather sharp drop in the northern lobe between regions 5 and 6. These findings are in excellent agreement with the spectral analysis of B2 0828+32 (between 609 MHz and 10.55 GHz) presented by Klein et al. (1995). The low-frequency spectral index (325 MHz - 609 MHz) shows little overall variation around the initial  $\alpha \approx -0.6$  in the active lobes.

Break frequencies have been obtained by fitting a JP-model to the spectra extracted in the various regions of B2 0828+32. It turned out, however, that allowing  $\alpha_{inj}$  to be a free fit parameter results in unsatisfactory fits. The injection index and the obtained break frequencies undergo large jumps from region to region. Therefore  $\alpha_{inj}$  was fixed to the value obtained from the fit to the integrated spectrum ( $\alpha_{inj} = -0.59$ ). Figure 6.29 displays the trend of break frequencies from the primary towards the secondary lobes. The errorbars have been obtained by refitting the model with  $\alpha_{inj}$  fixed to the upper and lower error boundaries as indicated by the integrated spectrum. There is a gradient in  $\nu_b$  starting at  $\approx 130$  GHz at the primary to  $< 10$  GHz at the tips of the secondary lobes. The change of  $\nu_b$  is gradual for the west→south lobe. The east→north lobe shows a similar behaviour except for regions 3-5 where an increase in break frequency takes place (the fits to these regions, however, were of low quality as indicated by the large error bars). Table 6.5 lists the calculated minimum energy properties of B2 0828+32. The highest minimum magnetic fields ( $B_{min} \approx 2 \mu\text{G}$ ) one finds in the active lobes. The field strength is steadily decreasing towards the secondary lobes reaching  $\approx 0.8 \mu\text{G}$  at their tips.

Finally, spectral ages have been computed for each region using the obtained values of  $B_{min}$  and  $\nu_b$ . The trend of the spectral age is displayed in Fig. 6.30. Both lobes show an increase of age from the primary ( $t \approx 10 \text{ Myr}$ )

to the secondary lobes ( $t \approx 40\text{Myr}$ ). The ages derived in this thesis are considerably lower than the values reported by Klein et al. (1995) who have reported spectral ages (by fitting KP models) of 74 Myr for the northern and 69 Myr for the southern lobe. As was pointed out by Murgia (1996) this discrepancy originates from a normalization problem inherent to the KP model. In order to be consistent with JP and CI models it is necessary to multiply KP break frequencies by a normalization factor of 2.25. Consequently, a factor of 0.66 needs to be applied to ages derived from KP-models which brings the ages of Klein et al. (1995) into perfect agreement with the values obtained in this thesis.

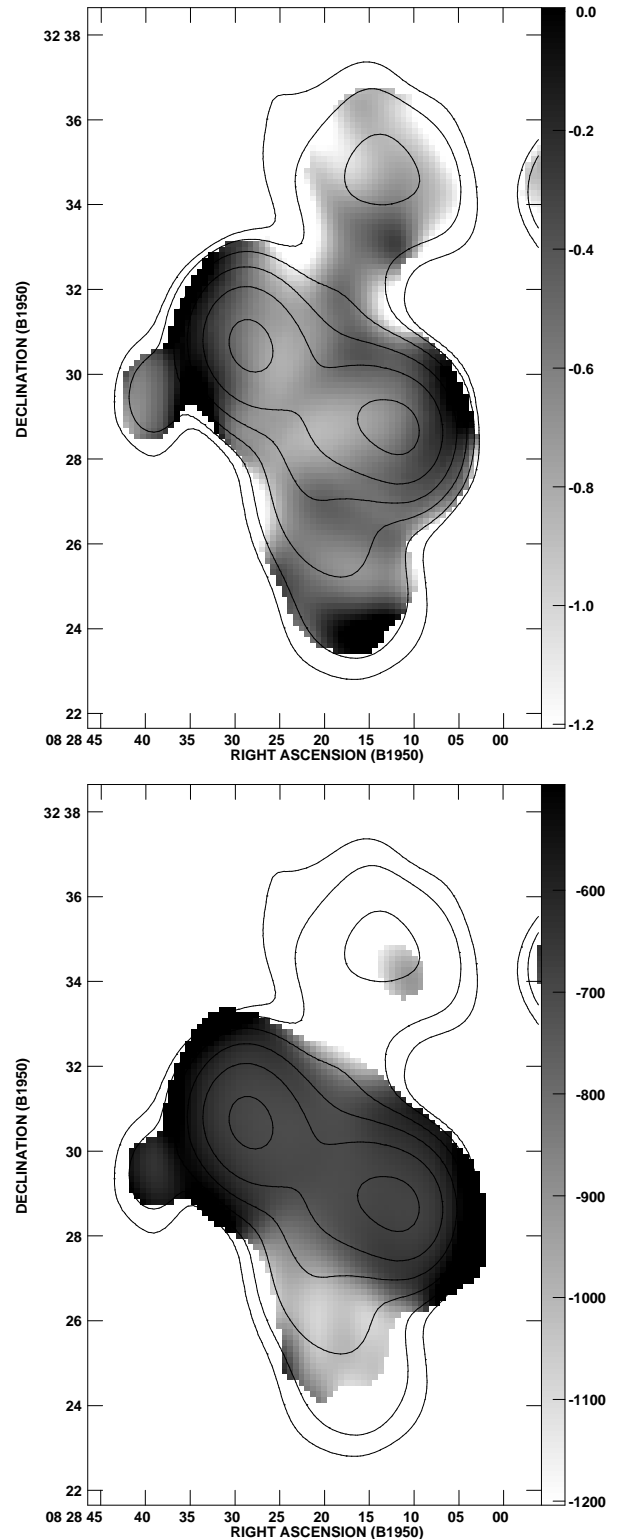


FIGURE 6.26— Spectral index maps of B2 0828+32 between 325 MHz and 609 MHz (upper panel), and between 1.4 GHz and 10.55 GHz (lower panel). The small extension to the southeast of the eastern primary lobe is due to a background source unrelated to B2 0828+32.

Lobe	Region	Luminosity [erg/s]	$U_{min}$ [erg]	$u_{min}$ [erg/cm <sup>3</sup> ]	$B_{min}$ [ $\mu$ G]	$t_{syn}$ [Myr]	$t_{max}$ [Myr]
East → North	1	$8.8 \times 10^{41}$	$2.0 \times 10^{58}$	$3.8 \times 10^{-13}$	2.0	12.3	13.6
	2					14.5	16.1
	3					14.0	15.5
	4					9.0	11.1
	5	$5.5 \times 10^{40}$	$2.9 \times 10^{57}$	$1.2 \times 10^{-13}$	1.1	15.2	18.7
	6					34.7	42.8
	7	$4.5 \times 10^{40}$	$4.6 \times 10^{57}$	$7.9 \times 10^{-14}$	0.9	36.8	48.8
	8					35.9	46.9
	9					41.1	53.6
	10					39.8	52.2
West → South	1	$1.3 \times 10^{42}$	$2.2 \times 10^{58}$	$4.5 \times 10^{-13}$	2.2	11.5	12.7
	2					13.7	15.2
	3					15.5	17.2
	4					19.9	22.0
	5	$6.7 \times 10^{40}$	$3.8 \times 10^{57}$	$1.3 \times 10^{-13}$	1.2	22.1	27.1
	6					25.8	31.6
	7	$2.8 \times 10^{40}$	$3.0 \times 10^{57}$	$6.4 \times 10^{-14}$	0.8	22.2	30.7
	8					23.5	32.4
	9					42.6	58.8

TABLE 6.5— Physical properties of 0828+32 for the source regions marked in Fig. 6.27. The minimum energies and fields have been determined in larger areas comprising of several regions.



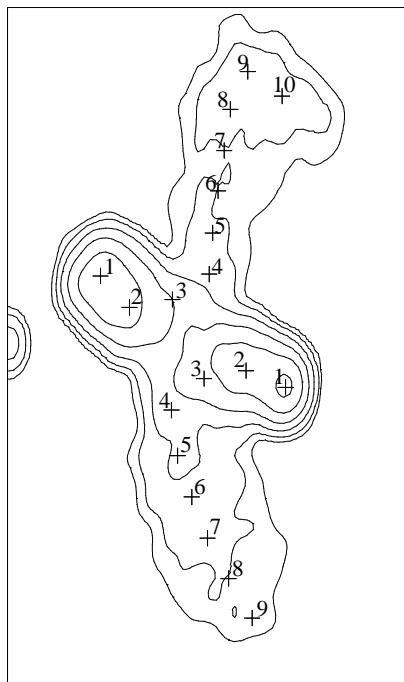


FIGURE 6.27— Equidistant points marked by numbers along the line connecting the active to the secondary lobes. Centered on these points integrated fluxes have been determined in  $9 \times 9$  pixel boxes.

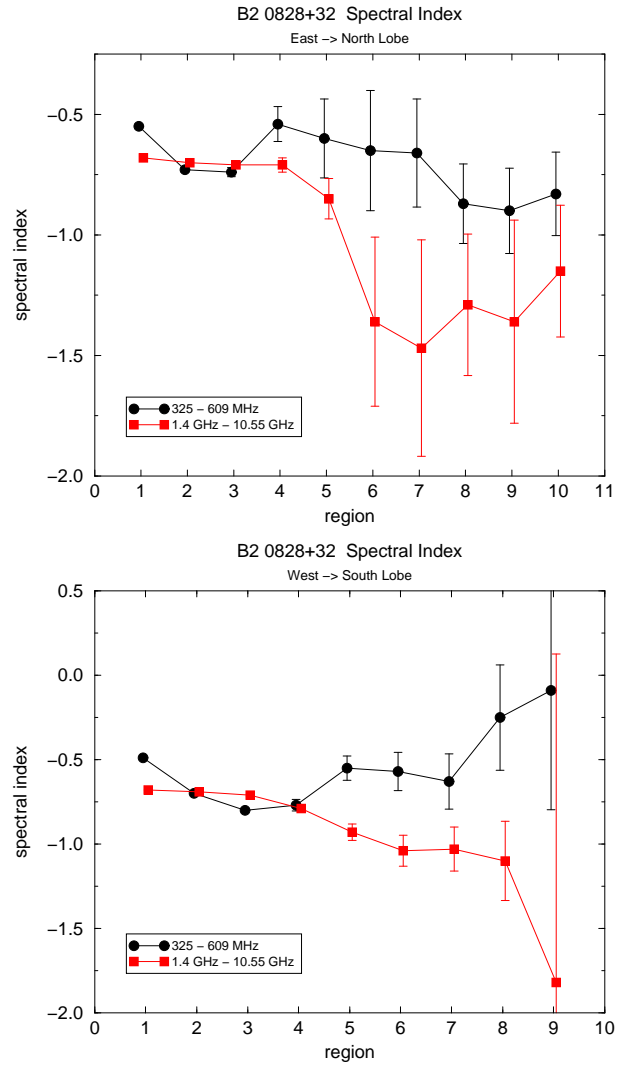


FIGURE 6.28— Trend of the spectral index between 325 MHz and 609 MHz, and between 1.4 GHz and 10.55 GHz, along the line connecting the active to the secondary lobes. The top panel represents the east→north, the bottom panel the west→south transition. For the location of the regions see Fig. 6.27.

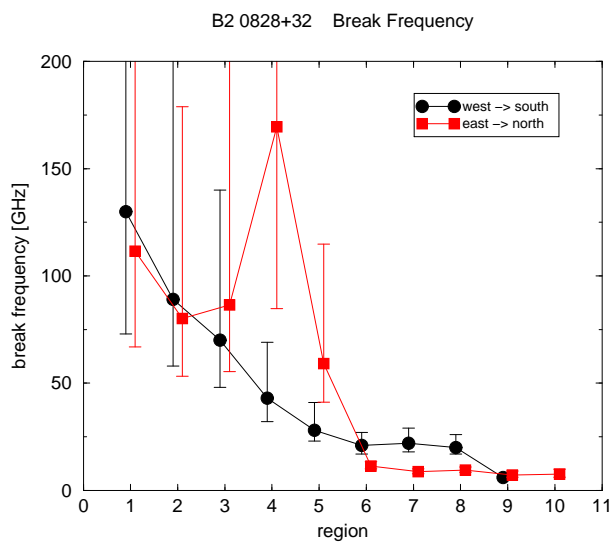


FIGURE 6.29— Trend of the break frequency along the path from the active to the secondary lobes.

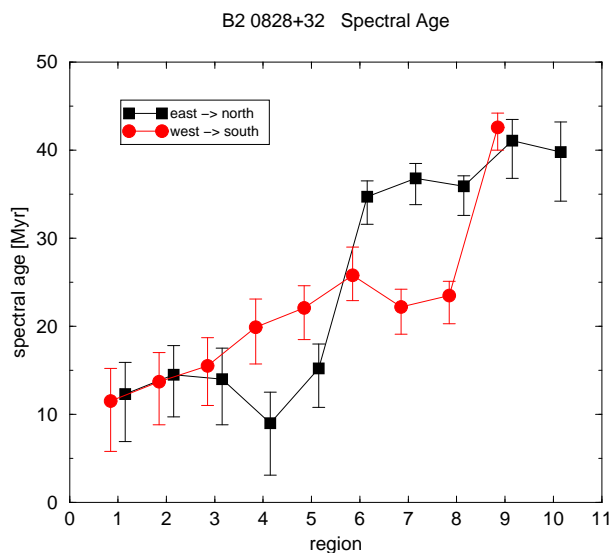


FIGURE 6.30— Trend of the spectral age for the east→north and west→south lobes.

### 6.5.6 3C223.1

The integrated spectrum of 3C223.1 is presented in Fig. 6.31. The solid line represents the best fitting CI model with  $\nu_b = 53$  GHz and  $\alpha_{inj} = -0.67$ . The fit indicates a slight increase of spectral slope towards higher frequencies. Dennett-Thorpe (1996) have presented a spectral analysis of 3C223.1 and have discussed the possibility of a high frequency break. However the author suspected the spectral curvature to be artificial due to missing flux in the high frequency 15 GHz image. The 32 GHz single-dish observation presented in this thesis confirms that indeed the spectrum begins to deviate from a pure powerlaw at frequencies above a few GHz. This fit result does not heavily depend on the 32 GHz measurement. Stability tests of the fitting procedure, conducted with the low frequency (38 MHz, 178 MHz) and high-frequency (32 GHz) datapoints being flagged yielded identical results for  $\nu_b$  and  $\alpha_{inj}$  within the errors.

Spectral index maps at a resolution of  $10'' \times 10''$  were constructed using images at 1.4 GHz, 4.9 GHz and 8.5 GHz (Fig. 6.32). The spectral index distribution of 3C223.1 is rather peculiar. Unlike other X-shaped sources (with the exception of 3C403; see section 6.5.9) the spectrum of the secondary lobes is considerably flatter than in the primary lobes. This can be more clearly seen in Fig. 6.33 where the trend of spectral index is displayed along the north→west and the south→east lobes. In order to increase the snr fluxes have been integrated in  $7 \times 7$  pixel boxes. Whereas regions close to the hotspots exhibit spectral indices of about  $-0.75$  typical values in the secondary lobes range from  $\alpha = -0.6$  to  $-0.65$ . The western secondary lobe exhibits an almost constant spectral index of  $\alpha \approx -0.62$ . More interestingly in the eastern secondary lobe the flattest spectral slope occurs at its tip with a progressive steepening towards the core. This apparent "spectral reversal" has already been noticed and discussed by Dennett-Thorpe (1996). The author could reproduce this effect even with different imag-

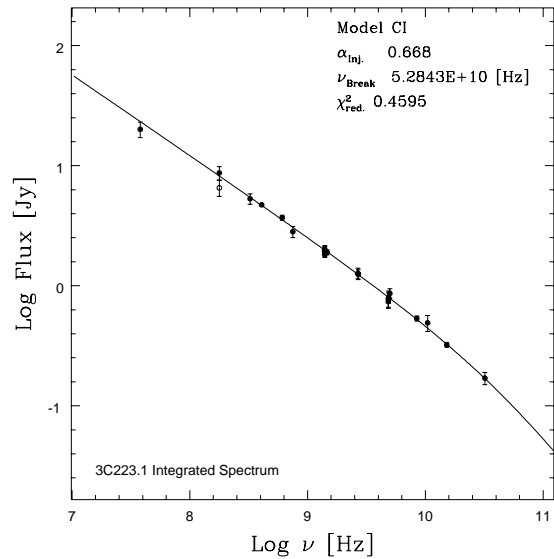


FIGURE 6.31— Integrated spectrum of 3C223.1. The datapoints were compiled from the literature and were complemented with fluxes obtained from the multifrequency radio images. The solid line represents the best fitting spectral model. The fit parameters can be found on the plot. The 178 MHz datapoint marked by an open circle has been flagged during the fitting procedure as it's flux value is most probably miscalibrated.

ing techniques employed and therefore concluded that the flatter spectrum throughout the secondary lobes is real. A possible explanation for this finding is particle reacceleration within the secondary lobes. However the absence of any shock signatures in which the particles would be reaccelerated argue against such a scenario. Also, the high degree of polarized emission observed in the secondary lobes indicates that stochastic reacceleration by plasma turbulence is not applicable in the case of 3C223.1. Alternatively, the primary and secondary lobes might consist of particle populations with an entirely different injection spectrum. This should manifest itself in different values of  $\alpha_{inj}$  for the two lobe systems. Figure 6.34 displays the trend of  $\alpha_{inj}$ . Even though there is a tendency for flatter injection spectra in the secondary lobes the fairly large errors are also consistent with constant injection indices across the whole of the lobes. On the other hand, it is possible that the

steeper spectrum of the primary lobes simply reflect higher radiation losses and enhanced magnetic fields due to the interaction of the hotspots with the ISM/IGM. If jet re-orientation is responsible for the formation of X-shaped sources we expect such increased losses. After the jet has been realigned it has to drill through the dense ambient medium in order to create a new lobe cavity. If this explanation is true it remains puzzling why a similar spectral reversal has not been observed in NGC 326 even though it is the youngest X-shaped source and is located in a denser environment than 3C223.1

Break frequencies have been obtained by fitting JP models to the synchrotron spectra of the various source regions of 3C223.1. The spectra include data at six frequencies (608 MHz, 1.39, 1.46, 4.89, 8.47 and 32 GHz). The corresponding maps were smoothed to a common resolution of  $46'' \times 30''$ . A plot of the break frequency trend can be found in Fig. 6.35. In most source regions the spectra exhibit virtually no curvature and are consistent with pure powerlaw models within the errorbars. As can be seen in Fig. 6.36 our inability to further constrain the high-frequency break is mainly caused by the poor quality of the 32 GHz data. The 32 GHz data is indeed crucial for the determination of the break frequency because the integrated spectrum indicates the location of the break to be above 50 GHz.

The trend of  $t_{syn}$  is displayed in Fig. 6.37. For most regions of 3C223.1 only upper limits of the spectral age could be obtained and for none of the regions a lower limit could be established. Consequently no definite statement about possible age gradients in the lobes of 3C223.1 can be made. The upper age limits indicate however that  $t_{syn}$  is smaller than 12 Myr everywhere in the source which makes 3C223.1 one of the youngest studied X-shaped source.

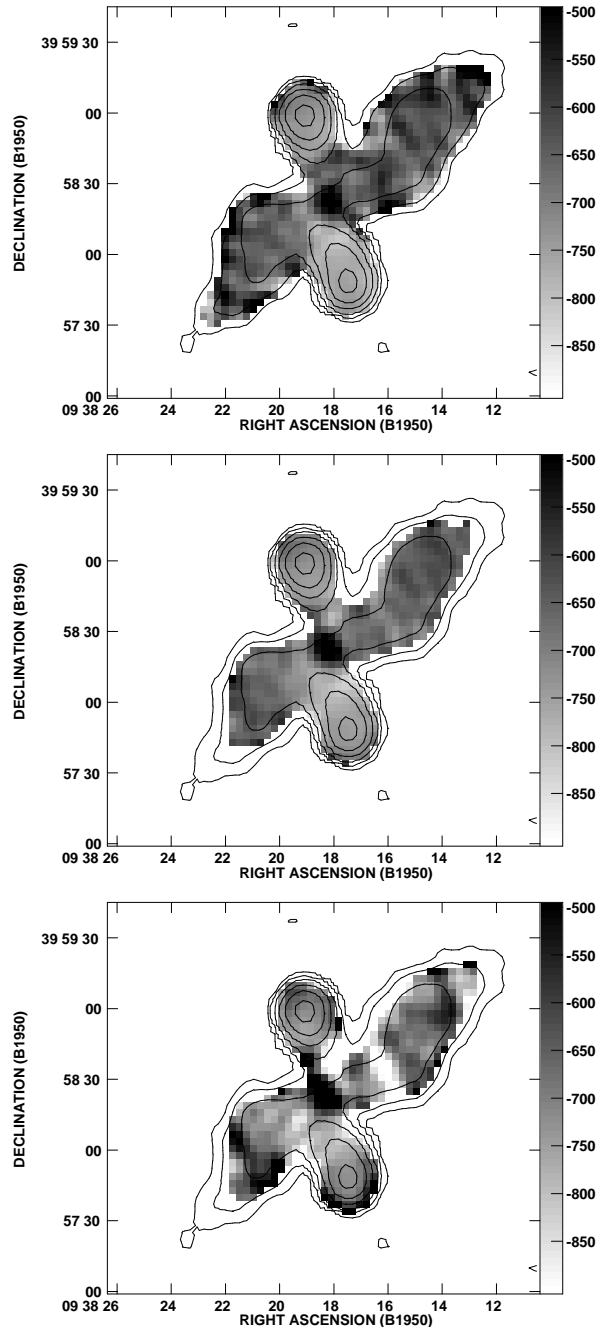


FIGURE 6.32— Spectral index maps of 3C223.1 between 1.5 GHz and 4.9 GHz (top), between 1.5 GHz and 8.5 GHz (middle), and between 4.9 GHz and 8.5 GHz (bottom) at a resolution of  $10'' \times 10''$ . For the calculation of the spectral index maps a total intensity cutoff level of  $6\sigma$  has been used.

Lobe	Region	Luminosity [erg/s]	$U_{min}$ [erg]	$u_{min}$ [erg/cm <sup>3</sup> ]	$B_{min}$ [ $\mu$ G]	$t_{syn}$ [Myr]	$t_{max}$ [Myr]
south → east	1	$2.0 \times 10^{42}$	$9.7 \times 10^{57}$	$4.7 \times 10^{-12}$	7.1	2.0	4.4
	2	$1.4 \times 10^{42}$	$7.6 \times 10^{57}$	$4.0 \times 10^{-12}$	6.6	< 4.2	< 8.5
	3					< 4.4	< 8.9
	4	$2.5 \times 10^{41}$	$2.8 \times 10^{57}$	$1.6 \times 10^{-12}$	4.2	< 7.1	< 10.2
	5	$2.7 \times 10^{41}$	$3.1 \times 10^{57}$	$1.6 \times 10^{-12}$	4.1	7.4	10.5
	6	$1.7 \times 10^{41}$	$2.8 \times 10^{57}$	$9.5 \times 10^{-13}$	3.2	9.3	12.0
	7	$1.0 \times 10^{41}$	$1.7 \times 10^{57}$	$9.1 \times 10^{-13}$	3.1	11.9	15.2
north → west	1	$2.1 \times 10^{42}$	$1.1 \times 10^{58}$	$4.4 \times 10^{-12}$	6.9	3.4	7.3
	2	$5.6 \times 10^{41}$	$5.6 \times 10^{57}$	$1.8 \times 10^{-12}$	4.4	4.8	7.1
	3					4.0	5.9
	4	$2.1 \times 10^{41}$	$3.3 \times 10^{57}$	$1.0 \times 10^{-12}$	3.3	< 8.8	< 11.3
	5	$3.0 \times 10^{41}$	$4.1 \times 10^{57}$	$1.2 \times 10^{-12}$	3.6	8.5	11.4
	6	$3.3 \times 10^{41}$	$3.9 \times 10^{57}$	$1.4 \times 10^{-12}$	3.9	< 10.5	< 14.7
	7	$1.8 \times 10^{41}$	$3.0 \times 10^{57}$	$9.3 \times 10^{-13}$	3.2	0.8	1.1

TABLE 6.6— Physical properties and ages of 3C223.1. Minimum energies and fields have been computed in the combined regions 2 & 3 in the southern and northern active lobe. For some regions only lower limits of  $\nu_b$  could be obtained from the spectral fits. For these regions upper limits of the spectral age are given in the table.

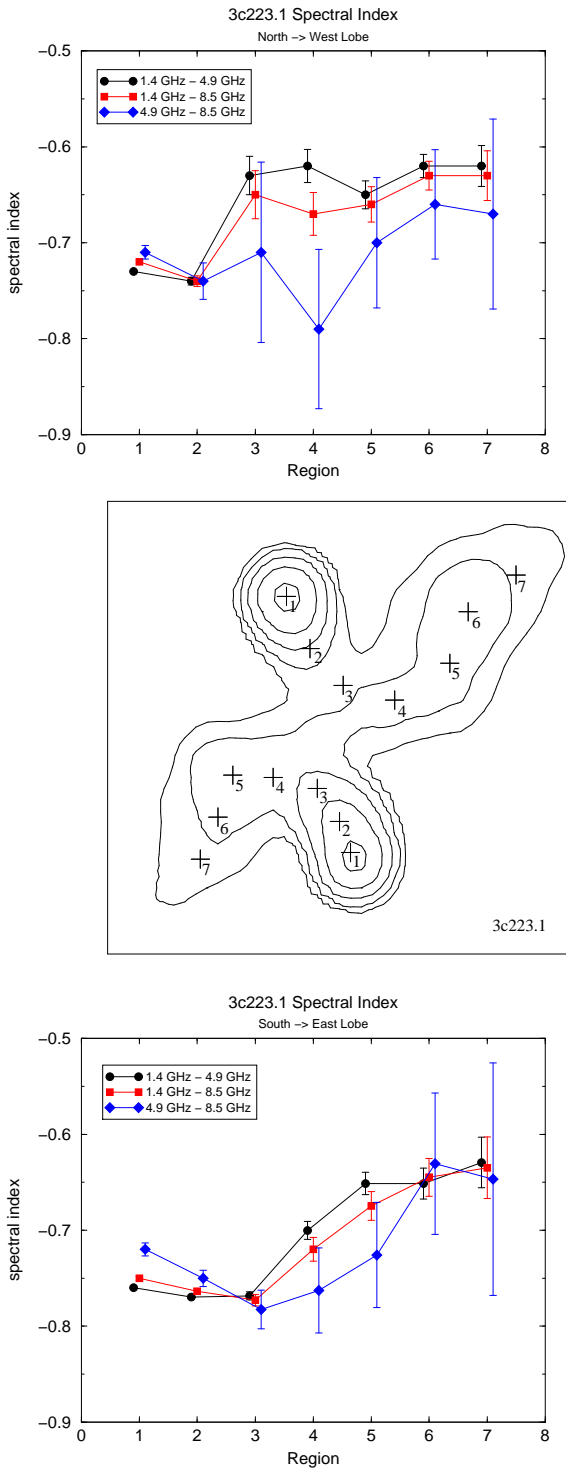


FIGURE 6.33— Trend of the spectral index along the ridge of maximum brightness (marked by crosses) for the north→west (top) and south→east lobe (bottom). The spectral index has been calculated using integrated fluxes obtained in  $7 \times 7$  pixel areas centered on the marked positions. For the sake of clarity only the bottom part of the error bars have been plotted for spectral indices between 4.9 and 8.5 GHz.

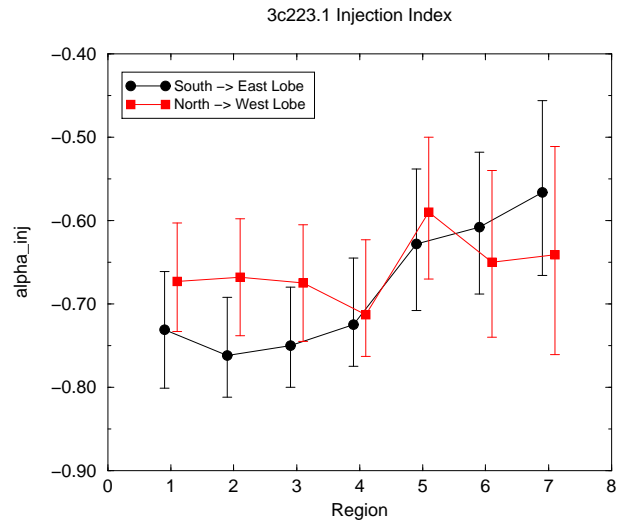


FIGURE 6.34— The distribution of the injection index along the north→west and south→east lobes of 3C223.1.

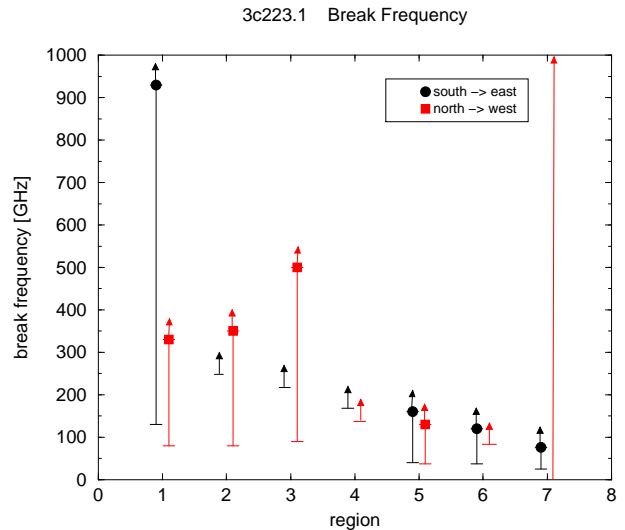


FIGURE 6.35— Break frequency distribution of 3C223.1. The break frequencies are plotted along the line of maximum brightness connecting the primary to the secondary lobes (see Fig. 6.33). Datapoints marked by arrows denote the cases when the spectral fits were consistent with an unbroken powerlaw and consequently no break frequency could be determined.

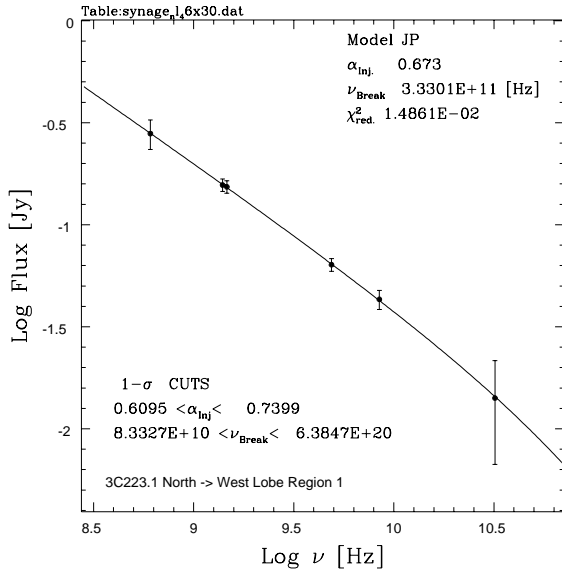


FIGURE 6.36— Spectrum of region 1 in the north→west lobe of 3C223.1. The solid line represents the best fitting JP model. As can be seen the rather large errors obtained for  $\nu_b$  are mainly introduced by the large noise of the 32 GHz data.

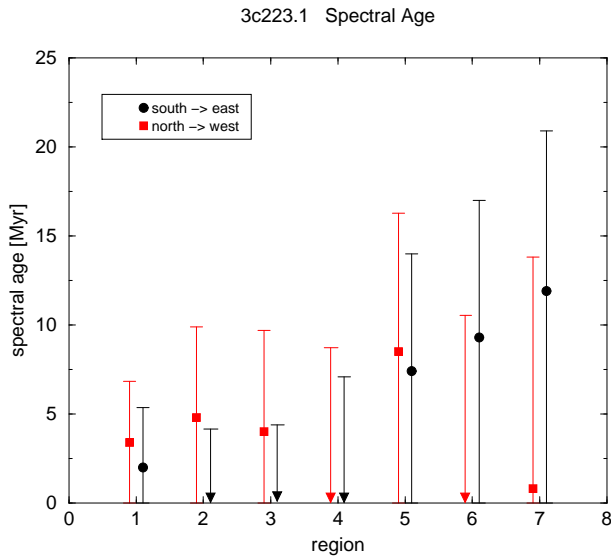


FIGURE 6.37— The trend of  $t_{syn}$  in 3C223.1 along the ridge of maximum brightness connecting the active to the secondary lobes (see Fig. 6.33). Datapoints marked by arrows represent the cases in which only lower limits of  $\nu_b$  could be determined from the spectral fits.

## 6.5.7 3C315

The integrated spectrum of 3C315 is displayed in Fig. 6.38. It consists of 33 datapoints extracted from the literature and 6 fluxes obtained from available datasets. The covered frequency range extends from 26 MHz to 32 GHz. The solid line represents the best fitting CI model indicating  $\alpha_{inj} = -0.76 \pm 0.01$  and  $\nu_b = 39.4 \pm_{9.3}^{13.9}$  GHz.

Due to the small angular size of 3C315 the number of images that provide sufficient resolution for further spectral analysis is rather small. The single-dish data at 4.85 GHz and 10.45 GHz (3.15 and 3.24) had to be excluded on the basis of resolution. Only the 32 GHz data has an adequately small beam ( $30'' \times 30''$ ) however the emission at this frequency is weak (see Fig. ??). The peak intensity which corresponds to the bright core is below the  $10\sigma$  level. Only the brightest parts of the radio lobes show up above  $3\sigma$ , which is too low to be used for a quantitative study. Consequently the spectral analysis has been performed with only 3 frequencies in a fairly small frequency range (1.42, 1.65 and 2.7 GHz). Figure 6.39 presents the corresponding spectral index maps at a resolution of  $9''1 \times 5''5$ . In order to increase the signal-to-noise, fluxes have been determined in  $9 \times 9$  pixel boxes centered on equidistant positions marked in Fig. 6.40. The trend of the spectral index along the north→west and south→east lobes is presented in Fig. 6.41. The steepest slope between 1.65 GHz and 2.7 GHz is located at the tips of the primary lobes ( $\alpha = -1.46$  and  $\alpha = -1.26$  for the southern and northern lobes respectively). The spectrum then becomes flatter in regions close to the core and again steepens towards the tips of the secondary lobes. The extremely steep spectral index of region 6 and possibly the flat index in region 7 of the northern lobe is caused by artificial sidelobe structure present in the 2.7 GHz image. The peculiar spectral behaviour is consistent with the findings of Alexander & Leahy (1987).

Break frequencies have been determined by fitting of JP models to the synchrotron spec-

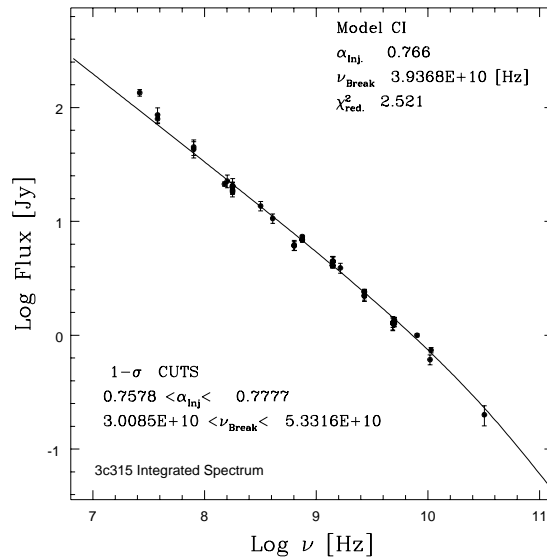


FIGURE 6.38— The integrated spectrum of 3C315. Fluxes have been extracted from the literature and have been complemented by values obtained from available datasets. The solid line represents the best fitting CI model. The fit parameters and the relevant fit errors can be found in the plot legend.

tra of the various regions of 3C315. Due to the poor frequency coverage the injection index had to be fixed to  $\alpha_{inj} = -0.766$  as has been obtained from the integrated spectrum. The trend of  $\nu_b$  along the north→west and south→east lobes is displayed in Fig. 6.42. Because the highest available frequency in this analysis is 2.7 GHz the location of the high frequency break is ill constrained by the fits. In several regions the upper limits of  $\nu_b$  were extremely large or consistent with pure power law spectra. These cases are denoted by arrows. Regions 6 and 7 in the north→west lobe suffer from the presence residual sidelobe emission in the 2.7 GHz image. Due to the large errors no clear trend of  $\nu_b$  along the north→west and south→east lobes is visible. In order to improve the situation sensitive high frequency observations with good resolution would be needed. Table 6.7 lists the physical properties and ages of the various regions of 3C315 obtained from minimum energy calculations. The minimum magnetic fields lie below  $7\mu\text{G}$  everywhere. The highest values of  $B_{min}$  are



found in regions 4 and 5 of the north→west and south→east lobes.

The trend of  $t_{syn}$  is plotted in Fig. 6.43. Despite the large errors there is indication in the south→east lobe for ageing away from the core towards the lobe tips. The highest ages of  $t_{syn}=33.7\pm_{11.3}^{10}$  occur at the tips of the primary and secondary lobes ( $t_{syn}=33.7\pm_{11.3}^{10}$  and  $t_{syn}=26.5\pm_{14.6}^{11.5}$  respectively) whereas the ages close to the core are somewhat lower ( $t_{syn}=9.2\pm_{9.2}^{8.9}$ ). The situation in the north→west lobe is however less clear and no obvious trend of the spectral is visible.

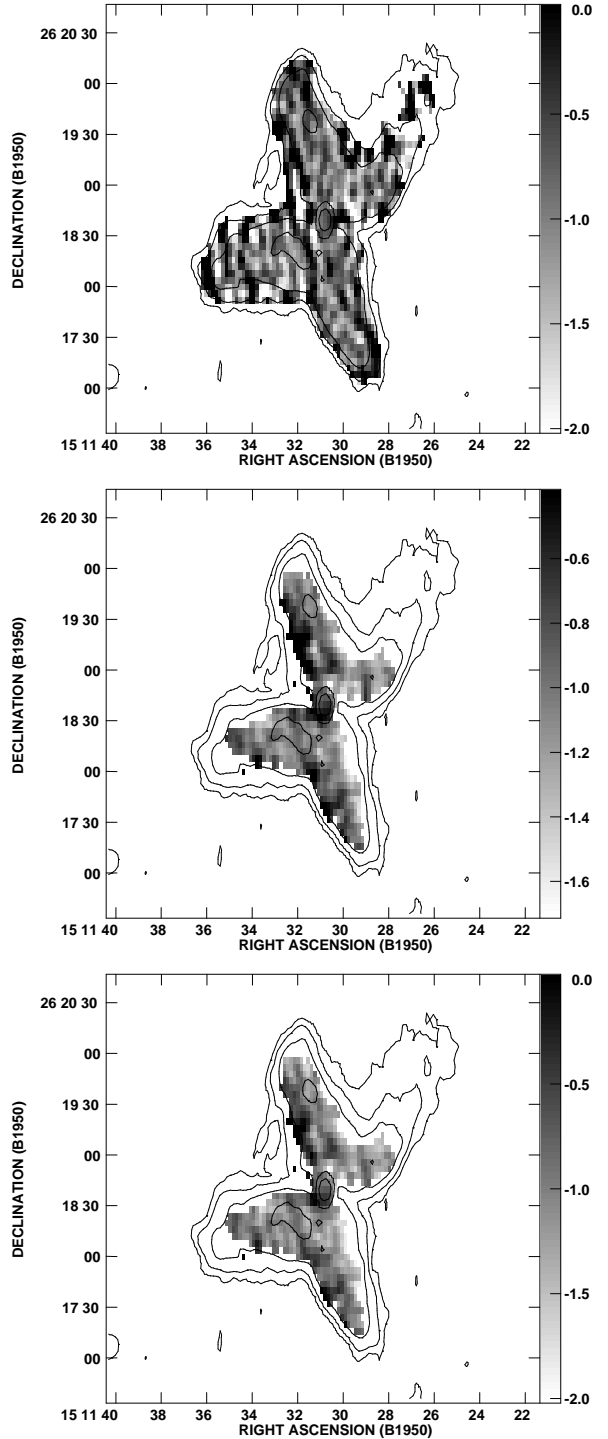


FIGURE 6.39— Greyscale spectral index maps of 3C315 between 1.42 GHz and 1.65 GHz (top), between 1.42 GHz and 2.7 GHz (middle), and between 1.65 GHz and 2.7 GHz (bottom). The superimposed contours represent the total intensity image of 3C315 at 1.42 GHz. The spectral index calculation has been clipped for fluxes below  $6\sigma$ .

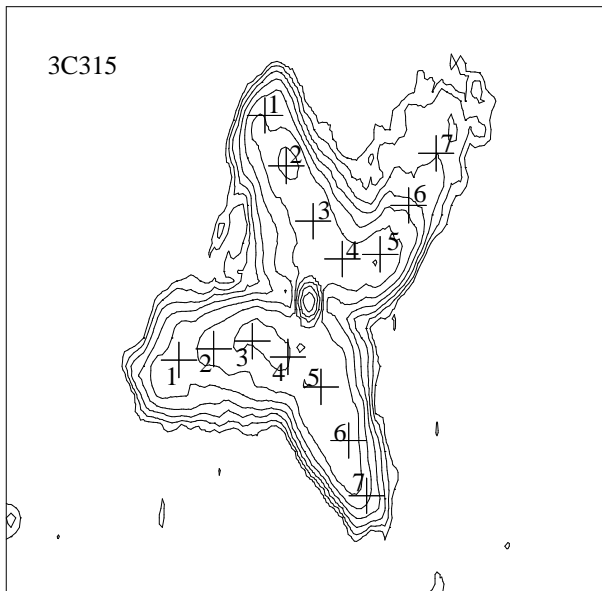


FIGURE 6.40—Equidistant point along the north→west and south→east lobe transition line. Crosses mark the positions where fluxes have been integrated in 9×9 pixel boxes.

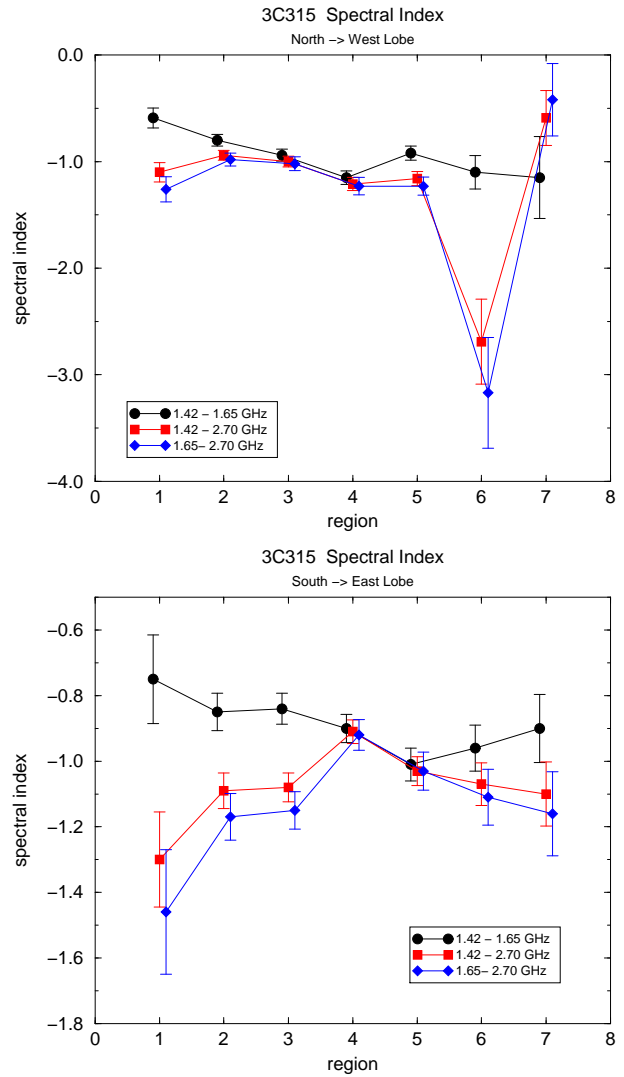


FIGURE 6.41—Spectral index distribution along north→west (top) and south→east (bottom) transition connecting the active to the secondary lobes. The location of the regions are marked by crosses in Fig. 6.40.

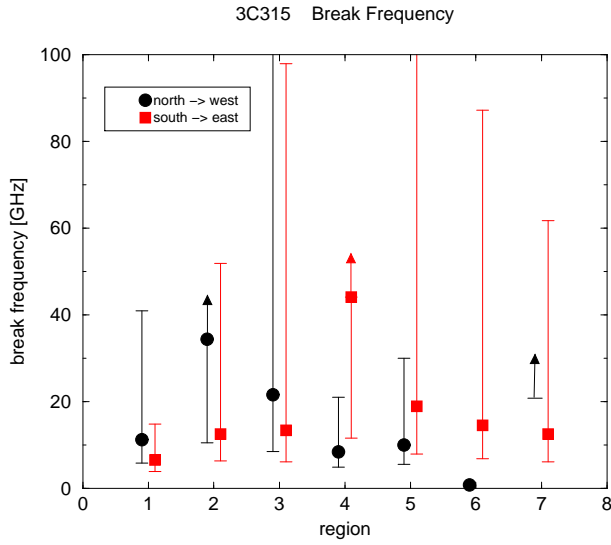


FIGURE 6.42— Trend of  $\nu_b$  along the north→west and south→east lobes. The break frequencies have been determined by fitting a JP model with  $\alpha_{inj} = -0.766$  to the synchrotron spectra. Datapoints marked by arrows denote cases where the fit was consistent with a pure powerlaw and no break frequency and/or no upper limit for  $\nu_b$  could be obtained.

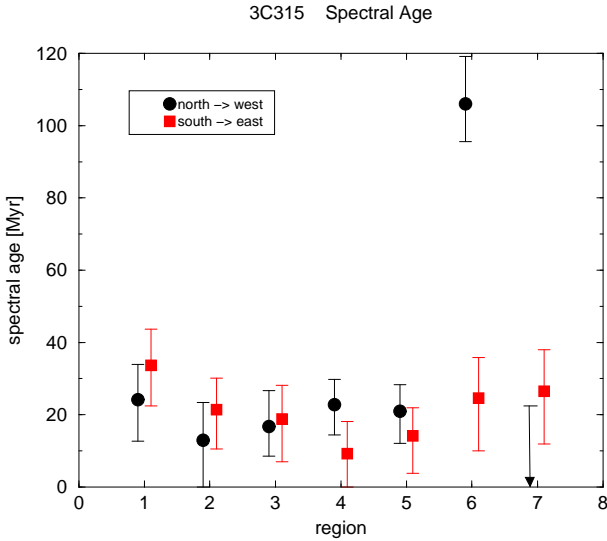


FIGURE 6.43— Trend of the spectral age along the north→west and south→east lobes of 3C315. Arrows denote the cases where only an upper limit of  $t_{syn}$  could be obtained. The regions are the same as marked in Fig. 6.40.

Lobe	Region	Luminosity [erg/s]	$U_{min}$ [erg]	$u_{min}$ [erg/cm <sup>3</sup> ]	$B_{min}$ [ $\mu$ G]	$t_{syn}$ [Myr]	$t_{max}$ [Myr]
north → west	1	$6.4 \times 10^{41}$	$6.7 \times 10^{57}$	$2.4 \times 10^{-12}$	5.1	24.2	39.7
	2	$1.6 \times 10^{42}$	$1.4 \times 10^{58}$	$2.9 \times 10^{-12}$	5.6	12.9	22.6
	3	$1.5 \times 10^{42}$	$1.5 \times 10^{58}$	$2.7 \times 10^{-12}$	5.4	16.7	28.6
	4	$1.7 \times 10^{42}$	$1.2 \times 10^{58}$	$3.9 \times 10^{-12}$	6.5	22.8	45.8
	5					21.0	42.1
	6	$5.1 \times 10^{41}$	$7.5 \times 10^{57}$	$1.5 \times 10^{-12}$	4.0	106.0	149.5
	7	$2.8 \times 10^{41}$	$5.9 \times 10^{57}$	$9.5 \times 10^{-13}$	3.2	< 22.7	< 29.1
south → east	1	$4.2 \times 10^{41}$	$5.0 \times 10^{57}$	$2.1 \times 10^{-12}$	4.7	33.7	52.1
	2	$1.1 \times 10^{42}$	$1.0 \times 10^{58}$	$2.9 \times 10^{-12}$	5.6	21.4	37.6
	3	$1.5 \times 10^{42}$	$1.2 \times 10^{58}$	$3.6 \times 10^{-12}$	6.2	18.8	36.3
	4	$1.8 \times 10^{42}$	$1.2 \times 10^{58}$	$4.6 \times 10^{-12}$	7.0	9.2	20.0
	5					14.1	30.6
	6	$8.6 \times 10^{41}$	$1.3 \times 10^{58}$	$1.5 \times 10^{-12}$	4.1	24.6	34.9
	7	$5.9 \times 10^{41}$	$8.7 \times 10^{57}$	$1.5 \times 10^{-12}$	4.1	26.5	37.6

TABLE 6.7— Source properties of 3C315.

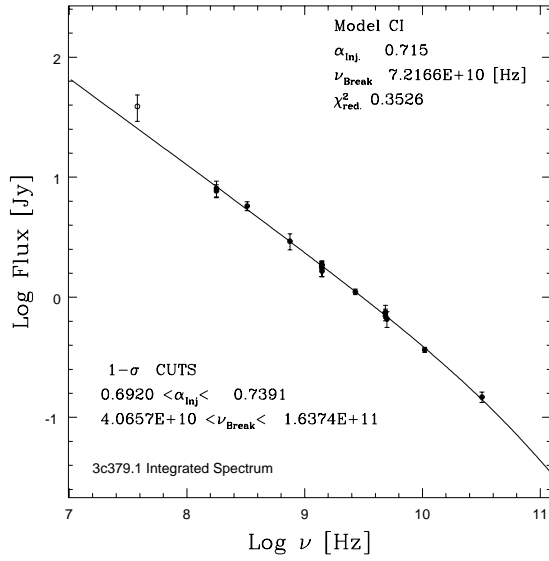


FIGURE 6.44— Integrated spectrum of 3C379.1. The solid line represents the best fitting CI-model. The fit parameters and errors can be found in the plot legend. The 38 MHz datapoint marked by an open circle has been flagged for the fitting procedure.

### 6.5.8 3C379.1

The integrated spectrum of 3C379.1 presented in Fig. 6.44 consists of 16 datapoints compiled from the literature and supplemented by fluxes obtained from available datasets. The covered frequency range extends from 38 MHz to 32 GHz. The best fitting spectral model is a CI-model with  $\alpha_{inj} = 0.72$  und  $\nu_b = 72.2$  GHz.

For the resolved spectral analysis only the images at 1.4 GHz (WSRT) and 32 GHz provide sufficient resolution. The spectral index map at a resolution of  $30'' \times 30''$  between these two frequencies is displayed in Fig. 6.45. Due to the low signal-to-noise of the 32 GHz image the calculation of spectral indices is limited to the brightest regions of the active lobes only. The short secondary lobes of 3C379.1 are only slightly resolved in the 1.4 GHz map and remain below the detection limit at 32 GHz. The southern and northern lobes have a mean spectral index of  $\alpha = -0.81 \pm 0.05$ , and  $\alpha = -0.78 \pm 0.06$ , respectively. Table 6.5.8 lists the minimum energy properties of 3C379.1. Break frequencies have been obtained using the two-point spectral index. An injection in-

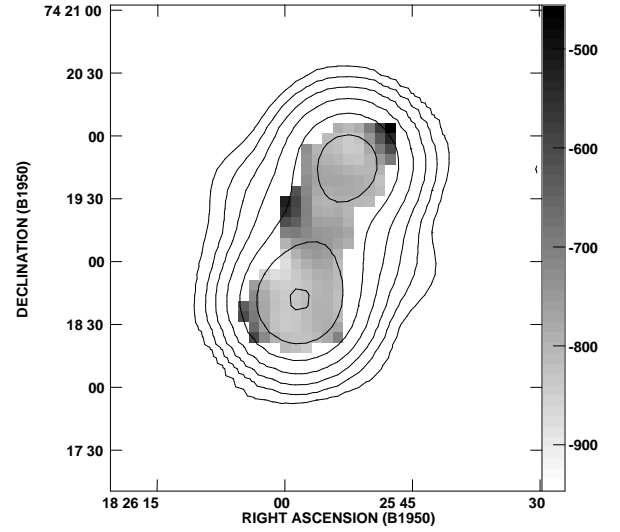


FIGURE 6.45— Spectral index distribution (greyscale) of 3C379.1 between 1.4 GHz and 32 GHz. Superimposed are contours of the 1.4 GHz total intensity convolved to a  $30'' \times 30''$  beam. The spectral index calculation has been clipped for fluxes below the  $3\sigma$  level.

dex of  $\alpha_{inj} = -0.72 \pm_{0.023}^{0.024}$  has been assumed as was determined by the fit to the integrated spectrum. The resulting break frequencies were  $\nu_b = 359 \pm_{115}^{255}$  GHz for the southern and  $\nu_b = 638 \pm_{266}^{853}$  GHz for the northern lobe. The inferred spectral ages are  $t_{syn} = 2.6 \pm 0.6$  (southern lobe) and  $t_{syn} = 2.2 \pm_{1.2}^{0.2}$  (northern lobe).

Lobe	Luminosity [erg/s]	$U_{min}$ [erg]	$u_{min}$ [erg/cm <sup>3</sup> ]	$B_{min}$ [ $\mu$ G]	$t_{syn}$ [Myr]	$t_{max}$ [Myr]
north	$1.1 \times 10^{43}$	$8.9 \times 10^{58}$	$3.6 \times 10^{-12}$	6.2	2.2	4.4
south	$2.4 \times 10^{43}$	$1.7 \times 10^{59}$	$4.7 \times 10^{-12}$	7.1	2.6	5.8

TABLE 6.8— Source properties of 3C379.1

## 6.5.9 3C403

The integrated spectrum of 3C403 is displayed in Fig. 6.46. The datapoints are best approximated by a CI model with  $\nu_b = 25$  GHz and  $\alpha_{inj} = -0.68$ . In order to test the stability of the fit all high-frequency datapoints above 5 GHz have been flagged for the fitting procedure. The effect on  $\nu_b$  and  $\alpha_{inj}$  was only marginal and the fit results were identical within the errorbars. As can be seen the 32 GHz datapoint lies well above the fit solution. Several possible reasons for this flux offset have been investigated. A possible explanation for a spectral upturn at high frequencies is the contribution of an additional thermal component produced by dust. Indeed 3C403 is the only X-shaped source that has significant infrared luminosity. The source was detected in the three shortest wavelength channels of the IRAS all sky survey (Golombek et al. 1988). We have investigated spectral fits including an extra dust component. It has turned out that a dust component with  $T < 10$  K must be present in order to create the observed spectral upturn at 32 GHz. This is considerably cooler than the canonical 30 K which is typically observed in active radio sources (Chini et al. 1989). Furthermore, spectra extracted at various locations indicate that the 32 GHz is offset by a constant offset *everywhere* within 3C403. If the upturn were due to thermal emission we would instead expect to find larger contributions towards the center of the host galaxy where the concentration of dust is higher than at greater distances from the core.

We therefore conclude that the increased flux at 32 GHz is most probably not physical. The flux can however be *systematically* overestimated in case the beam size of the 32 GHz

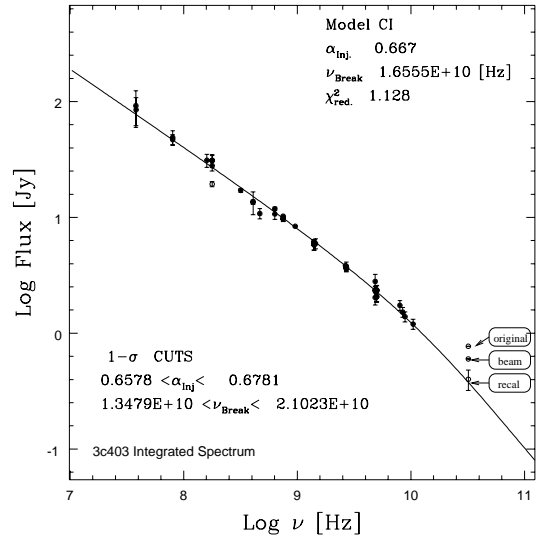


FIGURE 6.46— Integrated spectrum of 3C403. The datapoints have been compiled from the literature and have been supplemented with fluxes from own observations. The solid line represents the best fitting model (CI). The fit results and errors are marked on the plot. The open circles indicate that this datapoint has been flagged during the fitting procedure. At 32 GHz we show the original flux, the flux after correcting for the beam size, and the flux after recalibration.

map exceeds the assumed default  $30''$ . This might occur because of the poor beam and pointing characteristics at 32 GHz during the period of observation (see Sect. 3.1). To test the impact of an enlarged beam the HPBW of the two brightest source components (associated with the hotspots) of 3C403 have been determined and compared to that of the smoothed 1.5 GHz and 8.4 GHz images. We have found the beam size to be around  $34''$  which causes a flux correction of 28%. However, this correction is still insufficient to bring the 32 GHz datapoint into agreement with the other datasets. In fact still *no* spectral model at all is consistent with the 32 GHz

flux. We therefore conclude that the 32 GHz data must as well suffer from severe miscalibration. The integrated spectrum indicates a necessary flux correction of 50%. In order to investigate the possibility of an erroneous calibration we have applied the flux correction and have extracted spectra in various source regions. To better constrain the spectral fits we have first performed these tests at a fairly low resolution of  $69''$  in order to be able to include the 10.45 GHz data. Spectra with the corrected 32 GHz flux are displayed in Fig. 6.47. At  $69''$  resolution the source is only slightly resolved. Therefore we have chosen a CI-model for the spectral fitting procedure (which also resulted in the lowest  $\chi^2$  values). The 32 GHz datapoints have been flagged and the injection index has been fixed to  $\alpha_{inj} = -0.65$  as indicated by the integrated spectrum. Apparently the flux correction brings the 32 GHz data in good agreement with the model. Even though a meticulous re-inspection of the 32 GHz data has not revealed no evidence for a miscalibration we conclude that nevertheless it is the most likely explanation for the flux offset. Because of possible other problems with this dataset we have pursued the most conservative approach and have excluded the 32 GHz data entirely from the spectral analysis.

The spectral index map between 1.45 GHz and 8.35 GHz at a resolution of  $4''5$  resolution is displayed in Fig. ???. The steepest spectrum is coincident with the hotspot areas of the primary lobes. This can be more clearly seen in Fig. 6.49 which displays the trend of the spectral index along the east→south and west→north lobes. Close to the core (regions 2 & 3) the spectrum becomes flatter but then again steepens towards the tips of the secondary lobes. Most interestingly the flat spectrum areas coincide with regions of high fractional polarization (region 3 in the north lobe; region 3 & 4 in the south lobe). Possibly these areas are locations of strong shocks that reaccelerate the particles and thus lead to the apparent flattening of the synchrotron spectrum. One should note however that the spectral in-

dices in these areas are rather typical for the lobes of radio galaxies. More unusual are the steep spectra at the tips of the primary lobes. This is reminiscent of what has been observed in 3C223.1. The apparent spectral reversal can be understood if the reorientation event in 3C403 is ongoing or has ended very recently. The realigned jet would have to drill a new cavity in the dense ISM of the host galaxy which would lead to enhanced radiation losses in the hotspots.

Break-frequencies have been derived using the two-point spectral index between 1.5 GHz and 8.4 GHz. As was discussed in Sect. 6.3 this method depends heavily on the assumed value of  $\alpha_{inj}$ . In the case of 3C403  $\alpha_{inj}$  can be determined with high accuracy ( $\pm 1.7\%$ ) from the integrated spectrum thus yielding reasonably well constrained break-frequencies and ages. The minimum magnetic fields and calculated spectral ages of 3C403 are listed in Tab. 6.9. There is a gradient in magnetic fields from the primary ( $> 10\mu G$ ) towards the secondary lobes ( $\sim 5\mu G$ ). The calculated spectral ages along the east→south and west→north lobes are plotted in Fig. 6.50. The overall inferred ages are low ( $< 10\text{Myr}$ ) everywhere in 3C403. Also there is a clear age gradient from the active lobes towards the secondary lobes, even though the absolute difference in spectral age between these regions is only  $\approx 5\text{Myr}$ .



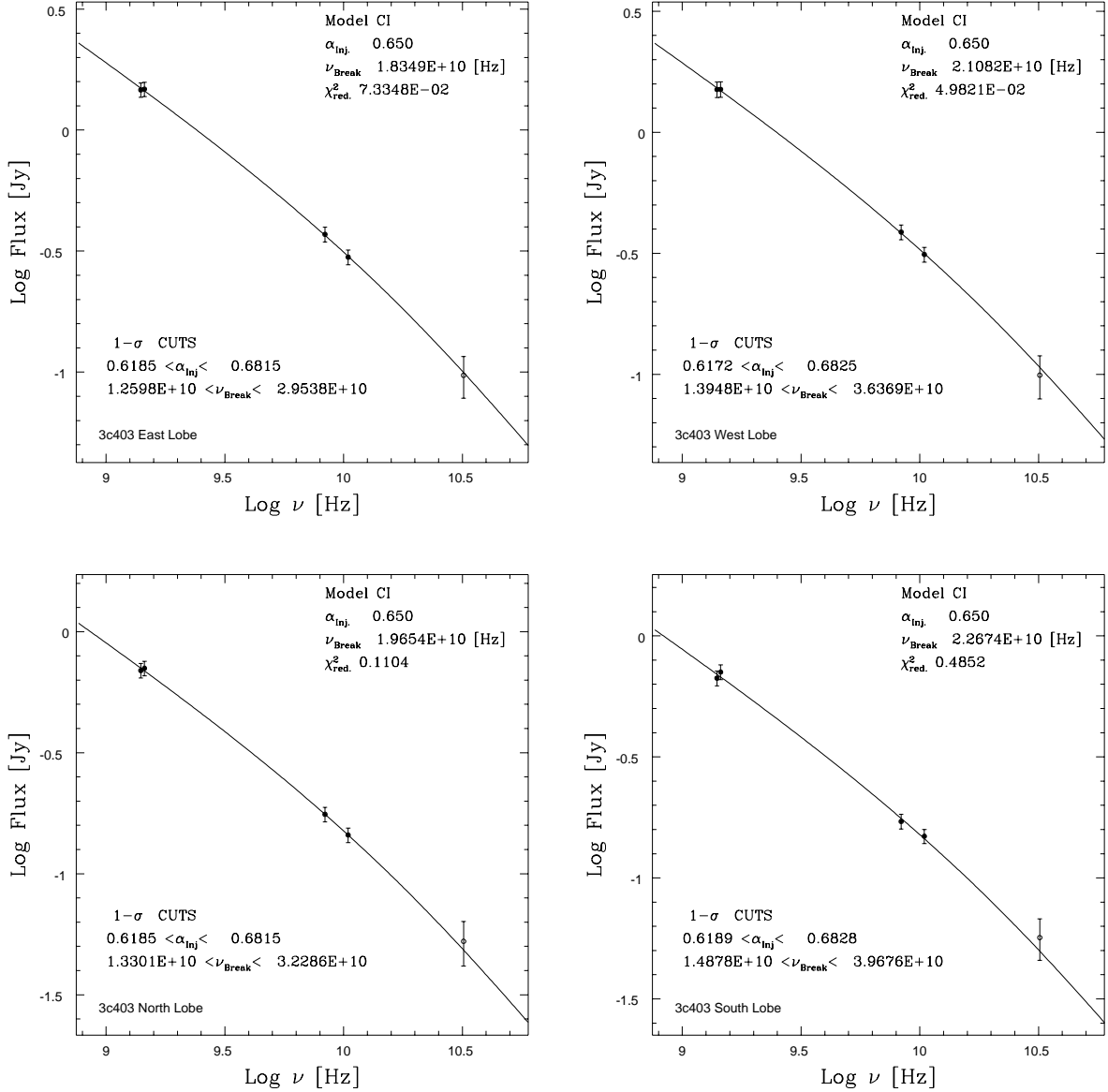


FIGURE 6.47— Spectra of the eastern (top left) and western (top right) active lobes and the northern (bottom left) and southern (bottom right) secondary lobes of 3C403. The solid lines represent the best fitting model. The fit results and errors can be found in the plot legend. Datapoints marked by open circles have been flagged for the fitting procedure. The displayed 32 GHz fluxes have been rescaled as described in the text. The injection index has been fixed to  $\alpha_{inj} = -0.65$  as indicated by fit to the integrated spectrum.

Lobe	Region	Luminosity [erg/s]	$U_{min}$ [erg]	$u_{min}$ [erg/cm <sup>3</sup> ]	$B_{min}$ [ $\mu$ G]	$t_{syn}$ [Myr]	$t_{max}$ [Myr]
east → south	1	$1.3 \times 10^{42}$	$4.2 \times 10^{57}$	$1.3 \times 10^{-11}$	11.9	3.9	16.2
	2	$3.3 \times 10^{41}$	$1.6 \times 10^{57}$	$6.4 \times 10^{-12}$	8.3	4.0	10.6
	3	$2.3 \times 10^{41}$	$1.1 \times 10^{57}$	$6.2 \times 10^{-12}$	8.2	3.9	9.9
	4	$1.8 \times 10^{41}$	$2.1 \times 10^{57}$	$1.8 \times 10^{-12}$	4.4	6.7	9.6
	5	$2.8 \times 10^{41}$	$3.6 \times 10^{57}$	$1.9 \times 10^{-12}$	4.5	9.9	14.4
	6	$9.4 \times 10^{40}$	$1.2 \times 10^{57}$	$2.0 \times 10^{-12}$	4.6	9.2	13.7
west → north	1	$1.8 \times 10^{42}$	$5.1 \times 10^{57}$	$1.6 \times 10^{-11}$	13.0	3.3	15.2
	2	$4.8 \times 10^{41}$	$3.1 \times 10^{57}$	$4.0 \times 10^{-12}$	6.6	4.7	9.6
	3	$2.8 \times 10^{41}$	$2.8 \times 10^{57}$	$2.0 \times 10^{-12}$	4.6	3.1	4.6
	4	$2.0 \times 10^{41}$	$2.7 \times 10^{57}$	$1.6 \times 10^{-12}$	4.1	8.3	11.4
	5	$2.1 \times 10^{41}$	$2.4 \times 10^{57}$	$2.4 \times 10^{-12}$	4.9	7.8	12.0
	6	$8.8 \times 10^{40}$	$8.8 \times 10^{56}$	$2.5 \times 10^{-12}$	5.2	8.6	13.9

TABLE 6.9— Source properties of 3C403.

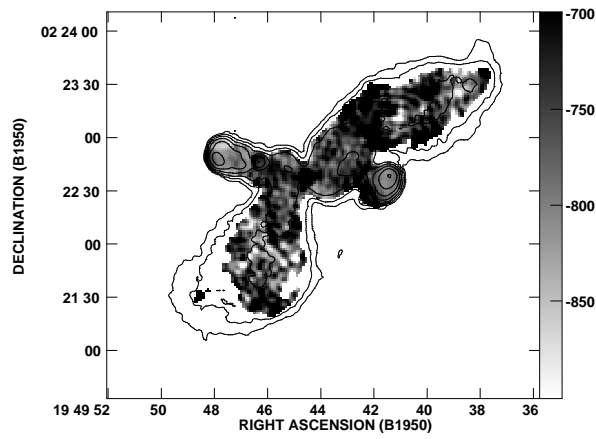


FIGURE 6.48— Spectral index map between 1.45 GHz and 8.35 GHz for 3C403.

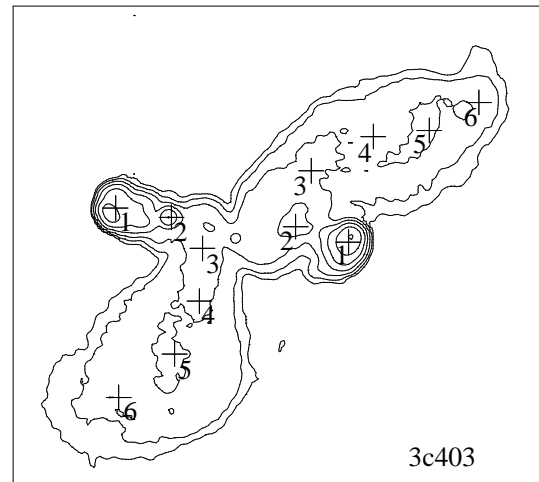
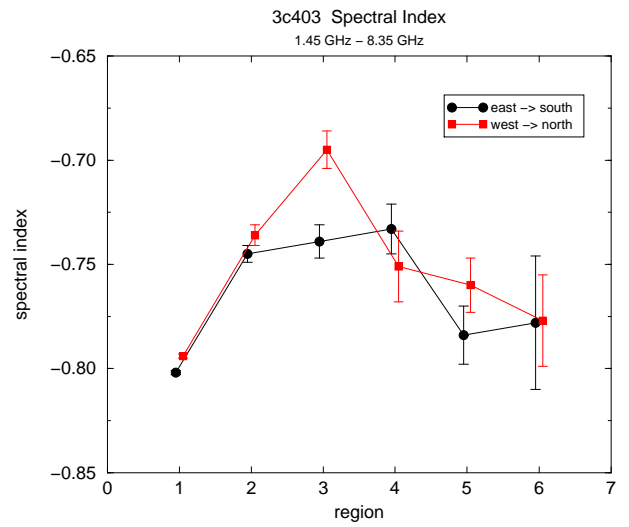


FIGURE 6.49— Trend of the spectral index (upper panel) along east→south and west→north lobes of 3C403. Fluxes have been extracted in 14×14 pixel boxes centered on the positions marked by crosses in the finding chart (lower panel).

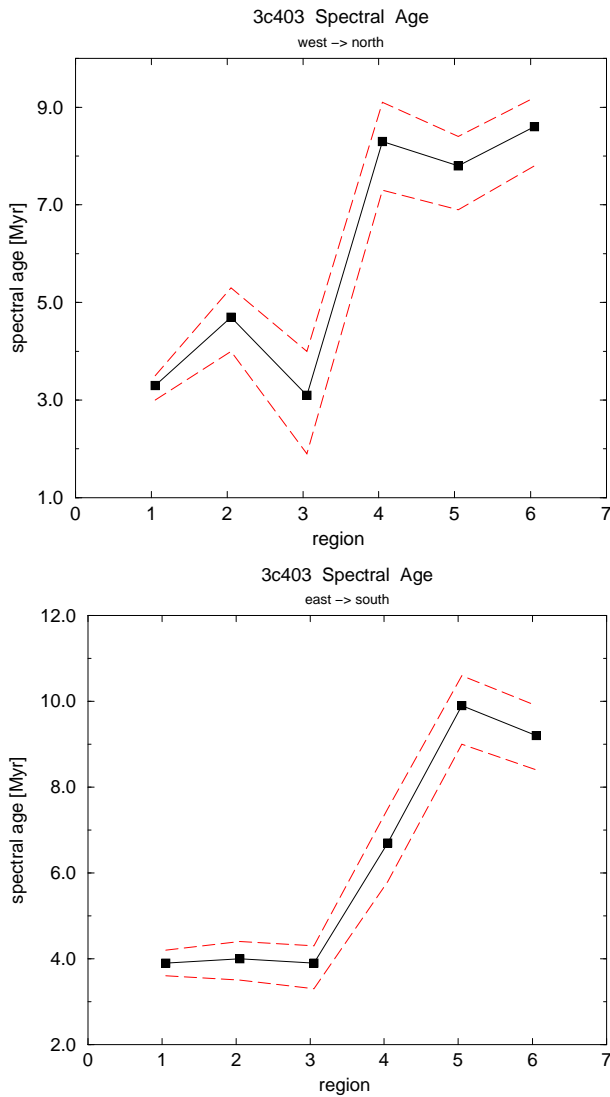


FIGURE 6.50— Trend of the spectral age along the transition line from west→north (upper panel) and east→south (lower panel). The relevant source regions are the same as marked in Fig. 6.49. The break frequencies have been derived from the two-point spectral index for a JP spectrum assuming  $\alpha_{inj} = -0.667$ . The dashed lines correspond to the spectral ages calculated for the upper ( $\alpha_{inj} = -0.678$ ) and lower ( $\alpha_{inj} = -0.658$ ) limit of the injection index as derived from the fit to the integrated spectrum.

## 6.6 Summary

### *Magnetic Fields*

We have derived minimum magnetic fields for all nine X-shaped sources. Typical values of  $B_{min}$  are of the order of a few  $\mu\text{G}$ . The highest minimum field ( $17.7\mu\text{G}$ ) has been found in 3C52 coincident with its northern hotspot. The lowest fields ( $< 1\mu\text{G}$ ) are located at the secondary lobe tips of B2 0828+32. In most cases there is a clear gradient of  $B_{min}$  from the primary towards the tips of the secondary lobes. The only exceptions are 3C315 and 4C12.03 (south lobe) where the highest fields were observed in regions in between the primary and secondary lobes. Typically the derived magnetic fields are a factor of 2-3 higher in the primary lobes as compared to the tips of the secondary lobes. In nearly all sources the trend of  $B_{min}$  is symmetric for the two lobe systems. An exception is 3C52 which has a considerably higher field strength at the northern hotspot as compared to its southern counterpart.

### *Spectral Index*

Most of the X-shaped sources of this sample exhibit a gradual decrease in spectral index from the primary towards the secondary lobes. Clear exceptions are 3C223.1 and 3C403. Both sources exhibit the steepest spectra at the hotspots with unusually low spectral indices of  $\alpha \approx -0.8$ . The reason for this is unknown. Either reacceleration occurs in the secondary lobes that creates a flatter spectrum with respect to the primary lobes or the radiation losses are enhanced in the hotspot regions. This can be understood in the frame of the reorientation models if the jet reorientation is ongoing or has finished very recently. The reoriented jet has to penetrate into the ISM of the host in order to drill a new lobe channel. Similar to what has been reported for Cygnus A (Barthel & Arnaud 1996) the confinement of the ambient medium would lead to increased synchrotron losses. The overall low ages inferred for 3C403 and 3C223.1 are consistent with this idea. It is however un-

clear why a similar effect has not been observed in NGC 326, which is located in a relatively denser medium and is even younger than 3C223.1 and 3C403.

### *Spectral Ages*

Spectral ages have been calculated for the sample of X-shaped sources. For most objects there is a trend of increasing ages from the primary towards the secondary lobes which is consistent with the reorientation scenarios. It should be noted however that some of the age calculations carry large uncertainties due to the partly poor quality of the available data. The youngest structures are the primary lobes of NGC 326, 3C223.1 and 3C403. Most interestingly these are also the sources having the shortest lobe lengths. Such a finding is expected in the frame of jet reorientation scenario. Young primary lobes indicate ongoing or recent realignment of the jet. After realignment we expect a short lobe due to its confinement by the dense ISM until a new channel has been drilled.

The oldest structures are the secondary lobes of B2 0828+32 ( $t \approx 40$  Myr). Note that this source is also the most extended of all known X-shaped sources.

The overall spectral ages of the secondary lobes of X-shaped sources are similar to the inferred ages of other radio galaxies (e.g. Alexander & Leahy 1987, Carilli et al. 1991, Klein et al. 1995).



# Formation of X-shaped Radio Sources

## Part II: Revisited

### 7.1 Reorientation and Flow Speeds

As has been outlined in Chap. 5 the timescales and speeds of the formation process provide a means to distinguish between the various proposed mechanisms. In case of the environmental formation processes – backflow and buoyancy – the requirement of subsonic backflows provides a limit to the flow speeds of the plasma from the hotspots towards the tips of the secondary lobes. In case of the reorientation models on the other hand the theory makes rigid predictions about the timescales of reorientation. The spectral ages derived in the previous chapter now allow us to actually calculate the flow and reorientation speeds. The speeds have been derived by dividing the flow distance by the corresponding spectral age. However, it is not obvious how to best estimate the correct flow distance. Because radio sources evolve with their hotspots propagating into the ISM/IGM it is not quite clear where matter having a particular spectral age was originally released by the hotspots. For matter now located at the tips of the secondary lobes there are two extreme cases:

- a) the matter was released close to the radio core. Then the flow distance is simply the length of the secondary lobe.

- b) the matter was released close to the current location of the hotspots. The flow distance is the combined length of the primary plus the secondary lobe.

These are the extreme cases and consequently yield lower and upper limits of the true flow velocities. In the following, flow speeds have been calculated for both scenarios by dividing the relevant flow distance by the spectral age measured at the tips of the secondary lobes. The parameters and calculated speeds are listed in Tab. 7.2. As can be seen the derived flow speeds spawn a range of a few  $10^6$  to a few  $10^7$  m/s. The distribution of speeds is displayed in Fig. 7.1 (scenario a) and Fig. 7.2 (scenario b). The average speed is marked in the histograms by arrows.

#### *Projection effects*

The calculation of speeds can in principle be strongly affected by projection effects. The radio maps allow the determination of *projected* lobe lengths only. Projection will thus show up in the speed calculations as a  $\cos i$  dependency of the lobe length (where  $i$  denotes the inclination with respect to the plane of the sky). The spectral ages on the other hand can be expected to be largely unaffected by projection except for the extreme case of large inclination angles  $i$ . For large inclina-

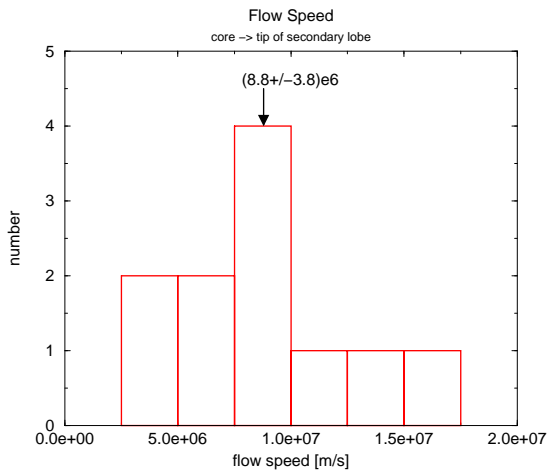


FIGURE 7.1— Histogram of the flow speed calculated by dividing the lengths of the secondary lobes by the spectral ages obtained at the tips of the lobes. The histogram contains only the cases in which speeds could be derived with errors smaller than one bin-width ( $2.5 \times 10^6$  m/s). The average speed is  $8.8 \times 10^6$  m/s with a standard deviation of  $3.8 \times 10^6$  m/s.

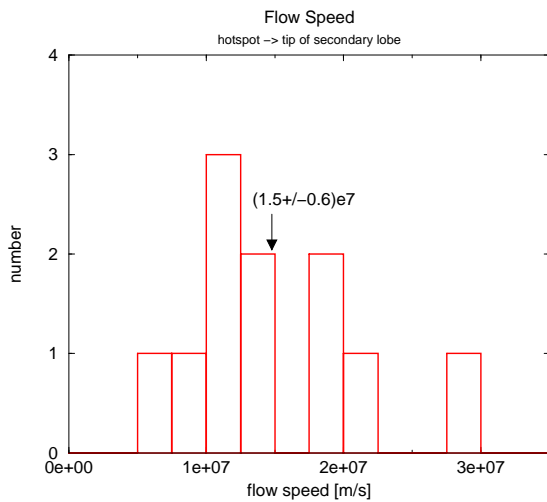


FIGURE 7.2— As in Fig. 7.1 but with the flow distance assumed to be the length of the secondary plus the active lobes. The average speed is  $1.5 \times 10^7$  m/s with a standard deviation of  $6.0 \times 10^6$  m/s

tions the synchrotron radiation is integrated along very long path lengths through the lobes and comprises radiation from particle populations in various stages of synchrotron ageing. Therefore spectral fits using JP or KP models would not accurately determine the true particle ages. However, sources having a very large secondary lobe inclination will also be

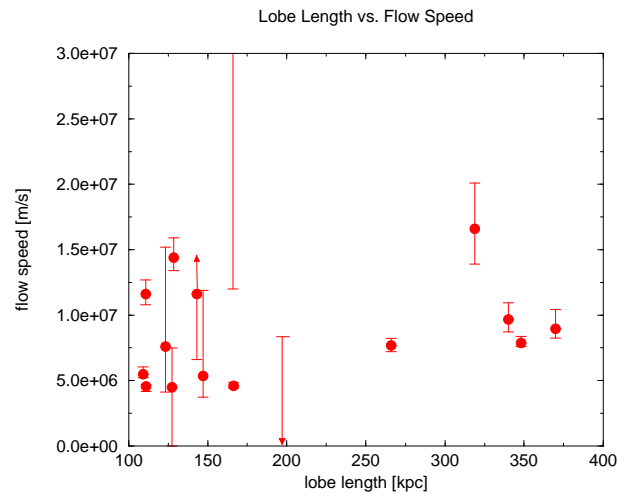


FIGURE 7.3— Flow speeds plotted vs. the lobe length. In case projection effects would strongly affect the derived flow speeds this should manifest itself in a trend of lower speeds to preferentially occur for short (projected) lobe lengths. However, no such trend is visible indicating that the fairly large range of speeds cannot be attributed to projection effects but must be intrinsic.

strongly affected by the selection effects outlined in Chap. 2 and consequently would have a low chance of being included in this sample of X-shaped sources. Assuming that all X-shaped sources have roughly the same intrinsic flow speed the imprint of projection should manifest itself in a dependency of the calculated speeds on the lobe length. In particular one should find a trend of apparently lower speeds to occur in the case of shorter lobe lengths because a good fraction of these lobes might appear short only due to projection effects. Figure 7.3 presents a plot of the lobe lengths vs. the calculated speeds. Even though the number of sources is small and the errors are quite large there seems to be no such trend in the studied sample of sources. We therefore conclude that the broad distribution of speeds of X-shaped sources cannot be caused mainly by projection effects but must be in most part intrinsic.

### Conclusions

The derived speeds are even in the most conservative case of assuming the shortest possible lobe lengths close to 10% of the speed



of light. Such high speeds pose a difficult problem for the backflow and buoyancy models in which an upper limit to the flow velocity is imposed by the sound speed. It has been demonstrated in Chap. 5 that the magnetosonic sound speed can be as high as a few percent of the speed of light with typical values of  $6 \times 10^6$  m/s. For the sample studied in this thesis the *average* value is already somewhat higher than this and individual sources lay considerably above. Assuming longer lobe lengths due to projection the situation becomes even more unfavorable. Also one should keep in mind that flows with velocities close to the magnetosonic sound speed might occur in the magnetized, low-density environment of the lobe cavity. When forming the secondary lobes the backflowing or buoyant matter has to eventually leave the lobe cavity and will have to penetrate into the denser ISM/IGM. Consequently ram-pressure effects should decrease the flow speed considerably and we can expect velocities in the secondary lobes close to the thermal sound speed which is about one to two orders of magnitude below the magnetosonic sound speed. We thus conclude that the speeds derived on the basis of spectral ages are inconsistent with the requirement of subsonic flows.

In the case of jet reorientation one is not faced with the sound speed limit because the secondary lobes are not formed by a flow of matter but consist of material left behind by a receding jet. Instead, the predicted reorientation timescales have to be compared with the derived spectral ages. The reorientation timescale  $t_{re}$  can be estimated from the spectral analysis since it is approximately equal to the age at the tips of the secondary lobe  $t_{tip}$ . This is illustrated in Fig. 7.4 which sketches the evolution of a reorientation event. When the reorientation of the radio jets has just been completed  $t_{tip}$  is *exactly* equal to  $t_{re}$ . This is not true anymore during later stages of the source evolution when  $t_{tip}$  will become larger than  $t_{re}$ . In this respect  $t_{tip}$  provides only an upper limit of the reorientation timescale. However there is a strong selection bias that

works in a way as to ensure that  $t_{tip}$  is always comparable to the reorientation timescale in the studied sample of X-shaped sources. Selection effects let us pick out such sources that are not much older than the reorientation event. Radiation losses will make the secondary lobes fade away quite rapidly once they are not being fed with fresh particles anymore. This selection bias will be studied in greater detail in the following chapter. It is worth to note again that  $t_{tip}$  provides an upper limit to the reorientation timescale. As has been discussed in Chap. 5 the two reorientation models – BBH merging and misaligned accretion – both predict reorientation timescales in the order of  $10^6$  to a few  $10^7$  years. Inspecting the spectral ages obtained at the tips of the secondary lobes listed in Tab. 7.2 we find them to span the range from  $8 \times 10^6$  to  $4 \times 10^7$  years which is in excellent agreement with the theoretical predictions.

## 7.2 Reorientation Angle

Very likely the peculiar morphology of X-shaped sources has been caused by a reorientation of their radio jets. The amount of change in orientation between the original and the realigned radio jets is visible as the angle between the primary and secondary lobes. Due to projection effects this *intrinsic* reorientation angle  $\phi$  cannot be inferred directly from the radio images. Instead only the *projected* reorientation angle  $\phi'$  can be measured directly. As the 3D-orientation of a particular X-shaped source is unknown it is impossible to re-construct its intrinsic reorientation angle. However, if projected angles for a larger number of sources exist then one can employ statistical methods to estimate the most likely distribution of intrinsic angles. The idea is to construct a theoretical distribution of projected angles for an ensemble of X-shaped sources having intrinsic angles between  $\phi_1$  and  $\phi_2$ . This theoretical distribution can then be compared with the observed distribution of projected angles in order to find the best fitting values of  $\phi_1$  and  $\phi_2$ . In order to obtain such a theoretical  $\phi'$  distribution it is neces-

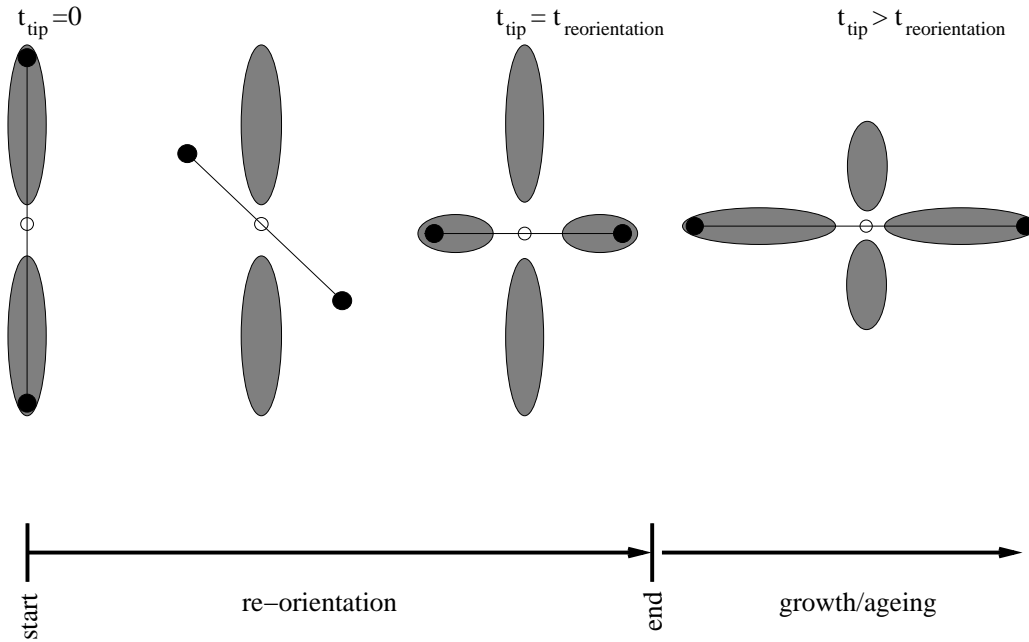


FIGURE 7.4— Sketch of the evolution of a jet reorientation event. The open circle depicts the radio core with the jet emerging along the solid line. The current hotspots are marked by filled circles and are embedded in the radio lobes (shaded ellipses). At the onset of the reorientation process the observed age at the tips of the lobes is  $t_{tip}=0$ . The jet then swings and finally becomes realigned in a new direction. The age at the tip of the secondary lobe is then equal to the reorientation timescale  $t_{re}$ . In the following, the active lobes will propagate into the ISM/IGM and become longer whereas the secondary lobes will fade away and become shorter. During this stage the observed  $t_{tip}$  will be somewhat longer than  $t_{re}$ .

sary to first construct a model representation of X-shaped sources. The source model is then projected to all possible viewing angles to obtain the expected distribution of projected angles  $\phi'$  corresponding to the intrinsic angle  $\phi$ .

#### The Model

We use a simplified model to describe an X-shaped source. In this model the source consists of two pairs of linear radio lobes having the full lengths (hotspot to hotspot)  $l_p$  and  $l_s$  for the primary and secondary lobes respectively (see Fig. 7.5). The primary and secondary lobes are oriented at the intrinsic (reorientation) angle  $\phi$ . We have defined the primary lobe to be oriented along the x-axis of the initial (un-projected) coordinate system. The z-axis defines the direction towards the observer. The primary and secondary lobes have been represented by the corresponding vectors  $\vec{p}$  and  $\vec{s}$ . The angle  $\phi$  is located in the

xy-plane.

$$\vec{p} = \begin{pmatrix} l_p/2 \\ 0 \\ 0 \end{pmatrix} \quad \vec{s} = \begin{pmatrix} l_s/2 \cdot \cos \phi \\ l_s/2 \cdot \sin \phi \\ 0 \end{pmatrix}$$

The projection to a different line-of-sight has been realized through an Euler-transformation in the following way (see Fig. 7.6):

- 1) a rotation about the initial x-axis (angle  $\beta$ ) which performs the following transformation:

$$\begin{aligned} x &\rightarrow x' (= x) \\ y &\rightarrow y' \\ z &\rightarrow z' \end{aligned}$$

- 2) a rotation about the  $z'$ -axis (angle  $\gamma$ ):

$$\begin{aligned} x' &\rightarrow x'' \\ y' &\rightarrow y'' \\ z' &\rightarrow z'' (= z') \end{aligned}$$

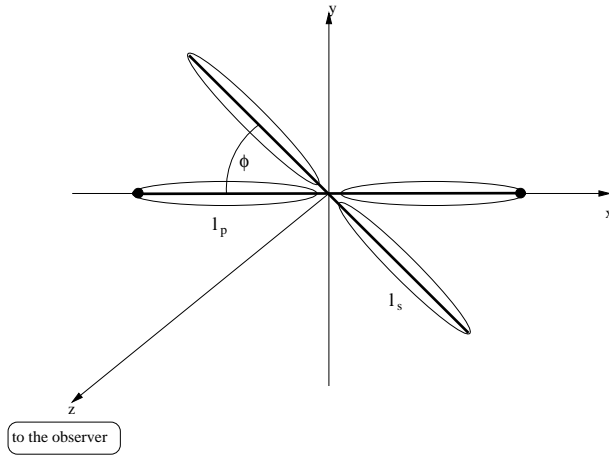


FIGURE 7.5— Sketch of the model used to derive the distribution of projected angles. In this simplified model an X-shaped source consists of two linear lobes of lengths  $l_p$  and  $l_s$  for the primary and secondary lobes respectively. The lobes are oriented at the intrinsic angle  $\phi$  and are located in the  $xy$ -plane. The line-of-sight to the observer is along the  $z$ -axis.

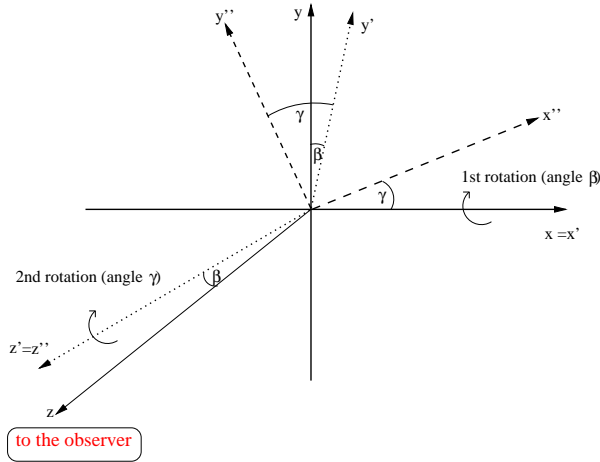


FIGURE 7.6— Sketch of the transformation used to project the X-shaped source model to different lines-of-sight. The first rotation (angle  $\beta$ ) is executed around the initial  $x$ -axis. Afterwards a second rotation (angle  $\gamma$ ) is performed around the  $z'$ -axis. The original  $z$ -axis is coincident with the line-of-sight to the observer.

Applying the transformation yields:

$$\begin{aligned} \vec{p} &\rightarrow \vec{p}' \\ \vec{s} &\rightarrow \vec{s}' \end{aligned}$$

with the lengths of the transformed vectors being  $l'_p$  and  $l'_s$ .

$$l'_p = 2 \cdot \sqrt{p'^2_x + p'^2_y}$$

$$l'_s = 2 \cdot \sqrt{s'^2_x + s'^2_y}$$

The projected source angle  $\phi'$  is then calculated as:

$$\phi' = \arccos \left( \frac{p'_x s'_x + p'_y s'_y}{l'_p/2 \cdot l'_s/2} \right)$$

The inclination with respect to the plane of the sky ( $xy$ -plane) is given as:

$$i = \arctan \frac{p'_z}{p'_x}$$

### Projected Angle Distribution

The outlined model allows to obtain the theoretical distribution of  $\phi'$  for a randomly oriented sample of X-shaped sources having a particular intrinsic source angle  $\phi$ . This has been realized by projecting the model to all lines-of-sight in the range:

$$\begin{aligned} 0^\circ < \beta < 90^\circ \\ 0^\circ < \gamma < 180^\circ \end{aligned}$$

However, this distribution cannot be compared “as is” with the observed angle distribution. In many cases a particular viewing angle will result in a projected source geometry that does not have X-shaped morphology any longer. Viewing angles that are affected by such selection effects (see Sect. 2.1) thus have to be excluded from the theoretical  $\phi'$  distribution before it can be compared with the observed distribution of projected angles. The following criteria have been used to take selection effects into account:

- $\phi' < 20^\circ$  or  $\phi' > 160^\circ$   
if the projected angle is too small or too large the emission of the secondary lobes will blend into the primary lobe. Hence, the existence of secondary lobes in such sources would be hidden.
- $i > 40^\circ$   
if the inclination of the jet with respect to plain of the sky becomes too large then

relativistic beaming will increase the dynamic range between primary and secondary lobes making the detection of the secondary lobes unlikely.

- $l'_s < 0.3 \cdot l'_p$

in cases where the secondary lobes will be shortened by projection effects to an extent where they will be considerably shorter than the (projected) primary lobes the source would not be classified as being X-shaped anymore.

The impact of these selection effects on the projected angle distribution is demonstrated in Fig. 7.7 (for the case of  $\phi=50^\circ$ ). Individual plots display the projected angle  $\phi'$  as a function of  $\beta$  and  $\gamma$ . Valid viewing angles (in the sense that they are not excluded due to selection effects) are marked in the plots by superimposed green box symbols ( $\Delta$ ). The full collection of figures corresponding to other values of  $\phi$  can be found in Appendix B.

After compensating for the selection effects we can finally construct the theoretical  $\phi'$  distribution that corresponds to a particular intrinsic angle  $\phi$ . Figure 7.8 displays the  $\phi'$  distribution for  $\phi=50^\circ$  (plots for other values of  $\phi$  are listed in Appendix B). As can be seen the distributions are always peaked around the value of the intrinsic angle. A measure for the sharpness of the distribution is given by the P[10] and P[20] parameters that give the cumulative probability to find a projected angle  $\phi'$  within  $\pm 10^\circ$  or  $\pm 20^\circ$  of the peak, respectively. The  $f_s$  value gives the fraction of valid viewing angles. Table 7.1 lists these parameters for  $10^\circ < \phi < 170^\circ$ . As documented by the  $f_s$  parameter selection effects have a large impact on the  $\phi'$  distribution only for angles close to  $0^\circ$  or  $180^\circ$ . In the extreme case of  $\phi=10^\circ$ , or  $\phi=170^\circ$  only a few percent of the lines-of-sight pass the selection criteria, whereas for  $\phi=90^\circ$  this fraction rises to 80%. An important thing to note is that the distribution of projected angles is always peaked around the initial intrinsic angle  $\phi$ . It is sharpest for small and large  $\phi$ , but even in the 'worst' case of  $\phi=90^\circ$  the probability to find a projected angle between  $80^\circ$  and  $100^\circ$  is still 65%.

$\phi$	P[10]	P[20]	$f_s$
$10^\circ$	0.92	1.0	0.01
$20^\circ$	0.98	0.99	0.26
$30^\circ$	0.97	0.99	0.64
$40^\circ$	0.84	1.0	0.72
$50^\circ$	0.78	0.91	0.74
$60^\circ$	0.73	0.86	0.76
$70^\circ$	0.70	0.82	0.77
$80^\circ$	0.68	0.79	0.78
$90^\circ$	0.65	0.76	0.80
$100^\circ$	0.65	0.76	0.79
$110^\circ$	0.66	0.78	0.79
$120^\circ$	0.70	0.81	0.78
$130^\circ$	0.74	0.87	0.75
$140^\circ$	0.84	0.90	0.74
$150^\circ$	0.86	0.91	0.67
$160^\circ$	0.91	0.93	0.33
$170^\circ$	0.70	0.83	0.02

TABLE 7.1— Table lists the P[10], P[20] and  $f_s$  parameters of the  $\phi'$  distribution as a function of the intrinsic angle  $\phi$ .

### Comparison with Observations

The aim is to obtain some idea about the most likely distribution of intrinsic angles  $\phi$  of the observed sample of X-shaped sources. This is done by creating a theoretical distribution of projected angles  $\phi'_{th}$  that corresponds to a sample of sources having intrinsic angles in the range from  $\phi_b$  to  $\phi_e$ . This theoretical distribution can then be compared to the observed  $\phi'_{obs}$  distribution in order to find the distribution that fits the observations best. The combined theoretical  $\phi'_{th}$  distribution is obtained by integrating the individual  $\phi'$  distributions (corresponding to one particular  $\phi$ ) over all angles between  $\phi_b$  and  $\phi_e$ . Examples of  $\phi'_{th}$  for different configurations of  $\phi_b$  and  $\phi_e$  can be found in Fig. 7.9. The  $\phi'_{th}$  distribution is represented by the solid line. The observed distribution of projected angles  $\phi'_{obs}$  is superimposed (dashed line).

The observed projected angles have been obtained from the highest resolution radio maps. The angle has been measured between the lines connecting core→hotspot and

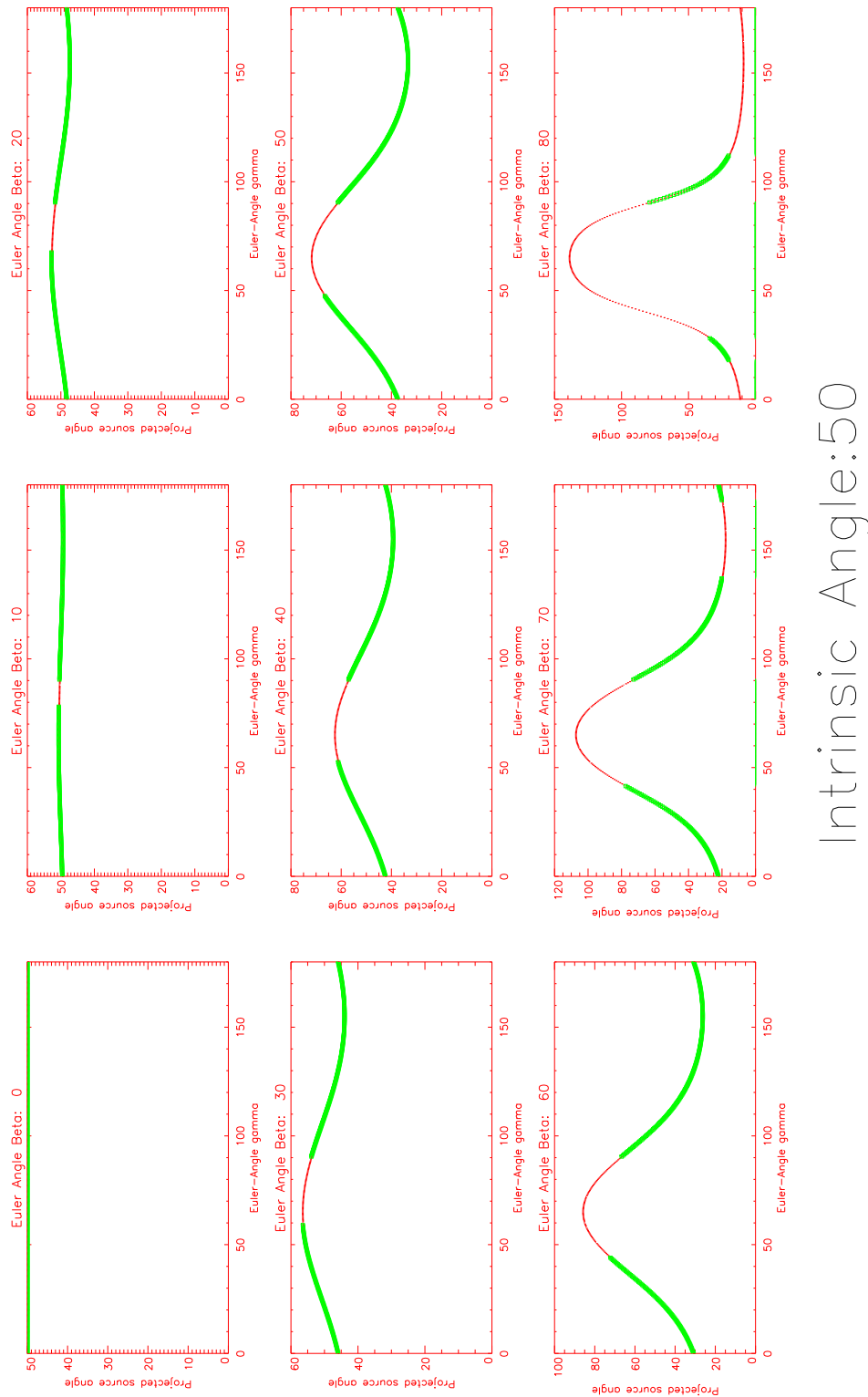


FIGURE 7.7— Plots of the projected angle  $\phi'$  as a function of the transformation angles  $\beta$  and  $\gamma$  for an intrinsic source angle of  $\phi=50^\circ$ . Each individual plot corresponds to a specific angle  $\beta$  as indicated in the plot title. Angles superimposed by green  $\Delta$  symbols represent viewing angles that would pass the selection criteria outlined above.

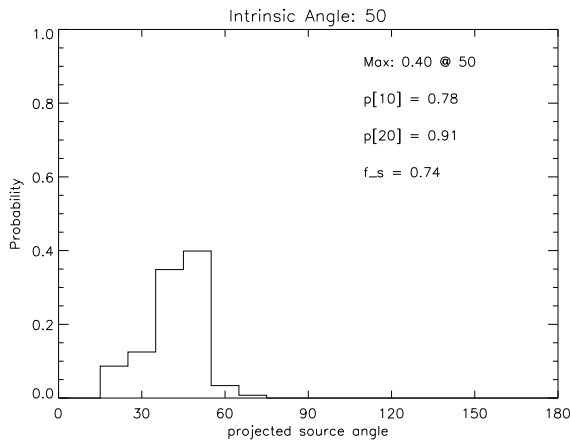


FIGURE 7.8— Histogram showing the expected distribution of projected angles  $\phi'$  for a randomly oriented sample of X-shaped sources having an intrinsic angle of  $\phi=50^\circ$ . The probabilities have been normalized in order to yield a total probability of unity over all viewing angles. Marked on the plot the maximum probability is given and the angle-bin where it occurs. The  $P[10]$  and  $P[20]$  parameters give the cumulative probability to observe a projected angle  $\phi'$  within  $\pm 10^\circ$ , or  $\pm 20^\circ$  of the maximum respectively.

core  $\rightarrow$  secondary lobe tip. Whereas the core  $\rightarrow$  hotspot connection can be easily found, the definition of the secondary lobe tip is somewhat arbitrary. Therefore, we assume a typical error of  $\pm 10\%$  in measuring the value of  $\phi'_{obs}$ . 3C379.1 has been excluded from the sample entirely. Its secondary lobes are too short to accurately determine the projected source angle. The observed distribution is rather narrow and is peaked at around  $50^\circ$ . It is important to note, that the absence of angles  $\phi'_{obs} > 90^\circ$  is *not* due to a symmetry effect. In all sources the morphology indicates a clear association of one of the secondary lobes with one of the primary lobes. For this reason, projected angles in the range from  $0^\circ$  to  $180^\circ$  could occur and would be distinguishable. From Fig. 7.9 it is obvious that none of the theoretical distributions fit  $\phi'_{obs}$  very well. As was outlined above the individual  $\phi'$  distributions tend to be narrowly peaked around the corresponding  $\phi$  value. We can therefore suspect that the wanted  $\phi'_{th}$  distribution will contain a rather narrow range of angles  $\phi$ . The distribution  $\phi'_{th}$  that fits the observed pro-

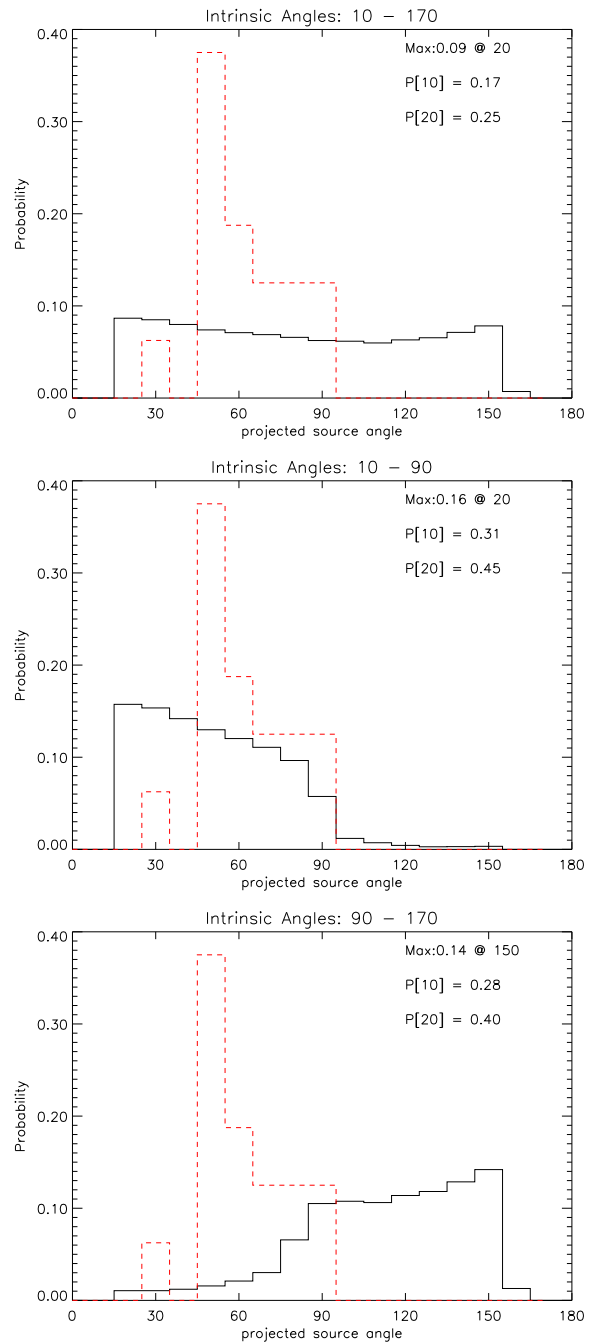


FIGURE 7.9— Distribution of projected angles  $\phi'$  for different configurations of  $\phi_b$  and  $\phi_e$ :  $10^\circ < \phi < 170^\circ$  (top),  $10^\circ < \phi < 90^\circ$  (middle), and  $90^\circ < \phi < 170^\circ$  (bottom). The solid line represents the theoretical  $\phi'$  distribution. The superimposed dashed line marks the observed distribution of projected angles. The two distributions have been normalized to have equal areas.

jected angle distribution best is displayed in Fig. 7.10. It was constructed with  $\phi_b=60^\circ$  and  $\phi_e=90^\circ$ .

### Conclusions

Even though the statistical errors are still quite large due to the small number of known X-shaped sources we have nevertheless obtained an idea about the most likely distribution of reorientation angles in the studied sample of X-shaped radio galaxies.

Most important: the distribution of intrinsic angles in the sample is rather narrow. The best fit was obtained for a range of  $60^\circ < \phi < 90^\circ$ . Inspecting Fig. 7.10 it is obvious that the fit does not reproduce the sharp peak of the  $\phi'_{obs}$  distribution. In the model outlined above we have used equal weighting for all angles between  $\phi_b$  and  $\phi_e$ . In order to better reproduce the peak at  $50^\circ$  it would be necessary to increase the weight of intrinsic angles around  $50^\circ$  to  $60^\circ$  with only a small contribution of large angles. The most likely reorientation angle of X-shaped sources therefore seems to lie in the regime of  $50^\circ$ - $60^\circ$ . However, a larger number of sources would be desirable in order to increase the statistics. In the light of the formation processes proposed for X-shaped sources such a narrow distribution of intrinsic angles cannot be understood easily.

In case of buoyancy one would expect a more homogeneous distribution of projected angles. The buoyant flow is directed along the gradi-

ent of maximum pressure. There is no obvious reason why pressure gradients in the ambient medium should preferentially occur in a direction of  $50^\circ$  with respect to the orientation of the radio jets.

Merging of a central BBH on the other hand should result in a reorientation angle that is defined by the spin vectors of the two black holes. The mechanism thus provides a simple explanation why no projected angles exceeding  $90^\circ$  have been observed in any of the X-shaped sources. The most extreme case of anti-parallel spins would result in a reorientation angle of  $90^\circ$ . On the other hand all BH spin orientations between  $0^\circ$  and  $180^\circ$  should occur with equal probabilities and therefore we would expect the  $\phi'$  distribution (accounting for selection effects) to be similar to the one displayed in Fig. 7.9 (middle). Either the selection effects at work have to be more severe or other processes during the BBH merger have impact on the spin orientation of the merged BH.

The situation in the case of misaligned matter accretion is more complicated. In principle the direction of the reoriented jet should be coincident with the angular momentum vector of the freshly deposited matter. Without assuming a preferred direction of angular momentum one would thus expect a  $\phi'$  distribution with an equal number of angles between  $0^\circ$  and  $180^\circ$  which is not the case. Much depends however on the details of the gas dynamics when it sinks to radii close to the accretion disk. Even though numerical models at present cannot predict the fate of the gas at these small radii it seems quite possible that the overall gas distribution of the host galaxy and the gravitational potential of the central stellar cluster can have influence on the dynamics of the accreted matter in such a way as to result in a preferred angular momentum direction.

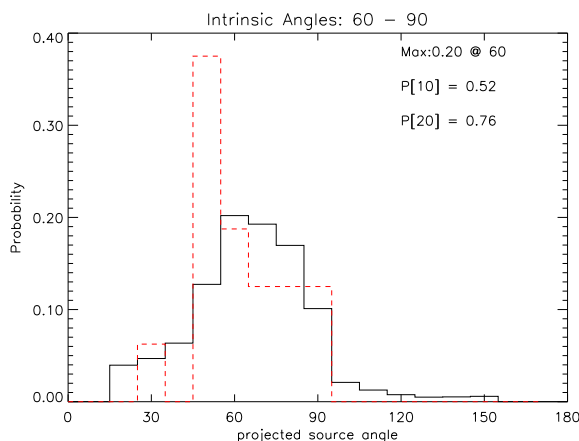


FIGURE 7.10— Best fitting  $\phi_{th}$  distribution (solid line). It was constructed with  $\phi_b=60^\circ$  and  $\phi_e=90^\circ$ . The superimposed histogram (dashed line) represents the observed distribution of projected angles.

### 7.3 Summary and Conclusions

On the basis of the intrinsic properties derived in this chapter – the reorientation angles and the reorientation timescales – we can

rule out the buoyancy and backflow scenarios as the primary formation processes of X-shaped radio sources. These mechanisms work on timescales that exceed the timespans inferred from the spectral analysis. Even in the case that spectral ages would provide vast underestimates of the true source ages the environmental formation models still lack any explanation for the observed distribution of the projected reorientation angles.

The jet realignment models – BBH mergers and matter accretion – work on timescales that are in excellent agreement with the derived reorientation timescales. The misaligned matter accretion is faced with the problem to reproduce the distribution of projected angles unless so far unknown mechanisms will roughly align the angular momentum of the accreted matter while it is sinking towards the accretion disk. From all proposed models BBH merging is in best agreement with the observations. It naturally explains the absence of projected angles exceeding  $90^\circ$  in the studied sample of X-shaped sources. However, at present it does not explain why the  $\phi'_{obs}$  distribution is so sharply peaked at around  $50^\circ$ .



Source	lobe length [kpc]		age [Myr]		speed [ $10^6$ m/s]				
	active lobe	secondary lobe			secondary		active + secondary		
4C12.03	232.8(n)	166.4(e)	266.0(w)	33.3(w)	34.8(e)	7.7 $\pm$ <sub>0.5</sub> <sup>0.5</sup> (w)	4.6 $\pm$ <sub>0.2</sub> <sup>0.2</sup> (e)	13.0 $\pm$ <sub>0.9</sub> <sup>0.9</sup> (w+s)	11.0 $\pm$ <sub>0.4</sub> <sup>0.6</sup> (e+n)
NGC 326	56.3(e)	68.3(w)	110.9 (n)	23.5 $\pm$ <sub>1.2</sub> <sup>0.7</sup> (n)	19.2 $\pm$ <sub>1.8</sub> <sup>0.9</sup> (s)	4.5 $\pm$ <sub>0.4</sub> <sup>0.1</sup> (n)	5.5 $\pm$ <sub>0.3</sub> <sup>0.6</sup> (s)	6.9 $\pm$ <sub>0.2</sub> <sup>0.4</sup> (n+e)	8.9 $\pm$ <sub>0.4</sub> <sup>0.9</sup> (s+w)
3C52	143.8(n)	147.9(s)	123.2(w)	15.7 $\pm$ <sub>15.7</sub> <sup>13.2</sup> (w)	27.4 $\pm$ <sub>11</sub> <sup>11</sup> (e)	7.6 $\pm$ <sub>3.5</sub> <sup>∞</sup> (w)	4.5 $\pm$ <sub>4.5</sub> <sup>3.9</sup> (e)	16.6 $\pm$ <sub>0.8</sub> <sup>∞</sup> (w+s)	9.5 $\pm$ <sub>9.5</sub> <sup>6.4</sup> (e+n)
3C136.1	220.0(w)	307.1(e)	318.8(n)	18.5 $\pm$ <sub>3.2</sub> <sup>3.6</sup> (n)	33.9 $\pm$ <sub>4</sub> <sup>3.7</sup> (s)	1.7 $\pm$ <sub>0.3</sub> <sup>0.4</sup> (n)	9.7 $\pm$ <sub>1.0</sub> <sup>1.3</sup> (s)	28.0 $\pm$ <sub>4.5</sub> <sup>5.9</sup> (n+w)	18.4 $\pm$ <sub>1.8</sub> <sup>2.4</sup> (s+e)
B2 0828+32	187.1(e)	182.8(w)	369.9(n)	39.8 $\pm$ <sub>5.6</sub> <sup>3.4</sup> (n)	42.6 $\pm$ <sub>2.6</sub> <sup>1.6</sup> (s)	9.0 $\pm$ <sub>0.7</sub> <sup>1.5</sup> (n)	7.9 $\pm$ <sub>0.3</sub> <sup>0.5</sup> (s)	13.5 $\pm$ <sub>1.1</sub> <sup>2.2</sup> (n+e)	12.0 $\pm$ <sub>0.4</sub> <sup>0.8</sup> (s+w)
3C223.1	96.1(n)	93.9(s)	165.9(w)	0.8 $\pm$ <sub>0.8</sub> <sup>13.0</sup> (w)	11.9 $\pm$ <sub>11.9</sub> <sup>9</sup> (e)	200 $\pm$ <sub>188</sub> <sup>∞</sup> (w)	11.6 $\pm$ <sub>5.0</sub> <sup>∞</sup> (e)	315 $\pm$ <sub>297</sub> <sup>∞</sup> (w+n)	19.2 $\pm$ <sub>8.3</sub> <sup>∞</sup> (e+s)
3C315	178.3(n)	181.1(s)	198.1(w)	< 22.7(w)	26.5 $\pm$ <sub>14.6</sub> <sup>11.5</sup> (e)	> 8.4(w)	5.4(e)	> 16.0(w+n)	11.9 $\pm$ <sub>3.6</sub> <sup>14.7</sup> (e+s)
3C403	60.8(e)	56.8(w)	128.4(n)	8.6 $\pm$ <sub>0.8</sub> <sup>0.6</sup> (n)	9.2 $\pm$ <sub>0.8</sub> <sup>0.7</sup> (s)	14.4 $\pm$ <sub>1.0</sub> <sup>1.5</sup> (n)	11.6 $\pm$ <sub>0.8</sub> <sup>1.1</sup> (s)	20.7 $\pm$ <sub>1.3</sub> <sup>2.2</sup> (n+w)	18.0 $\pm$ <sub>1.3</sub> <sup>1.7</sup> (s+e)

TABLE 7.2— Flow speeds of X-shaped radio galaxies. The speeds have been calculated by dividing the lobe length (listed in col. 2-5) by the spectral ages derived at the tips of the secondary lobes (col. 6 & 7). Speeds have been determined assuming two different flow paths: (a) the length of the secondary lobe (col. 8 & 9), and (b) the length of the secondary plus the corresponding active lobe (col. 10 & 11). The letters given in brackets denote the lobe name: e=east lobe, w=west lobe, s=south lobe, and n=north lobe.



# 8

---

## Jet Reorientation: A Common Event?

At this point we can conclude that the most likely formation process of X-shaped radio galaxies is reorientation of their radio jet axis. Whether this reorientation occurs because of merging binary black holes in the galactic centers or through accretion of misaligned material onto the accretion disk or whether both processes contribute cannot be decided with absolute certainty at present time. However, both scenarios require galaxy merging as the initial trigger of the reorientation event. Most interestingly both models suggest that jet reorientation does *inevitably* occur every time two galaxies merge, if one or both of them contains a massive central black hole. Mergers are thought to occur quite frequently, however X-shaped sources appear to be a very rare species of radio galaxies. In the following we will investigate this apparent contradiction.

### 8.1 X-shaped Sources in Hiding

Galaxies are known to contain large amounts of gas and most galaxies are believed to contain massive central black holes. Mergers of such galaxies thus naturally provide the ingredients needed to induce realignment of the central BH spin axis. Merger events containing an AGN should then always result in a visible reorientation of the jets. An apparent contradiction of the jet reorientation models is posed by the small number of X-shaped radio galaxies compared to the rather large

number of merger events. Certainly, selection effects due to projection and beaming (see Chap. 2 can conceal the X-shaped nature of some sources on unfavorable viewing angles. For moderate intrinsic angles the fraction of sources hidden by selection effects is about 25% (see Sect. 7.2). This suggests that – unless there is a large, hidden population of objects with very small reorientation angles – selection effects are not sufficient to account for the low number of X-shaped sources. Another problem for the connection of merging and reorientation arises when inspecting the environments in which the hosts of X-shaped sources are embedded. None of the known sources lay in dense clusters, only a few sources seem to be located in small, low-mass clusters or groups whereas most sources seem to be isolated field galaxies. This is surprising because mergers do occur more frequently in clusters and therefore one would expect to find X-shaped sources preferentially in dense environments.

Both apparent contradictions – the small number of X-shaped source and their preferred location in poor environments – might however be resolved when another selection bias inherent to the classification of X-shaped sources is taken into account.

It is important to note again that the classification of X-shaped sources is purely morphological and is defined only by the presence of visible secondary lobes. However the sec-

ondary lobes of X-shaped sources will eventually fade away due to synchrotron and inverse-Compton losses once they are not being fed by fresh particles anymore. A short fading time compared to the total active lifetime of the source would then naturally explain the apparent low number of X-shaped sources. We also expect the fading timescale in clusters to be considerably shorter than in low density environments due to enhanced radiative losses (as in the case of Cyg A; see Barthel & Arnaud 1996). This would explain the relative overpopulation of X-shaped sources in poor environments. Support to this idea is given by the apparent absence of X-shaped sources at redshift above  $z=0.3$ . While this is due in part to a lack of sensitivity and resolution we also *expect* to see fewer X-shaped objects with increasing redshift due to the increasing strength of the inverse-Compton process.

## 8.2 Simulated Source Evolution

As was outlined above the length of the lobe fading time is the crucial parameter in the further evolution of the source. The actual secondary lobe fading time of a particular X-shaped source cannot be calculated a priori. It depends on the luminosity of the secondary lobes, the initial electron energy distribution, the magnetic fields at work and as well on observational parameters like frequency and sensitivity. If however the radiation spectrum and magnetic field strength of a particular source are known with sufficient accuracy the evolution of the radiation spectrum and thus the morphology of the source with progressing time can be simulated.

### *Lobe Fading Time*

The break frequency is linked to the spectral age through Eq. 6.5. Knowing the magnetic field strength  $B$  and the redshift  $z$  the formula can thus be used to predict the shape of an observed synchrotron spectrum at later times. Such a spectral evolution is sketched in Fig. 8.1 for 4C12.03. Because of the exponential shape of the spectrum for  $\nu > \nu_b$  the flux at a particular frequency  $\nu_{obs}$  will decrease

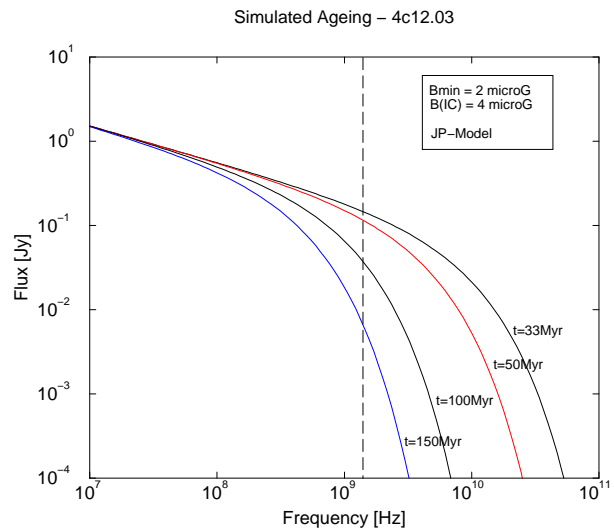


FIGURE 8.1— Model spectra of 4C12.03 demonstrating the evolution of the synchrotron spectrum with progressing time. The line corresponding to an age of  $t=33$  Myr represents the actual observed spectrum at the tips of the secondary lobes of 4C12.03. The curves corresponding to higher ages were constructed using the standard ageing formula with the minimum magnetic field at the secondary lobe tip of  $2\mu\text{G}$ . The dashed line marks the observation frequency of 1.4 GHz. As can be seen the secondary lobes become undetectable at a given frequency quite rapidly once the break frequency becomes comparable to or smaller than the observation frequency. Such a plot can be used to estimate at which age the flux of the secondary lobes will be below the sensitivity limit of an observation.

rapidly in time once the break frequency becomes comparable to  $\nu_{obs}$ . Assuming a specific flux level that can still be detected by our observation one can thus determine at which break frequency and age this particular source region will have faded away. To estimate the lobe fading time of the sample of X-shaped sources we have extracted spectra in the central regions of the secondary lobes. These spectra have then been artificially aged until the flux has dropped below the  $3\sigma$  limit obtained from the radio maps at  $\nu_{obs}$ . The corresponding break frequency  $\nu_{crit}$  then yields the lobe fading time  $t_{fade}$ . Of course the fading time is not constant across the whole secondary lobe due to the point-to-point differences of the spectral shape and the observed gradients in magnetic fields. Because the inferred ages at the tips of the secondary lobes

are generally the highest they can be expected to fade away somewhat faster than source regions close to the core. Due to the rather small derived gradients in age and magnetic field (see Chap. 6) we expect the differences in the lobe fading time to be small. The employed method to study the spectral evolution of radiation from the central regions of the secondary lobes therefore will be sufficient for a rough estimate of the relevant fading timescales. Table 8.1 lists the lobe fading times and the parameters used for deriving them.

All sources have very similar lobe fading times  $t_{fade}$  (at  $\nu \approx 1.4$  GHz) between 110 Myr and 180 Myr. These values are comparable to the inferred lifetimes of some of the oldest radio sources (Saripalli et al. 1994, Schoenmakers et al. 1998). Unless adiabatic expansion further enhances the overall radiation losses we thus have to conclude that the secondary lobes of the sources studied here will most probably be visible throughout their whole active lifetime. It is however important to note that the radiation losses depend on the redshift and the local environment of the source. The impact that these parameters have on the expected lobe fading time will be studied in the following.

#### *Environment and Redshift*

The radiation losses due to the inverse-Compton process are proportional to  $(1+z)^2$ . For most radio sources with typical lobe magnetic fields of a few  $\mu G$  the equivalent inverse-Compton field  $B_{IC}$  usually is of comparable size. Already at moderate redshifts the inverse-Compton process typically becomes the dominant radiation loss mechanism. The lobe fading time would therefore decrease if the source were located at a higher redshift. The same is true if the source were located in a denser environment. There is indication that the radiation losses increase due to the interaction with the magnetized cluster medium (Barthel & Arnaud 1996), which can be expressed by an increased source magnetic field. We have used Eq. 6.5 to calculate the lobe fading time as a function of  $z$  and  $B_{min}$  with

the break frequency being fixed at  $\nu_{crit}$ . This is displayed in Fig. 8.2 for 4C12.03. Assuming the actual magnetic field strength in the secondary lobe of  $B_{min} \approx 2 \mu G$  the lobe fading time decreases with increasing redshift from its current value of  $\approx 130$  Myr to  $\approx 50$  Myr at  $z=0.5$ . Assuming higher fields (to simulate a denser local environment) the lobe fading time at low redshifts are somewhat lower but with increasing redshift the differences in magnetic field have less and less impact on the lobe fading time. At  $z=0.5$  all curves 'converge' at a typical value of  $t_{fade} \approx 50$  Myr. The plots corresponding to the other studied sources can be found in Fig. 8.3. With the exception of 3C223.1 all lobe fading times at  $z=0.5$  are less than 50 Myr. Assuming that the feeding of the secondary lobes has stopped with the onset of the reorientation and recalling our findings from Chap. 7 that this has happened about 10-40 Myr ago we conclude that the secondary lobes would be visible for another few  $10^7$  years if these sources were located at higher redshifts or in denser environments. While this is rather short it is difficult to decide whether such a timescale is consistent with the low number of known X-shaped sources.

Also it is unclear whether the sources of this sample are representative for the whole class of X-shaped sources. Possibly the sources of our sample are untypical in the sense that they have unusually long lobe fading times. As we have seen  $t_{fade}$  becomes more or less independent of  $B_{min}$  at higher redshifts. Sources with very short fading times must have high-frequency critical frequencies  $\nu_{crit}$ . This would imply either spectra with extremely steep injection indices or very faint secondary lobes. Even though at present there is no indication for such a population of sources, its existence cannot be ruled out completely. Such sources – if they exist – can have lobe fading times of  $10^6$  years and less, which would make their detection rather unlikely.

Source	$\nu_{obs}$ [GHz]	$B_{min}$ [ $\mu$ G]	$B_{IC}$ [ $\mu$ G]	$\nu_{crit}$ [MHz]	$t_{fade}$ [Myr]
4C12.03	1.5	2.0	4.0	675	130
NGC 326	1.4	3.0	3.6	480	180
3C136.1	1.4	2.0	3.7	593	160
B2 0828+32	1.5	1.0	3.6	1020	110
3C223.1	1.5	3.5	4.0	701	120
3C403	1.5	5.0	3.6	678	110

TABLE 8.1— The lobe fading times and the relevant parameters that have been used in deriving them.  $\nu_{obs}$  denotes the frequency for which the lobe fading time has been calculated.  $B_{min}$  and  $B_{IC}$  are the minimum and inverse-Compton magnetic field strengths.  $\nu_{crit}$  is the critical break frequency at which the flux of the secondary lobes has dropped below the  $3\sigma$  limit and  $t_{fade}$  is the corresponding lobe fading time.

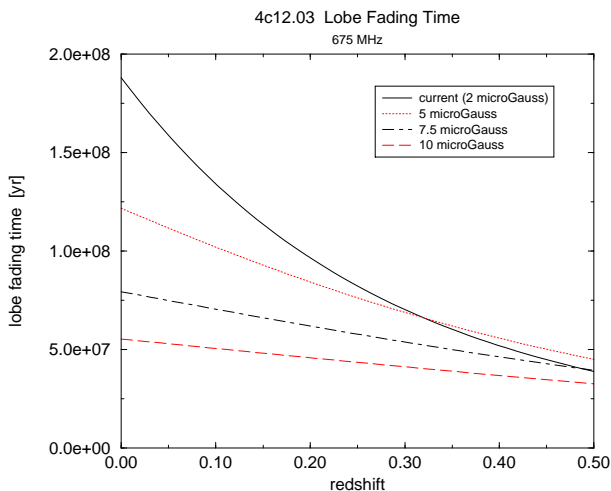


FIGURE 8.2— Plot of the lobe fading time as a function of redshift for 4C12.03. Different curves correspond to different values of the source magnetic field. The solid line curve represents the actual minimum field strength measured in the central region of the secondary lobes.

### 8.3 Simulated Maps

This section is intended to give an impression of what we can expect a former X-shaped source with faded secondary lobes to look like. Simulated maps of X-shaped sources at various time steps have been created following a simple procedure. The simulated spectra (see Fig. 8.1) have been used to estimate by which factor  $f(t)$  the flux of a particular area within the secondary lobe decreases with time at a given frequency  $\nu_{obs}$ . The radio map at this frequency was then scaled with  $f(t)$

and clipped at the initial  $3\sigma$  noise level of the unscaled image. The simulated images are displayed in Figs. 8.4 - 8.9. The employed method of creating these images is somewhat crude as it simply scales the entire image by a constant factor. In reality the primary lobes which are constantly fed with fresh particles would remain more or less unaffected by the ageing. Also the point-to-point differences of the magnetic field and spectral shape have not been taken into account. Proper treatment would require the extraction of the synchrotron spectra and minimum fields at each point of the secondary lobes and then calculating and applying a factor  $f(t)$  which depends on the location. However, to obtain a first impression the method followed here is probably sufficient.

As we can see, at later stages of their evolution X-shaped sources will appear more or less like normal double-lobed radio galaxies. In most cases short extrusions remain in regions close to the core. This is reminiscent of what has been observed in a large number of apparently normal double-lobed radio sources. Leahy & Williams (1984) have reported that in their complete sample of 3C sources with large angular sizes about two-thirds show similar lobe distortions near the central galaxy. Interestingly nearly all of these distortions exhibit the same rotational symmetry as has been observed in X-shaped sources. Even the prototypical double-lobed radio galaxy – Cyg A – has clearly visible lobe extension which

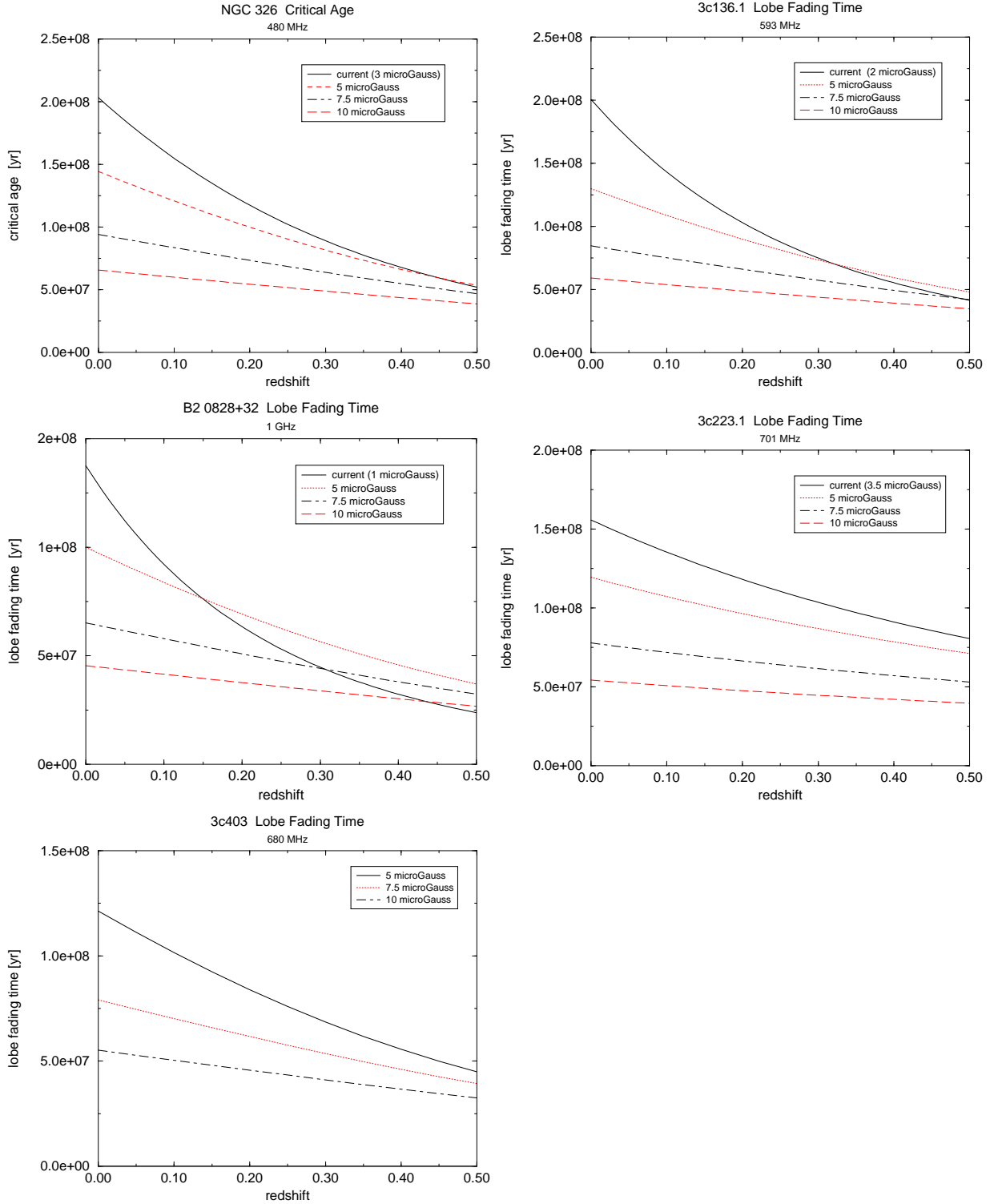


FIGURE 8.3— Plots of the lobe fading time as a function of redshift for five different X-shaped sources. Different curves correspond to different values of the source magnetic field. The solid line curve represents the actual minimum field strength measured in the central region of the secondary lobes.

were termed 'plumes' by Carilli et al. (1991). The usually explanation for these extrusions

is backflow. However, backflow cannot easily explain the observed rotational symmetry (see

Chap. 5).

We instead speculate that the symmetric lobe extrusions observed in many radio sources might be the relic emission of faded secondary lobes. This would indicate that the phenomenon of jet reorientation would be more common than presently believed. Support to this idea comes from a new class of objects, the so-called double-double radio galaxies (DDRG). DDRGs are characterized by the presence of a pair of double-lobed radio sources with a common center (Schoenmakers et al. 2000a, Kaiser et al. 2000, Schoenmakers et al. 2000b). In many cases the inner and outer radio sources are misaligned by a small angle. Schoenmakers et al. (2000a) also note that – like X-shaped sources – DDRG occupy the luminosity range between the FRI and FR II regime. The authors have speculated that DDRG might simply be X-shaped sources having small reorientation angles. Also a number of compact and presumably young radio sources (CSOs) have been found that are clearly associated with larger scale emission which is considerably misaligned with the radio source axis (Baum et al. 1990b, Owsianik et al. 1998, Schoenmakers et al. 1999).

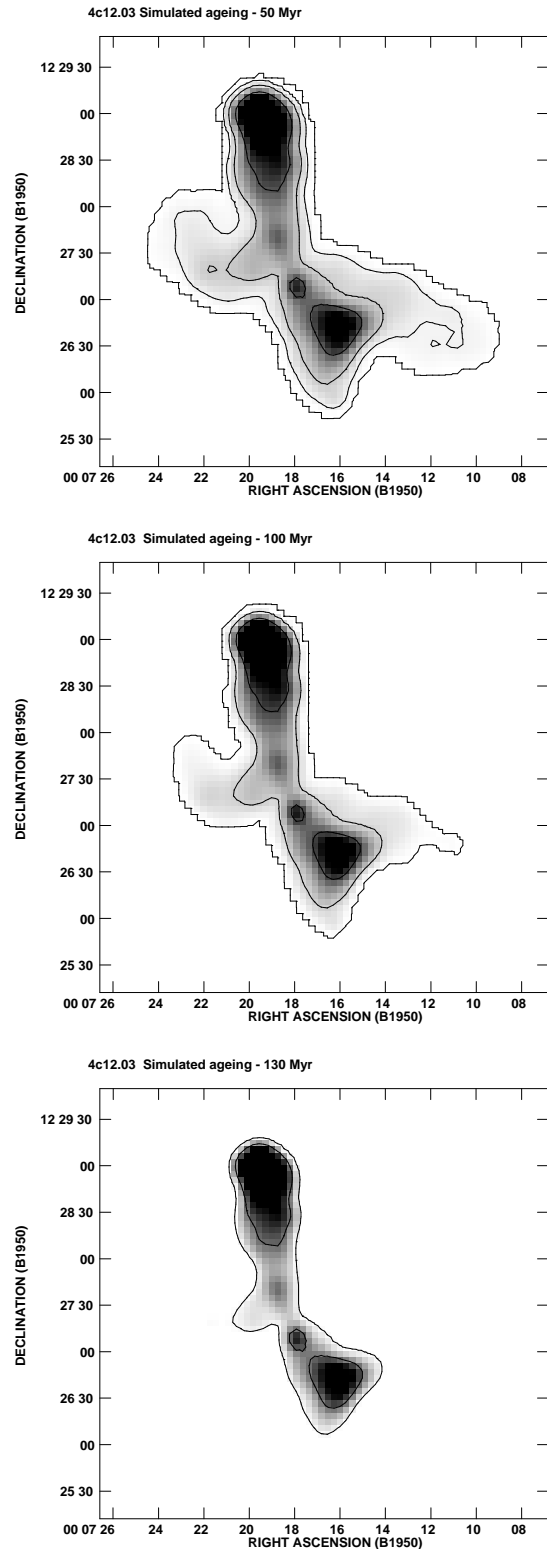


FIGURE 8.4— Maps simulating the ageing of 4C12.03. With increasing time the intensity of the secondary lobes decreases until they have completely faded away.



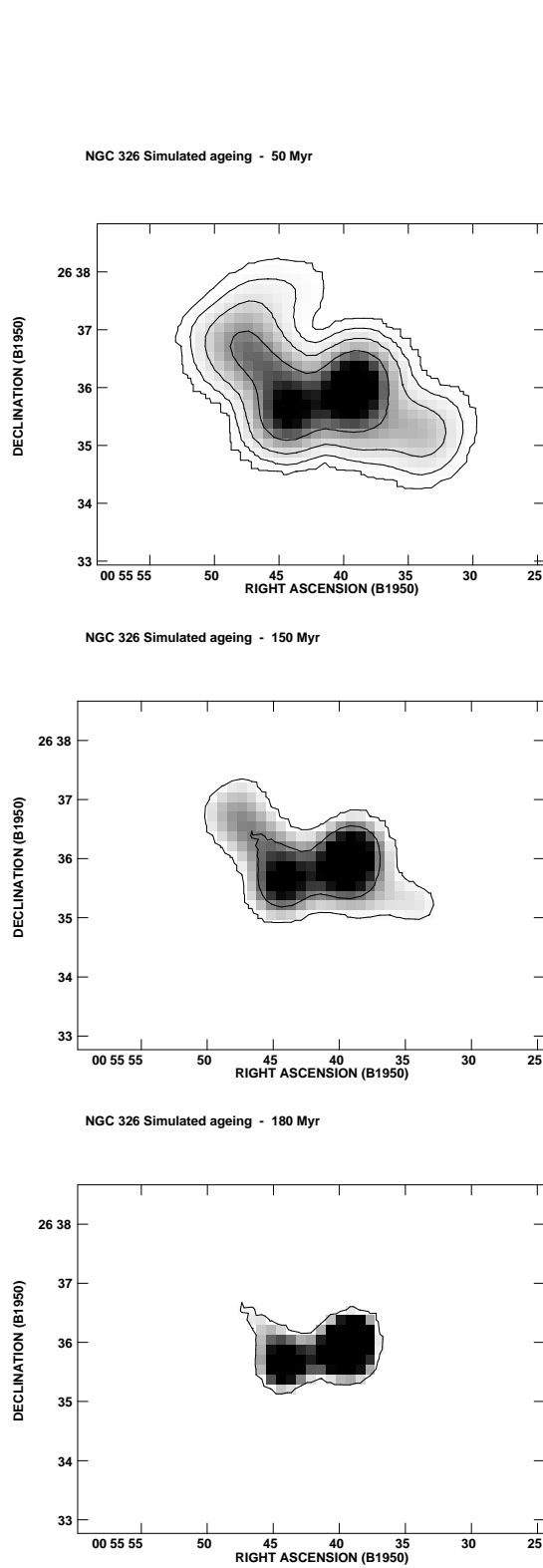


FIGURE 8.5— NGC 326 - Simulated ageing.

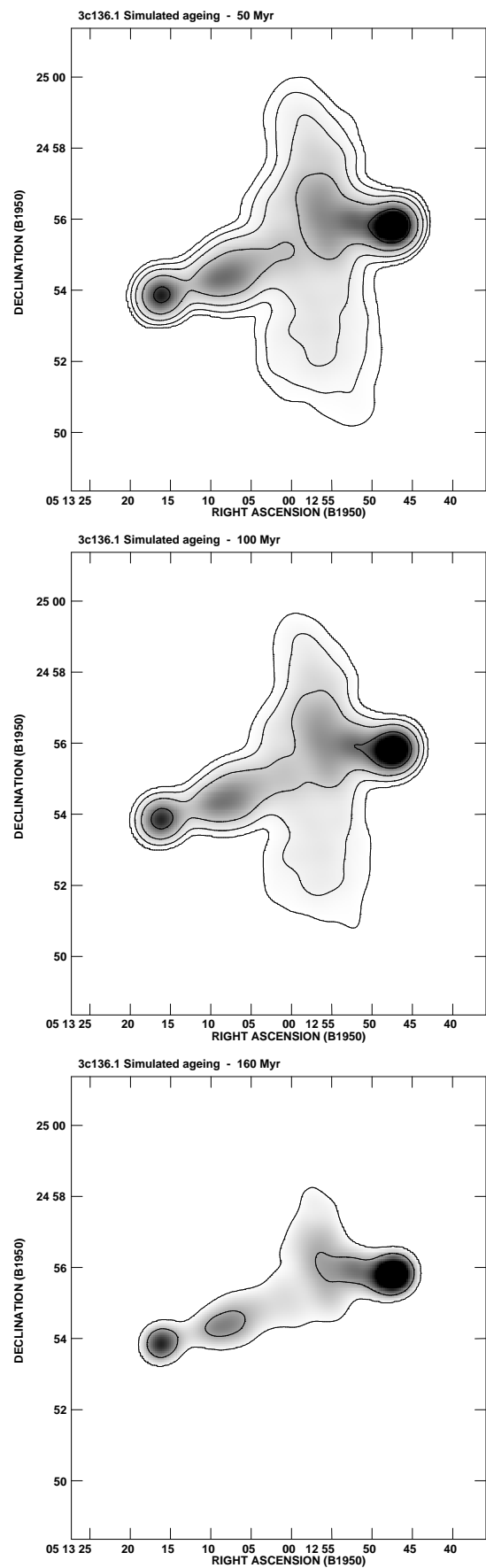
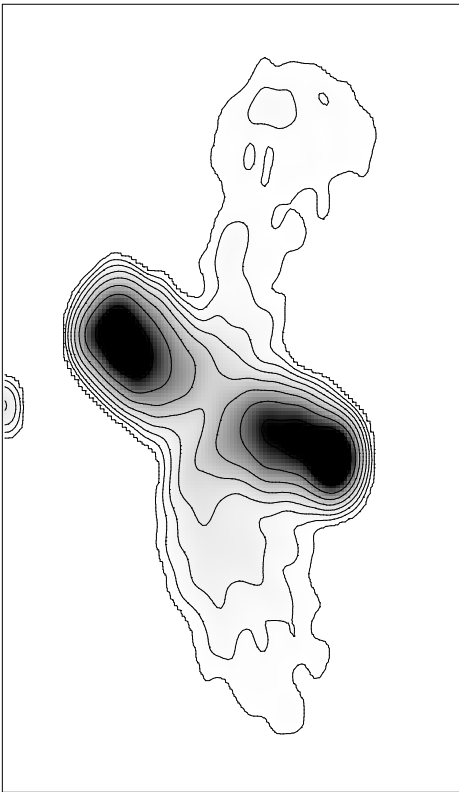
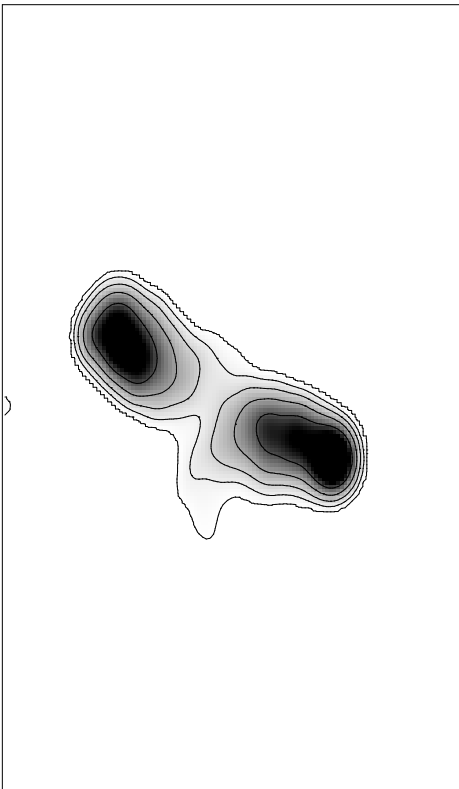


FIGURE 8.6— 3C136.1 - Simulated ageing.

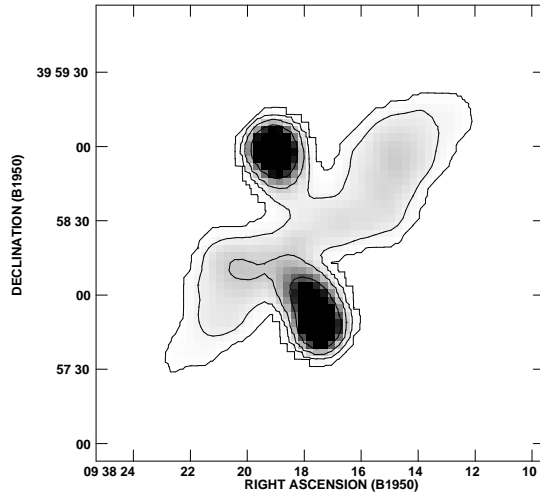
B2 0828+32 Simulated ageing - 50 Myr



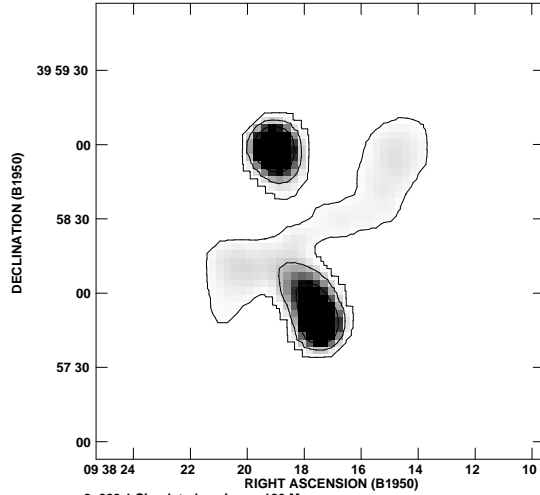
3c136.1 Simulated ageing - 110 Myr



3c223.1 Simulated ageing - 50 Myr



3c223.1 Simulated ageing - 100 Myr



3c223.1 Simulated ageing - 120 Myr

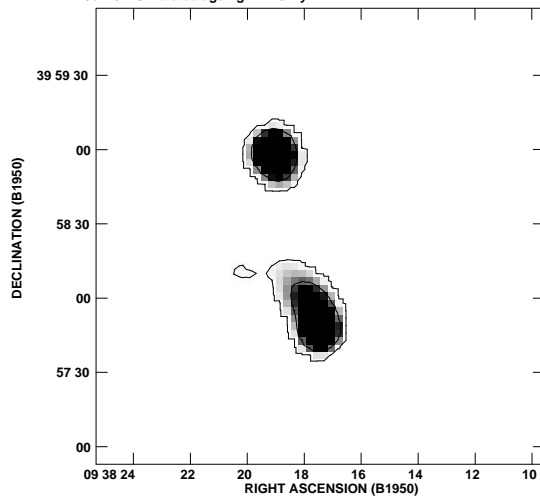


FIGURE 8.8— 3C223.1 - Simulated ageing.

FIGURE 8.7— B2 0828+32 - Simulated ageing.

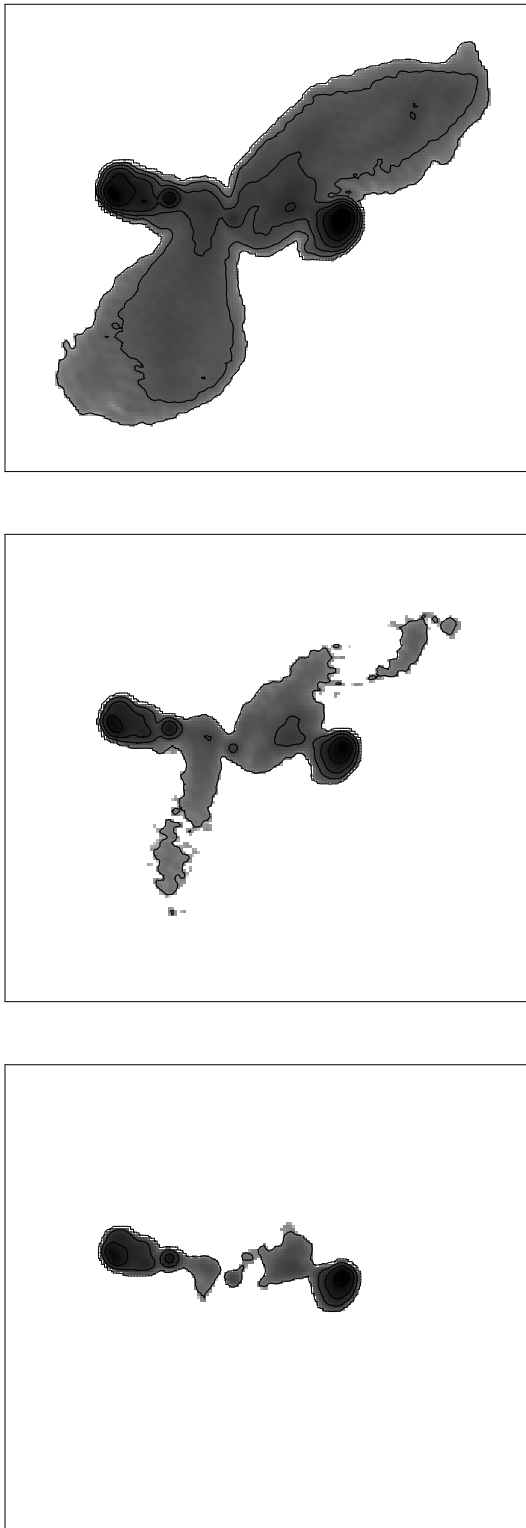


FIGURE 8.9— 3C403 - Simulated ageing.



# 9

---

## Summary

The thesis set out to investigate the nature and genesis of the peculiar class of X-shaped radio galaxies. X-shaped sources are puzzling because of the extremely low number of objects of that type. Three scenarios were investigated:

- X-shaped sources are a class by itself and are formed through a mechanisms unlike normal radio galaxies.
- X-shaped sources are normal radio galaxies but they are currently in an unusual and/or short lived phase.
- X-shaped sources are numerous, but selection effects keep us from identifying more of them.

The backbone of this work is the multi-frequency spectral analysis. Magnetic fields were calculated using the standard minimum energy assumptions. Break frequencies were determined from the synchrotron spectra by fitting spectral models. The break frequencies were then used to calculate spectral ages following the method proposed by Alexander & Leahy (1987).

In nearly all sources we have found a gradient of decreasing magnetic fields and spectral indices from the primary towards the secondary lobes. Furthermore, the trend of spectral age clearly indicates increasing ages towards the tips of the secondary lobes. Spectral ages of the secondary lobes have been

found to be of the order of a few  $10^7$  years, which is rather typical for the lobes of 'normal' radio galaxies. Some of the primary lobes (3C223.1, 3C403, NGC 326) however are quite young ( $10^6$  years). The young spectral ages of these sources and the short lengths of their primary lobes indicates that possibly the re-orientation of their jets is ongoing or has finished only recently.

The spectral ages have been used to test the proposed formation scenarios. The required flow speeds in the case of the buoyancy and backflow models is inconsistent with the calculated spectral ages. The predictions of the jet reorientation mechanisms are in excellent agreement with the inferred spectral ages.

In the following we have compared the theoretical distribution of projected source angles for a randomly oriented sample of X-shaped sources with the distribution of observed angles. It has turned out that the studied sample of X-shaped sources must have a distribution of intrinsic angles, which is rather narrow and contains angles between  $50^\circ$  and  $90^\circ$ . This finding does not fit well into any of the proposed formation mechanisms. The absence of observed angles larger than  $90^\circ$  is however predicted by the model of merging binary black holes.

The impact of radiation losses on the radiation lifetime of the secondary lobes has been investigated. It has turned out that all sources

studied in this thesis have similar secondary lobe fading times of 110-180 Myr. This suggests that their secondary lobes will remain visible throughout the total lifetime of the sources. We have demonstrated that the lobe fading times are considerably shorter (a few  $10^7$  years) for sources located at higher redshifts or in denser environments. Such fast lobe fading times are consistent with the apparent absence of X-shaped sources at redshifts exceeding  $z=0.3$  and are most probably able to account for the problem of 'missing X-shaped sources'.

Finally, we have created images of X-shaped sources that simulate their morphologies during later stages of their evolution. Even though the employed simulation is rather simple, we have obtained simulated maps that are remarkably reminiscent of 'normal' double-lobed radio galaxies. In particular the symmetric lobe extensions that have been reported in a large number of radio galaxies can be reproduced. We speculate that jet reorientation might occur more frequently in radio galaxies than believed up to present. The existence of misaligned large-scale emission in the compact CSOs and the misaligned inner lobes of DDRG give support to this interpretation.

# A

---

## Test Observations with the 100-m Telescope at 32 GHz

We briefly report on test observations with the 32 GHz system installed in the secondary focus of the 100-m telescope. These tests were performed 20th of June 1999 during night time. The aim of the tests was to investigate the present status of the main beam of the telescope after replacement of the outer surface panels.

Prior to these tests we had encountered strange results when observing strong point sources (e.g. for pointing and calibration). The pointing seemed to make fairly big jumps ( $\sim 30''$ ) and frequently calibration maps resulted in elongated or disrupted source images.

We have observed a series of 11 calibration maps on 3C286 in an elevation range from  $68^\circ$  to  $30^\circ$ . The results are displayed in Fig. A.1. The strong influence of the elevation on the quality of the telescope's beam is evident. With increasing elevation the main beam becomes more and more elliptical and distorted. At the very highest elevation of  $68^\circ$  the main beam has fragmented into several blobs. Also the amplitude of the main beam decreases with increasing elevation. In order to quantify these findings we have fitted gauss profiles to the calibration maps. The results are displayed in Tab. A.1. The amplitude drops nearly linearly with increasing elevation. The dependence is plotted in Fig. A.2. The HPBW along the major beam axis is increasing with increasing elevation. Along the minor beam axis the HPBW is more or less constant at  $\sim 25''$  (which is slightly less than the default value of  $27''$  which was determined during previous test observations). The position angle of the major axis is staying more or less constant with elevation.

### **Conclusions:**

The gain and the beam characteristics of the 100-m telescope at 32 GHz are currently strongly dependent on the elevation. Up to elevations of  $35^\circ$  the beam elongation along the major beam axis is less than 30% and the gain loss is less than 10%. We suggest that one should restrict the elevation range to values below this margin of  $35^\circ$  when observing at 32 GHz until the quality of the surface will be improved by holography in fall 1999.

Elev.	Max	$B_{maj}$	$B_{min}$	P.A.
30	39798	30''	25.5''	32.4
32	37452	33.6''	25.2''	24.5
34	36883	33.0''	25.2''	24.4
37	31721	36.0''	25.8''	26.9
39	32512	36.0''	24.6	35.1
41	29000	39.6''	25.2''	27.2
43	29083	37.8''	25.2''	33.8
45	27346	42.0''	25.8''	31.7
49	24823	42.0''	25.5''	34.3
51	24279	40.8''	27.0''	31.5

TABLE A.1— Results of the elliptical Gaussian fit to the main beam at various telescope elevations. Listed are the elevation (col.1), the amplitude (col.2), the major and minor axes (col.3 and col.4), and the position angle (col.5).



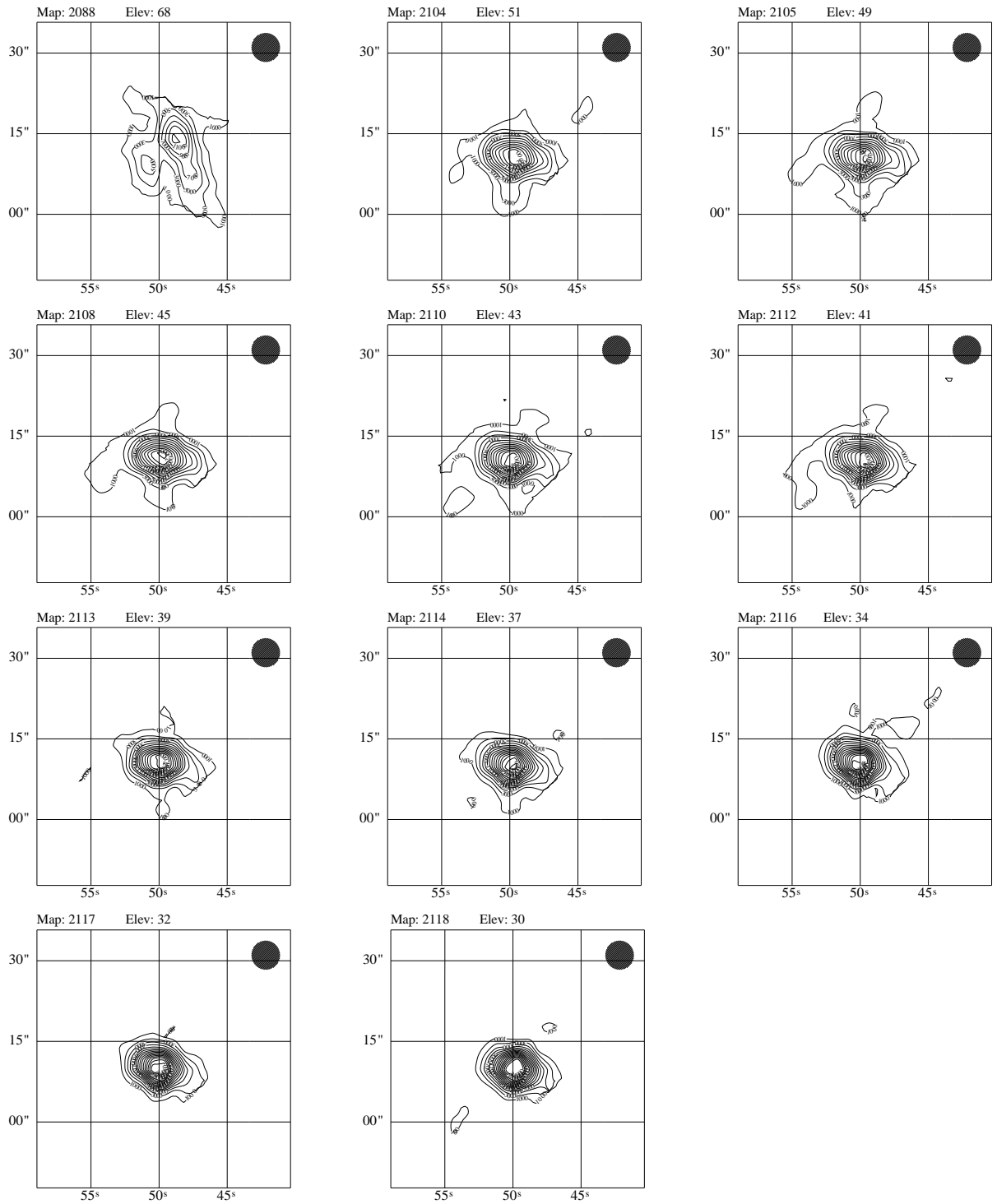


FIGURE A.1— Consecutive observations of 3C286 with decreasing telescope elevation.

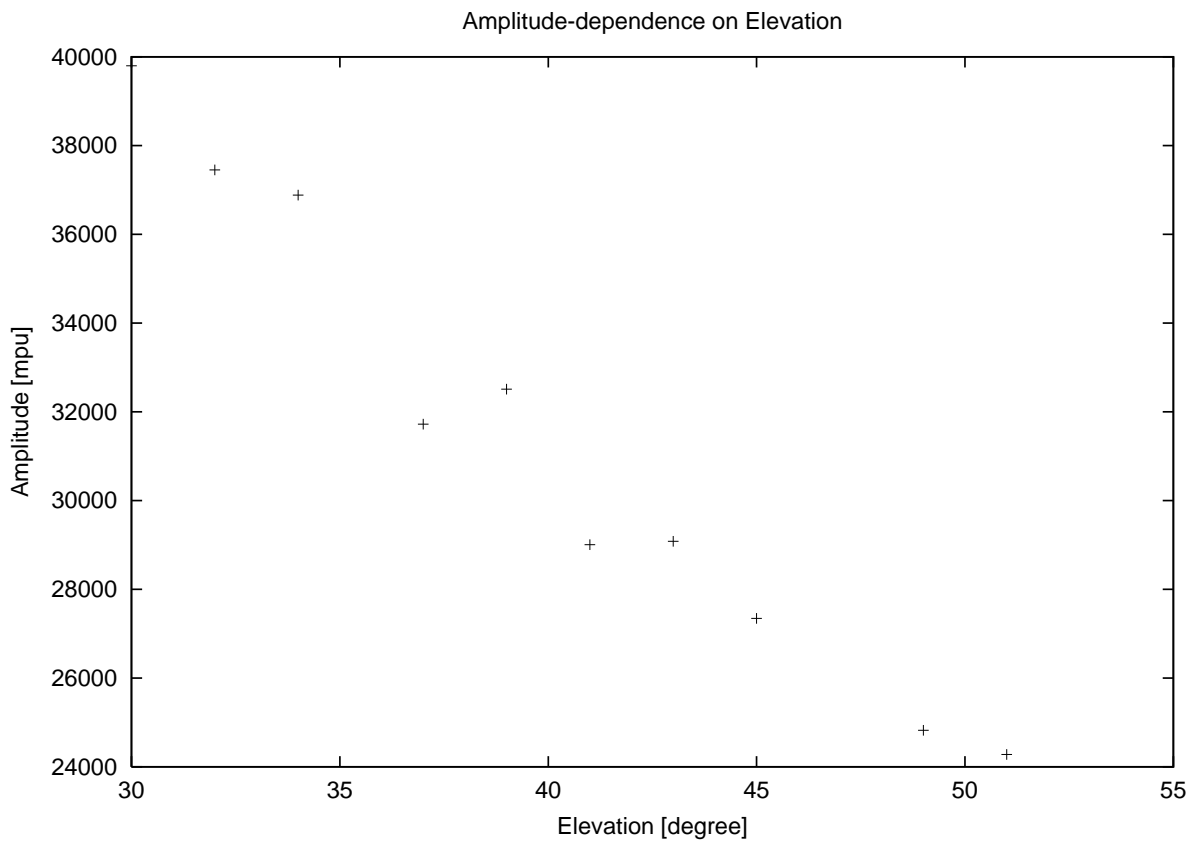


FIGURE A.2— The dependence of the amplitude (determined by gauss fitting) of the main beam with elevation. One can see an almost linear decrease with increasing telescope elevation.

# B

---

## Projected Angle Distributions

In this section the complete list of projected angle distributions of Chap. 7 can be found. Figures B.1 to B.17 display plots of the projected angle  $\phi'$  as a function of the transformation angles  $\beta$  and  $\gamma$ . Each figure corresponds to a single intrinsic angle  $\phi$ . Viewing angles that pass the selection criteria outlined in Chap. 7 are marked by superimposed green  $\Lambda$  symbols.

Figure B shows the theoretical distributions of projected angles for a randomly oriented sample of X-shaped sources. Each plot corresponds to a particular intrinsic angle  $\phi$ . Invalid viewing angles that violate the selection criteria described in Chap. 7 have been discarded and are not contained anymore in the distributions.

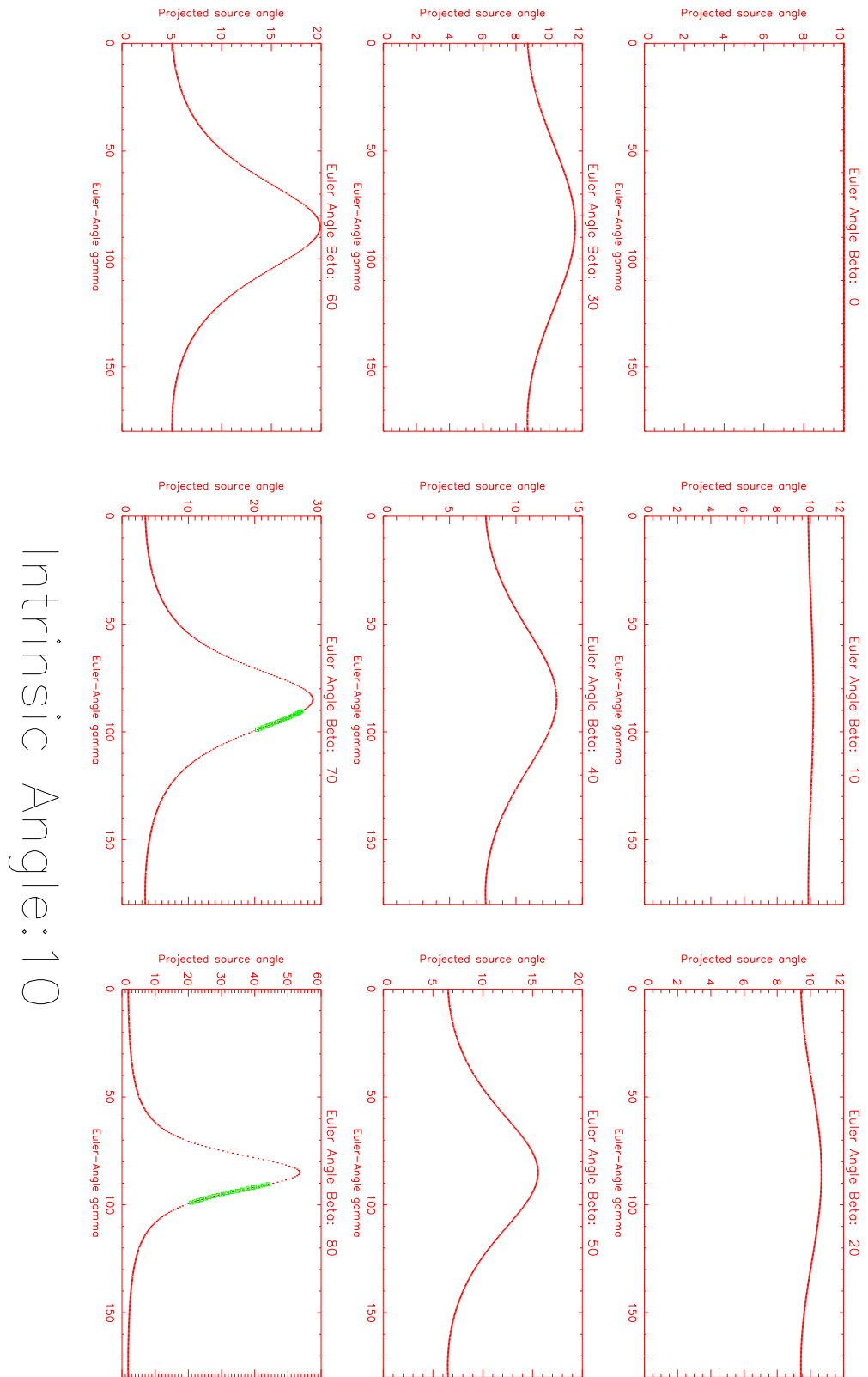
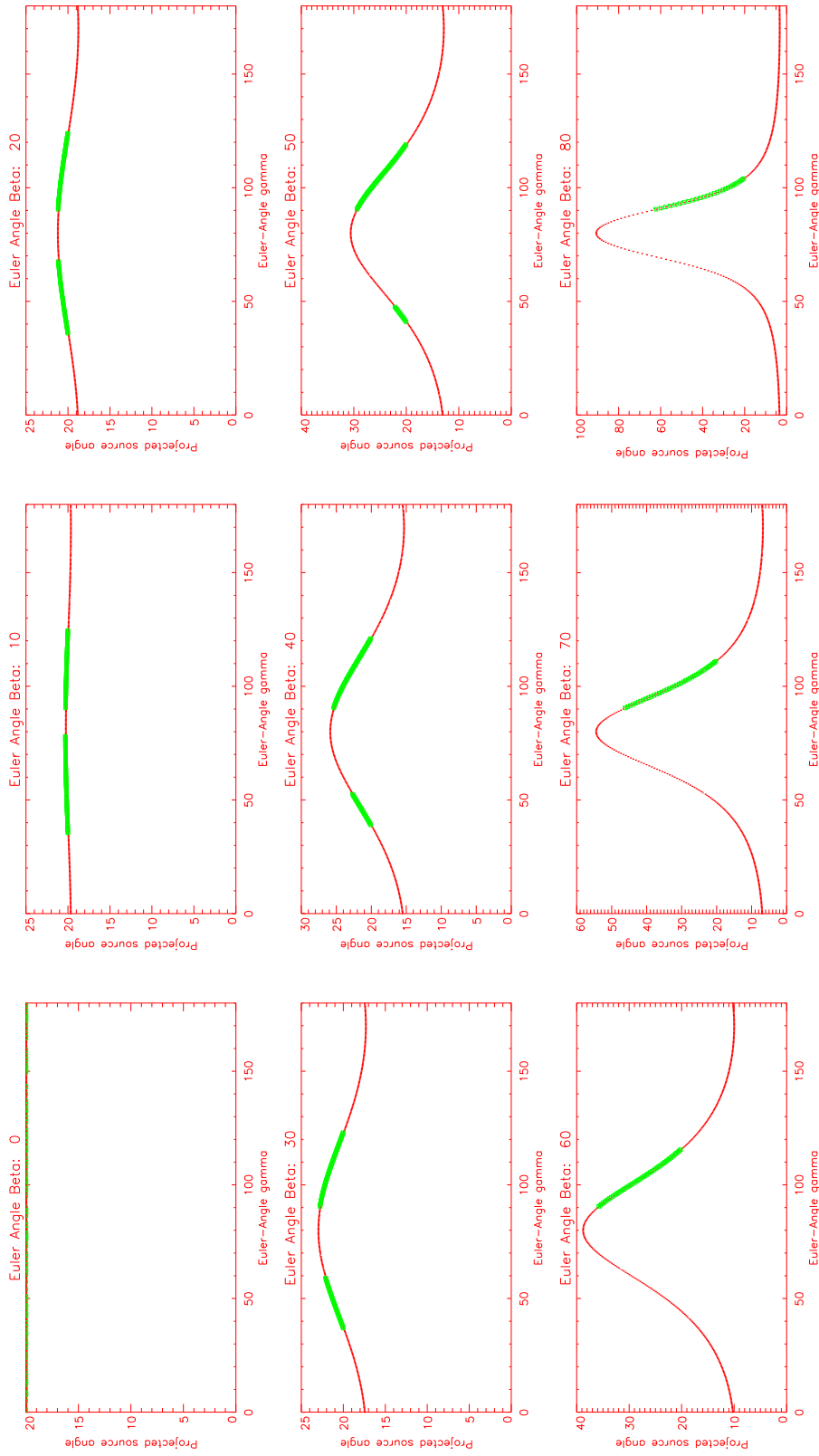


FIGURE B.1— Projected angle distributions corresponding to an intrinsic angle of  $\phi=10^\circ$ . Individual plots display the  $\phi'$  distribution for one particular transformation angle  $\gamma$ . Superimposed green  $\Delta$  symbols mark valid viewing angles that pass the selection criteria for X-shaped sources.



Intrinsic Angle: 20

FIGURE B.2— Projected angle distributions corresponding to an intrinsic angle of  $\phi=20^\circ$ . The plot layout is identical to Fig. B.1.

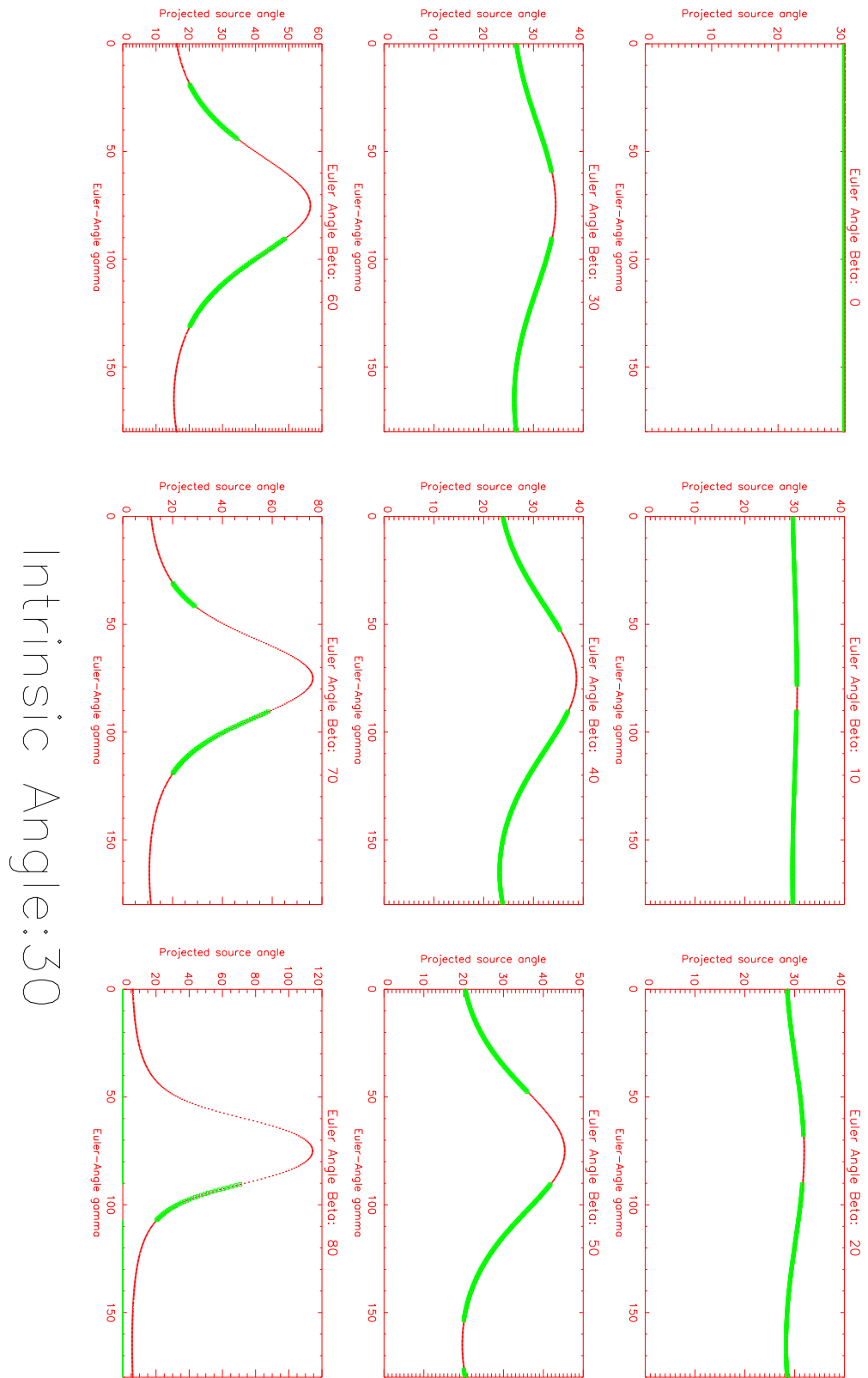
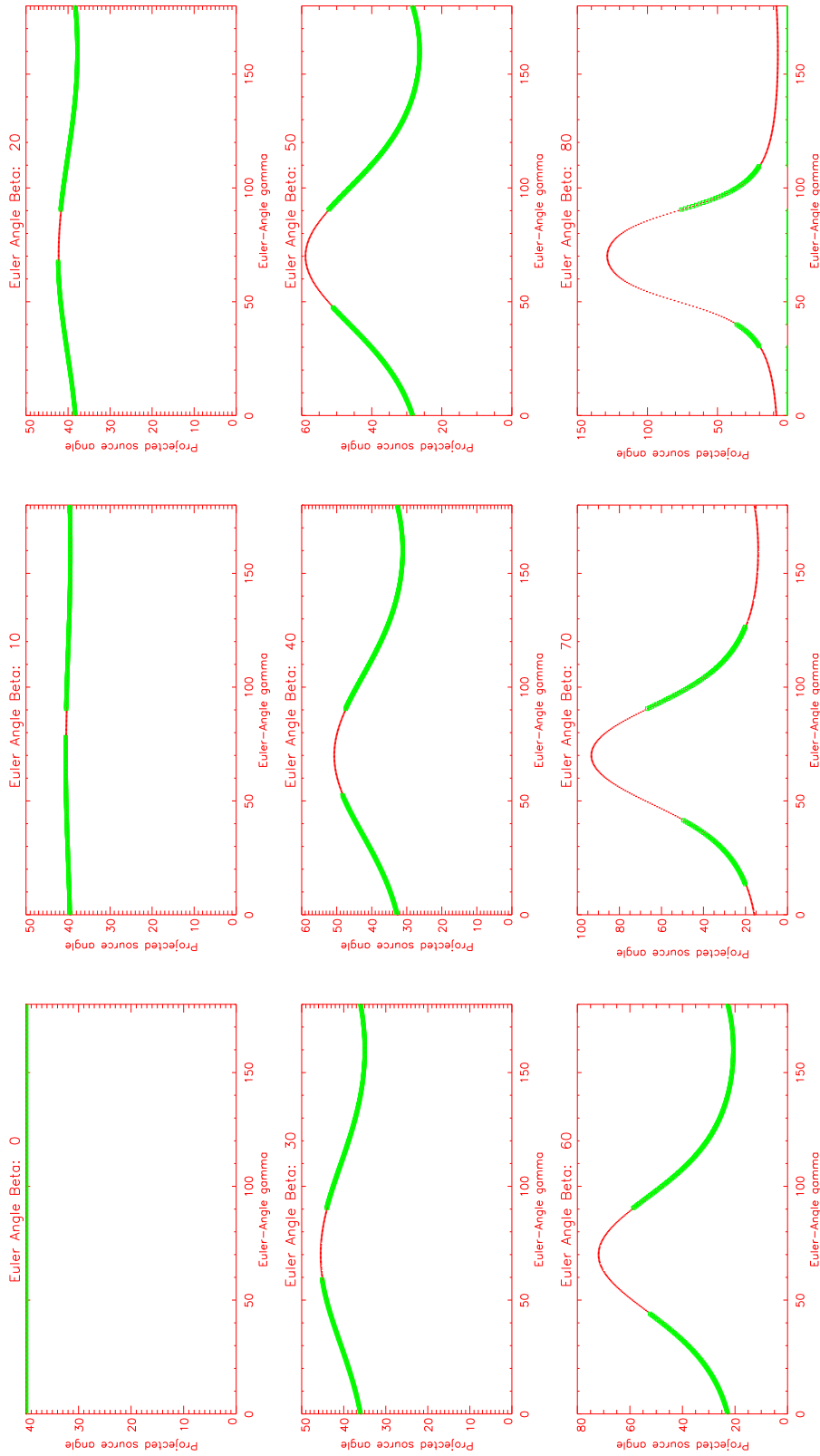


FIGURE B.3— Projected angle distributions corresponding to an intrinsic angle of  $\phi=30^\circ$ . The plot layout is identical to Fig. B.1.



Intrinsic Angle: 40

FIGURE B.4— Projected angle distributions corresponding to an intrinsic angle of  $\phi=40^\circ$ . The plot layout is identical to Fig. B.1.

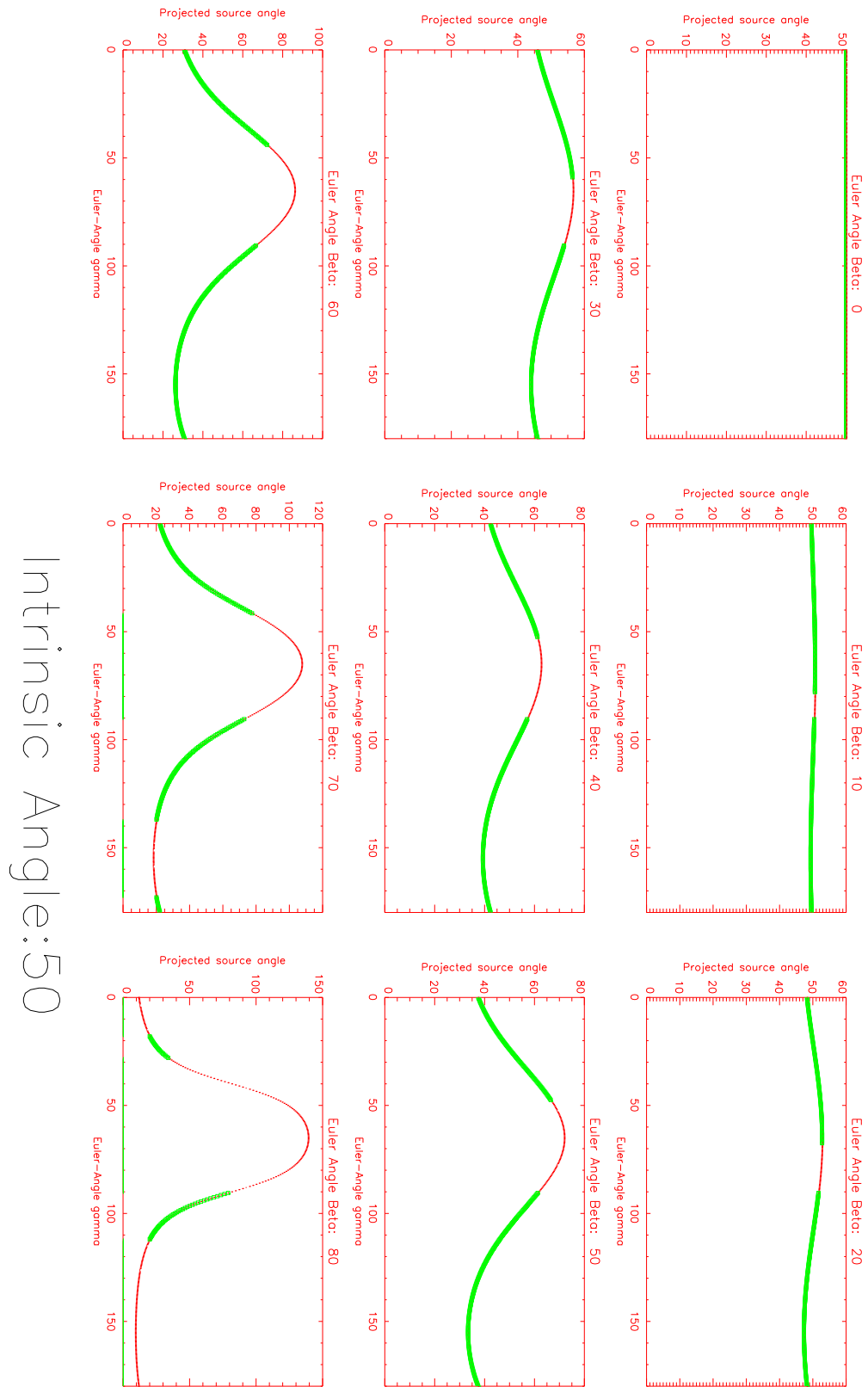
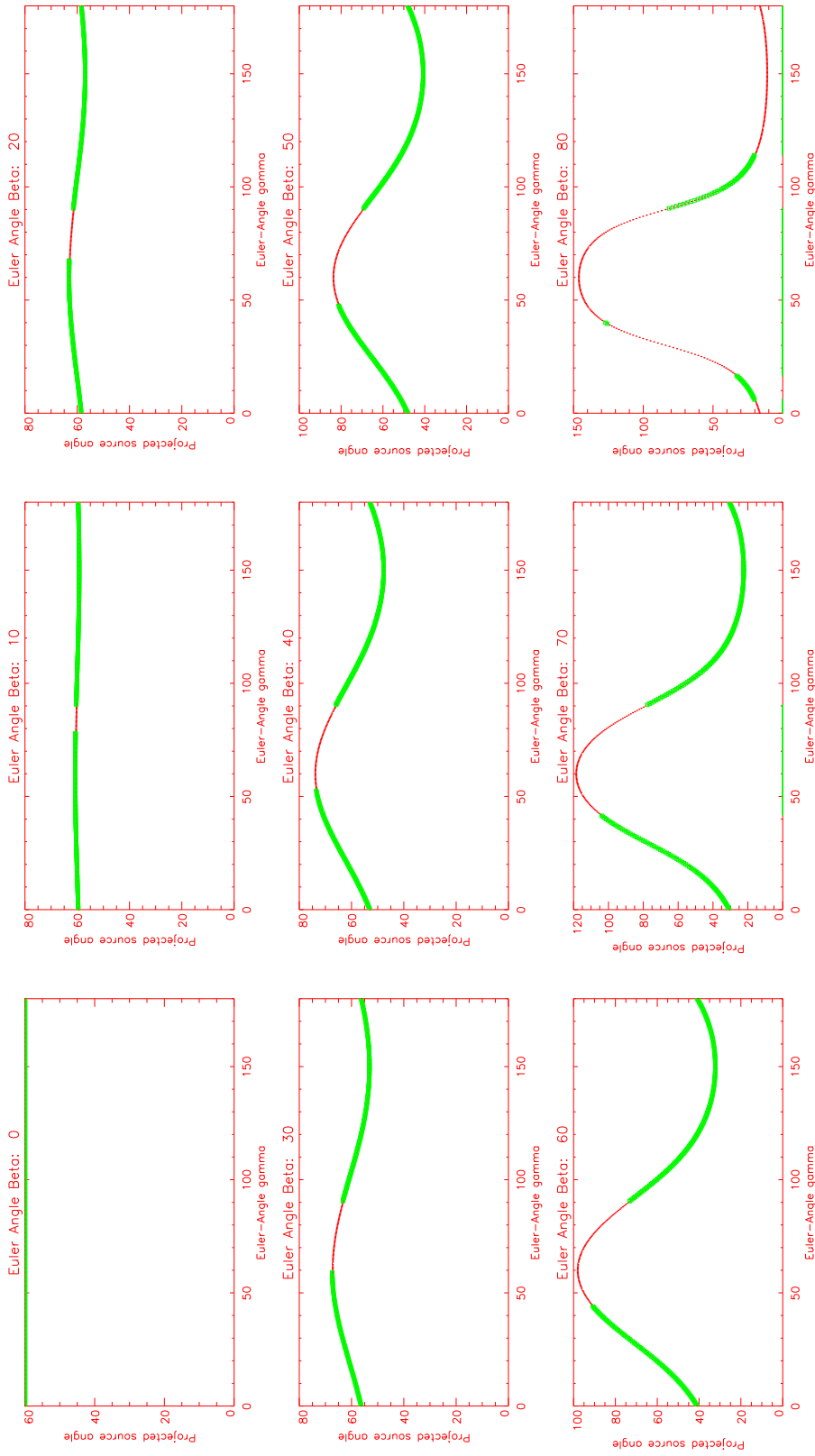


FIGURE B.5— Projected angle distributions corresponding to an intrinsic angle of  $\phi=50^\circ$ . The plot layout is identical to Fig. B.1.





Intrinsic Angle:60

FIGURE B.6— Projected angle distributions corresponding to an intrinsic angle of  $\phi=60^\circ$ . The plot layout is identical to Fig. B.1.

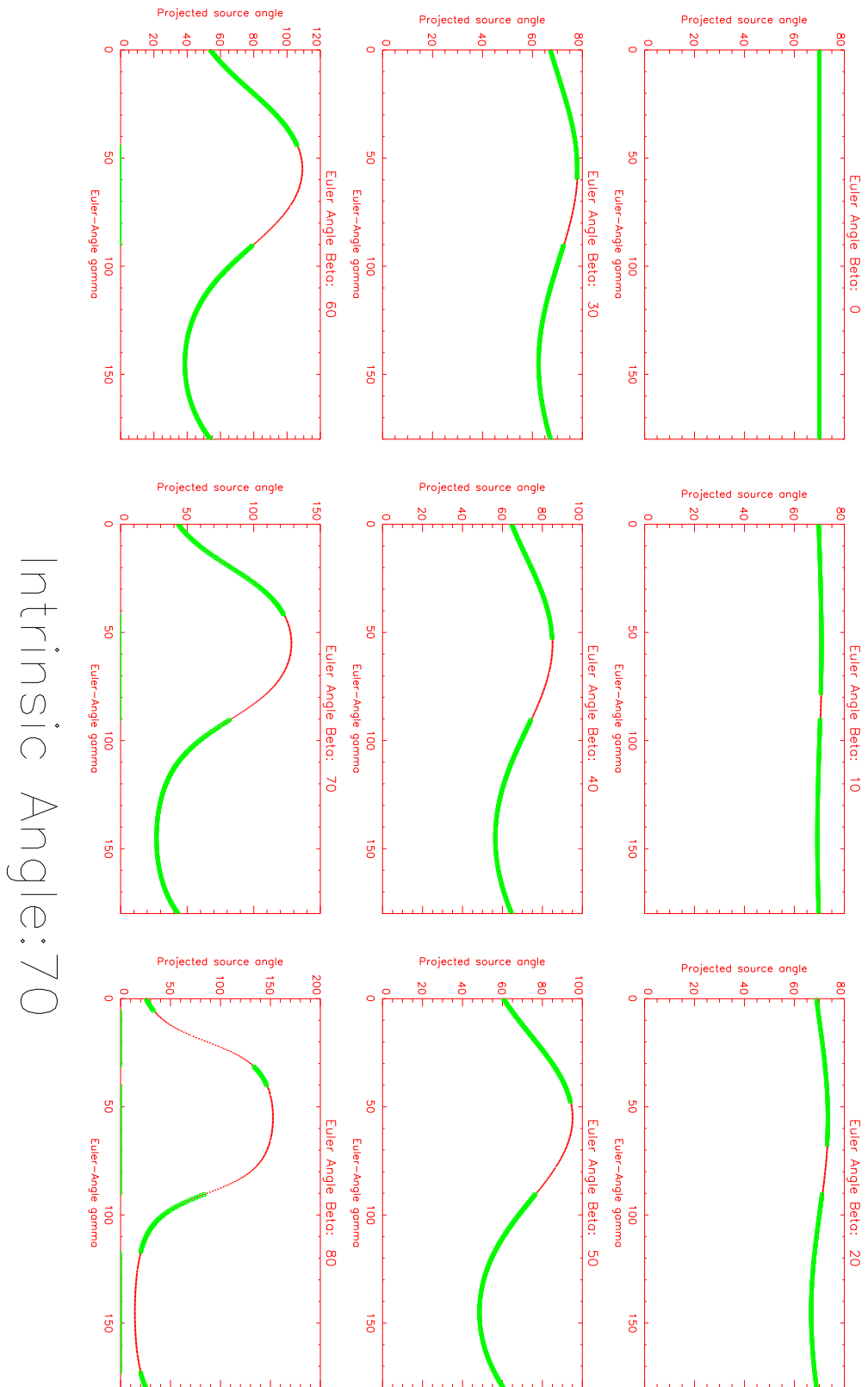
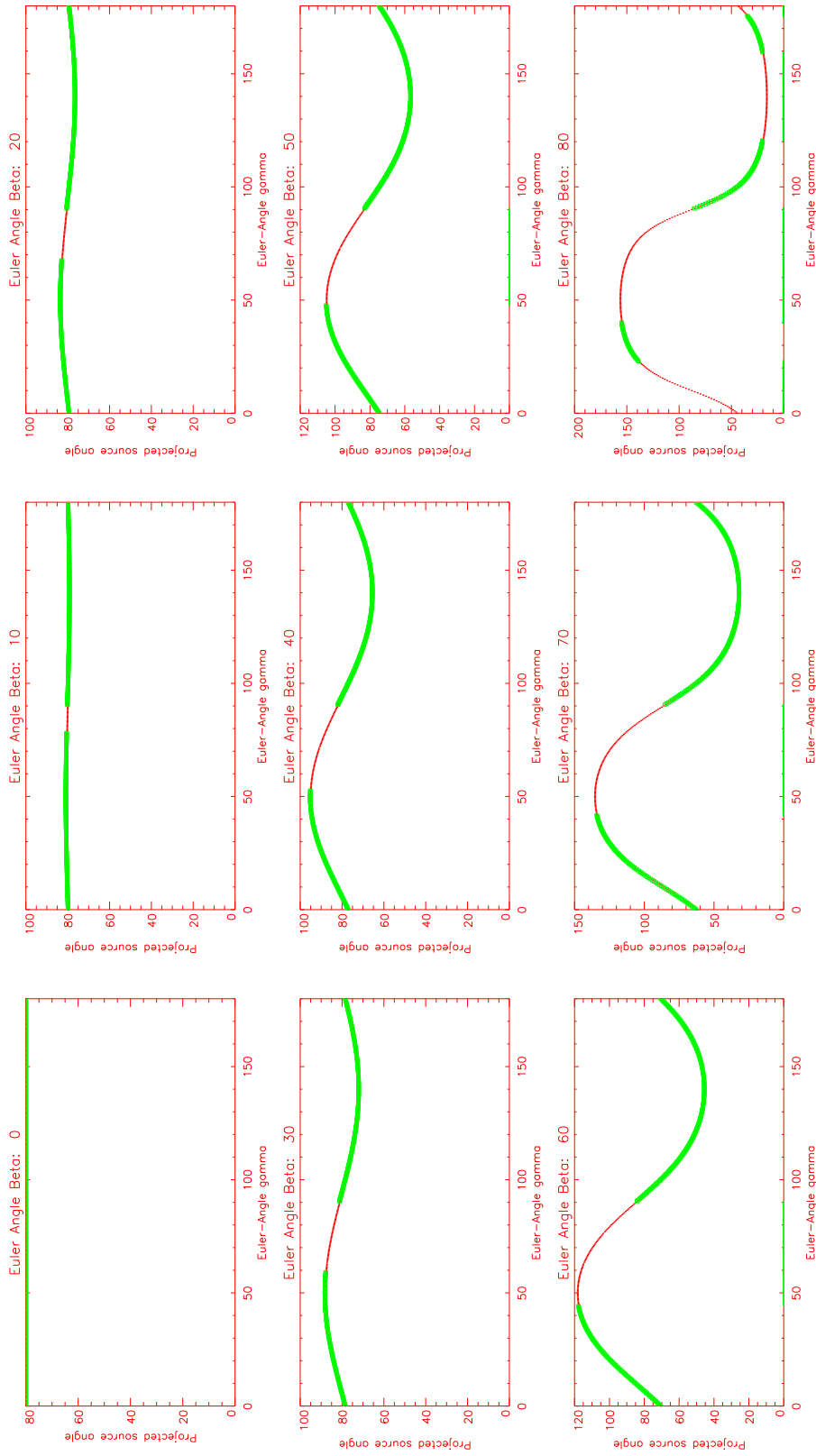


FIGURE B.7— Projected angle distributions corresponding to an intrinsic angle of  $\phi = 70^\circ$ . The plot layout is identical to Fig. B.1.



Intrinsic Angle:80

FIGURE B.8— Projected angle distributions corresponding to an intrinsic angle of  $\phi=80^\circ$ . The plot layout is identical to Fig. B.1.

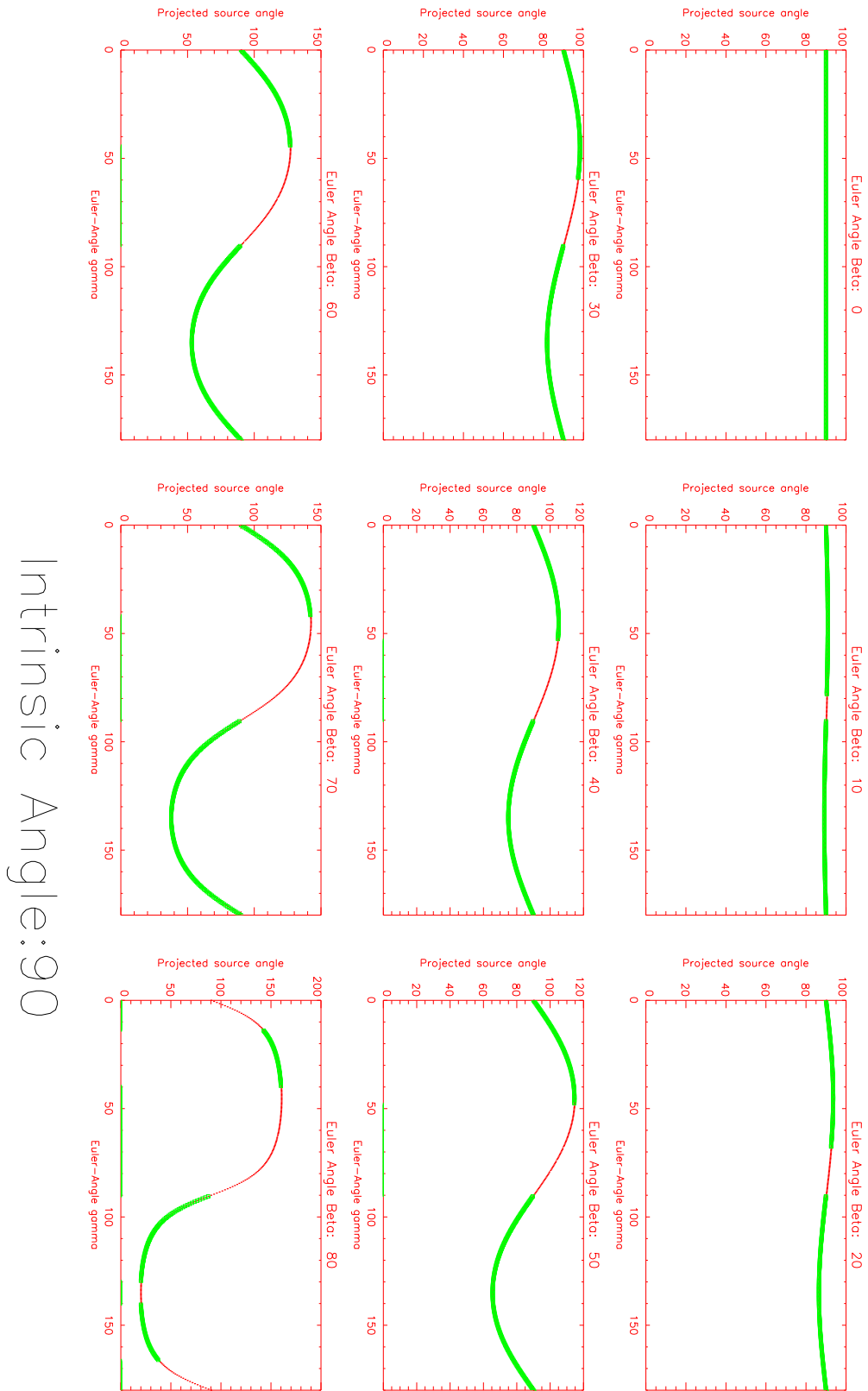
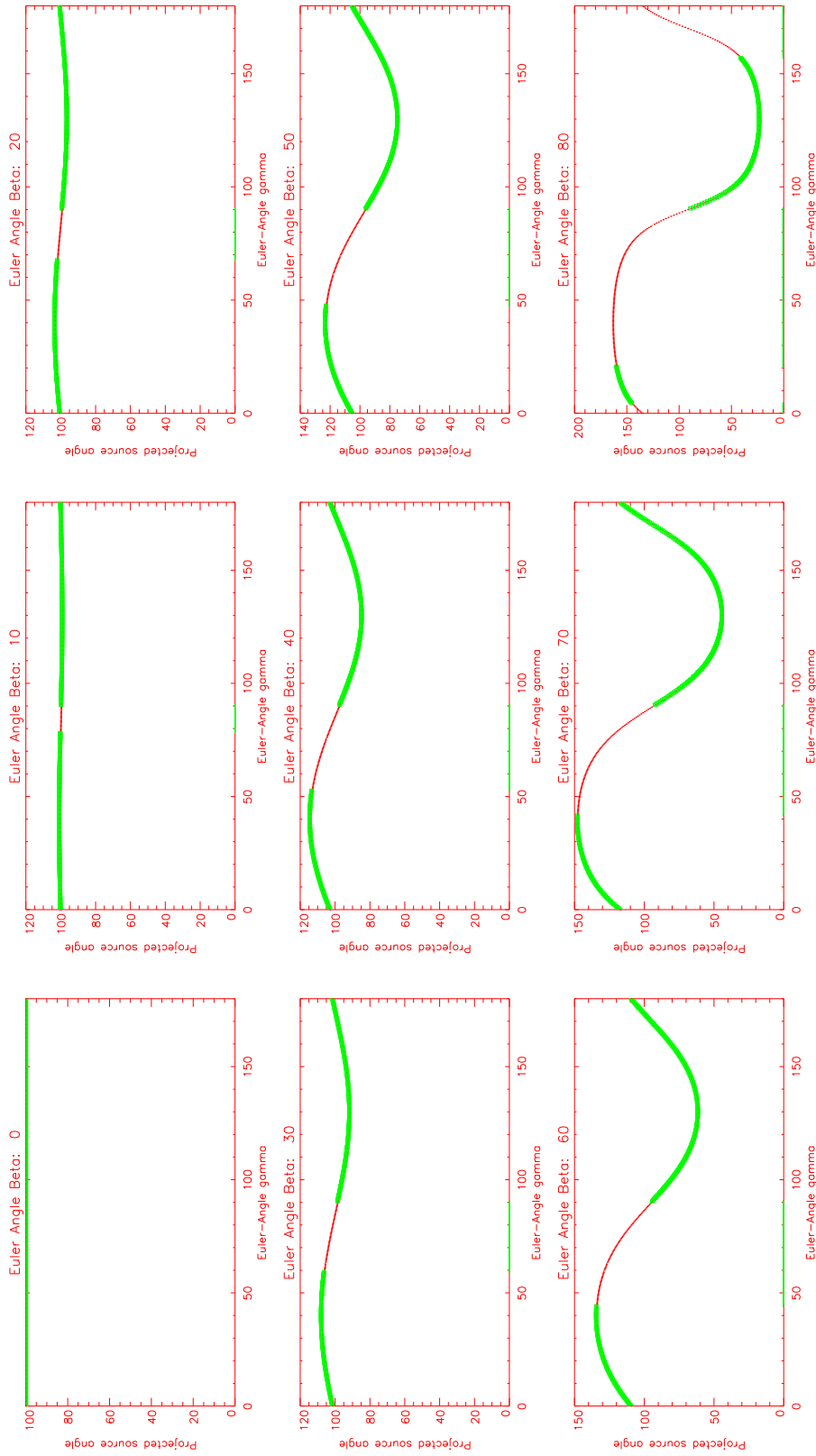


FIGURE B.9— Projected angle distributions corresponding to an intrinsic angle of  $\phi=90^\circ$ . The plot layout is identical to Fig. B.1.



Intrinsic Angle:100

FIGURE B.10— Projected angle distributions corresponding to an intrinsic angle of  $\phi=100^\circ$ . The plot layout is identical to Fig. B.1.

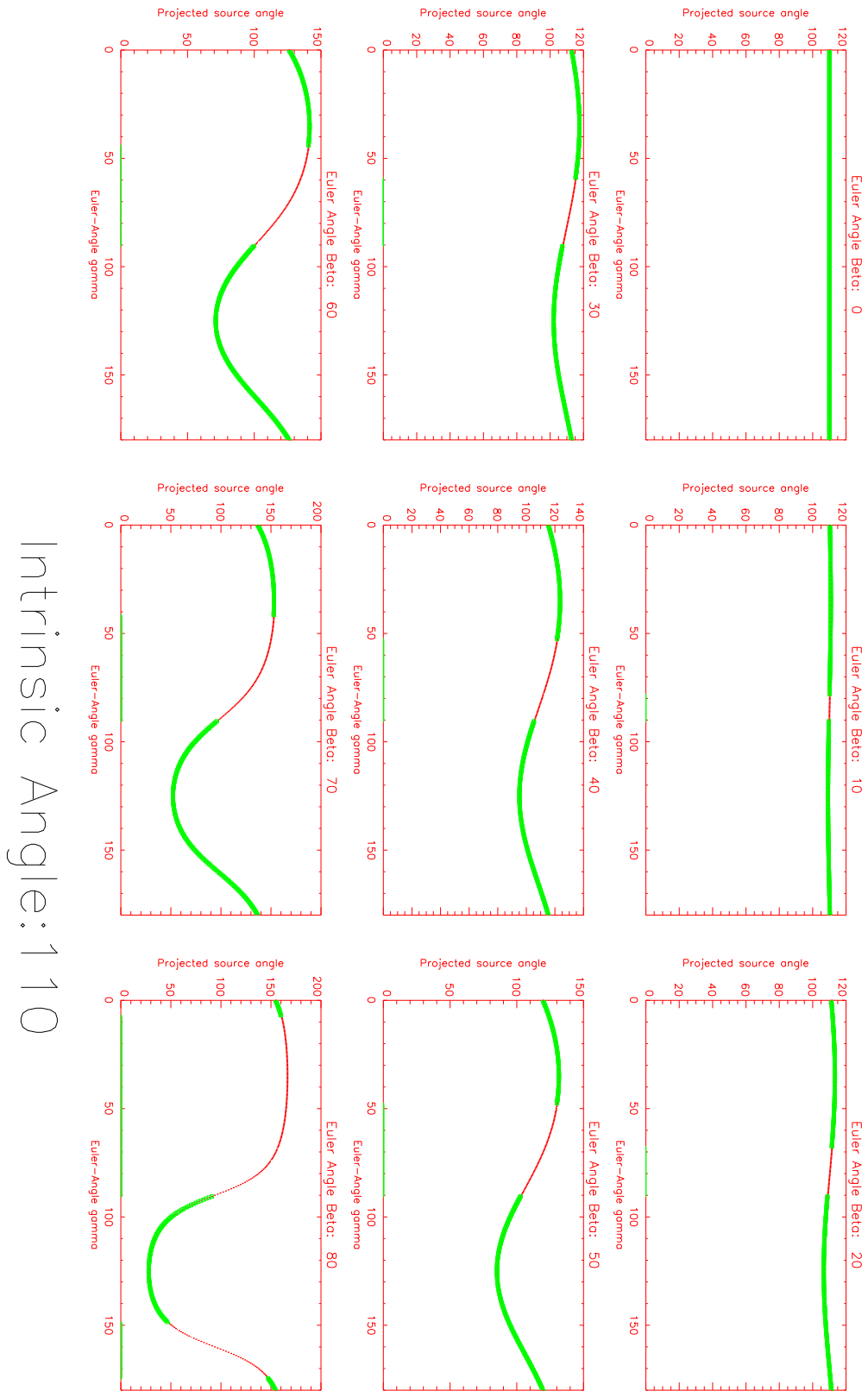
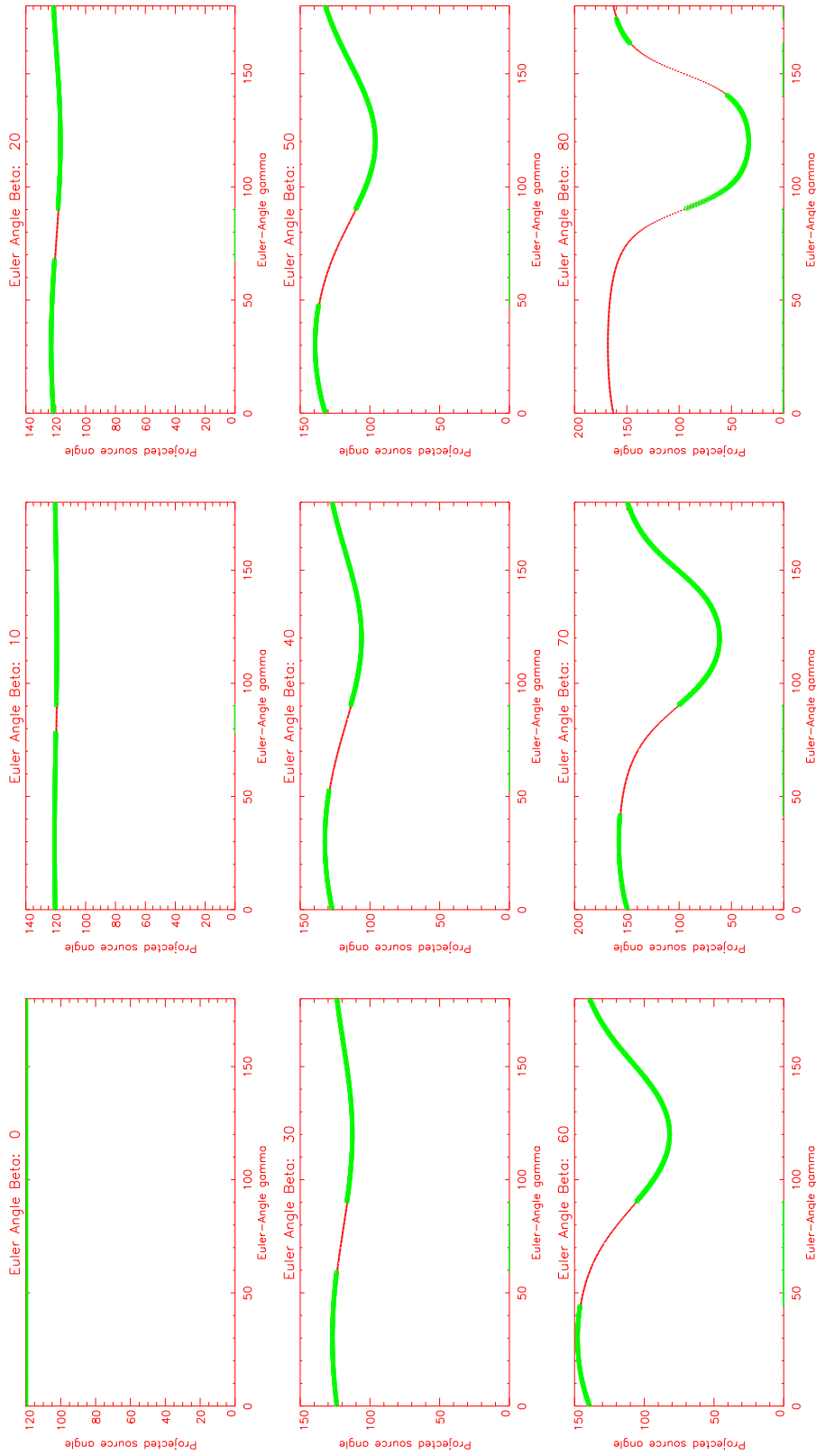


FIGURE B.11— Projected angle distributions corresponding to an intrinsic angle of  $\phi = 110^\circ$ . The plot layout is identical to Fig. B.1.



Intrinsic Angle: 120

FIGURE B.12— Projected angle distributions corresponding to an intrinsic angle of  $\phi=120^\circ$ . The plot layout is identical to Fig. B.1.

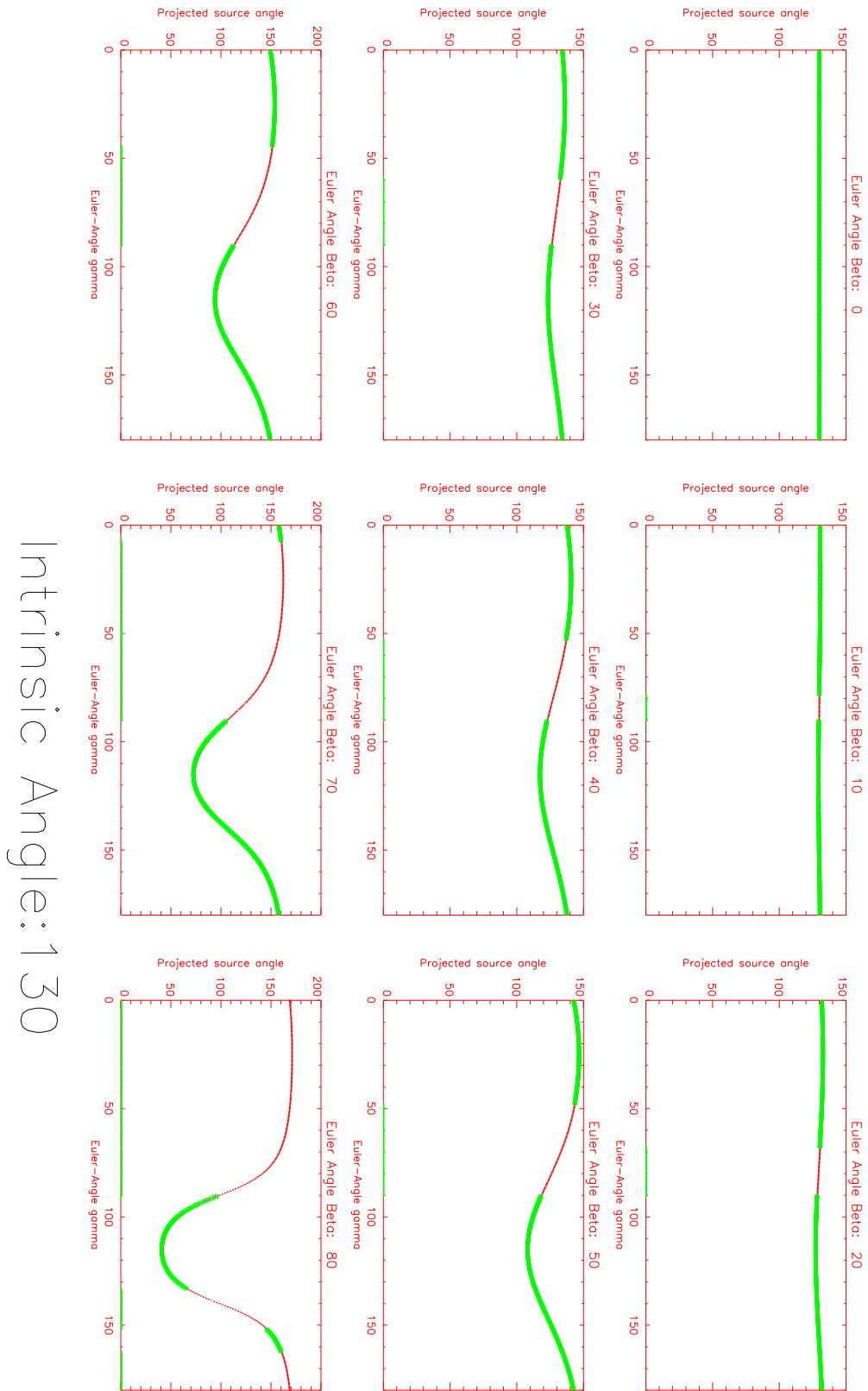
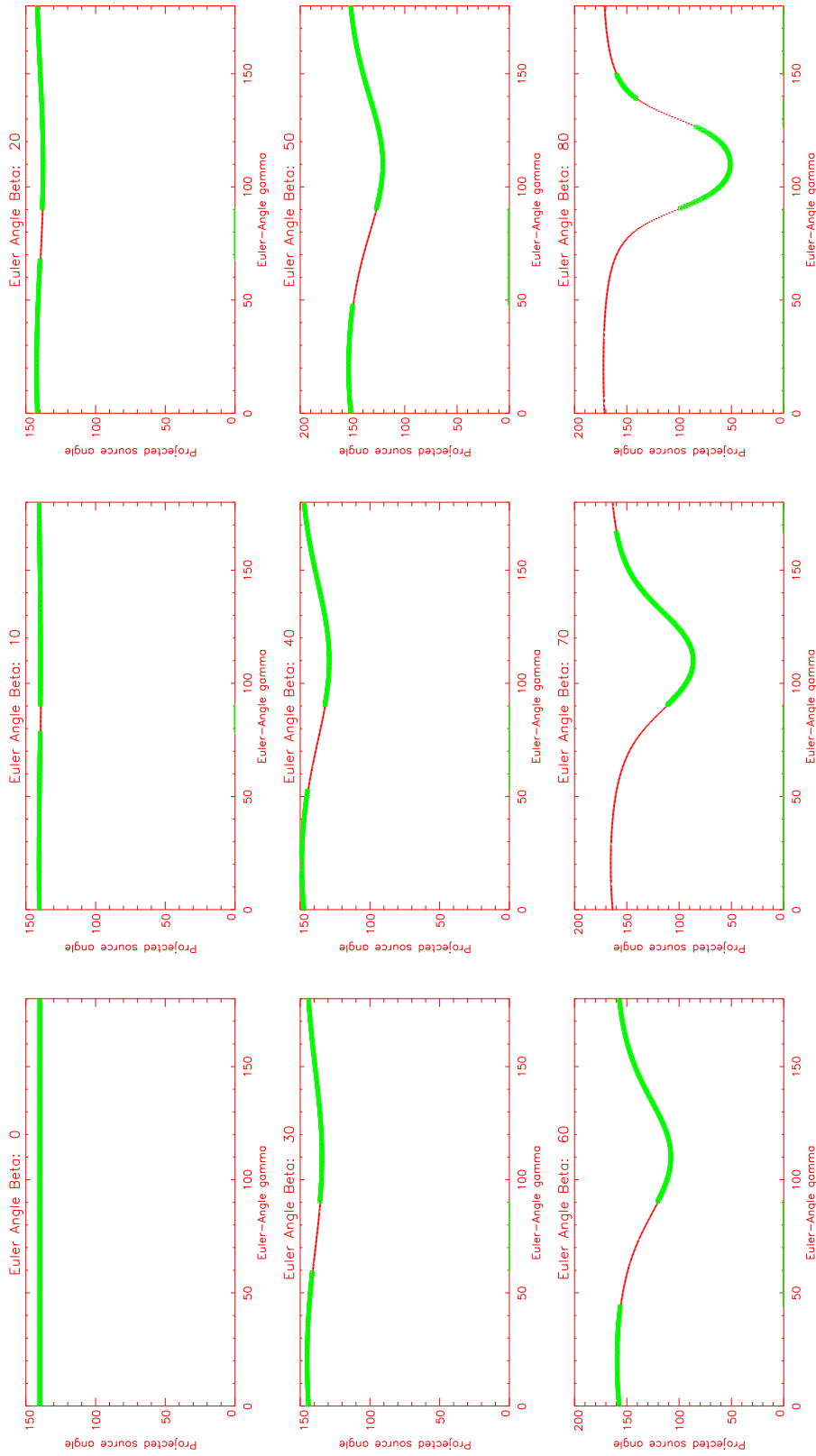


FIGURE B.13— Projected angle distributions corresponding to an intrinsic angle of  $\phi=130^\circ$ . The plot layout is identical to Fig. B.1.





Intrinsic Angle: 140

FIGURE B.14— Projected angle distributions corresponding to an intrinsic angle of  $\phi=140^\circ$ . The plot layout is identical to Fig. B.1.

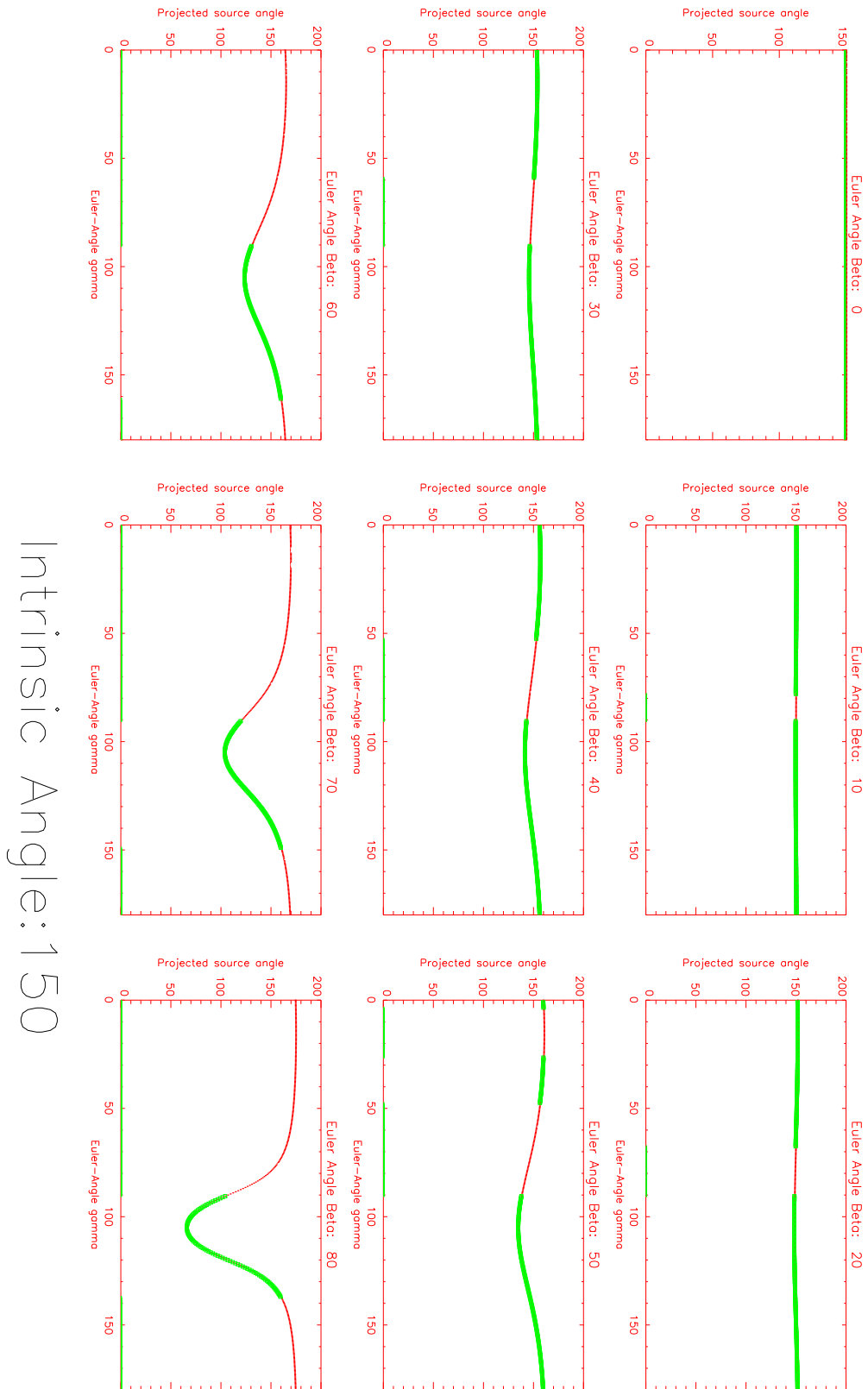
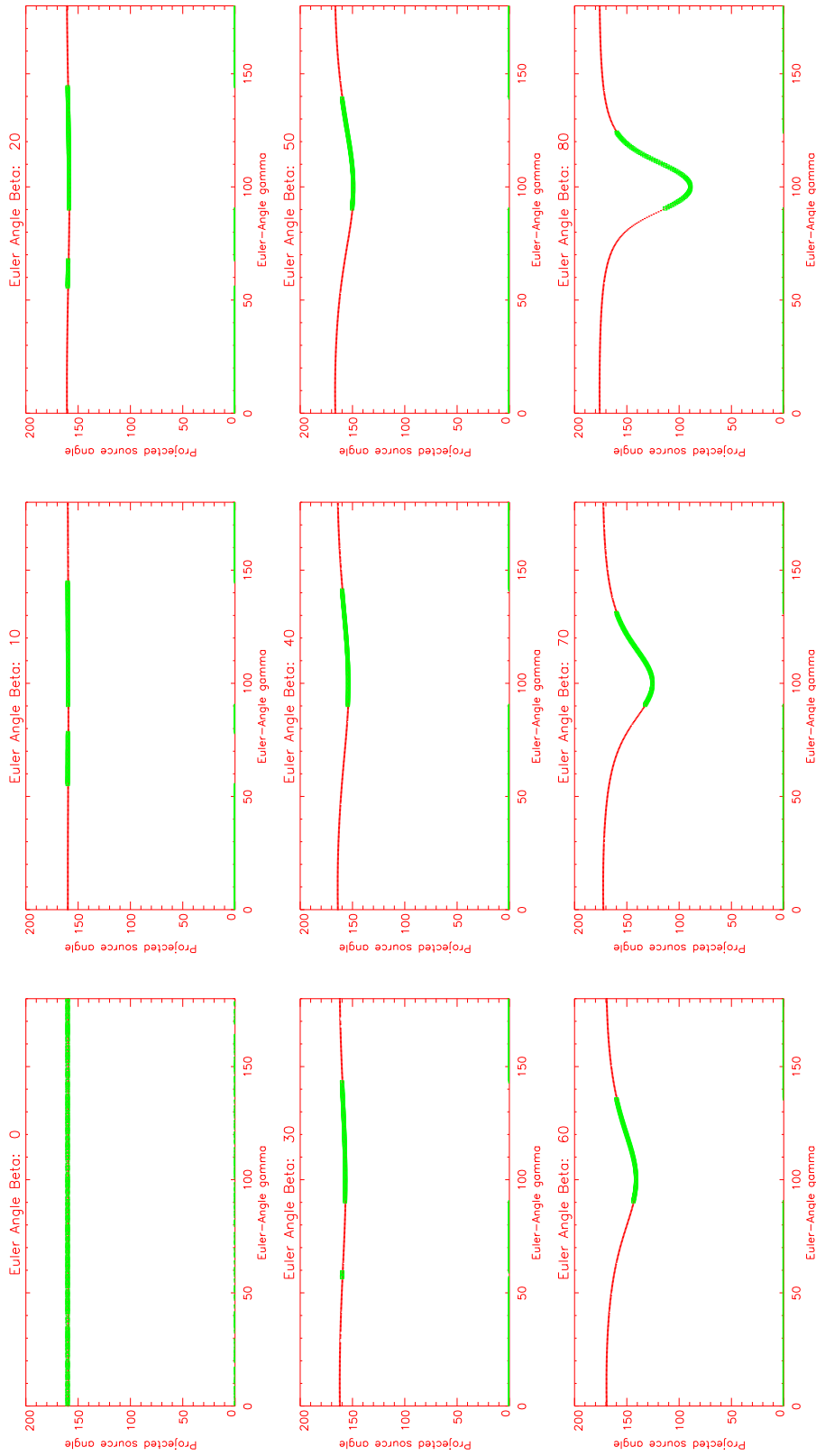


FIGURE B.15— Projected angle distributions corresponding to an intrinsic angle of  $\phi=150^\circ$ . The plot layout is identical to Fig. B.1.



Intrinsic Angle: 160

FIGURE B.16— Projected angle distributions corresponding to an intrinsic angle of  $\phi=160^\circ$ . The plot layout is identical to Fig. B.1.

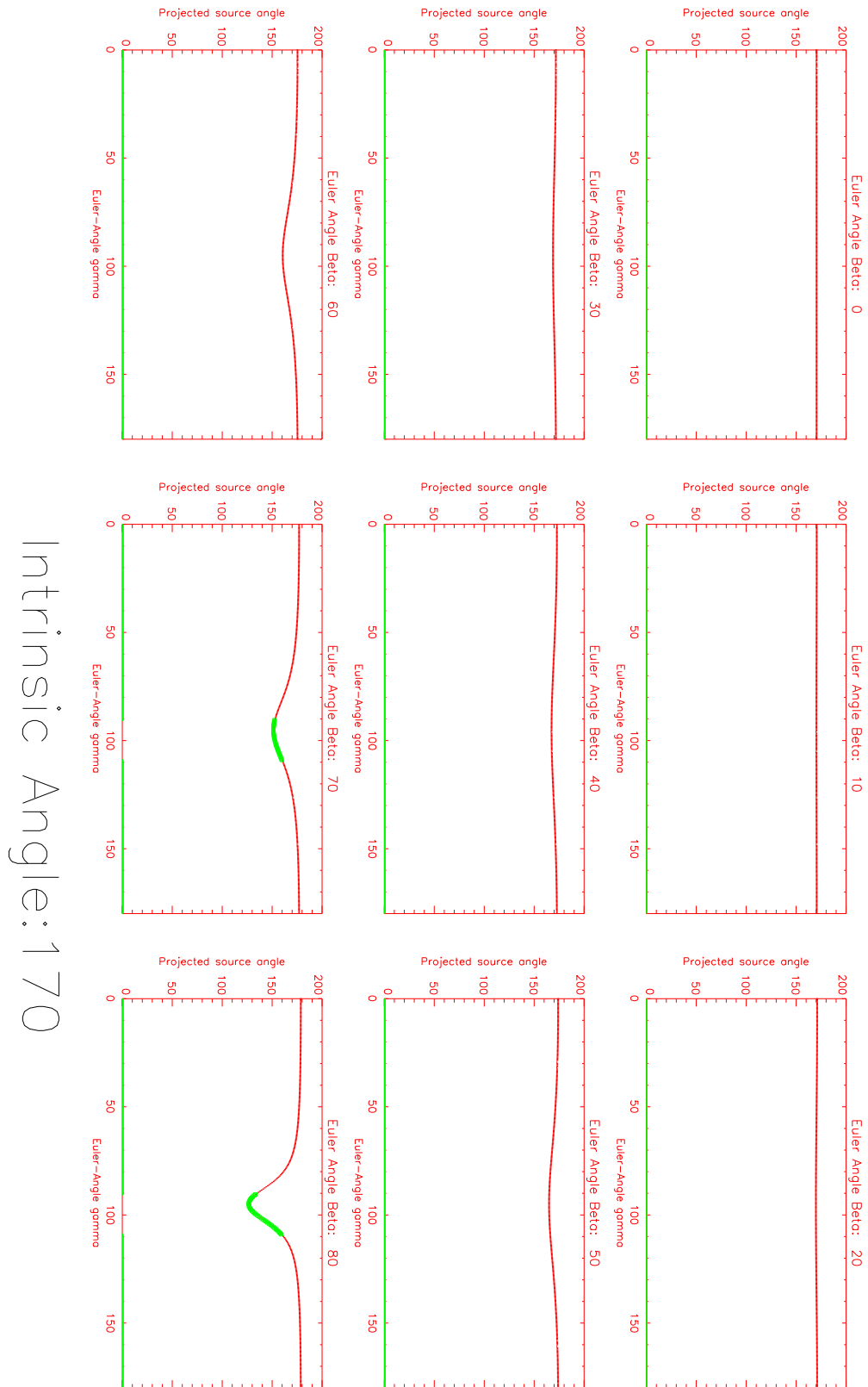


FIGURE B.17— Projected angle distributions corresponding to an intrinsic angle of  $\phi=170^\circ$ . The plot layout is identical to Fig. B.1.

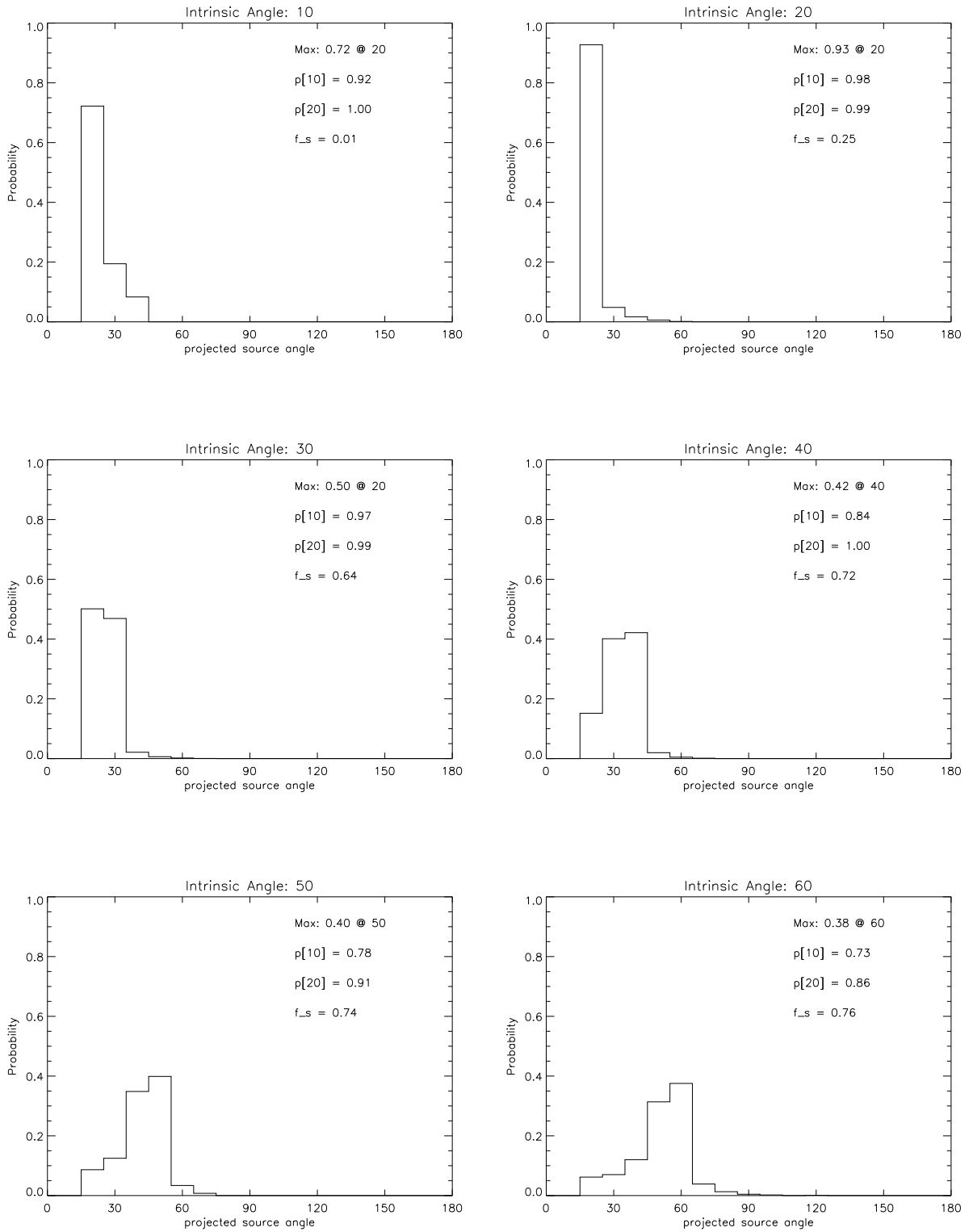


FIGURE B.18— Theoretical distribution of projected angles for a randomly oriented sample of X-shaped sources. Each plot corresponds to a particular intrinsic angle  $\phi$  as indicated in the plot title. These distributions take into account the selection effects outlined in Chap. 7.

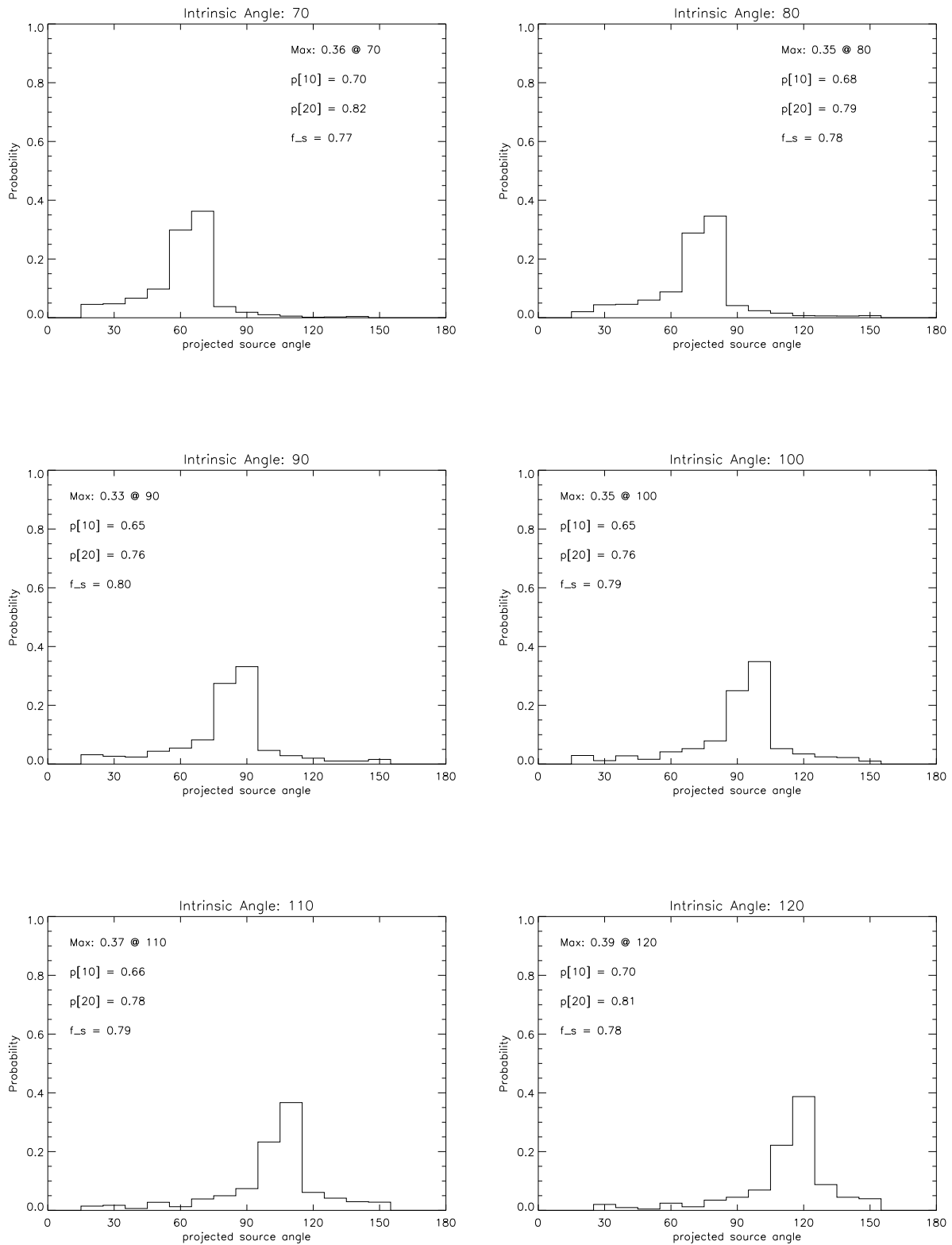


FIGURE B.18— continued

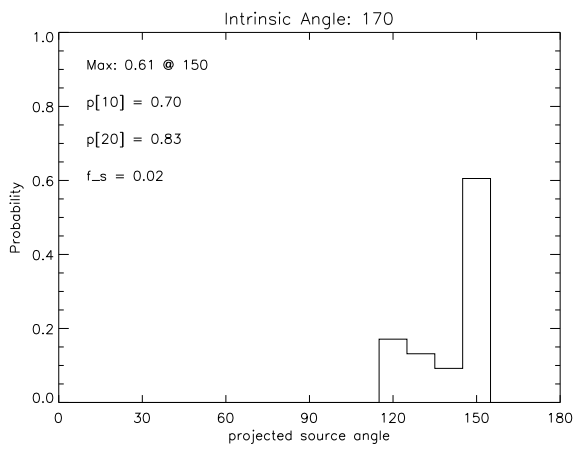
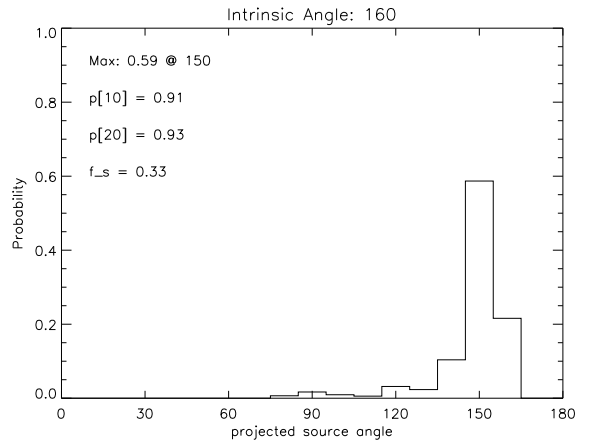
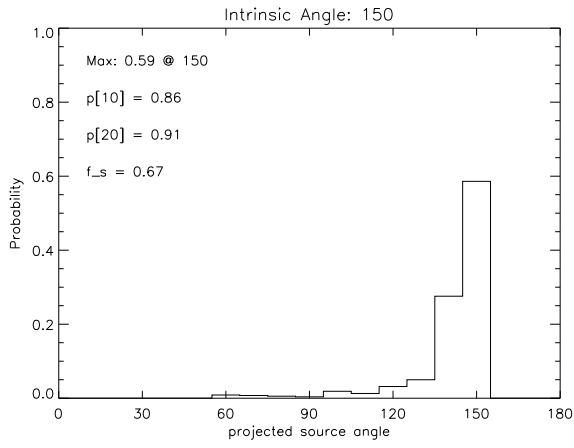
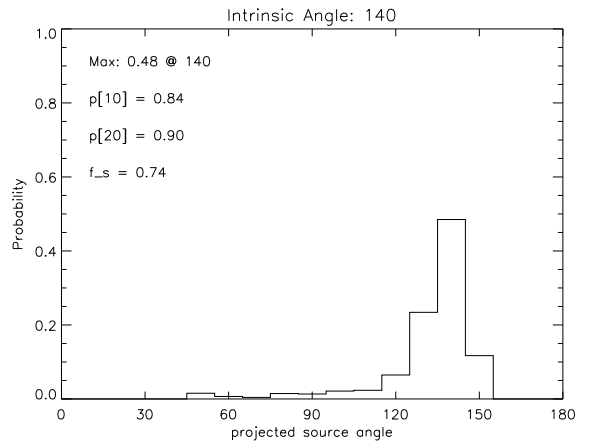
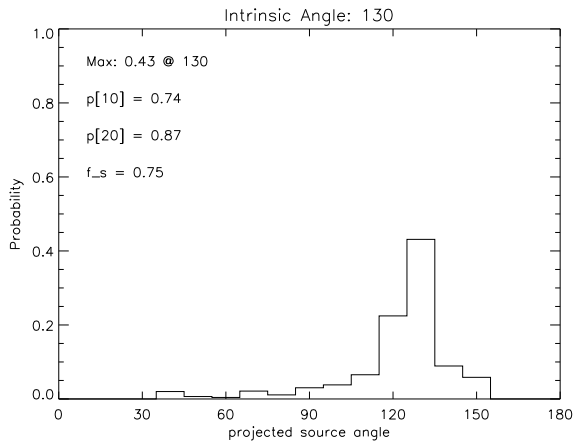


FIGURE B.18— continued





# C

---

## Acronyms

AGN	:	Active Galactic Nuclei
AIPS	:	Astronomical Image Processing System
BH	:	Black Hole
BBH	:	Binary Black Hole
BLRG	:	Broad Line Radio Galaxy
BLR	:	Broad Line Region
CSO	:	Compact Symmetric Object
DDRG	:	Double Double Radio Galaxy
FRI	:	Fanaroff-Riley Type 1
FRII	:	Fanaroff-Riley Type 2
HPBW	:	Half Power Beam Width
HEG	:	High-Excitation Narrow-Line Galaxy
HST	:	Hubble Space Telescope
IGM	:	Intergalactic Medium
IRAS	:	Infrared Astronomical Satellite
ISM	:	Interstellar Medium
NED	:	Nasa Extragalactic Database
NLRG	:	Narrow Line Radio Galaxy
NLR	:	Narrow Line Region
NVSS	:	NRAO VLA Sky Survey
VLA	:	Very Large Array
VLBI	:	Very Long Baseline Interferometry
WAT	:	Wide Angle Tail source
WSRT	:	Westerbork Synthesis Radio Telescope



**References**

- Alexander, P. & Leahy, J. P., 1987. *MNRAS*, 225, 1.
- Aloy, M. A., Ibáñez, J. M., Martí, J. M., Gómez, J. & Müller, E., 1999. *ApJL*, 523, L125.
- Armitage, P. J. & Natarajan, P., 1999. *ApJ*, 525, 909.
- Bardeen, J. M. & Petterson, J. A., 1975. *ApJL*, 195, L65.
- Barthel, P. D. & Arnaud, K. A., 1996. *MNRAS*, 283, L45.
- Barthel, P. D., 1989. *ApJ*, 336, 606.
- Baum, S. A., Heckman, T. M., Bridle, A., Van Breugel, W. & Miley, G. K., 1988. *ApJS*, 68, 643.
- Baum, S. A., Heckman, T. M. & van Breugel, W., 1990. *ApJS*, 74, 389.
- Baum, S. A., O’Dea, C. P., Murphy, D. W. & de Bruyn, A. G., 1990b. *A&A*, 232, 19.
- Baum, S. A., Heckman, T. M. & van Breugel, W., 1992. *ApJ*, 389, 208.
- Begelman, M. C., Blandford, R. D. & Rees, M. J., 1980. *Nature*, 287, 307.
- Black, A. R. S., Baum, S. A., Leahy, J. P., Perley, R. A., Riley, J. M. & Scheuer, P. A. G., 1992. *MNRAS*, 256, 186.
- Bolton, J. G., Stanley, G. J. & Slee, O. B., 1949. *Nature*, 164, 101.
- Borovsky, J. E. & Eilek, J. A., 1986. *ApJ*, 308, 929.
- Burbidge, G. R., 1959. *ApJ*, 129, 849.
- Burns, J. O. & Balonek, T. J., 1982. *ApJ*, 263, 546.
- Burns, J. O., Owen, F. N. & Rudnick, L., 1979. *AJ*, 84, 1683.
- Burns, J. O., Gregory, S. A. & Holman, G. D., 1981. *ApJ*, 250, 450.
- Carilli, C. L., Perley, R. A., Dreher, J. W. & Leahy, J. P., 1991. *ApJ*, 383, 554.
- Chini, R., Kruegel, E., Kreysa, E. & Gemuend, H., 1989. *A&A*, 216, L5.
- Cimatti, A., di Serego-Alighieri, S., Fosbury, R. A. E., Salvati, M. & Taylor, D., 1993. *MNRAS*, 264, 421.
- Cohen, R. D. & Osterbrock, D. E., 1981. *ApJ*, 243, 81.
- Condon, J. J., Frayer, D. T. & Broderick, J. J., 1991. *AJ*, 101, 362.
- Condon, J. J., Anderson, E. & Broderick, J. J., 1995. *AJ*, 109, 2318.
- Condon, J. J., Cotton, W. D., Greisen, E. W., Yin, Q. F., Perley, R. A., Taylor, G. B. & Broderick, J. J., 1998. *AJ*, 115, 1693.
- Cowie, L. L. & McKee, C. F., 1975. *A&A*, 43, 337.

- de Koff, S., Baum, S. A., Sparks, W. B., Biretta, J., Golombek, D., Macchetto, F., McCarthy, P. & Miley, G. K., 1996. *ApJS*, 107, 621.
- Dennett-Thorpe, J., Bridle, A. H., Laing, R. A. & Scheuer, P. A. G., 1999. *MNRAS*, 304, 271.
- Dennett-Thorpe, J., 1996. PhD thesis, University of Cambridge.
- Eilek, J. A. & Arendt, P. N., 1996. *ApJ*, 457, 150.
- Eilek, J. A. & Hughes, P. A., 1991. In: *Beams and Jets in Astrophysics*, 429, ed. Hughes, P. A., Cambridge University Press.
- Eilek, J. A., 1996a. In: *ASP Conf. Ser. 100: Energy Transport in Radio Galaxies and Quasars*, p. 281, eds Hardee, P. E., Bridle, A. H. & Zensus, J. A.
- Eilek, J. A., 1996b. In: *IAU Symp. 175: Extragalactic Radio Sources*, 483, eds Ekers, R., Fanti, C. & Padrielli, L.
- Eisenhardt, P. R. M. & Lebofsky, M. J., 1987. *ApJ*, 316, 70.
- Ekers, R. D., Fanti, R., Lari, C. & Parma, P., 1978. *Nature*, 276, 588.
- Ekers, R., 1982. In: *Extragalactic Radio Sources*, IAU Symposium No. 97, 465, eds Heeschen, D. & Waade, C., Reidel (Boston).
- Fabbiano, G., Trinchieri, G., Elvis, M., Miller, L. & Longair, M., 1984. *ApJ*, 277, 115.
- Fanaroff, B. L. & Riley, J. M., 1974. *MNRAS*, 167, 31P.
- Fomalont, E., 1981. In: *Origin of Cosmic Rays*, 111, eds Setti, G., Spada, G. & Wolfendale, A., Reidel (Boston).
- Golombek, D., Miley, G. K. & Neugebauer, G., 1988. *AJ*, 95, 26.
- Goodson, R. E., Palimaka, J. J. & Bridle, A. H., 1979. *AJ*, 84, 1111.
- Gregorini, L., Padrielli, L., Parma, P. & Gilmore, G., 1988. *AASS*, 74, 107.
- Gregorini, L., Klein, U., Parma, P., Schlickeiser, R. & Wielebinski, R., 1992. *AASS*, 94, 13.
- Gregory, S. A. & Burns, J. O., 1982. *ApJ*, 255, 373.
- Gull, S. F. & Northover, K. J. E., 1973. *Nature*, 244, 80.
- Heckman, T. M., Smith, E. P., Baum, S. A., van Breugel, W. J. M., Miley, G. K., Illingworth, G. D., Bothun, G. D. & Balick, B., 1986. *ApJ*, 311, 526.
- Heckman, T. M., O'Dea, C. P., Baum, S. A. & Laurikainen, E., 1994. *ApJ*, 428, 65.
- Heggie, D. C., 1975. *MNRAS*, 173, 729.
- Hey, J. S., Parsons, S. J. & Phillips, J., 1946. *Nature*, 158, 234.
- Högbom, J. A. & Carlsson, I., 1974. *A&A*, 34, 341.
- Högbom, J. A., 1979. *AASS*, 36, 173.
- Jaffe, W. J. & Perola, G. C., 1973. *A&A*, 26, 423.

- Kaiser, C. R., Schoenmakers, A. P. & Röttgering, H. J. A., 2000. *MNRAS*, 315, 381.
- Kardashev, N. S., 1962. *SvA*, , 317.
- Kellermann, K. I., Pauliny-Toth, I. I. K. & Williams, P. J. S., 1969. *ApJ*, 157, 1.
- Klein, U., Mack, K. H., Gregorini, L. & Parma, P., 1995. *A&A*, 303, 427.
- Laing, R. A. & Peacock, J. A., 1980. *MNRAS*, 190, 903.
- Laing, R. A., Riley, J. M. & Longair, M. S., 1983. *MNRAS*, 204, 151.
- Leahy, J. P. & Perley, R. A., 1991. *AJ*, 102, 1627.
- Leahy, J. P. & Williams, A. G., 1984. *MNRAS*, 210, 929.
- Leahy, J. P., Black, A. R. S., Dennett-Thorpe, J., Hardcastle, M. J., Komissarov, S., Perley, R. A., Riley, J. M. & Scheuer, P. A. G., 1997. *MNRAS*, 291, 20.
- Lense, J. & Thirring, H., 1918. *Phys.Z.*, 19, 156.
- Longair, M. S., 1997. *High Energy Astrophysics*, Vol. 2, Cambridge University Press.
- Mack, K. H., Gregorini, L., Parma, P. & Klein, U., 1994. *AASS*, 103, 157.
- Mack, K.-H., 1996. PhD thesis, University of Bonn.
- Martel, A. R., Baum, S. A., Sparks, W. B., Wyckoff, E., Biretta, J. A., Golombek, D., Macchetto, F. D., De Koff, S., McCarthy, P. J. & Miley, G. K., 1999. *ApJS*, 122, 81.
- Matthews, T. A., Morgan, W. W. & Schmidt, M., 1964. *ApJ*, 140, 35.
- McCarthy, P. J., Spinrad, H. & van Breugel, W., 1995. *ApJS*, 99, 27.
- Meier, D. L., Ulrich, M. H., Fanti, R., Gioia, I. & Lari, C., 1979. *ApJ*, 229, 25.
- Morganti, R., Oosterloo, T. A., Reynolds, J. E., Tadhunter, C. N. & Migenes, V., 1997. *MNRAS*, 284, 541.
- Murgia, M., Fanti, C., Fanti, R., Gregorini, L., Klein, U., Mack, K. H. & Vigotti, M., 1999. *A&A*, 345, 769.
- Murgia, M., 1996. Laurea Thesis, University of Bologna.
- Myers, S. T. & Spangler, S. R., 1985. *ApJ*, 291, 52.
- Natarajan, P. & Armitage, P. J., 1999. *MNRAS*, 309, 961.
- Norman, M. L., 1996. In: *Energy transport in radio galaxies and quasars*, p. 319, eds Hardee, P. E., Bridle, A. H. & Zensus, J. A., ASP, San Francisco.
- Owen, F. N., Eilek, J. A. & Kassim, N. E., 1998. In: *American Astronomical Society Meeting*, 3811.
- Owsianik, I., Conway, J. E. & Polatidis, A. G., 1998. *A&AL*, 336, L37.
- Pacholczyk, A. G., 1970. *Radio Astrophysics*, Freeman.

- Parma, P., Ekers, R. D. & Fanti, R., 1985. *AASS*, 59, 511.
- Perley, R. A., Dreher, J. W. & Cowan, J. J., 1984. *ApJL*, 285, L35.
- Pilkington, J. D. H. & Scott, P. F., 1965. *Mem. R. astr. Soc.*, 69, 183.
- Pooley, G. G., Leahy, J. P., Shakeshaft, J. R. & Riley, J. M., 1987. *MNRAS*, 224, 847.
- Quinlan, G. D. & Hernquist, L., 1997. *New Astronomy*, 2, 533.
- Quinlan, G. D., 1996. *New Astronomy*, 1, 35.
- Raymond, J. C. & Smith, B. W., 1977. *ApJS*, 35, 419.
- Rees, M. J., 1978. *Nature*, 275, 516.
- Rees, M. J., 1984. *ARAA*, 22, 471.
- Rengelink, R. B., Tang, Y., de Bruyn, A. G., Miley, G. K., Bremer, M. N., Roettgering, H. J. A. & Bremer, M. A. R., 1997. *AASS*, 124, 259.
- Roger, R. S., Bridle, A. H. & Costain, C. H., 1973. *AJ*, 78, 1030.
- Roos, N., 1981. *A&A*, 104, 218.
- Roos, N., 1988. *ApJ*, 334, 95.
- Sakelliou, I., Merrifield, M. R. & McHardy, I. M., 1996. *MNRAS*, 283, 673.
- Sandage, A., 1972. *ApJ*, 178, 25.
- Saripalli, L., Subrahmanyam, R. & Hunstead, R. W., 1994. *MNRAS*, 269, 37.
- Scheuer, P. A. G. & Feiler, R., 1996. *MNRAS*, 282, 291.
- Scheuer, P. A. G., 1995. *MNRAS*, 277, 331.
- Schoenmakers, A. P., Mack, K., Lara, L., Roettgering, H. J. A., de Bruyn, A. G., van der Laan, H. & Giovannini, G., 1998. *A&A*, 336, 455.
- Schoenmakers, A. P., de Bruyn, A. G., Röttgering, H. J. A. & van der Laan, H., 1999. *A&A*, 341, 44.
- Schoenmakers, A. P., de Bruyn, A. G., Röttgering, H. J. A., van der Laan, H. & Kaiser, C. R., 2000. *MNRAS*, 315, 371.
- Schoenmakers, A. P., de Bruyn, A. G., Röttgering, H. J. A. & van der Laan, H., 2000. *MNRAS*, 315, 395.
- Shepherd, M. C., Pearson, T. J. & Taylor, G. B., 1995. *BAAS*, 27, 903.
- Siebert, J., Brinkmann, W., Morganti, R., Tadhunter, C. N., Danziger, I. J., Fosbury, R. A. E. & di Serego Alighieri, S., 1996. *MNRAS*, 279, 1331.
- Smith, E. O., Spinrad, H. & Smith, H. E., 1976. *PASP*, 88, 621.
- Spangler, S. P. & Sakurai, T., 1985. *ApJ*, 97, 84.

- Spinrad, H., Djorgovski, S., Marr, J. & Aguilar, L., 1985. *PASP*, 97, 932.
- Strom, R. G. & Conway, R. G., 1985. *AASS*, 61, 547.
- Tadhunter, C. N., Scarrott, S. M., Draper, P. & Rolph, C., 1992. *MNRAS*, 256, 53P.
- Tadhunter, C. N., Morganti, R., di Serego-Alighieri, S., Fosbury, R. A. E. & Danziger, I. J., 1993. *MNRAS*, 263, 999.
- Ulrich, M. H. & Rönnback, J., 1996. *A&A*, 313, 750.
- Vigotti, M., Grueff, G., Perley, R., Clark, B. G. & Bridle, A. H., 1989. *AJ*, 98, 419.
- Werner, P. N., Worrall, D. M. & Birkinshaw, M., 1999. *MNRAS*, 307, 722.
- Williams, P. J. S., Collins, R. A., Caswell, J. L. & Holden, D. J., 1968. *MNRAS*, 139, 289.
- Williams, A., 1991. In: *Beams and Jets in Astrophysics*, p. 342, ed. Hughes, P., Cambridge University Press.
- Wirth, A., Smarr, L. & Gallagher, J. S., 1982. *AJ*, 87, 602.
- Worrall, D. M. & Birkinshaw, M., 1994. *ApJ*, 427, 134.
- Worrall, D. M., Birkinshaw, M. & Cameron, R. A., 1995. *ApJ*, 449, 93.
- Wyndham, J. D., 1966. *ApJ*, 144, 459.
- Zier, C., 2000. PhD thesis, University of Bonn.
- Zirbel, E. L., 1996. *ApJ*, 473, 713.
- Zirbel, E. L., 1997. *ApJ*, 476, 489.
- Zwicky, F. & Kowal, C. T., 1968. *Catalogue of Galaxies and Clusters of Galaxies*, Pasadena, Caltech.





# Acknowledgments

Now that the thesis is completed and I have time to review the years I have spend on writing it I am left with many people to thank that have contributed to the work in one way or the other. First of all I'd like to thank my supervisor Uli Klein who had the initial idea for the thesis work and has encouraged me to do my PhD in the first place. Thanks also to Richard Wielebinski for the financial support and his seemingly infinite patience during my extended finishing phase of the thesis.

I am indebted to Jane Dennett-Thorpe. Many of the ideas of the thesis have evolved out of enlightening discussions with her. I am very grateful to Peter Biermann for his valued scientific input at many points of the thesis, his constant interest in my work, and all the enthusiasm that he was able to convey to me.

Thanks to Ulrich Mebold, Klaas de Boer and the Bonn-GK for 'nurturing' me through the final time of completing the thesis.

I would like to thank all the people from the '1st floor' for the great atmosphere in and outside of the institute.

I am indebted to the many people that have provided me with data from their personal archives or for making their data publicly available.

Thanks to Richard Strom and Tony Foley of NFRA that have introduced me to the NEWSTAR package and helped me immensely in the reduction of the WSRT data.

Thanks to the entire crew of Effelsberg – especially the operators – who have made all the long nights at the telescope an enjoyable time.

Thanks to Izabela...for being on this planet!

Last but not least many, many thanks to my parents that were always there for me and have always supported me in every possible way. Thanks!

*Helge Rottmann, Bonn, July 2001*

This research has made use of the NASA/IPAC Extragalactic Database (NED) which is operated by the Jet Propulsion Laboratory, California Institute of Technology, under contract with the National Aeronautics and Space Administration.



# Lebenslauf

## Persönliche Daten

Name : Helge Rottmann  
geboren am : 21.11.1968  
in : Aachen  
Familienstand : verheirated  
Staatsangehörigkeit : deutsch  
Anschrift : An den Markthallen 2  
53119 Bonn  
E-mail : rottmann@mpifr-bonn.mpg.de

## Ausbildung

1975 - 1985 : Grundschule und Gymnasium  
1985 - 1986 : Amerikanischer Schulabschluß an der Reedley High-School, Reedley CA, USA  
Apr 1989 : Abitur am Konrad-Heeresbach Gymnasium, Mettmann  
1989 - 1996 : Physik und Astronomie Studium an der Uni Bonn  
1989 - 1992 : Studentische Hilfskraft am Max-Planck-Institut für Radioastronomie (MPIfR);  
Gruppe Prof. G. Weigelt (Speckle Masking und optische Interferometrie)  
1992 - 1994 : Studentische Hilfskraft am MPIfR;  
Gruppe Prof. P. Mezger (mm/sub-mm Astronomie)  
1994 - 1996 : Studentische Hilfskraft an der Uni Bonn  
Gruppe Prof U. Klein (Extragalaktische Radioastronomie)  
Apr 1996 : Diplom-Arbeit an der Uni Bonn  
1996 - 2001 : Doktorarbeit am MPIfR  
Betreuer: U. Klein (RAIUB), R. Wielebinski (MPIfR)

